

**Mineral-Fluid interactions and their implications for the  
sequestration of CO<sub>2</sub> in saline aquifers**

Benoit Lamy-Chappuis

Submitted in accordance with the requirements for the degree of  
Doctor of Philosophy

The University of Leeds  
School of Earth and Environment

January, 2015

The candidate confirms that the work submitted is his own, except where work which has formed part of jointly-authored publications has been included. The contribution of the candidate and the other authors to this work has been explicitly indicated below. The candidate confirms that appropriate credit has been given within the thesis where reference has been made to the work of others.

Chapter 3 contains work published in Lamy-Chappuis, B., D. Angus, Q. Fisher, C. Grattoni, and B. W. D. Yardley (2014), Rapid porosity and permeability changes of calcareous sandstone due to CO<sub>2</sub>-enriched brine injection, *Geophys. Res. Lett.*, 41, doi:10.1002/2013GL058534. I carried out all the practical work and interpretation under the supervision of Angus, Fisher and Yardley as part of my PhD studies, while Grattoni provided lab training, guidance and practical assistance.

This copy has been supplied on the understanding that it is copyright material and that no quotation from the thesis may be published without proper acknowledgement.

The right of Benoit Lamy-Chappuis to be identified as Author of this work has been asserted by him in accordance with the Copyright, Designs and Patents Act 1988.

© 2015 The University of Leeds and Benoit Lamy-Chappuis

## **Acknowledgements**

I first would like to thank my main supervisor Bruce Yardley for his trust, support and guidance throughout my time in Leeds. Your positive and open minded attitude has been invaluable to me! Thank you for sharing with me your passion for science!

I also would like to thank my co-supervisors Doug Angus and Quentin Fisher for their availability and their help to identify flaws and strengths in my work.

Thanks to Jörgen Rosenqvist, Andrew Kilpatrick and Bruce Yardley for welcoming me into their team, I truly enjoyed those Monday morning brainstorming sessions. Thank you also for taking me out of home once in a while, to go to the pub, to a football game or for a nice walk in the countryside.

It was a great pleasure to work at the Wolfson laboratory with Carlos Grattoni, John Martin and Phil Guise. Thanks for helping me design new experiments, always showing great flexibility and interest.

Thanks to lab managers and technicians at the University of Leeds who helped me at various stages of my PhD. I'm thinking of Sam Allshorn, Lesley Neve, Tony Windross, the IT and supercomputer staff and many others I must forget.

I also enjoyed working with all members of the CO2FLIP project including Shuisheng He, Yingqing Zu and Jianfei Xie at the University of Sheffield, Dubravka Pokrajac at the University of Aberdeen and Ruina Xu, Peixue Jiang and Jin Ma from Tsinghua University (China). It was great gaining broader perspectives and working as a team with you all.

Thanks to Simon Bottrell and Sevcet Durucan for doing a great job at examining my thesis.

Thanks to my family: parents, brother and sisters for their love and support, for helping me at times escape and at time refocus on my work.

Thanks to my wife Jin and my son Matia for giving a greater purpose to my work; and thanks again to Jin for her practical help in writing this thesis and for the numerous scientific discussions!

Finally I would like to warmly acknowledge the EPSRC for funding this work.

## **Abstract**

It is known that acidification of reservoirs pore fluids during CO<sub>2</sub> subsurface injection leads to fluid-rock interactions. Understanding the effect that these interactions could have on transport and mechanical properties of rocks is particularly relevant for calcite-bearing reservoirs in which rapid pores network evolution could compromise or reinforce the injection operation.

In this work, specific experiments were conducted to study the impact of fluid rock interactions on petrophysical properties. The experiments involved the injection into rock cores of CO<sub>2</sub>-saturated brines to investigate rapid calcite dissolution effects and CO<sub>2</sub> plus calcite saturated water to study calcite re-precipitation. Complementary fluid flow modelling at the pore scale was carried out to simulate changes in permeability brought by calcite dissolution.

Calcite dissolution directly impacted the permeability and the rock strength in a way that would have been underestimated in classical reservoir simulations. The permeability increase ranged between 50 and 80% while widely used porosity-permeability relationships would predict 10 to 20%, pore scale modelling predictions were found to be more reliable. The change in the rock strength was even more spectacular with a decrease of the shear and bulk moduli of 20% when empirical equations would give a negligible change.

Combined experiments and simulations were also used to test the long term CO<sub>2</sub> stabilization process known as capillary trapping. The study concluded that CO<sub>2</sub> dissolution in brine could give rise to CO<sub>2</sub> accumulation in regions of the reservoirs containing larger pores. This could significantly modify CO<sub>2</sub> mobility and goes against common belief of capillary trapping stability.

This dissertation demonstrate CO<sub>2</sub> injection can lead to critical modifications in rock petrophysical properties as well as CO<sub>2</sub> trapping processes and that laboratory experiments and pore scale modelling can provide valuable insight into these changes.

## Table of Contents

<b>Acknowledgements</b> .....	<b>iii</b>
<b>Abstract</b> .....	<b>iv</b>
<b>Table of Contents</b> .....	<b>v</b>
<b>List of Tables</b> .....	<b>x</b>
<b>List of Figures</b> .....	<b>xi</b>
<b>List of Abbreviations</b> .....	<b>xix</b>
<b>Chapter 1 Introduction</b> .....	<b>1</b>
1.1 Why Geological Carbon Sequestration? The global warming issue.....	1
1.1.1 Causes and consequences.....	1
1.1.2 Challenges and solutions.....	6
1.2 Introduction to Geological Carbon Sequestration (GCS).....	7
1.2.1 Aim and timescale of GCS.....	7
1.2.2 Technical aspects and feasibility of GCS.....	8
1.2.3 Cost, safety and efficiency.....	9
1.2.4 General motivation for this thesis.....	10
1.2.5 Thesis outline.....	11
<b>Chapter 2 The Physics and Chemistry underpinning GCS</b> .....	<b>12</b>
2.1 Introduction.....	12
2.2 Physics of GCS.....	13
2.2.1 Fluid viscosities and densities.....	13
2.2.1.1 CO <sub>2</sub> density and viscosity.....	14
2.2.1.2 Water density and viscosity.....	16
2.2.1.3 NaCl brine density and viscosity.....	18
2.2.1.4 Carbonated NaCl brine density and viscosity.....	18
2.2.2 Single Phase flow.....	19
2.2.3 Multiphase flow.....	23
2.2.3.1 Relative Permeability.....	23
2.2.3.2 Capillary pressure.....	25
2.2.3.3 Fingering.....	27
2.2.3.4 Residual trapping.....	28
2.2.3.5 Injection pressure.....	30
2.2.4 Geomechanics.....	31

2.2.4.1 Fault leakage risks .....	32
2.2.4.2 Well leakage risk .....	38
2.2.4.3 Seismic monitoring .....	38
2.2.5 Transition.....	39
2.3 Chemistry of GCS .....	39
2.3.1 CO <sub>2</sub> -Brine mutual solubility.....	39
2.3.2 Fluid-rock interactions .....	42
2.3.2.1 Mineral dissolution.....	43
2.3.2.2 Mineral precipitation/trapping .....	45
2.3.2.3 Impurities in the injected gas phase .....	47
2.3.2.4 Field evidence of fluid-rock interactions .....	47
2.4 Implications of fluid-rock interactions.....	48
2.4.1 Impact on caprock petrophysical properties .....	49
2.4.2 Impact on reservoir petrophysical properties.....	50
2.5 Conclusion and knowledge gaps.....	52
2.5.1 Scale problem .....	53
2.5.2 Porosity-permeability relationship.....	54
2.5.3 Geomechanics .....	55
2.5.4 Aim, methods and limitations.....	55
<b>Chapter 3 The effect of CO<sub>2</sub>-enriched brine injection on the hydrological properties of sandstones. ....</b>	<b>57</b>
3.1 Samples .....	57
3.1.1 Cayton Bay sandstone .....	57
3.1.1.1 Mineralogy.....	57
3.1.1.2 Minerals distribution maps.....	58
3.1.1.3 Petrophysical properties.....	59
3.1.2 Bramhope sandstone .....	61
3.2 Experimental conditions and protocol.....	61
3.2.1 Rock and fluid properties monitoring .....	61
3.2.1.1 Permeability monitoring.....	61
3.2.1.2 Fluid chemistry monitoring.....	62
3.2.1.3 Porosity monitoring.....	63
3.2.2 Injection fluid preparation .....	66
3.3 Experimental results .....	69
3.3.1 Cayton Bay non-reactive baseline experiment .....	69
3.3.2 CO <sub>2</sub> -saturated brine injection experiments .....	71

3.3.2.1 Calcite dissolution at the core scale .....	71
3.3.2.2 Calcite dissolution at the pore scale .....	74
3.3.2.3 Transport-control of calcite dissolution .....	75
3.3.3 Bramhope sandstone .....	78
3.4 Porosity-permeability relationship .....	79
3.4.1 Model fitting of Cayton Bay sandstone results .....	79
3.4.2 Hypotheses to explain model and experiments discrepancies .....	80
3.4.3 Changes in tortuosity.....	83
3.5 Conclusion .....	85
<b>Chapter 4 Pore scale simulation of fluid flow in original and modified rock models. ....</b>	<b>87</b>
4.1 Introduction .....	87
4.2 Generation of a porosity model .....	89
4.2.1 Micro-CT scans and mesh extraction .....	89
4.2.2 Mesh modification .....	94
4.2.3 Estimation of the representative elementary volume.....	96
4.3 Absolute permeability predictions from original and modified models.....	98
4.3.1 Simulations setup and parameters.....	98
4.3.2 Qualitative observations .....	100
4.3.3 Statistics of fluid flow.....	106
4.4 Comparison of results from modelling and experiments.....	112
4.4.1 FLUENT permeability predictions compared with a simple capillary tube model.....	112
4.4.2 Comparison of the calcite dissolution case with experimental observations .....	122
4.5 Conclusions.....	126
<b>Chapter 5 The effect of CO<sub>2</sub>-enriched brine injection on the mechanical properties of calcite bearing sandstone.....</b>	<b>128</b>
5.1 Introduction .....	128
5.2 Sonic velocity measurements.....	128
5.2.1 Basic concepts .....	128
5.2.2 Experimental design and sample preparation .....	130
5.2.3 Rock and fluid controls on velocity .....	135
5.2.4 Gassmann modelling of fluid substitution.....	138
5.3 Sonic velocity measurements on reacted and unreacted cores ..	144

5.3.1 Fluid-rock reaction effects on sonic velocity .....	144
5.3.2 Calcite dissolution effect for the Cayton Bay sandstone...	145
5.3.3 Significance for 4D seismic monitoring of GCS .....	152
5.4 Peak and Yield strength .....	157
5.4.1 Basic concepts .....	157
5.4.2 Strength measurements on reacted and unreacted cores .....	159
5.5 Conclusion.....	164
<b>Chapter 6 Experimental study of calcite precipitation triggered by fluid depressurization and CO<sub>2</sub> degassing. ....</b>	<b>166</b>
6.1 Introduction.....	166
6.2 Experiment description .....	168
6.2.1 Experimental system and methodology.....	168
6.2.2 Sample description.....	170
6.2.3 Injected fluid description .....	171
6.3 Experimental results .....	172
6.3.1 CO <sub>2</sub> degassing preliminary test .....	172
6.3.2 Calcite precipitation main experiment.....	174
6.4 Conclusions.....	179
<b>Chapter 7 Long term evolution of capillary trapped CO<sub>2</sub> bubbles, experiments and simulations.....</b>	<b>181</b>
7.1 Introduction.....	181
7.2 Experimental design .....	182
7.3 Experimental results .....	185
7.4 Numerical Simulation of CO <sub>2</sub> Redistribution .....	191
7.4.1 Code description .....	191
7.4.2 Simulation results .....	193
7.5 Conclusions.....	202
<b>Chapter 8 Conclusions and future work.....</b>	<b>203</b>
8.1 Summary and conclusions. ....	203
8.1.1 CO <sub>2</sub> -Fluid-Rock reactions.....	203
8.1.1.1 Experimental investigations on the nature and implications of geochemical reactions.....	203
8.1.1.2 Simulating and predicting the outcome of geochemical reactions.....	205
8.1.1.3 Integration of this thesis work for improved injection monitoring. ....	206

8.2 Remaining questions and future work. ....	206
<b>Bibliography .....</b>	<b>209</b>
<b>List of Parameters .....</b>	<b>238</b>
<b>Appendix A</b>	
<b>Construction of mineral maps. ....</b>	<b>239</b>
<b>Appendix B</b>	
<b>Details of the calculation of dimensionless parameters for</b>	
<b>Table 3.3.....</b>	<b>240</b>
<b>Appendix C Random walk Matlab code.....</b>	<b>241</b>
<b>Appendix D Residual bubbles Matlab simulation code .....</b>	<b>245</b>

## List of Tables

<b>Table 3.1 Mineralogy of two Cayton bay sandstone samples acquired with QXRD technique.....</b>	<b>58</b>
<b>Table 3.2 Mineralogy of Bramhope sandstone acquired with QXRD technique. ....</b>	<b>61</b>
<b>Table 3.2 PHREEQC simulations results.....</b>	<b>68</b>
<b>Table 3.3 Summary of experimental conditions and results, tabulated by experiment number .....</b>	<b>71</b>
<b>Table 4.1 Porosity models properties.....</b>	<b>93</b>
<b>Table 5.1 Summary of sonic velocity experiment.....</b>	<b>134</b>
<b>Table 5.2 Mineral bulk moduli and volume fraction used for the calculation of the <math>K_m</math> parameter. ....</b>	<b>139</b>
<b>Table 5.3 Fluid properties used for the Gassmann modelling .....</b>	<b>140</b>
<b>Table 7.1 Parameters used for the different simulation series.....</b>	<b>194</b>

## List of Figures

Figure 1.1 <i>Line plot of global mean land-ocean temperature index.</i> .....	2
Figure 1.2 <i>Observed atmospheric CO<sub>2</sub> increase derived from direct measurements</i> .....	3
Figure 1.3 <i>Radiative forcing, relative to 1750, of all the long-lived greenhouse gases</i> .....	4
Figure 1.4 <i>Model simulations by the IPCC (IPCC, 2007) estimating Earth warming, depending on CO<sub>2</sub> emissions scenarios</i> .....	5
Figure 1.5 <i>Key technologies for a global CO<sub>2</sub> emissions reduction strategy</i> .....	6
Figure 1.6 <i>IEA roadmap for CCS projects by 2050</i> .....	8
Figure 1.7 <i>World prospective areas for GCS according to Bradshaw and Dance (2004)</i> .....	9
Figure 2.1 <i>P-T diagram colored by CO<sub>2</sub> density where two end-member P-T paths with reservoir depth are also represented</i> .....	15
Figure 2.2 <i>P-T diagram colored by CO<sub>2</sub> viscosity where two end-member P-T paths with reservoir depth are also represented</i> .....	16
Figure 2.3 <i>P-T diagram colored by water density where two end-member P-T paths with reservoir depth are also represented</i> .....	17
Figure 2.4 <i>P-T diagram colored by water viscosity where two end-member P-T paths with reservoir depth are also represented</i> .....	17
Figure 2.5 <i>Viscosity evolution with reservoir depth for water and two NaCl brines (1M and 5M concentration)</i> .....	18
Figure 2.6 <i>Viscosity evolution with reservoir depth for pure brines and carbonated brines at various pressures (only the hydrostatic curve is used for reference in the pure brine case)</i> .....	19
Figure 2.7 <i>Time-lapse seismic images from Sleipner showing vertical sections (along the top) and maps of the expanding plume in 1994, 2001, 2004 and 2006 (along the bottom)</i> .....	21
Figure 2.8 <i>Time-lapse evolution of the CO<sub>2</sub> plume in a horizontal reservoir showing gravity effect.</i> .....	22
Figure 2.9 <i>Illustration of a channeling phenomenon.</i> .....	23
Figure 2.10 <i>pressure and temperature conditions of the drainage CO<sub>2</sub>-brine relative permeability measurements reported in the literature</i> .....	24
Figure 2.11 <i>“Cartoon of a droplet of supercritical CO<sub>2</sub> confined by water on a mineral substrate, showing different wetting properties with respect to supercritical CO<sub>2</sub></i> .....	25

Figure 2.12 <i>Saturation patterns for various capillary number (<math>Ca</math>), viscosity ratio (<math>M</math>), and wettability conditions (varying with mineralogy)</i> .....	28
Figure 2.13 Time evolution of the injection pressure at the well for fixed reservoir porosity and injection rate and variable reservoir permeability.....	31
Figure 2.14 <i>Stress measurements made in brittle rock</i> .....	33
Figure 2.15 <i>Effect of the differential stress decrease due to fluid pressure (pore pressure) increase on the fracture type in two-dimensional Mohr diagram</i> .....	34
Figure 2.16 <i>Changes in faulting regime depending on the relative magnitude of the vertical (<math>S_v</math>) and horizontal (<math>S_H</math> and <math>S_h</math>) stresses</i> .....	35
Figure 2.17 <i>Mohr diagrams showing the evolution of shear and normal stresses within reservoir domains</i> .....	36
Figure 2.18 <i>Schematic illustration explaining how the reservoir stress path operates</i> .....	37
Figure 2.19 <i>Schematic cross-section of a reservoir-caprock system, showing how <math>CO_2</math> injection can lead to stress arching effects, wherein the vertical stress becomes heterogeneous across the reservoir</i> .....	38
Figure 2.20 <i><math>CO_2</math> solubility as a function of depth below the surface</i> .....	40
Figure 2.21 Inter-relations between the principal processes involved in GCS, from Johnson et al. (2004).....	52
Figure 3.1 Mineralogical map showing the minerals and pores distribution and size on a 2D section of Cayton Bay sandstone.....	59
Figure 3.2 NMR $T_2$ curves representing the pore size distributions of two Cayton Bay sandstone cores.....	60
Figure 3.3 SEM image of the bulk rock (Cayton Bay sandstone).....	60
Figure 3.4 Schematic overview and picture of the experimental setup.....	63
Figure 3.5 2mm thick cross section of a Cayton Bay rock core as seen in the PICKER PQ 2000 medical CT scanner.....	64
Figure 3.6 3D reconstruction of a rock core taken during a $CO_2$ injection experiment.....	65
Figure 3.7 Breakthrough curves resulting from a 1D reactive transport simulations performed with PHREEQC.....	67
Figure 3.8 Temperature and differential pressure traces from the Cayton Bay unreactive experiment.....	69
Figure 3.9 Breakthrough curves from the Cayton Bay experiment displaying main cations concentrations.....	70

Figure 3.10 Time series to demonstrate porosity evolution in experiment 3 .....	72
Figure 3.11 Breakthrough curves from experiment .....	73
Figure 3.12 Back pressure (same as pore pressure) and pH traces from experiment 3 .....	75
Figure 3.13 Breakthrough curves from experiments 1 and 6 .....	76
Figure 3.14 Permeability and pH curves for experiments 3, 4 and 5 ....	77
Figure 3.15 Relative changes of porosity and permeability for 6 experiments .....	80
Figure 3.16 Comparison of the pore size distribution and cumulative porosity curves before and after calcite dissolution for two side experiments .....	81
Figure 3.17 SEM images of rock sample before experiment (left) and afterwards (right) .....	82
Figure 3.18 3D reconstruction from micro-CT scans representing a 9 mm <sup>3</sup> volume of Cayton Bay sandstone .....	83
Figure 3.19 Random walk simulation results.....	84
Figure 4.1 CT scan cross section of a Cayton Bay cylindrical sample.....	90
Figure 4.2 3D volume reconstruction composed of 1400 horizontal CT scans .....	91
Figure 4.3 Illustration of the segmentation process .....	92
Figure 4.4 Comparison of a small sub-volume permeability.....	94
Figure 4.5 Comparison of three models containing 400 <sup>3</sup> , 300 <sup>3</sup> and 200 <sup>3</sup> elements .....	95
Figure 4.6 Example of subdivision branch used to evaluate porosity convergence with model volume.....	97
Figure 4.7 Porosity convergence with model volume.....	98
Figure 4.8 Test of the wall boundary conditions .....	99
Figure 4.9 Pressure drop in the A1 model with constant velocity condition at the inlet.....	100
Figure 4.10 Flow paths colored by velocity magnitude in the initial A1 model with constant pressure conditions on the left and right faces.....	101
Figure 4.11 Close up on the Figure 4.10 (0.5x0.5x0.5 mm <sup>3</sup> sub-volume) showing flow velocity dependence on the pore geometry.....	101
Figure 4.12 Flow paths colored by velocity magnitude in the A1 model with dilated pores.....	102
Figure 4.13 Flow paths colored by velocity magnitude in the A1 model with calcite dissolved.....	103

Figure 4.14 Pores (light blue) and calcite (blue) distribution in the A1 model. ....	103
Figure 4.15 Pressure drop visualization in the B1 model. ....	104
Figure 4.16 Comparison of the pressure drop in A1 model with constant velocity inlet (left) and constant outlet pressure in the A1 model in three different cases.....	105
Figure 4.17 Example of velocity magnitude histogram in the initial A1 model .....	106
Figure 4.18 Example of transverse velocity histogram in the initial B1 model .....	107
Figure 4.19 Comparison of the flow velocity histogram (in the main flow direction) for the B1 model at various resolutions .....	108
Figure 4.20 Comparison of velocity histogram (in the main flow direction) for A1 at the lowest resolution and in the three different porosity cases.....	109
Figure 4.21 Comparison of velocity histogram (in the main flow direction) for A1 at the highest resolution and in the three different porosity cases.....	109
Figure 4.22 Comparison of the velocity magnitude in the main flow direction on cross sections of the A1 model in the three different porosity cases.....	110
Figure 4.23 Visualization of pressure gradient at lowest and highest resolution (Top part) and comparison at low resolution between the B1 and C1 models (lower part).....	112
Figure 4.24 Porosity of the B1 and B2 models at various resolutions.....	113
Figure 4.25 Wetted area of the B1 and B2 models. ....	114
Figure 4.26 Mean hydraulic radius of the various B1 and B2 models.....	115
Figure 4.27 Permeability calculated with Equation 4.2 of the B1 and B2 models.....	116
Figure 4.28 Comparison between FLUENT permeability calculations and Equation 4.1 for the B1 and B2 model.....	118
Figure 4.29 Comparison between FLUENT results for A1, B1 and B2 with experimental results (on the vertical axis) and Equation 4.2 where $R_h$ =voxel size was used.....	119
Figure 4.30 Increase in permeability after pore dilatation calculated with FLUENT (dotted lines) and Equation 4.2 (symbols). ....	120
Figure 4.31 Increase in permeability after calcite dissolution calculated with FLUENT (dashed lines), Equation 4.2 (empty symbols) and Equation 4.3 (filled symbols).....	122

<b>Figure 4.32 SEM images (Lower part of Figure 3.3) presenting silica fragments filling the pores before and after calcite dissolution experiments (left and right).</b> .....	<b>123</b>
<b>Figure 4.33 Comparison of the change in permeability after calcite dissolution determined with core scale experiments (6 crosses), FLUENT simulations (disk symbols) and K-C equation (curves)</b> .....	<b>125</b>
<b>Figure 4.34 Conceptual rock model summarizing observations made on the model ability to correctly capture calcite dissolution features but overestimating absolute permeability.</b> .....	<b>125</b>
<b>Figure 5.1 Triaxial cell equipped with sample heater used for sonic velocity determination. The pump used to apply confining pressure had a large manual control valve (not on the picture).</b> .....	<b>131</b>
<b>Figure 5.2 Steel platens placed on both sides of the sample inside the heater and used to generate sonic waves and to inject fluids.</b> .....	<b>132</b>
<b>Figure 5.3 Example of S wave manual travel time measurement.</b> .....	<b>133</b>
<b>Figure 5.4 Effect of fluid composition and pressure on the P wave velocity of sample 3.1.</b> .....	<b>135</b>
<b>Figure 5.5 Effect of fluid composition and pressure on the S wave velocity of sample 3.1.</b> .....	<b>136</b>
<b>Figure 5.6 Fluid saturation and pressure effect on the Vp/Vs ratio of sample 3.1.</b> .....	<b>138</b>
<b>Figure 5.7 Comparison between Gassmann prediction (GM) and experimental data for the bulk modulus of sample 3.1.</b> .....	<b>141</b>
<b>Figure 5.8 Comparison between Gassmann prediction (GM) and experimental data for the shear modulus of sample 3.1.</b> .....	<b>141</b>
<b>Figure 5.9 Comparison between Gassmann prediction (GM) and experimental data for the P wave velocity of sample 3.1.</b> .....	<b>143</b>
<b>Figure 5.10 Comparison between Gassmann prediction (GM) and experimental data for the S wave velocity of sample 3.1.</b> .....	<b>143</b>
<b>Figure 5.11 Comparison between Gassmann prediction (GM) and experimental data for the Vp/Vs ratio of sample 3.1.</b> .....	<b>144</b>
<b>Figure 5.12 Comparison of P wave velocity before and after calcite dissolution for 4 samples.</b> .....	<b>146</b>
<b>Figure 5.13 Comparison of S wave velocity before and after calcite dissolution for 4 samples.</b> .....	<b>147</b>
<b>Figure 5.14 Comparison of Vp/Vs ratio before and after calcite dissolution for 4 samples.</b> .....	<b>148</b>
<b>Figure 5.15 Change in bulk modulus caused by calcite dissolution and increase in effective pressure (<math>P_{eff}</math>).</b> .....	<b>149</b>

Figure 5.16 Change in bulk modulus caused by calcite dissolution at constant effective pressure.....	149
Figure 5.17 Change in shear modulus caused by calcite dissolution and increase in effective pressure ( $P_{eff}$ ).....	150
Figure 5.18 Change in shear modulus caused by calcite dissolution at constant effective pressure.....	150
Figure 5.19 Comparison between empirical velocity-porosity correlations and experimental data. ....	151
Figure 5.20 Comparison between empirical and experimental variation in velocity with porosity. Linear fit of the experimental data is also shown. ....	152
Figure 5.21 Normalized Gassmann prediction of $V_p$ under brine saturation conditions and under $CO_2$ saturation conditions before and after calcite dissolution. ....	153
Figure 5.22 Normalized Gassmann prediction of $V_s$ under brine saturation conditions and under $CO_2$ saturation conditions before and after calcite dissolution. ....	153
Figure 5.23 Normalized $V_p$ evolution after brine pressurization, $CO_2$ invasion and calcite dissolution.....	154
Figure 5.24 Normalized $V_s$ evolution after brine pressurization, $CO_2$ invasion and calcite dissolution.....	155
Figure 5.25 Normalized $V_p/V_s$ evolution after brine pressurization, $CO_2$ invasion and calcite dissolution.....	155
Figure 5.26 Fluid substitution effects on $V_p$ according to Gassmann theory including the effect of a porosity change and the effect of a $K_{dry}$ change .....	156
Figure 5.27 Typical rock strain stress curve obtained during a triaxial test .....	158
Figure 5.28 Example of multiple failure test data .....	160
Figure 5.29 Yield envelopes for all samples and possible reservoir stress state at increasing depths of 1000, 2000 and 3000 meters .....	161
Figure 5.30 Same yield envelope representation as Figure 5.29 shown in $P$ - $Q$ space. ....	161
Figure 5.31 Linear fit of the average peak envelopes before and after dissolution .....	162
Figure 5.32 Failure plane on two samples before and after calcite dissolution .....	163
Figure 5.33 Experimental data showing the yield stress-porosity correlation.....	164
Figure 5.34 Experimental data showing the peak stress-porosity correlation.....	164

Figure 6.1 SEM images of the groove cut in a Lochaline sandstone core.....	167
Figure 6.2 Schematic representation of the calcite precipitation experiment. ....	169
Figure 6.3 Picture of the experimental assembly corresponding to Figure 6.2 with fluid preparation and injection on the left.....	169
Figure 6.4 Hopeman sandstone disc and Lochaline core montage....	171
Figure 6.5 The curves represent calcite solubility variations with CO <sub>2</sub> partial pressure in pure water along various isotherms .....	172
Figure 6.6 CT value profiles under 100% water, 100% CO <sub>2</sub> and experimental conditions .....	174
Figure 6.7 Comparison of calcium concentrations at the inlet and outlet of the core holder during the main experiment. ....	175
Figure 6.8 Calcite grains, about 5µm in size, present at the inlet and middle of the core .....	176
Figure 6.9 Views of carbonate structures present at the outlet of the core at increasing magnification.....	178
Figure 6.10 Carbonates present at the outlet of the Hopeman sandstone disc at increasing magnification.....	179
Figure 7.1 Example of deformation bands and associated variations in flow properties presented in Torabi and Fossen (2009).....	182
Figure 7.2 Picture of two Orange Sandstone cores prepared for the experiments showing variations in grain size and cementation .....	183
Figure 7.3 Schematic representation of the region close to the large grains/small grains transition.....	183
Figure 7.4 Experimental set up .....	185
Figure 7.5 Image segmentation of the CT scans .....	186
Figure 7.6 Cross section division in three zones that correspond to the rock core layering.....	186
Figure 7.7 Porosity profiles showing the dichotomy between the top layer (red triangles) and the middle and bottom layers (blue squares and green triangles respectively) .....	187
Figure 7.8 Time evolution of the average saturation profile (averaged over the whole core). ....	188
Figure 7.9 Time evolution of the CO <sub>2</sub> saturation in the different layers.....	189
Figure 7.10 Time evolution of the mean CO <sub>2</sub> saturation over the core length in each layer. ....	191
Figure 7.11 Schematic representation of a simulation volume with basic parameters involved in the calculations .....	193

<b>Figure 7.12 Results from the simulation series 1a, 1b and 1c.....</b>	<b>196</b>
<b>Figure 7.13 Results from simulations 2a (top) and 2b (bottom).....</b>	<b>197</b>
<b>Figure 7.14 Results from simulations 3a, 3b and 3c .....</b>	<b>198</b>
<b>Figure 7.16 Results from simulations 3c, 4a and 4b .....</b>	<b>201</b>
<b>Figure A1 Binarization of element maps. ....</b>	<b>239</b>

## List of Abbreviations

ACC	Amorphous Calcium Carbonate
CCS	Carbon Capture and Sequestration (or Storage)
CT	Computerized Tomography
DECC	Department of Energy and Climate Change
EDS	Energy Dispersive X-Ray Spectroscopy
EIA	Energy Information Administration
EOR	Enhanced Oil Recovery
EOS	Equation of State
GCS	Geological Carbon Sequestration (or Storage)
GHG	Green House Gas
GM	Gassmann (theory)
IAPWS	International Association for the Properties of Water and Steam
IEA	International Energy Agency
IPCC	Intergovernmental Panel on Climate Change
KC	Kozeny-Carman (equations)
NMR	Nuclear Magnetic Resonance
REV	Representative Elementary Volume
SEM	Scanning Electron Microscope
WAG	Water alternating Gas



## **Chapter 1 Introduction**

### **1.1 Why Geological Carbon Sequestration? The global warming issue**

In its fifth assessment report the United Nations Intergovernmental Panel on Climate Change (IPCC) reaffirmed the urge for drastic reductions in greenhouse gas emissions in order to stop the earth global warming (IPCC, 2013). This chapter introduces the issue of global warming and one possible solution to help reduce emissions, that is Geological Carbon Sequestration/Storage (GCS).

#### **1.1.1 Causes and consequences**

The average surface temperature of the Earth as shown a steady increase since the industrial revolution, a century ago (Figure 1.1). Currently, the global temperature increase compared to the pre-industrial era is approximately 1°C (Hansen et al, 2006). Although on geological timescales the earth temperature can display such variations due to orbital parameters only (i.e. Milankovitch Cycles), there is extensive evidence that this recent and particularly fast temperature variation is caused by the rising concentrations of greenhouse gases (GHG) in the atmosphere (Santer et al, 1996,2003; Ramaswamy et al, 2006; IPCC, 2007, 2013).

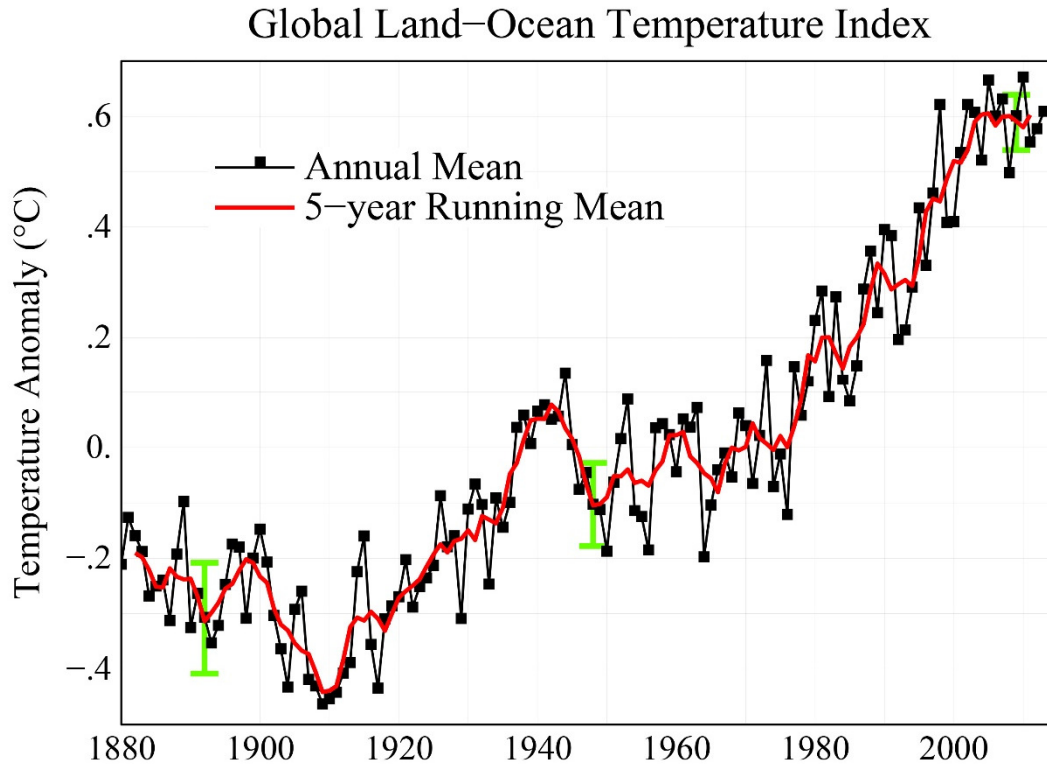


**Figure 1.1** “Line plot of global mean land-ocean temperature index, 1880 to present, with the base period 1951-1980. The dotted black line is the annual mean and the solid red line is the five-year mean. The green bars show uncertainty estimates. This is an update of Fig. 1A in Hansen et al. (2006).” Source: [http://data.giss.nasa.gov/gistemp/graphs\\_v3/](http://data.giss.nasa.gov/gistemp/graphs_v3/).

GHG are the cause of the greenhouse effect which consist of the trapping of heat between the atmosphere and the earth surface (Kiehl and Trenberth, 1997). This effect is essential to life as we know it, warming up the Earth’s surface from  $-18^{\circ}\text{C}$ , which is the theoretical black body Earth equilibrium temperature, to about  $14^{\circ}\text{C}$  (Lashof, 1989). The right amount of greenhouse effect is needed to reach life sustaining temperatures, Mars and Venus present striking illustrations of the consequences of having too few or too much GHG in the atmosphere. Both planets’ atmospheres are almost entirely made of carbon dioxide, with a pressure of 6 mbar on Mars and 90 bars on Venus. The surface temperatures of these planets are  $-50^{\circ}\text{C}$  and  $450^{\circ}\text{C}$  respectively with the greenhouse effect being virtually inexistent on Mars (i.e. Mars’ temperature depends almost exclusively on its distance from the sun) and accounting for about  $400^{\circ}\text{C}$  of Venus’ excess temperature (Rasool and De Bergh, 1970).

The main GHG naturally present in the earth atmosphere are water vapour ( $\text{H}_2\text{O}$ ), carbon dioxide ( $\text{CO}_2$ ), methane ( $\text{CH}_4$ ), nitrous oxide ( $\text{N}_2\text{O}$ ) and ozone ( $\text{O}_3$ ). Water vapour alone accounts for 70% of the total greenhouse effect,

while CO<sub>2</sub> accounts for 20%. However the CO<sub>2</sub> part is increasing due to the burning of fossil fuels and to deforestation (Figure 1.2).

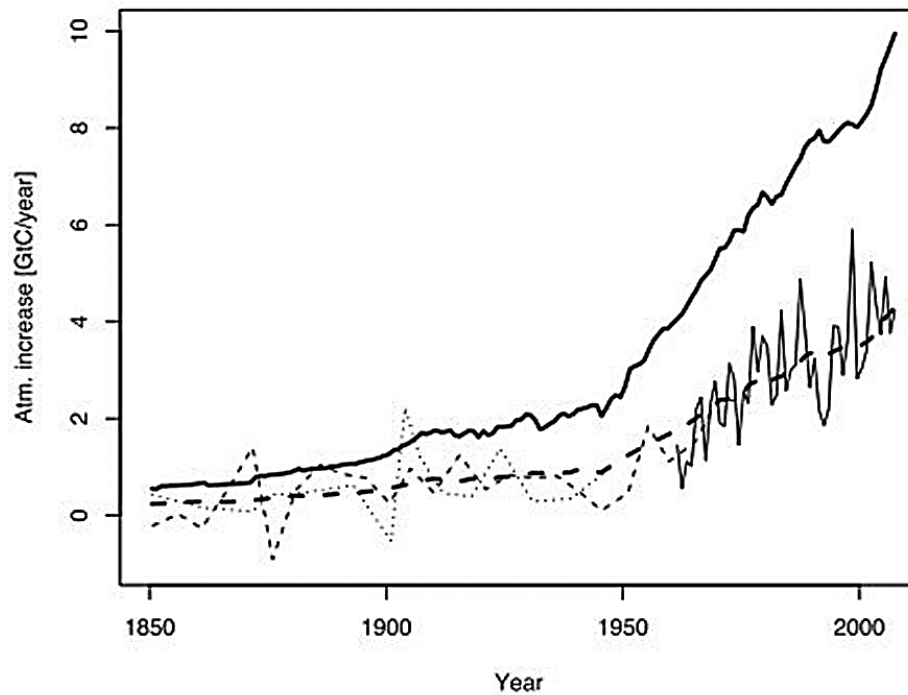


**Figure 1.2** “Observed atmospheric CO<sub>2</sub> increase derived from direct measurements, taking the average of Mauna Loa (Hawaii) and the South Pole (thin solid line), and two ice cores: Law Dome (dashed thin line) and Siple (dotted thin line). This is compared to total anthropogenic emissions (thick solid line) and 46% of total emissions (thick dashed line).” Taken from Knorr et al. (2009)

The increase in atmospheric CO<sub>2</sub> levels introduces an imbalance in the Earth’s energy budget, called radiative forcing. According to recent studies, the radiative forcing caused by anthropogenic CO<sub>2</sub> is responsible for most of the temperature increase of the last century, see Figure 1.3 taken from Butler and Montzka (2013).

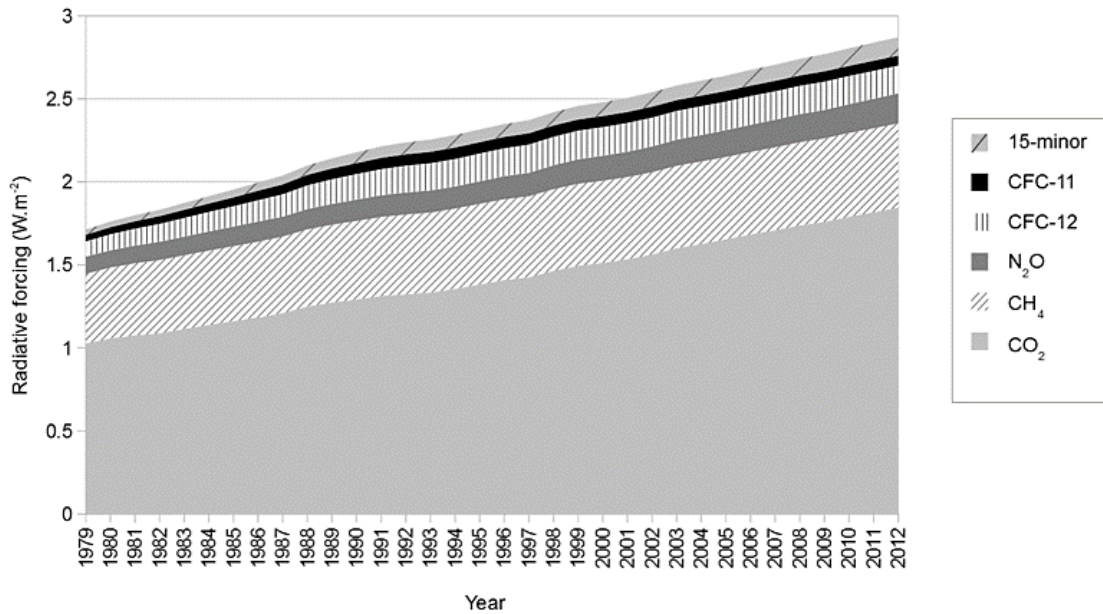


**Figure 1.3** “Radiative forcing, relative to 1750, of all the long-lived greenhouse gases. Adapted from Butler and Montzka (2013).” Source: [http://en.wikipedia.org/wiki/Radiative\\_forcing](http://en.wikipedia.org/wiki/Radiative_forcing) accessed on 13/11/2014.

In the meantime, socio-economic models predict a growth in global energy consumption during the next decades (EIA, 2014). This will inevitably induce a continuing rise in atmospheric CO<sub>2</sub> concentration as carbon-emitting sources of energy are likely to remain the cheapest ones in this time period. As a consequence, climatic models predict an additional increase of 2 to 5°C by the year 2100. Figure 1.4 from IPCC (2007) presents the results from different projections of CO<sub>2</sub> emissions and shows that they should at least stop to rise in order to avoid these temperature increase scenarios.

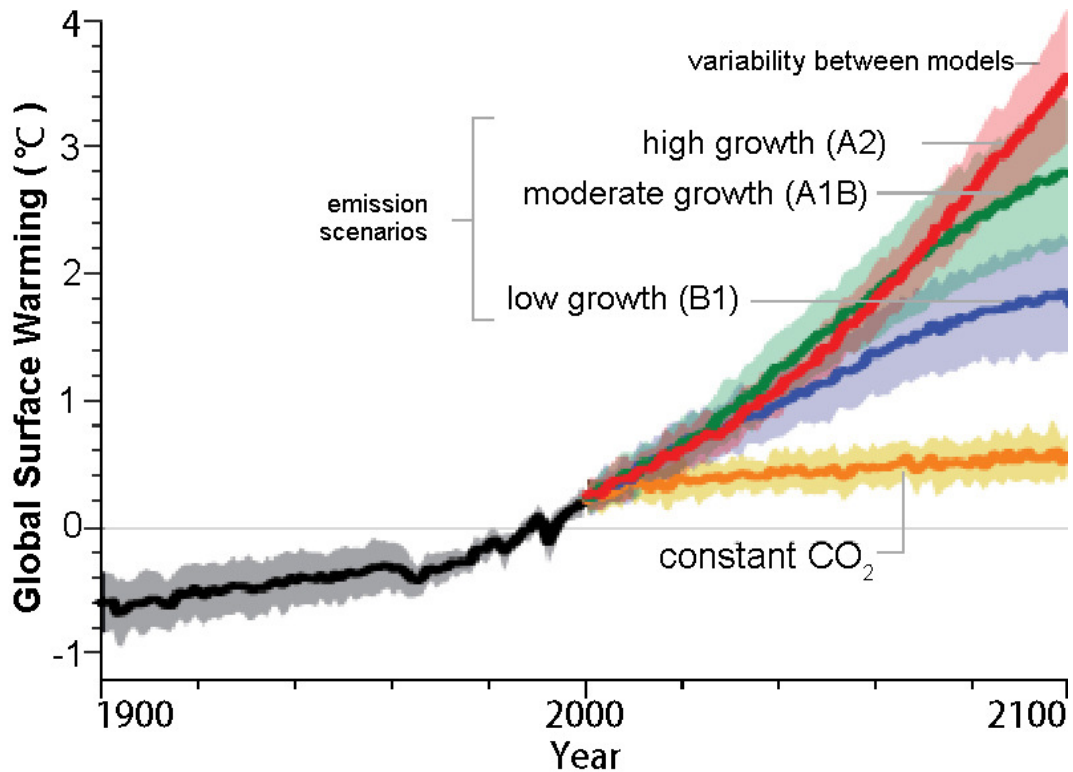


**Figure 1.4** Model simulations by the IPCC (IPCC, 2007) estimating Earth warming, depending on CO<sub>2</sub> emissions scenarios. The orange line provides an estimate of global temperatures if GHG emissions stayed at year 2000 levels. Source: <http://earthobservatory.nasa.gov/Features/GlobalWarming> accessed on 13/11/2014

As small as it may seem, a few degrees increase could be dramatic for life on Earth with possible mass extinctions due to modifications of natural habitats. The onset of such modifications, like ocean acidification (Sabine et al, 2004) or ice sheet melting (Kwok & Rothrok, 2009), are already observable. Other notable consequences of global warming would be an increase in the sea level (Church and White, 2006), as most of the world's population lives in coastal cities, and a higher frequency of extreme weather events.

The consequences of global warming do not directly threaten human life, but it will induce major environmental, financial and social issues in a few decades if nothing is done to stop this temperature trend. The mitigation of CO<sub>2</sub> emissions has to start now to appropriately limit the temperature increase before the end of the century and do so at the lowest expense.

### 1.1.2 Challenges and solutions

Despite the historic agreement of many developed countries to reduce their CO<sub>2</sub> emissions by a few percent through the Kyoto protocol (signed in 1997), more efforts and much bigger challenges await us. The third IPCC report (IPCC, 2007) identified a maximum allowable temperature increase of 2°C (corresponding to a CO<sub>2</sub> concentration of 450 ppmv) to avoid major harmful effects. This goal implies that worldwide CO<sub>2</sub> emissions have to be halved by 2050 (IEA, 2008).

A series of complementary approaches have been explored to cut down CO<sub>2</sub> emissions (Figure 1.5). According to the International Energy Agency (IEA), Carbon capture and Sequestration/Storage (CCS) could provide an important wedge for reducing emissions from the 2050 baseline. This could be achieved by capturing the CO<sub>2</sub> at large stationary sources like coal power plants.

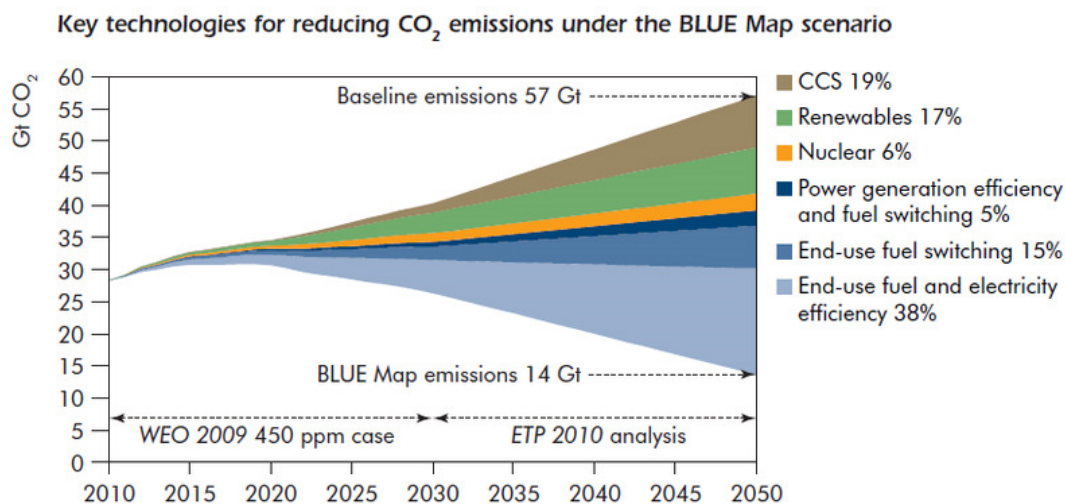


**Figure 1.5** Key technologies for a global CO<sub>2</sub> emissions reduction strategy, taken from IEA (2010a, p75).

CCS is divided into three separate steps: capture, transport and sequestration. Several CO<sub>2</sub> capture technologies are already available and have already been successfully applied in industrial projects (White et al, 2003; Figueroa et al, 2008; Mondal et al, 2012). This was initially motivated by regulations forcing gas producers to decrease the CO<sub>2</sub> content of natural gas to 2.5%. The idea of capturing the CO<sub>2</sub> to subsequently store it emerged recently and there is still research aiming to lower the cost of those capture technologies or even create an additional value in the process.

After capture, the CO<sub>2</sub> will be liquefied and transported in pipelines or by boat to the injection site. The main technical difficulties associated with the transport of CO<sub>2</sub> concerns the risk of leaks and possible corrosion of the

pipelines (Cole et al., 2011). Techniques to detect leaks already exist. The solution to reduce corrosion is to dehydrate the CO<sub>2</sub> or use stainless steel pipelines, the later solution being costly it would only be viable if the distance from the capture site to the sequestration site were small.

Several solutions are studied to store the captured CO<sub>2</sub>. Active research is underway to develop carbon fixation in carbonate minerals, in plants like micro algae or in methanogens (bacteria). But for the time being, the simplest and most efficient solution might be Geological Carbon Sequestration (GCS) referring to the injection of CO<sub>2</sub> in geological formations. In contrast this is also the solution with the lowest financial incentive as it does not generate any added value, one important exception being the injection of CO<sub>2</sub> for enhanced oil recovery (EOR). This lack of financial incentive together with remaining knowledge gaps associated with GCS are obstacles to its full development.

## **1.2 Introduction to Geological Carbon Sequestration (GCS)**

### **1.2.1 Aim and timescale of GCS**

There is an incompatibility between the urgent need to drastically reduce GHG emissions and the time needed to fully develop low carbon sources of energy for electricity generation and for transportation. Geological sequestration of CO<sub>2</sub> could provide a convenient and affordable solution to this transition period. Current GCS operations (not including EOR) total about 10 Mt/year of CO<sub>2</sub> sequestration. According to the IEA, a world wide effort is necessary to increase this figure by several orders of magnitude by the year 2050 (Figure 1.6).

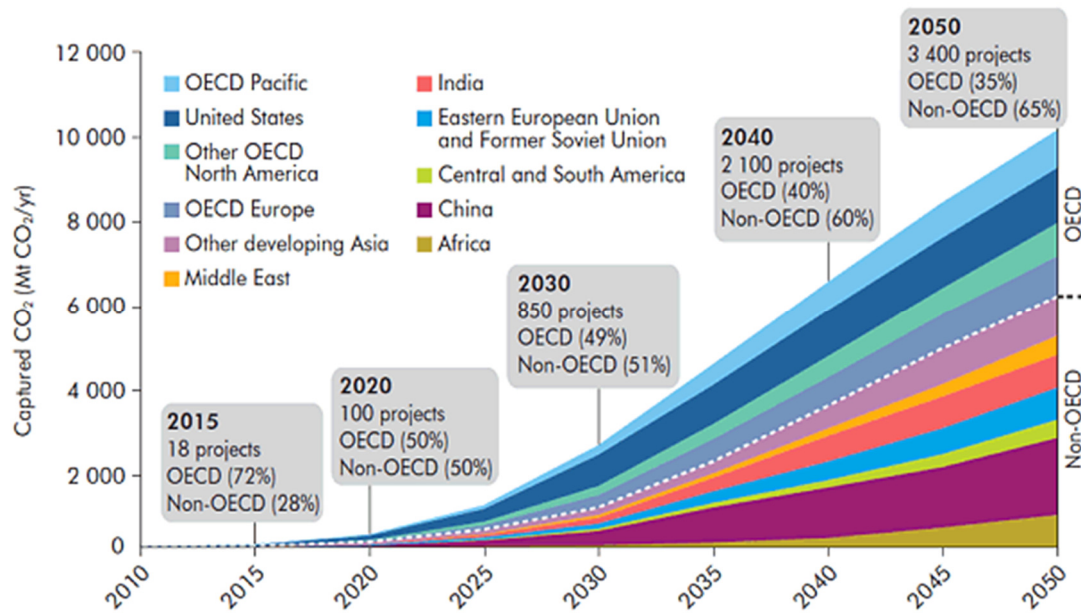


**Figure 1.6** IEA roadmap for CCS projects by 2050 (IEA, 2009). *“Based on these projections, the quantity of CO<sub>2</sub> stored permanently underground by 2035 would be equivalent to the 2005 level of oil production.”*

Ideally CO<sub>2</sub> would be immobilized in deep geological formations for thousands of years, however a small leakage rate is acceptable with regard to the predicted decline of fossil fuel production in the next decades. Given the life time of CO<sub>2</sub> in the atmosphere, controlled primarily by the ocean-atmosphere exchanges (Solomon et al, 2009), a sequestration time of a few centuries could be sufficient. Nonetheless, for public acceptance, leakage of CO<sub>2</sub> into potable water aquifers has to be avoided.

### 1.2.2 Technical aspects and feasibility of GCS

Injection of CO<sub>2</sub> into geological formations has already been done on an appropriate scale notably on EOR projects. Similarly, the sequestration of natural gas in geological formations is a common practice. Three types of CO<sub>2</sub> repositories are possible: deep saline aquifers, depleted gas/oil fields and coal seams. Saline aquifers are currently the preferred solution due to their widespread distribution around the world (Figure 1.7) and consequently their proximity to CO<sub>2</sub> sources. It is widely accepted that sequestration capacity of saline aquifers is sufficient to meet IEA goals by 2050; even if large uncertainties remain it is estimated to be at least 1000 Gt of CO<sub>2</sub> (Bachu & Adams, 2003).

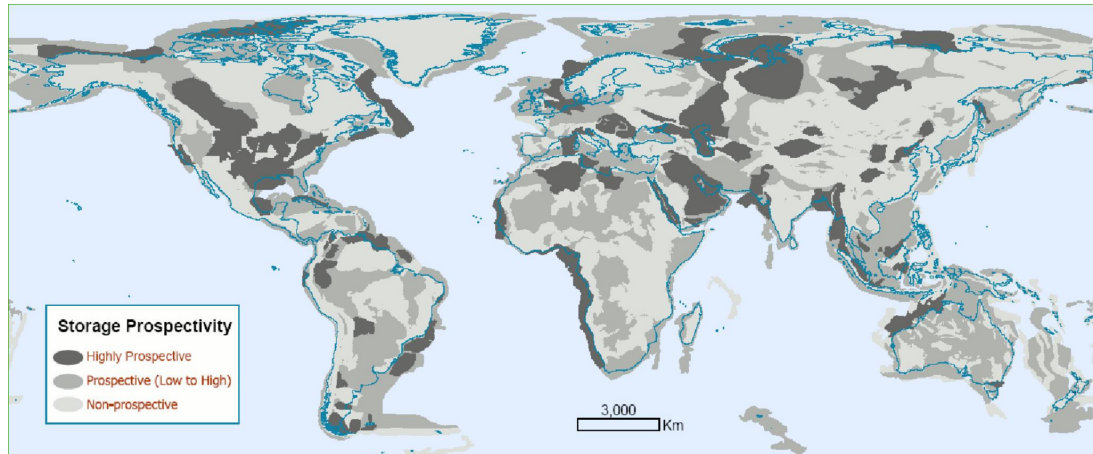


**Figure 1.7** World prospective areas for GCS according to Bradshaw and Dance (2004).

### **1.2.3 Cost, safety and efficiency**

Cost and safety questions must be addressed to allow the wide application of GCS. The functional cost of GCS is estimated to be between 30 and 80\$ per ton of CO<sub>2</sub> (Finkenrath, 2011), a reasonable goal is to lower it to 20-25\$ per ton by 2030. It is difficult to estimate GCS costs because of the lack of large scale projects and a high variability is expected depending on the type of installation, the capture process, the distance from the injection site and the type of repository.

Considering a GCS project as a whole the major expenditure is incurred at the onset as costs to create the infrastructures needed. If 3000 power plants need to be upgraded to do GCS then this could also mean building thousands of transport pipelines towards hundreds of different geological repositories. This multiplicity introduces an uncertainty and a financial risk factor. The most sensitive issue is project failure due to inadequate choice of the injection site. GCS is a relatively unknown territory and in this respect investments are needed to ensure project efficiency and safety.

Cost and safety issues are interrelated on the question of capture and transport. There is an uncertainty on the rate of steel corrosion and in general on the thermodynamical properties of impure CO<sub>2</sub> (Wang et al, 2011). The problem of leaks can be locally serious for health and environment but is also quite well documented and can be controlled. However the possible deterioration of the pipeline poses a medium to long term threat. Neglecting this possibility, the cost of transport is low, 1-5\$ per ton per 100 km (McCoy et al, 2008).

The last aspect of expense concerns the repository. Uncertainties related to the repository are the most important when considering uncertainties on

project cost, efficiency and safety. It is crucial to ensure that the injectivity and the confinement of the CO<sub>2</sub> remains as planned during the life time of the project. Depleted gas/oil fields and saline aquifers have different advantages and disadvantages. Depleted gas/oil fields are very well characterized and have a proven confinement history, but they will also be cut by abandoned wells, each of them being a possible leakage pathway (Gasda et al, 2004). In contrast, undrilled saline aquifers are not well known so that more investments are needed to first characterize and select potential sites.

#### **1.2.4 General motivation for this thesis**

Cost, safety and efficiency questions demand a detailed investigation of the consequences of CO<sub>2</sub> injection. These investigations must provide answers for sequestration site selection, for the validation of long-term CO<sub>2</sub> trapping processes and for injection monitoring.

The selection of a saline aquifer is difficult and many parameters are taken into consideration. One fundamental prerequisite is the presence of a confining layer, called caprock to prevent the upward migration of the CO<sub>2</sub>. Secondly, the volume and the petrophysical properties of the host rock, the general geological setting and the presence of faults need careful examination. All these parameters condition the sequestration capacity, cost, safety and efficiency.

Two petrophysical properties are of fundamental interest: porosity and permeability of the reservoir. A high porosity and permeability is preferred as this would maximize the sequestration capacity and injectivity. A higher injectivity means fewer injection wells to drill and a safer, lower injection pressure. Depending on those parameters and on the depth of the aquifer, the sequestration cost can vary between 1 and 15\$ per ton.

A key complication arises from the fact that rock reactions with the CO<sub>2</sub> can modify porosity and permeability (Izgec et al., 2008; Luquot and Gouze, 2009; Gouze and Luquot, 2011). Hence correct understanding of future rock modifications is critical to assess the suitability of an aquifer. This is even more critical if the choice of the aquifer is geographically limited to repositories of mediocre initial quality.

Sonic velocity and yield strength and their possible evolution are also of interest. Understanding sonic velocity variations with fluid-rock interactions may help detect reservoir processes and aid in monitoring the underground displacement of the CO<sub>2</sub>. As for yield strength, it is vital to know if fluid rock

interactions can weaken the rock to a point where large and irreversible deformations could occur. Rock deformation in the vicinity of the well would compromise its integrity.

### **1.2.5 Thesis outline**

The specific goal of this thesis is to study pore scale CO<sub>2</sub>-fluid-rock interactions and their feedbacks to macroscopic flow and mechanical properties of aquifers. These feedbacks are not yet well integrated in existing continuum scale simulations.

Chapter 2 gives an overview of the individual physical and chemical processes associated with GCS. It will present the rationale for the following chapters by highlighting some poorly understood feedback interactions and introduce the methods that have been used to investigate them in this study.

Chapter 3 presents experimental results of CO<sub>2</sub> enriched brine injection into a calcite bearing sandstone. The effect of dissolution on the rock permeability was found to be much larger than expected due to the associated creation of new efficient flow paths.

Chapter 4 presents a method to evaluate this effect by direct computation of fluid flow with the commercial software FLUENT. Real rock pore and calcite geometries were obtained at 2.5 microns resolution and used to calculate the change in permeability triggered by calcite dissolution.

Chapter 5 focusses on the potential modifications of the mechanical properties of the reservoir. Calcite dissolution was found to have a large impact on the sonic velocity and yield/peak strengths of rock cores. This could affect the reservoir and caprock integrity as well as lead to interpretation errors for injection monitoring.

Chapter 6 presents results from a calcite precipitation experiment. Following calcite dissolution it is expected that calcite will precipitate out of the saturated fluid if the pressure drops. The experiments focused on CO<sub>2</sub> degassing and calcite precipitation and the effect on permeability of rock cores.

Chapter 7 is an attempt to assess the long term viability of one CO<sub>2</sub> trapping mechanism: capillary trapping. Residually trapped CO<sub>2</sub> was left in a layered core for three months. A significant transfer of CO<sub>2</sub> between the layers was observed and this could impact CO<sub>2</sub> containment provisions in the long-term.

## **Chapter 2**

### **The Physics and Chemistry underpinning GCS**

#### **2.1 Introduction**

Carbon dioxide sequestration in deep saline aquifers is a new technology which is currently receiving considerable attention in the scientific community. It is viewed as an effective means of fighting global warming by preventing the return of carbon dioxide to the atmosphere (Holloway and Savage, 1993; Bachu et al., 1994; Bachu and Adams, 2003). Saline aquifers are good candidates for carbon dioxide reservoirs due to their good sequestration capacity and their worldwide distribution (Hendriks et al 2004). The high cost of CCS and regulatory issues are slowing down its extensive application.

Scientific challenges remain to quantitatively understand the magnitude, nature and rate of the processes that stabilize CO<sub>2</sub> in the subsurface and ultimately optimize the injection efficiency and the long-term CO<sub>2</sub> immobilization. The first step for optimization is the proper selection of the aquifer in terms of capacity and injectivity. The second step is to design injection schemes that enhance CO<sub>2</sub> trapping mechanisms. In order to carry out the optimization, it is necessary to be able to forecast the evolution of the system in response to CO<sub>2</sub> injection, as this will inevitably acidify the pre-existing formation brine and could potentially trigger physical modifications of the aquifer.

CO<sub>2</sub> sequestration combines fluid flow with chemical, thermal, mechanical and biological interactions. These interactions and their various feedbacks give rise to a complex behaviour and raise questions about the sustainability of the injectivity (Bacci et al., 2011), the integrity of the wellbore, and the capacity to remotely monitor the CO<sub>2</sub> injection. Additionally, a key environmental issue is the possible CO<sub>2</sub> leakage to the surface and the potential for pollution of potable aquifers (Knauss et al 2005; Apps et al., 2010).

A challenge in reaching an overarching understanding of the consequences of CO<sub>2</sub> sequestration lies in the immense variety of aquifer conditions in terms of pressure, temperature, rock composition, brine composition, aquifer geometry and possibly gas composition. One can expect that each individual aquifer will host different fluid-rock interactions that will depend on the

mineralogy, thickness, grain size and porosity of individual beds. It is nevertheless possible that only a handful of those interactions will be critical at various stages of the operation.

It is useful to examine and sort individual processes in terms of their relative importance in order to focus on immediate threats and benefits in responses to GCS deployment. Currently, numerical simulators such as CRUNCH (Steeffel, 2009) FLOTRAN (Lichtner, 1999) or TOUGHREACT (Xu and Pruess, 2001) aim at integrating simple hydrodynamic and geochemical processes to provide a useful tool for initial aquifer screening and for designing injection operations. However, calibration and improvement of reactive transport codes demand more experimental investigations.

## **2.2 Physics of GCS**

### **2.2.1 Fluid viscosities and densities**

The examination of CO<sub>2</sub> and brine thermodynamic properties is a fundamental step for the study of physical and chemical processes related to GCS. It has been proposed that CO<sub>2</sub> will be injected in a compressed gas, liquid or supercritical state (van der Meer, 1992; Hendriks and Block, 1993; Bachu, 1994). This is done to improve space usage. At typical targeted reservoir conditions (P=10 MPa and T=50°C) the CO<sub>2</sub> is supercritical and its volume is divided by 600 with respect to standard conditions (Bodnar et al., 2013). Under these conditions CO<sub>2</sub> density and viscosity are approximately 50-70% and 5-10% of that of typical brines respectively (Benson and Cole, 2008; Lemmon et al 2005), see figures 2.1, 2.2, 2.3 and 2.4. These differences affect the mobility of the individual phases and therefore the propagation pattern of CO<sub>2</sub> and the dissipation of the injection pressure (Sasaki et al, 2008).

Close to the critical point, CO<sub>2</sub> properties are also very sensitive to pressure and temperature; injection simulations sensitivity analysis showed that in this region, minor Pressure-Temperature (P-T) variations could cause large differences in the predicted CO<sub>2</sub> plume propagation and final size (Jordan and Doughty 2009). With increasing depth, the properties of CO<sub>2</sub> become somewhat closer to those of brine which will enhance the injection efficiency by limiting gravity override (i.e. the buoyant upward migration of CO<sub>2</sub> in the brine leading to the preferential flow of CO<sub>2</sub> at the top of the reservoir) and by facilitating the entry of CO<sub>2</sub> into smaller pores, this is however balanced by a higher drilling cost.

### **2.2.1.1 CO<sub>2</sub> density and viscosity**

Figures 2.1 and 2.2 are P-T diagrams of CO<sub>2</sub> density and viscosity where the interest of injecting at depths below 800m is clearly visible. CO<sub>2</sub> density was calculated using the equation of state (EOS) developed by Span and Wagner (Span and Wagner, 1996) and the viscosity using the procedure described in Fenghour et al. (1998). Transient thermal effects were neglected and the assumption was made that the CO<sub>2</sub> temperature was equal to that of the reservoir rocks. Despite considerable cost the injection temperature is usually controlled on site to mitigate deleterious thermal effects.

Two curves on the P-T diagram represent end-member P-T conditions with depth. The dotted curve represents the maximum injection pressure and temperature with depth. The maximum injection pressure is set to 60-70% of the lithostatic pressure; above this pressure vertical fractures can develop and progress into the sealing caprock (Bredehoeft et al, 1976; Zoback and Zinke, 2002; Rutqvist et al., 2008). The solid curve represents the hydrostatic pressure and temperature with depth given a hydrostatic pressure gradient of 10.5 MPa/km (based on a continuous brine phase with 8wt% NaCl) and a geothermal gradient of 25°C /km. For a given depth, the actual P-T conditions when traveling from the well to the reservoir will lie between the curves, with most of the time significantly higher densities and viscosities close to the well (i.e. at the maximum injection pressure). The primary consequence is the emergence of a more stable and viscosity controlled CO<sub>2</sub> propagation near the well.

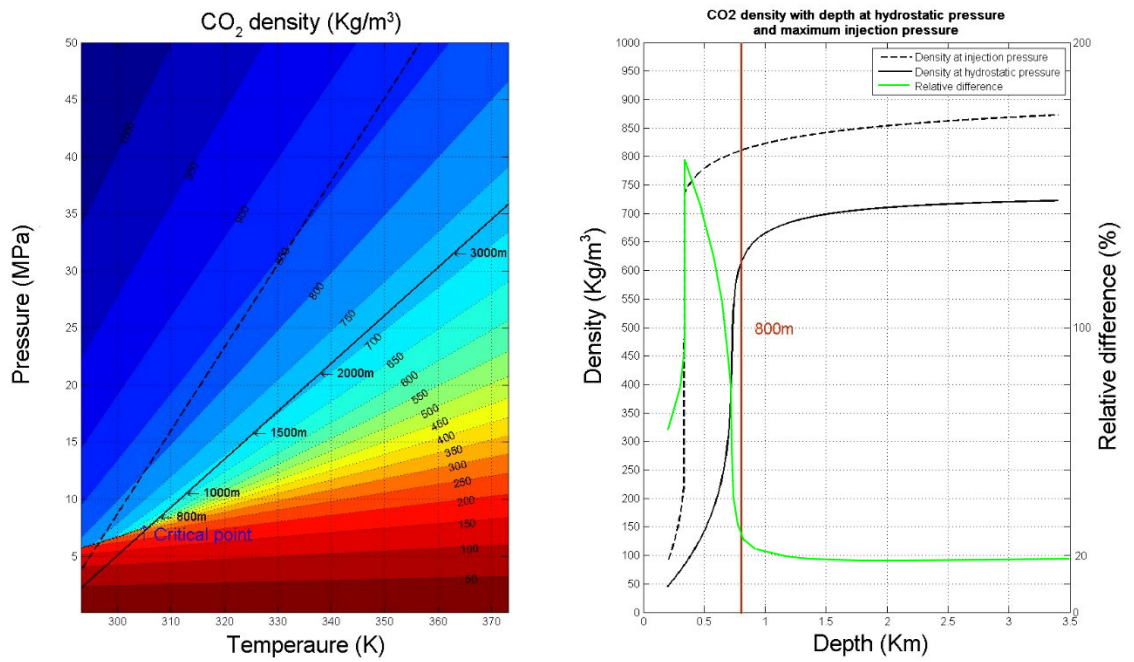


**Figure 2.1** On the left: P-T diagram coloured by CO<sub>2</sub> density where two end-member P-T paths with reservoir depth are also represented (see explanations in text). On the right: evolution of CO<sub>2</sub> density with depth for two end-member P-T paths as well as relative difference (e.g. CO<sub>2</sub> density is approximately 20% higher at injection pressure than at hydrostatic pressure at depth below 800m)

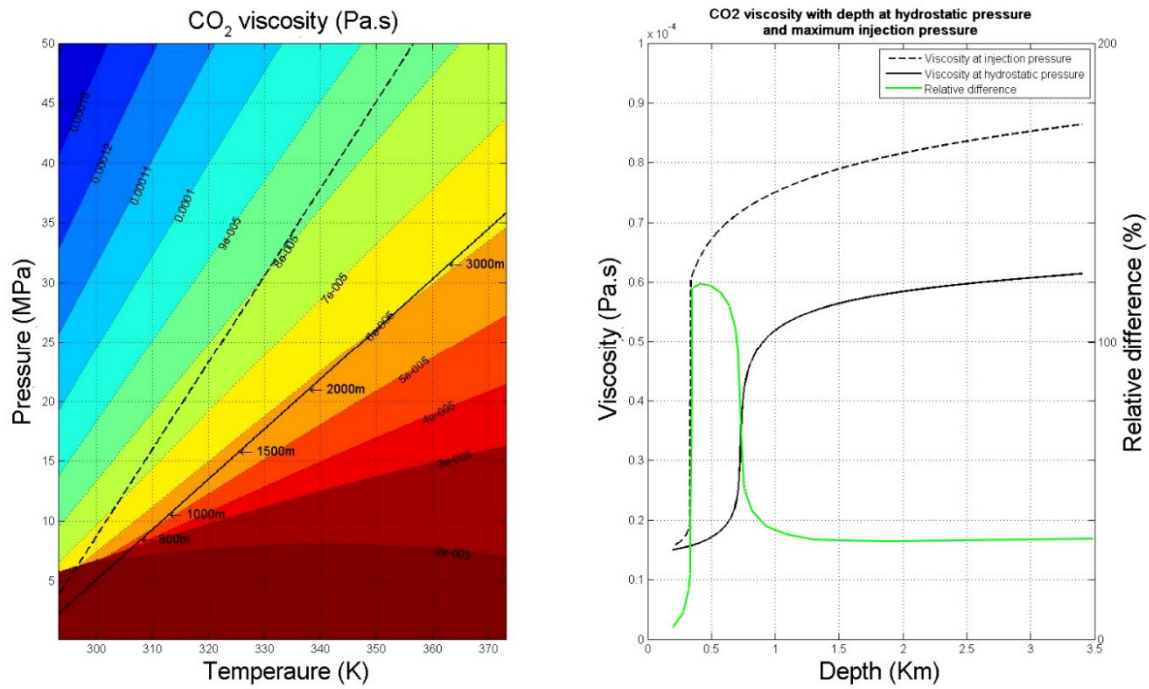


**Figure 2.2** On the left: P-T diagram coloured by CO<sub>2</sub> viscosity where two end-member P-T paths with reservoir depth are also represented (see explanations in text). On the right: evolution of CO<sub>2</sub> viscosity with depth for two end-member P-T paths.

### 2.2.1.2 Water density and viscosity

The equation of state used to calculate the density and viscosity of water can be found in the 2014 and 2008 releases of the International Association for the Properties of Water and Steam (IAPWS). For water, vertical or horizontal density-viscosity variations in the reservoir can probably be totally neglected.

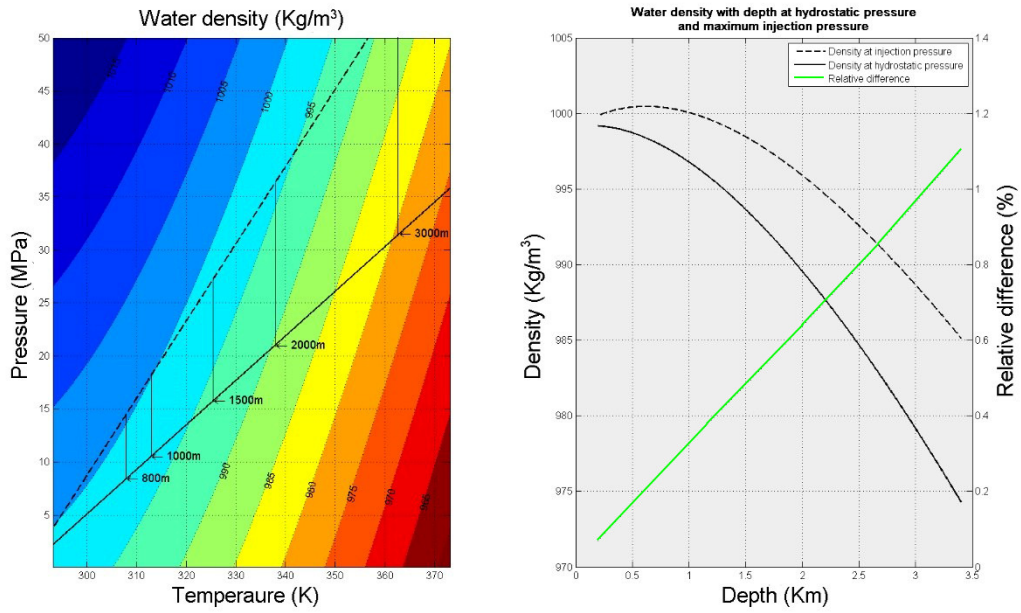


**Figure 2.3** On the left: P-T diagram coloured by water density where two end-member P-T paths with reservoir depth are also represented (see explanations in text). On the right: evolution of water density with depth for two end-member P-T paths.

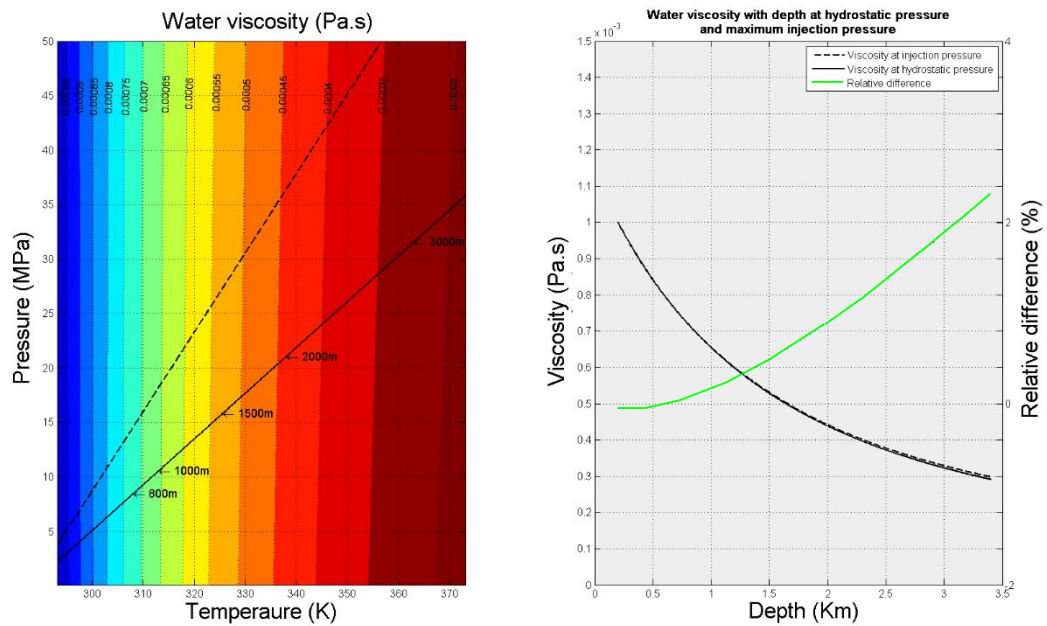


**Figure 2.4** On the left: P-T diagram coloured by water viscosity where two end-member P-T paths with reservoir depth are also represented (see explanations in text). On the right: evolution of water viscosity with depth for two end-member P-T paths.

### 2.2.1.3 NaCl brine density and viscosity

Knowing the density and viscosity of pure water, the density and viscosity of NaCl brine can be calculated using the models of Mao and Duan (2008; 2009). Figure 2.5 compares densities and viscosities of pure water, 1M NaCl brine and 5M NaCl brine. Addition of salt into water causes a density increase up to 10% and a viscosity increase up to 80%. These are not negligible and are one of the reasons why brine salinity has to be carefully evaluated.

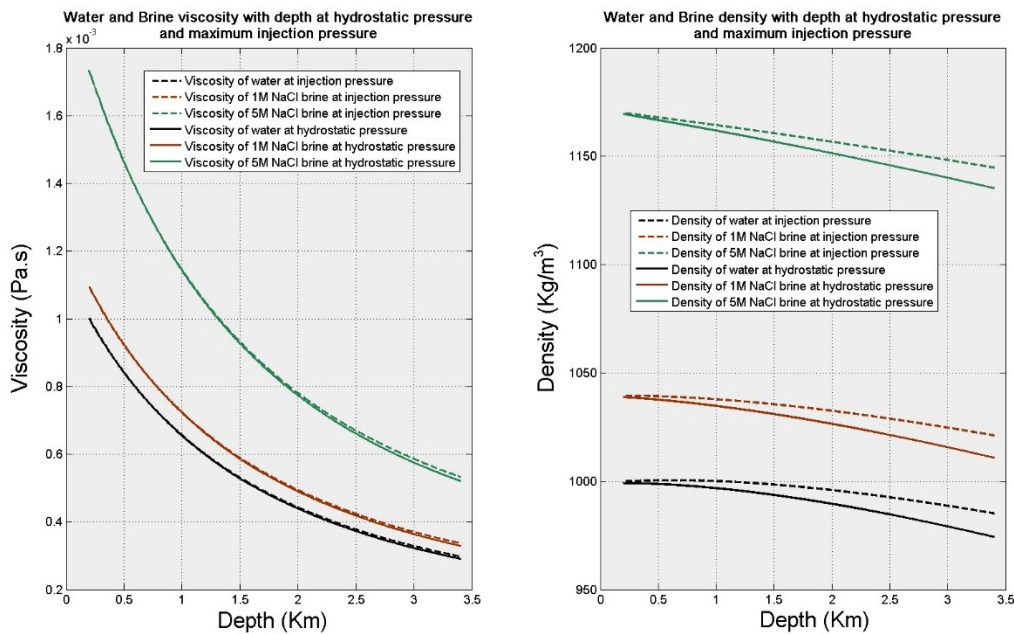


**Figure 2.5** On the left: viscosity evolution with reservoir depth for water and two NaCl brines (1M and 5M concentration). The dotted lines correspond to the injection pressure path and the continuous line to the hydrostatic pressure path as described earlier in previous figures and text. On the right: the same for density.

### 2.2.1.4 Carbonated NaCl brine density and viscosity

One complication in applying data for the end-member fluids is that CO<sub>2</sub> and brine show some limited mutual solubility under reservoir conditions. A carbonated water EOS has been proposed by Hu et al (2007) and there is a good knowledge of the density of simple carbonated brines (Duan et al., 2008; Mao and Duan, 2009; Mao et al., 2010). However more work is needed on carbonated brine viscosity (Bando et al., 2004; Fleury and Deschamps, 2009). There are fewer data on the effect of dissolved H<sub>2</sub>O on CO<sub>2</sub> properties, but it seems that the differences from pure CO<sub>2</sub> are not significant (Bodnar et al, 2014).

To compute the properties of CO<sub>2</sub>-saturated brines it is first necessary to know the brine properties and the CO<sub>2</sub> solubility. Models for carbonated brine density can be found in Duan et al. (2008) and Mao et al. (2010); for viscosity in Bando et al. (2004) and Fleury and Deschamps (2009). Figure 2.6 shows that density and viscosity differences between a CO<sub>2</sub>-saturated brine (carbonated brine) and pure brine are small and tend to vanish with depth. The first order effect of CO<sub>2</sub> dissolution in brine is a small increase in the density and viscosity of the brine. Despite being small the density difference between carbonated brine and pure brine can be enough to trigger reservoir scale convective circulation of the brine thereby enhancing CO<sub>2</sub>-brine mixing (Neufeld, 2010).

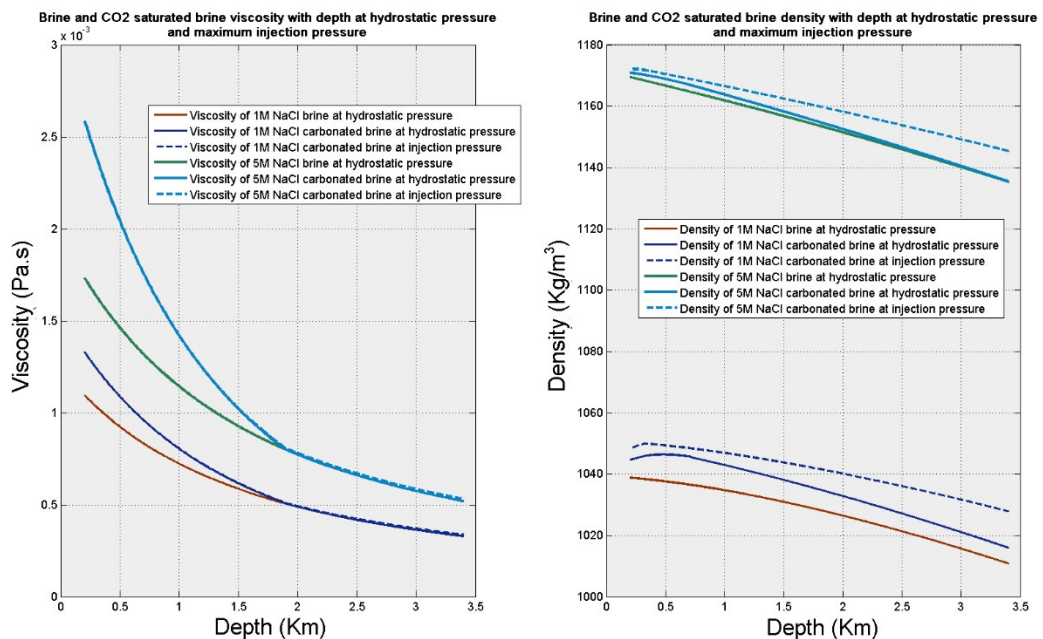


**Figure 2.6** On the left: viscosity evolution with reservoir depth for pure brines and carbonated brines at various pressures (only the hydrostatic curve is used for reference in the pure brine case). The dotted lines correspond to the injection pressure path and the continuous line to the hydrostatic pressure path as described earlier in previous figures and text. On the right: the same for density.

### 2.2.2 Single Phase flow

If fluid properties can affect CO<sub>2</sub> sequestration it is essential to consider the rock framework and its properties to achieve a complete description of the fluid flow in the reservoir. The flow of a single phase fluid in the pores of the rock is controlled by inertial, viscous and gravity forces. Inertial forces arise from the acceleration of the fluid mass. The viscous forces stem from the friction of the fluid against the pore walls that transmit into the fluid (as exemplified by the classic Poiseuille's flow profile in tubes). Additionally,

gravity will force the fluids to flow through buoyancy effects. At fluid velocities encountered in injected reservoirs, the flow of brine is incompressible and laminar; and the Reynolds number (the ratio of inertial to viscous forces) is very low. The CO<sub>2</sub> flow can also be considered incompressible because of the very low Mach number (ratio of flow velocity to Mach velocity) and the fact that CO<sub>2</sub> is significantly less compressible at liquid-like supercritical conditions than when a gas. In these conditions the fluid flow can be accurately described at the pore scale by the Stokes equation and the conservation of mass equation as follows:

$$\eta \nabla^2 u - \nabla P + f = 0$$

$$\nabla \cdot u = 0 \tag{2.1}$$

where  $u$  (m.s<sup>-1</sup>) is the velocity of the fluid,  $\nabla P$  (Pa.m<sup>-1</sup>) is the pressure gradient,  $\eta$  (Pa.s) is the fluid dynamic viscosity and  $f$  is an applied body force (e.g. gravity).

The Stokes equation means that the flow of CO<sub>2</sub> is triggered by the competition between a driving force caused by the injection pressure and a resisting viscous force. The pore volume and geometry are the major factors determining this viscous force. At otherwise constant geometry, larger volumes for individual pores will provide less resistance to flow. At constant volume, different pore topographies may produce vastly different resistances. For example, tortuous pathways or pathways presenting constrictions can slow down the flow by several orders of magnitudes. From an up-scaled perspective (hundreds of pores) those effects are summed up into a single parameter: the permeability. The permeability of a rock can be measured using Darcy's equation:

$$q = \frac{-\kappa A}{\eta L} \Delta P \tag{2.2}$$

where  $q$  (m<sup>3</sup>.s<sup>-1</sup>) is the fluid flow rate through the medium,  $\kappa$  (m<sup>2</sup>) is the permeability of the medium,  $\eta$  (Pa.s) is the fluid dynamic viscosity,  $A$  (m<sup>2</sup>) is the medium cross-sectional area,  $L$  (m) is the medium length and  $\Delta P$  (Pa) is the fluid pressure difference across the medium. The permeability  $\kappa$  can be expressed in Darcy units (D) with 1 D = 9.869233.10<sup>-13</sup> m<sup>2</sup>.

The permeability can theoretically be obtained from the porosity (the fraction of pore volume in a given rock volume), if simple pore geometries are assumed (Carman, 1997; Pape et al, 2000; Chapuis and Aubertin, 2003). As mentioned earlier porosity and permeability are fundamental properties of the rock that are critical for aquifer selection as they control its capacity and

injectivity respectively. At the first order, the permeability of the reservoir will determine how many injection wells are necessary for a given CO<sub>2</sub> injection rate.

From the reservoir point of view, the migration of CO<sub>2</sub> will be largely determined by gravity forces and reservoir scale permeability heterogeneities, as observed in the Sleipner GCS site (Figure 2.7).

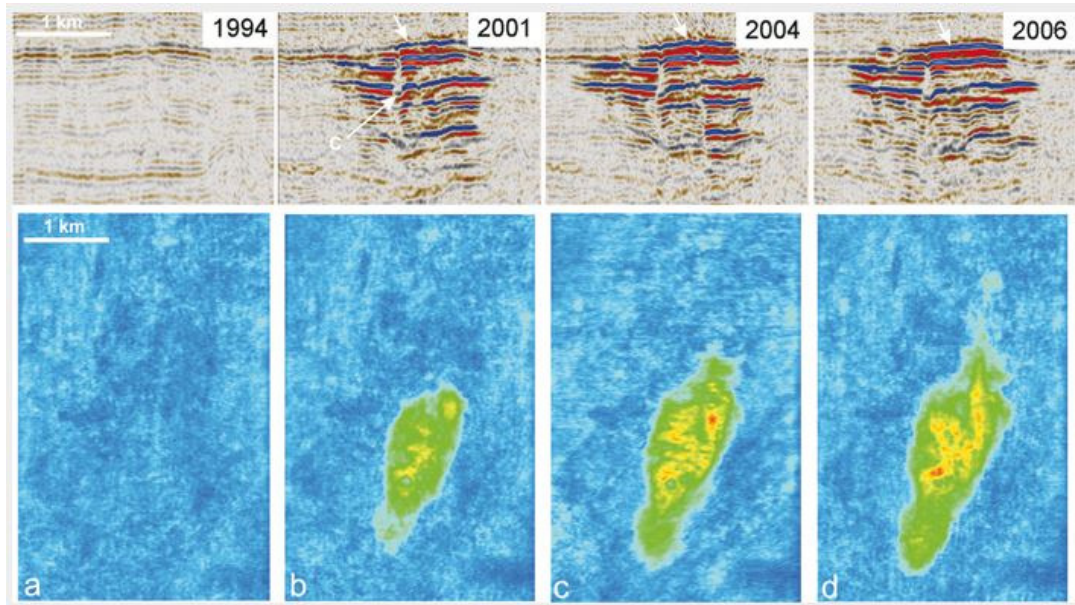


**Figure 2.7** “Time-lapse seismic images from Sleipner showing vertical sections (along the top) and maps of the expanding plume in 1994, 2001, 2004 and 2006 (along the bottom). The total height of the plume is about 250 meters, with a total width in 2001 of around 2 km. Post injection profiles since 2001 show bright reflections where CO<sub>2</sub> is accumulating below thin and low permeability mudstone layers.”  
Source: <http://www.bgs.ac.uk/science/CO2/home.html>. Modified after Chadwick et al. 2006a.

Since brine is denser than CO<sub>2</sub> in the upper crust, gravity forces will cause an upward, buoyancy driven flow also referred to as gravity override. Figure 2.8 illustrates the migration of a CO<sub>2</sub> plume front calculated with the equations developed by Nordbotten and Celia (2006) using the parameters explained in the caption. The magnitude of the gravity override is controlled by the ratio of viscous to gravity forces which ultimately depend on the density difference as well as on the vertical permeability. It implies that the CO<sub>2</sub>-brine contact area and the distance travelled by the CO<sub>2</sub> along the top sealing formation will be much larger than if the propagation front were vertical (without buoyancy effects).

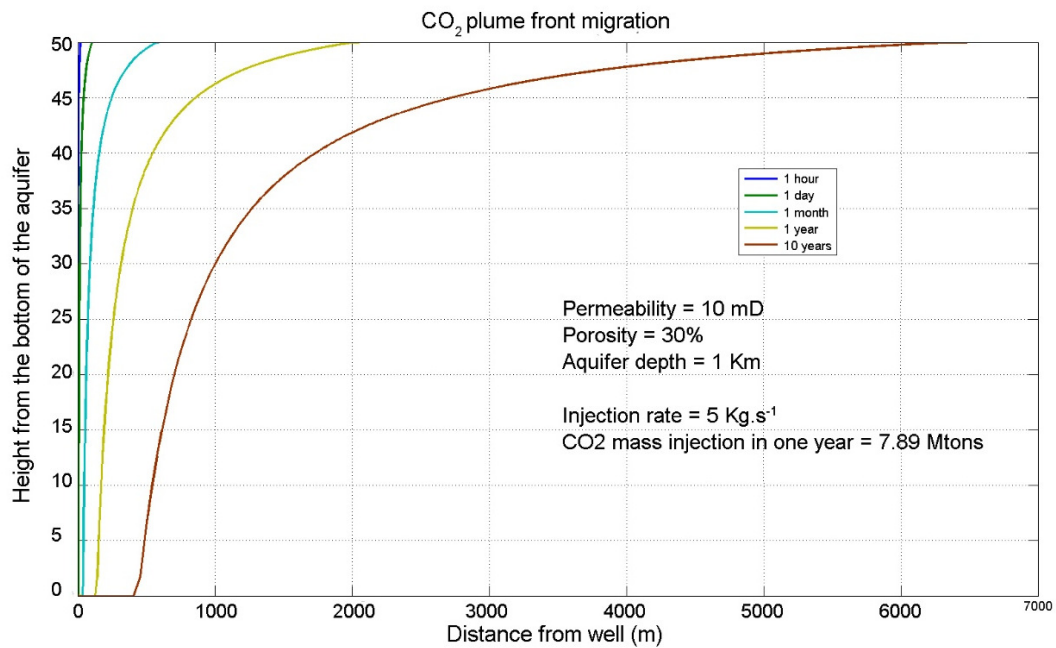


**Figure 2.8** Time-lapse evolution of the CO<sub>2</sub> plume in a horizontal reservoir showing gravity effect. The CO<sub>2</sub> is injected on the left across the whole width of the reservoir. The gravity tongue shape greatly enhances the CO<sub>2</sub>-brine interfacial area as well as the distance travelled by the CO<sub>2</sub> at the top of the formation.

Maybe more important concerning the distribution of CO<sub>2</sub> and in particular the CO<sub>2</sub>-brine contact area is the channeling phenomena that take place in the presence of large scale correlations of the permeability field (Figure 2.9). Current numerical studies frequently employ nearly homogeneous descriptions of the reservoir either because information on permeability heterogeneity is lacking, or for computational power reasons. The consequence of heterogeneity in permeability on various scales is a CO<sub>2</sub> distribution with much larger CO<sub>2</sub>-brine interfacial areas than are commonly assumed (Sato et al 2011) and in turn this leads to more extensive CO<sub>2</sub> dissolution in the brine and more fluid-rock interactions.

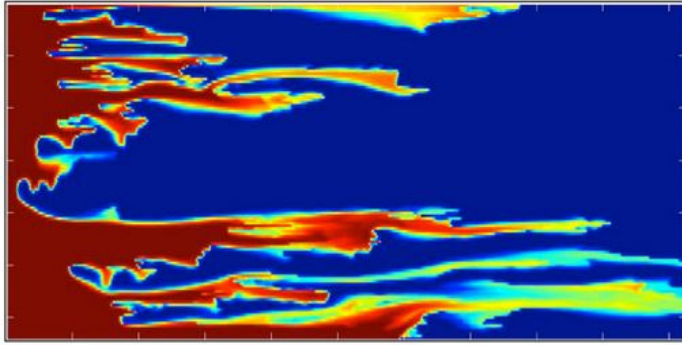


**Figure 2.9** Illustration of a channeling phenomenon. A fluid (in red) is propagating from left to right in a medium that has permeability heterogeneities. Source: <http://stanford.edu/~micon/research.html>

### **2.2.3 Multiphase flow**

In reality the injection of CO<sub>2</sub> cannot simply be considered as a single phase flow problem since CO<sub>2</sub> only occupies a fraction of the pore space (of an otherwise brine saturated rock volume). Generally the two-phase flow should involve CO<sub>2</sub> as the non-wetting phase and brine as the wetting phase (i.e. brine adheres more to the rock surface than CO<sub>2</sub> does). This complex flow is controlled by pore structure, capillary forces and general fluid dynamics.

During the injection phase, the CO<sub>2</sub> will displace the brine already in place but the latter will tend to remain as films on the pore walls (Kim et al, 2012, Espinoza and Santamarina 2010) and may impede CO<sub>2</sub> invasion into pores connected by very small pore throats; this is referred as primary drainage. After the injection has stopped, CO<sub>2</sub> pressure will decline and the brine will reinvade some of the space occupied by CO<sub>2</sub>, principally in the lower part of the reservoir; this is referred as imbibition. The key concepts of relative permeability, capillary forces and wettability will now be introduced in more detail.

#### **2.2.3.1 Relative Permeability**

The presence of the brine phase wetting pores and pore throats makes it more difficult for the CO<sub>2</sub> to propagate through the reservoir. There are several reasons for that. Firstly the effective porosity available for CO<sub>2</sub> flow is lower because of the presence of the brine phase. Secondly, in water-wet rocks the brine cannot be totally expelled from small pores except by dissolution into the CO<sub>2</sub> phase. Brine cannot be expelled because of the emergence of new force affecting the CO<sub>2</sub> flow: the capillary force. In rock pores the capillary force gives rise to a pressure discontinuity at the interface between the two fluids. The capillary pressure in an ideal cylindrical pore can be calculated with the Young-Laplace equation:

$$\Delta P = \frac{2\gamma \cos \theta}{a} \quad (2.3)$$

where  $\Delta P$  is the pressure difference across the fluid interface,  $\gamma$  is the surface tension,  $\theta$  is the contact angle of the fluids interface against the pore wall and  $a$  is the radius of the pore. This equation means that the capillary pressure increases with decreasing pore radius which renders some pores less accessible or even inaccessible to the injected  $\text{CO}_2$ . In the latter case the immobile brine left behind in inaccessible pores is called residual brine.

Macroscopically the sum of these effects is described by the relative permeability parameter, which is defined for each phase as the ratio of the effective permeability to the absolute permeability and is comprised between 0 and 1 (Sahimi, 1993). Usually it is represented as a function of the phase saturations (that is to say the fraction of each phase in the pore space) as shown in Figure 2.10. The relative permeability of reservoir rocks is generally poorly constrained because experimental investigation is difficult, highly transient and time consuming. An encouraging finding from Blunt et al. (2002) is that pore network flow models can in some cases accurately predict relative permeability. Attempts are currently under way to estimate relative permeability in pore-scale simulations using real rock geometries (Bondino et al., 2013).

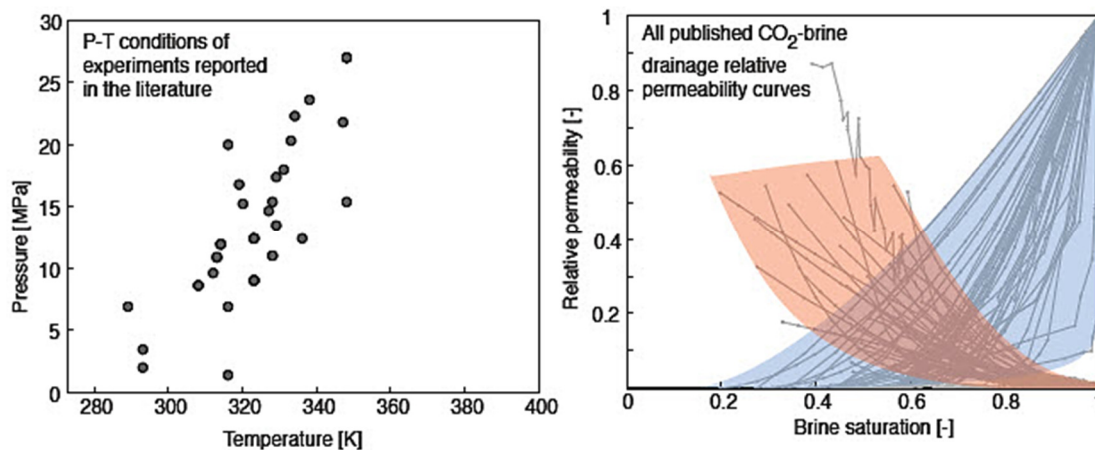


**Figure 2.10** “On the left: pressure and temperature conditions of the drainage  $\text{CO}_2$ -brine relative permeability measurements reported in the literature. Many experiments were performed at similar conditions, with different rock samples. Right: the corresponding relative permeability curves as a function of brine saturation for  $\text{CO}_2$  (in red) and brine (in blue).” Taken from Benson et al. (2013).

### 2.2.3.2 Capillary pressure

Three types of interface exist in the CO<sub>2</sub>-brine-pore system illustrated in Figure 2.11: CO<sub>2</sub>-brine, CO<sub>2</sub>-pore and brine-pore (where the term “pore” is used to denote any mineral substrate).

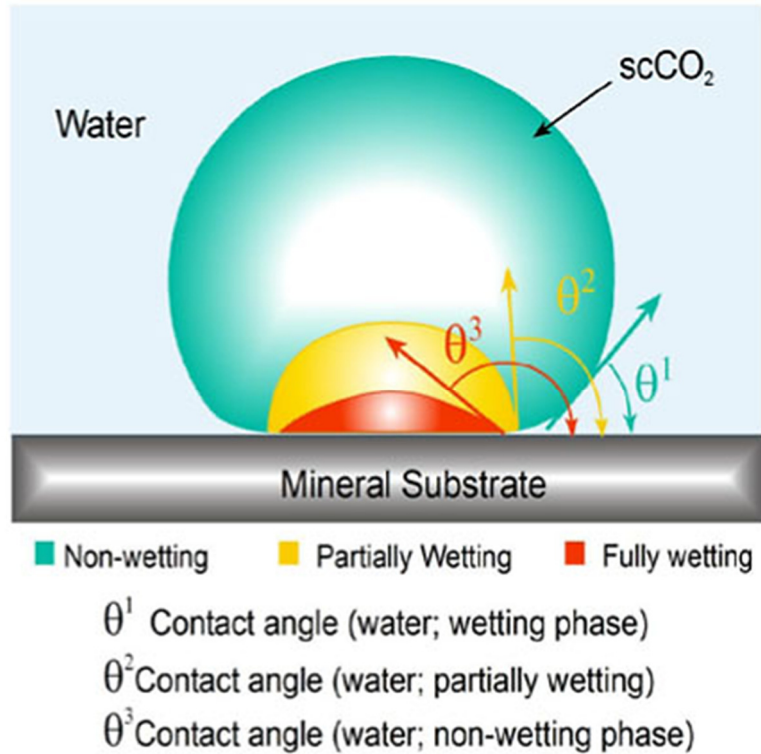


**Figure 2.11** “Cartoon of a droplet of supercritical CO<sub>2</sub> confined by water on a mineral substrate, showing different wetting properties with respect to supercritical CO<sub>2</sub>.” Source: <http://decarboni.se/publications/caprock-systems-co2-geological-storage/21-seal-capacity>. Accessed on 30/11/2013.

Under static conditions, the contact angle  $\theta$  where all three interfaces meet is a function of the interfacial tensions through Young’s equation:

$$\gamma_{SP_1} = \gamma_{SP_2} + \gamma_{P_2P_1} \cos \theta \quad (2.4)$$

Where  $\gamma$  is the surface tension between two phases with S standing for solid (mineral matter) and P<sub>1</sub> and P<sub>2</sub> for phase one and two (for example CO<sub>2</sub> and brine).

The contact angle together with the CO<sub>2</sub>-brine interfacial tension defines the curvature of the interface and the capillary pressure (Nielsen et al 2012) through the Young-Laplace equation (section 2.2.3.1). In summary the capillary pressure which depends on pore size, wetting properties and

interfacial properties will partly control fluid distributions and saturations and therefore reservoir capacity for CO<sub>2</sub> (Tokugana and Wan 2013).

The investigation of CO<sub>2</sub>-brine-mineral interfacial tension at GCS conditions has only recently begun but there is already a significant amount of experimental data on CO<sub>2</sub>-brine interfacial tensions. Bachu and Bennion (2009) performed a series of experiments at different pressure, temperature and salinity conditions and the average CO<sub>2</sub>-brine interfacial tension was found to be 35 mN.m<sup>-1</sup>. The interfacial tension has been found to increase with salinity (Jung and Wan, 2012) and decrease with pH (Chiquet et al 2007) so that fluid chemistry is considered to be very important for determining wettability (Wang et al 2013). Pressure seems to have a major effect on CO<sub>2</sub>-brine interfacial tension (Bachu and Bennion, 2009; Chiquet et al., 2007; Espinoza and Santamarina, 2010; Plug and Bruining, 2007), with interfacial tension decreasing with increasing pressure. However this effect is counterbalanced by the chemical effect of the increased solubility of CO<sub>2</sub> in brine at higher pressures (Duchateau and Broseta 2012). These experimental findings have also been confirmed with molecular simulations (Li et al, 2013; Hamm et al, 2013).

The capillary pressure is further dependent on mineral physical and chemical properties. The interfacial tension at the solid-brine interface depends on the mineral roughness in a way that is poorly constrained. The capillary pressure may also vary with different mineral interfaces (Ellis and Bazylak 2012, 2013). Most agree that the system will always remain water wet but there is still an ambiguity over typical values of contact angles. The difficulty lies in the fact that the wettability is different for each mineral surface and that the surface properties change in presence of CO<sub>2</sub> (because of the pH change), sometimes producing weakly water wet systems. This variability is significant and pore network model results from Ellis and Bazylack (2013) show that contact angle heterogeneity significantly increases CO<sub>2</sub> saturation.

Wettability studies are also important for evaluating the performance of caprocks (Angeli et al 2009, Wollenweber et al 2009; 2010). This is done by calculating the capillary entry pressure of a caprock and predicting how it will evolve as a result of chemical interactions with CO<sub>2</sub>. Although caprocks have very low permeabilities, the pressure build up in the underlying zone could lead to a gas breakthrough either by capillary displacement or by exploiting pre-existing faults or fractures. Differences in gas breakthrough behaviour are governed by interfacial tension and wettability behaviour, which are

specific to individual lithologies. Depending on the conditions the risk should not be totally neglected, even if it seems that it is generally low (Gherardi et al 2007).

### **2.2.3.3 Fingering**

Emerging further complication to arise from two phase flow behavior is the so-called fingering phenomena. Fingering refers to the unstable migration of CO<sub>2</sub> irrespective of media heterogeneities and thus is not to be confused with channeling which is caused by heterogeneities. At GCS conditions, instabilities in the brine-CO<sub>2</sub> interface are expected due to the low viscosity ratio  $N$  of CO<sub>2</sub> viscosity to brine viscosity. These instabilities can take different forms depending on the relative importance of the viscous, capillary and gravity forces (Lenormand et al, 1988), it can be expressed with the capillary number  $C_a$  (ratio of viscous to capillary forces) and the Bond number  $Bo$  (ratio of gravity to capillary forces).

Wang et al (2013) showed with micro-models that capillary fingering was the dominant mechanism in steady injection experiments. Viscous fingering is still expected near the well, during the injection phase, because of the high fluid velocities and elevated densities and viscosities of the CO<sub>2</sub>.

Comparison between viscous and capillary fingering is shown in Figure 2.12 which presents pore network simulations from Ellis and Bazylak (2013). One important implication of fingering for GCS is the great enhancement of CO<sub>2</sub> and brine mixing at small scales, meaning that more CO<sub>2</sub> can dissolve into the brine.

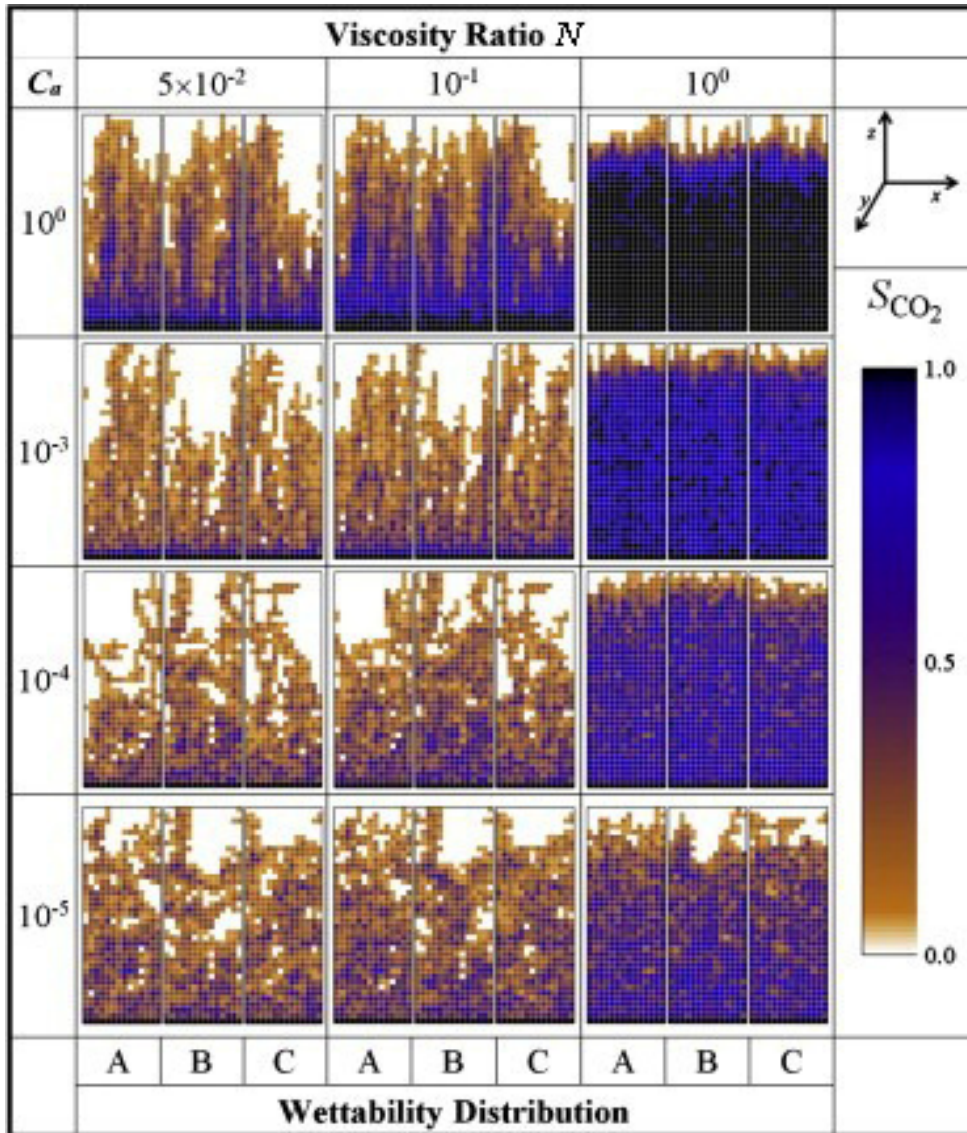


**Figure 2.12** “Saturation patterns for various capillary number ( $C_a$ ), viscosity ratio ( $N$ ), and wettability conditions (varying with mineralogy). The colour values indicate the averaged relative supercritical  $CO_2$  saturation. The bottom face is the inlet in each case, and the mean pore diameter is  $5 \mu m$ . The figure illustrates the stable displacement ( $C_a = 1$  and  $M = 1$ ; top right) and viscous fingering ( $C_a = 1$  and  $M = 0.1$  and  $0.05$ ; top-left) domains. It also shows capillary fingering patterns ( $C_a = 10^{-4}$  and  $10^{-5}$ ; bottom-left). In each of these domains, the general shapes of the saturation and fingering patterns were similar for the A, B, and C distributions, although the changes in entry pressure due to the wettability distributions led to non-identical saturation patterns.” Source: Ellis and Bazylak (2013).

#### 2.2.3.4 Residual trapping

After injection stops and pressure decays, the brine will naturally flow back towards the  $CO_2$ -dominated plume. This quasi-static, capillary-controlled flow will trap some  $CO_2$  in the form of isolated bubbles at the pore scale or in the form of highly  $CO_2$ -saturated zones enclosed by brine-saturated material

at larger scales. This is similar to brine residual trapping during drainage (Ham et al., 2009). The residual (or capillary trapped) CO<sub>2</sub>, may amount to 5-50% of the total injected volume and so residual trapping could be an important process to stabilize CO<sub>2</sub> (Holloway and Savage, 1993; Bennion and Bachu, 2008). It has been demonstrated in short term and core scale experiments that the magnitude of capillary trapping primarily depends on rock properties including porosity, pore size distribution and pore aspect ratio (Iglauer et al 2011; Pentland et al 2011; Tanino and Blunt 2012). It was also found that small scale capillary heterogeneities could greatly increase residual saturations (Krevor et al., 2011).

From the reservoir scale point of view, several issues arise for the calculation of the capillary trapping magnitude. Firstly, leaving aside permeability heterogeneities, the final shape of the CO<sub>2</sub> invasion will depend on the ratio of gravity to viscous forces (Ide et al, 2007). A high ratio will promote the propagation of the CO<sub>2</sub> at the top of the formation and in this case the flow reversal of brine at the end of injection will produce less capillary trapping. In contrast, a low ratio will produce a more vertical CO<sub>2</sub> plume front allowing more homogeneous horizontal return flow of brine at the end of injection and so more capillary trapping. The main parameters controlling the ratio of gravity to viscous forces are the injection rate and the vertical permeability.

Secondly, simulations of Water Alternating Gas (WAG) injections shown that this strategy could enhance capillary trapping and thus sequester more CO<sub>2</sub> in a more secure way (Ide et al., 2007; Juanes et al., 2006; Qi et al., 2009). This kind of injection scheme would allow rapid immobilization of the CO<sub>2</sub> and would also increase the interfacial area between the fluids, favouring solubility trapping.

Finally, when the solubility of the gas phase in the liquid phase is taken into account, there must be some uncertainty in the long term stability of capillary trapped CO<sub>2</sub>. It is predicted from thermodynamic considerations that smaller CO<sub>2</sub> bubbles will be more soluble than large ones. If this is a significant effect over the size range of CO<sub>2</sub> bubbles trapped in nearby pores of different sizes, then there is a gradient to drive dissolved CO<sub>2</sub> from the vicinity of small bubbles to be released into large ones. This "Ostwald ripening" of CO<sub>2</sub> bubbles could in turn generate regions of increasing CO<sub>2</sub> saturation and therefore increasing CO<sub>2</sub> mobility. This aspect of capillary trapping is discussed in detail in Chapter 6.

### 2.2.3.5 Injection pressure

The CO<sub>2</sub> accumulation at the top of the formation could lead to leaks and the leakage risk must be assessed. Several leakage scenarios are possible. As the pressure in the accumulation increases, CO<sub>2</sub> could enter the caprock by capillary displacement. In addition, the pressure build up could propagate into the caprock (Zhou and Birkholzer 2011) and lead to fault activation (Shi et al., 2012) and in extreme cases fracturing, thereby creating new leakage pathways (Zoback and Zinke 2002, Zoback and Gorelick 2012) and induced seismicity (Lucier et al., 2006). The pressure is particularly sensitive to the presence of flow barriers (Chadwick et al., 2009). Thus, in closed systems, the leakage risk could limit the utilization of the pore space to 1-2%. A solution may be to inject CO<sub>2</sub> while producing formation fluid elsewhere (Bergmo et al., 2011).

Implications for GCS operation safety must in particular be addressed for low permeability reservoirs (Rutqvist 2007). It is possible to calculate the bottomhole pressure at the well using the simplified framework of a homogeneous and horizontal aquifer, vertically confined, where CO<sub>2</sub> would be injected through a vertical well along the whole width of the aquifer. A solution was derived by Mathias et al. (2009) by neglecting capillary pressure and considering immiscible two-phase flow and vertical equilibrium.

Figure 2.13 shows calculated bottomhole pressure evolutions at the well for different permeabilities and for an injection rate of 25 Kg/s and a porosity of 30%. The initial reservoir pore pressure at 1000 meters is 10.6 MPa. The bottomhole pressure increases quickly in the first seconds and then increases slowly along a linear trend. The magnitude of the pressure build-up increases dramatically with decreasing permeability but is negligible for a high reservoir permeability of 1 Darcy, as present at Sleipner (Chadwick et al., 2009).

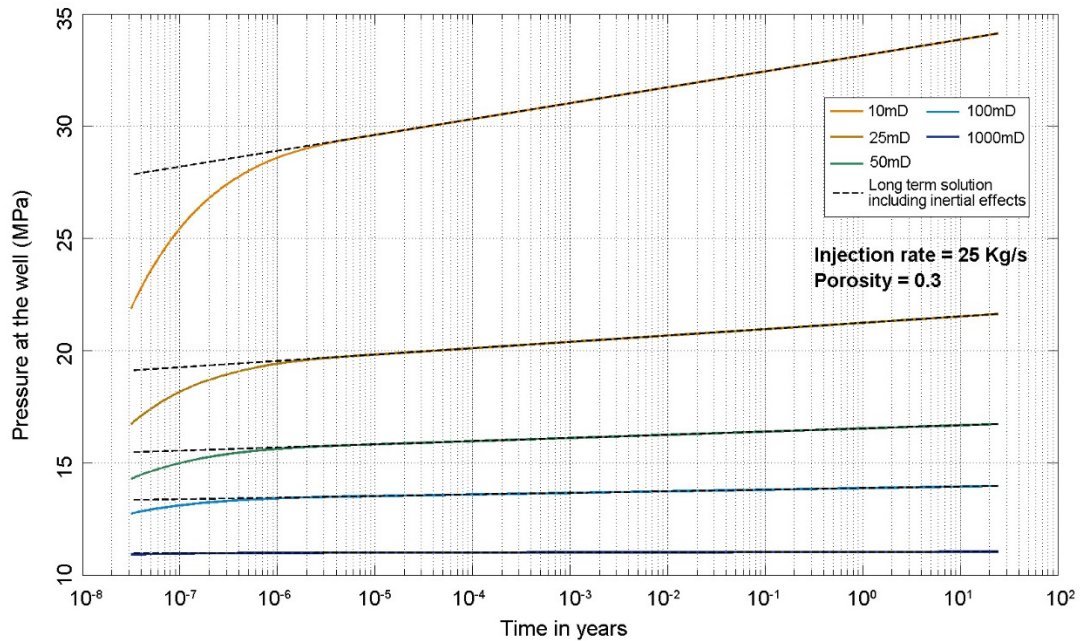


**Figure 2.13** Time evolution of the injection pressure at the well for fixed reservoir porosity and injection rate and variable reservoir permeability. The reservoir is considered to be homogeneous, 50 meters thick and centered at a depth of 1000 meters. Fluid properties are calculated at hydrostatic pressure. Pressure and temperature dependences on the fluid properties are neglected. This is based on Mathias et al., (2009) equations.

In the ideal case presented in Figure 2.13, a doubling of the reservoir permeability caused by CO<sub>2</sub> reaction with calcite would immediately double the maximum injection rate by reducing the fluid pressure. For low permeability reservoirs it is therefore critical to assess the initial porosity and permeability and their possible evolution upon fluid rock interactions to evaluate the feasibility and to properly design GCS operations.

### 2.2.4 Geomechanics

Together with injection pressure considerations, the understanding of rock geomechanic properties is essential to evaluate leakage and wellbore integrity risks and to calibrate seismic monitoring techniques. Fundamental concepts of rock mechanics are well defined but relatively few studies have focused on their implications for GCS operations. Uncertainties on security and confinement are viewed by the Department of Energy and Climate Change (DECC) as major risk factors regarding GCS cost (DECC, 2012).

If the distribution of the gas is not controlled by permeable layers within the target formation the presence of a very low permeability caprock will be

essential to effectively trap the free CO<sub>2</sub> phase. Long term confinement is necessary to satisfy regulations and for public acceptance. Acceptable leakage rates of 0.01 to 0.1% per year have been calculated by Hepple and Benson (2005). Possible leakage paths include caprock defects (faults and fractures) and wells.

#### **2.2.4.1 Fault leakage risks**

One caprock vulnerability is the presence of faults and fractures. Faults are known to be a barrier to lateral flow but also a potential pathway for vertical flow as their permeability is usually orders of magnitude higher than the rock matrix. Faults are present everywhere in the crust so that in practice the stress state of reservoirs is at critical shear failure conditions. This means that any incremental increase in shear stress is impossible as it would be accommodated by fault slipping. Fault slipping ultimately depends on frictional strength of the rock according to Coulomb failure theory. This theory states that the critical shear stress is linked to the effective normal stress and the frictional strength as follows:

$$\tau = \tau_0 + \mu\sigma_n = \tau_0 + \sigma_n \tan \varphi \quad (2.5)$$

where  $\tau_0$  is the rock cohesion and is equal to zero in the case of faults,  $\mu$  is the frictional strength and  $\varphi$  is the angle of internal friction. According to Byerlee's law the best fit to existing underground stress data is  $\tau = 0.85\sigma_n \approx \tan(40^\circ)\sigma_n$  for  $\sigma_n < 200$  MPa which will be verified for GCS operations. Figure 2.14 is a plot of measured stresses in various reservoirs around the world.

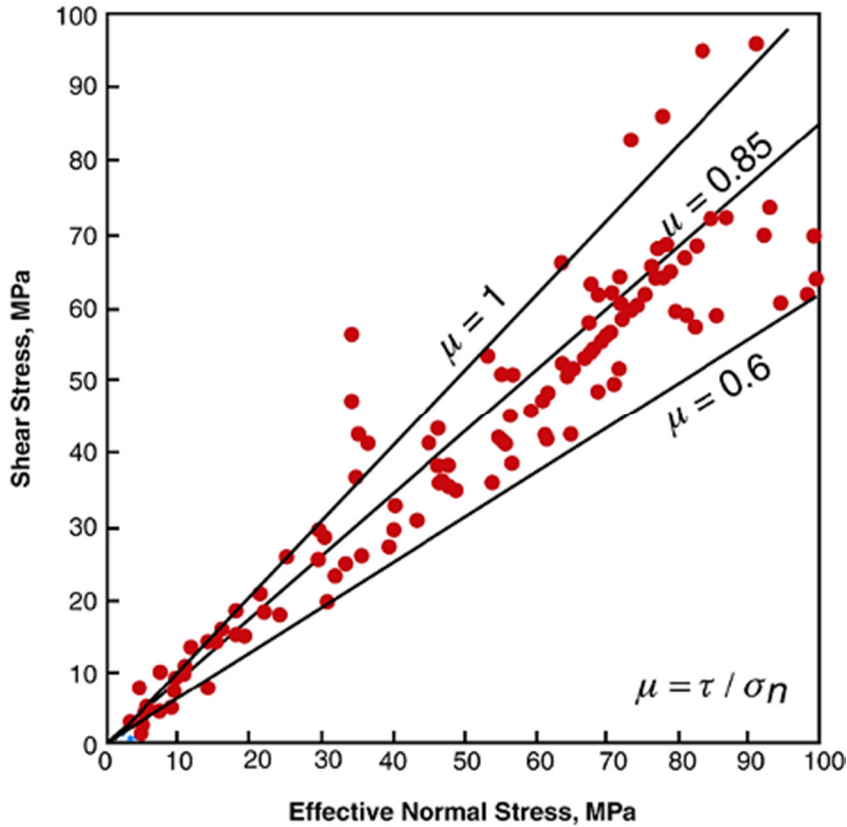


**Figure 2.14** “Stress measurements made in brittle rock (dots) reveal that in most of the world, the crust is in a state of frictional equilibrium for fault slip for coefficients of sliding friction between 0.6 and 1.0 as measured in the laboratory (modified after Townend and Zoback, (2000)).”  
 Source : [http://petrowiki.org/Subsurface\\_stress\\_and\\_pore\\_pressure](http://petrowiki.org/Subsurface_stress_and_pore_pressure) accessed on the 29/11/2014.

The shear stress and effective normal stress can be expressed in term of the maximum ( $\sigma_1$ ) and minimum ( $\sigma_3$ ) principal stresses which act in vertical and horizontal planes.

$$\tau = \frac{(\sigma_1 - \sigma_3)}{2} \sin 2\varphi$$

$$\sigma_N - P_f = \frac{(\sigma_1 + \sigma_3 - 2P_f)}{2} + \frac{(\sigma_1 - \sigma_3)}{2} \cos 2\varphi \quad (2.6)$$

Where  $P_f$  is the pore fluid pressure,  $\frac{(\sigma_1 - \sigma_3)}{2}$  is the differential stress,  $(\sigma_N - P_f)$  is the effective normal stress in the  $\sigma_N$  direction and  $\frac{(\sigma_1 + \sigma_3 - 2P_f)}{2}$  is the mean effective stress. The effect of reservoir pressurization during CO<sub>2</sub> injection can be illustrated on a Mohr diagram (Figure 2.15). In essence, reservoir pressurization reduces the effective normal stresses without changing the differential stress, and so drives the stress state towards shear or tensile failure conditions which a priori can pose a threat to caprock integrity and CO<sub>2</sub> containment (Hawkes et al., 2005).

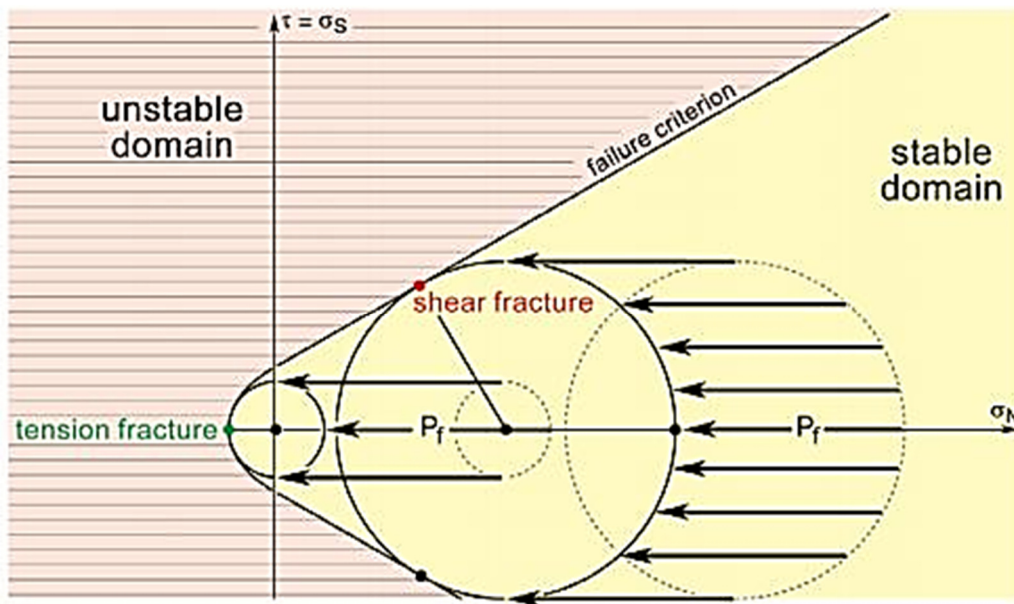


**Figure 2.15** “Effect of the differential stress decrease due to fluid pressure (pore pressure) increase on the fracture type in two-dimensional Mohr diagram.” Source: <http://www.files.ethz.ch/structuralgeology/JPB/files/English/2faulting.pdf>. Accessed on 30/11/14.

The fault planes make an angle  $\varphi$  with respect to the direction of the minimum principal stress. The magnitude of the vertical and horizontal stresses and therefore the orientation of the faults depends on the tectonic regime (Anderson, 1905) as is shown in Figure 2.16. It is clear that failure in a normal stress regime will be the most problematic as it will result in steep fault planes to be activated (Rutqvist et al., 2008a).

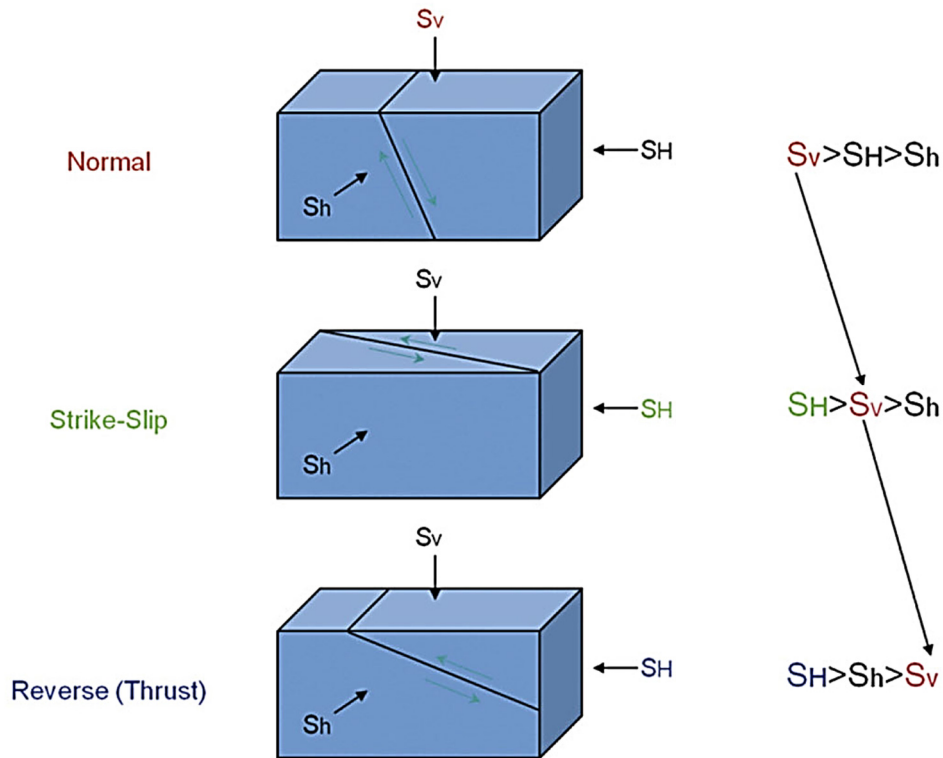


**Figure 2.16** “Changes in faulting regime depending on the relative magnitude of the vertical ( $S_v$ ) and horizontal ( $S_H$  and  $S_h$ ) stresses.”  
Source: <http://csegrecorder.com/articles/view/geomechanics-bridging-the-gap-from-geophysics-to-engineering>. Accessed on 30/11/14.

The stress change in the reservoir following pressurization is further complicated by the reservoir stress path (Hillis, 2001; Teufel et al., 1991). Reservoir expansion in the horizontal direction leads to an increased horizontal stress. Typically the horizontal effective stress is only reduced by 50-80% of the change in pore pressure change while the vertical effective stress is reduced by 100%. This is because the lateral bounding of the reservoir tend to counteract the effect of pore pressure increase through elevated horizontal stress while there is no counter action in the vertical direction due to the existence of a moving boundary at the surface. In a normal faulting regime, an increase in horizontal stress ( $\sigma_3$ ) implies a stabilization of the faults by reducing the differential stress (which is the diameter of the Mohr circle), see Figure 2.17.

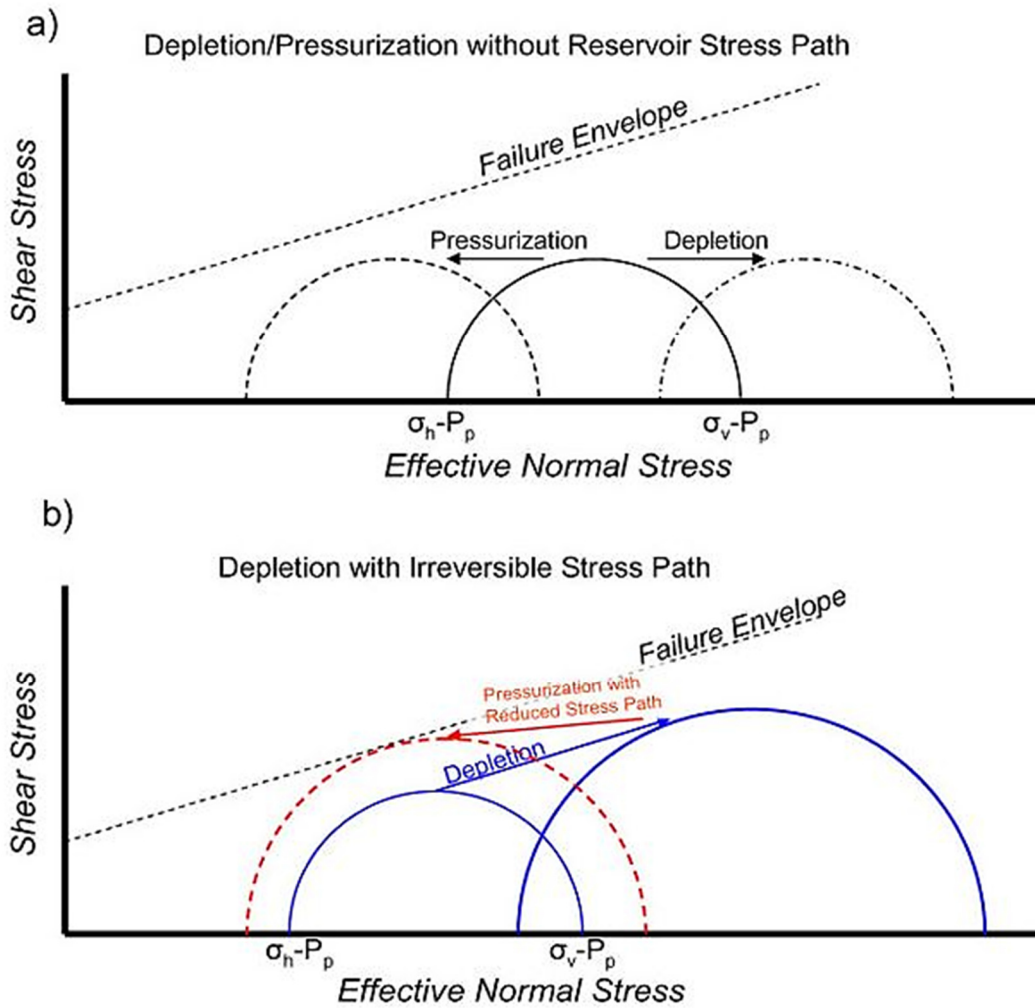


**Figure 2.17** “Mohr diagrams showing the evolution of shear and normal stresses within reservoir domains. In a) there is no reservoir stress path associated with depletion or pressurization. As a result, the difference between the effective minimum horizontal stress and the vertical stress stays the same. Figure b) shows the implications of having a strong reservoir stress path during depletion, which is not followed by the same behavior during re-pressurization. During depletion, the effective horizontal stress does not increase at the same rate as the vertical stress due to a strong reservoir stress path which leads to a reduction in the *in situ* minimum horizontal stress. This leads to an increase in the differential stress on the reservoir.” Source: <http://decarboni.se/publications/caprock-systems-co2-geological-storage/34-geomechanical-response-caprocks-during>. Accessed on 30/11/14.

The stress transfer from the reservoir to the caprock is twofold. Firstly, an increase in horizontal stress in the reservoir provokes a decrease in horizontal stress in the caprock and the underlying formation as shown in Figure 2.18. Secondly, reservoir expansion can also cause an elevation of

the vertical stress in the caprock due to stress arching effects (Rutqvist et al., 2010), this is illustrated in Figure 2.19.

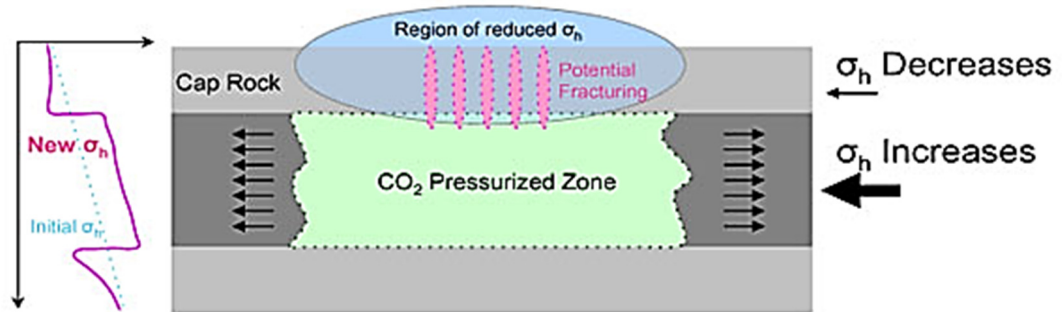


**Figure 2.18** “Schematic illustration explaining how the reservoir stress path operates. As a reservoir is pressurized with CO<sub>2</sub> the reservoir tries to expand laterally due to poroelastic deformation. However, because the reservoir is confined laterally, the minimum horizontal stress increases together with the increase in pore pressure, albeit at a reduced rate. The increase in the minimum horizontal stress at reservoir level leads to a corresponding decrease in horizontal stress in the cap rock due to stress transfer processes. This reduced stress in the cap rock may lead to potential fracturing due to a lowering of the fracture gradient (modified from Marsden, 2007).” Source: <http://decarboni.se/publications/caprock-systems-co2-geological-storage/34-geomechanical-response-caprocks-during>. Accessed on 30/11/14.

The combination of these two effects is an increase in the differential stress localized in the caprock and therefore potential fracturing and fault slipping. In complex systems with layers of various lithologies and mechanical properties the stress transfer can only be studied with coupled hydro-mechanical simulations.

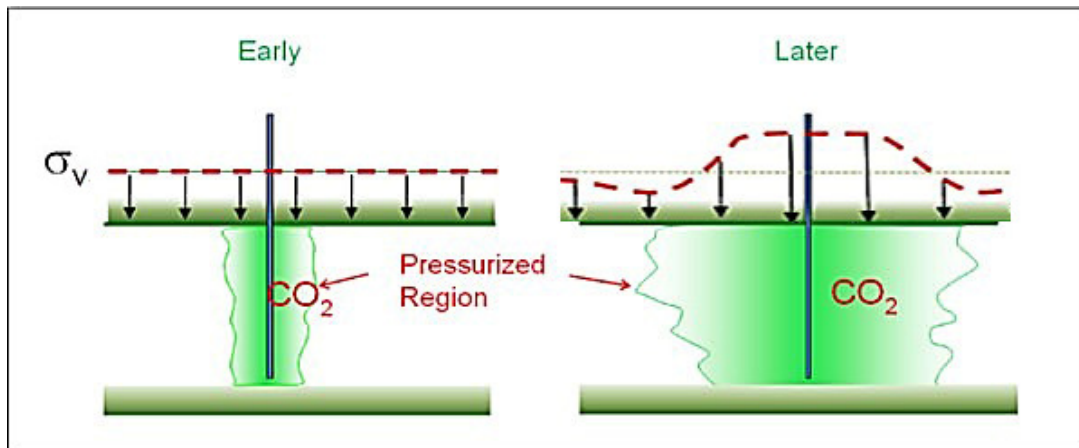


**Figure 2.19** “Schematic cross-section of a reservoir-caprock system, showing how CO<sub>2</sub> injection can lead to stress arching effects, wherein the vertical stress becomes heterogeneous across the reservoir. In the case that the cap rock possesses sufficient stiffness, reservoir dilatancy during injection can lead to an increase in vertical stress above the reservoir, which is accompanied by reduced vertical stress at the edges of the injection zone. In a normal faulting regime, increases in vertical stress within the reservoir and cap rock will increase the reactivation propensity of near-vertically oriented faults.” The extent of the pressurized region is larger than the CO<sub>2</sub> volume due to pressure propagation in the surrounding brine. Source: <http://decarboni.se/publications/caprock-systems-co2-geological-storage/34-geomechanical-response-caprocks-during>. Accessed on 30/11/14.

#### 2.2.4.2 Well leakage risk

Another caprock vulnerability is the wells drilled across it, either the injection well or previously abandoned wells. In fact wells are expected to be the primary leakage path (Birkholzer et al., 2011; Celia et al., 2011) and are central for risk analysis (Gasda et al., 2004; Nordbotten et al., 2008).

Reservoir pressurization and cooling during cold CO<sub>2</sub> injection is greatest near the injection well. The combination of mechanical, thermal and chemical effects can produce and enhance defects in the well. The flow in the cement matrix being negligible (Matteo and Scherer, 2012) these defects will act as preferential leakage paths.

#### 2.2.4.3 Seismic monitoring

Monitoring surveys could be conducted during GCS operations, initially to image the CO<sub>2</sub> migration and after well closure for the detection of leaks. One monitoring method is time-lapse seismic surveys, which examines changes in reflectivity and sonic velocity through time (Chadwick et al, 2005) and detects changes in fluid saturation. The quantitative interpretation of

seismic velocity information relies on Gassmann's equations (Gassmann, 1951) which relates the bulk modulus of the fluid-rock system to the bulk modulus of the individual components and the fluid saturation. In practice the sonic velocity of the system does not depend on fluid saturation alone but is also a function of fluid distribution, which ultimately depends on small scale mixing processes.

P waves normally provide enough information for the determination of fluid saturations. Chapter 5 demonstrates that neglecting fluid rock interactions can invalidate estimates of fluid saturation as they modify both the bulk and shear moduli of the rock. Multicomponent surveys examining P and S waves simultaneously can however discriminate between the effects of physical modifications of the rock by fluid-rock interactions and the effect of fluid substitution (CO<sub>2</sub> replacing brine in the reservoir).

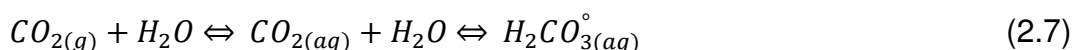
### **2.2.5 Transition**

The complex hydrological processes that are instigated during CO<sub>2</sub> injection lead to a heterogeneous distribution of CO<sub>2</sub> in the reservoir at all scales. This is critical for the mixing of CO<sub>2</sub> with brine and subsequent interactions between the acidified brine and the rock. Chemical interactions can significantly affect all the physical processes presented above by modifying fundamental parameters of the rock such as porosity, permeability, wettability, sonic velocity, bulk modulus, cohesion, and so on. Fluid-rock interactions can have beneficial effects by stabilizing the CO<sub>2</sub> or deleterious effects by modifying injectivity, facilitating leakage or complicating monitoring techniques. The impact of fluid-rock interactions is still the subject of intense study and is the main object of this thesis. Various chemical processes that may occur during carbon sequestration will now be presented and their potential impacts discussed.

## **2.3 Chemistry of GCS**

### **2.3.1 CO<sub>2</sub>-Brine mutual solubility**

From a hydrodynamic perspective, CO<sub>2</sub> and brine can be treated as perfectly distinct phases. However as injected CO<sub>2</sub> contacts the brine and partly invades it, a small fraction of the CO<sub>2</sub> dissolves and forms carbonic acid (Equation 2.7).



Similarly, some water dissolves into the gas stream. The magnitude and rates of CO<sub>2</sub>-brine exchange depends on thermodynamic and hydrological parameters.

The thermodynamics of CO<sub>2</sub>-brine solubility are well understood for NaCl-H<sub>2</sub>O brines. Solubility models exist at relevant pressures, temperatures and brine salinities (Duan and Sun, 2003; Duan et al., 2006; Spycher et al., 2003). These models are simply best-fits to large databases of experimental results. First order observations are that the solubility of CO<sub>2</sub> increases with pressure and decreases with temperature. This translates into a solubility maximum at conditions encountered around 1000 metres below the surface on average. The solubility decreases with brine salinity due to the “salting-out” effect (Diamond and Akinfiev, 2003). Figure 2.20 summarizes these constraints.

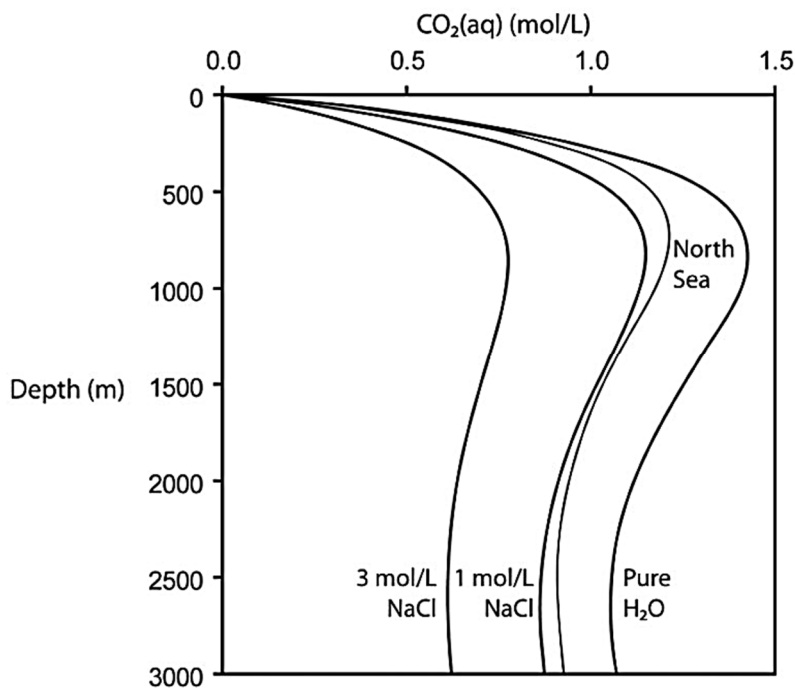


**Figure 2.20** “CO<sub>2</sub> solubility as a function of depth below the surface. Solubility profiles calculated using equations from (Duan et al., 2006), considering typical geothermal gradients of 25C/km and hydrostatic pressure gradients, in pure water and fluid salinities of 1M and 3M NaCl. An example for a typical North Sea geothermal gradient of 25C/km and pore salinity profile of 25,000ppm/km (Bjorlykke and Gran, 1994) is also shown.” Taken from Kampman et al. (2014).

It is well known that CO<sub>2</sub> fugacity must be corrected in geochemical models to account for non-ideal behavior at the pressures and salinities encountered at GCS conditions, (Allen et al., 2005). Additionally, conversion of CO<sub>2</sub> into

bicarbonate ions at pH values above 6 enhances the total dissolved inorganic carbon (Rosenquist et al., 2013). Integrating these effects, CO<sub>2</sub> solubility in brine at GCS conditions is between 1 and 5 wt% (Spycher and Pruess, 2005). For real dynamic systems, estimating the amount and impact of CO<sub>2</sub> dissolution in brine is complex and requires taking into account fluid hydrodynamics.

For short term effects, careful analysis is needed because CO<sub>2</sub> dissolution kinetics are fast but CO<sub>2</sub> diffusion in brine is slow, of the order of 1m per year (Mutoru et al., 2011), or a few times this amount with mechanical dispersion (Backhaus 2011). Therefore the area and the topography of the CO<sub>2</sub>-brine contact controls the extent of CO<sub>2</sub> dissolution. These parameters depend on dispersion, permeability and relative permeability (Bradshaw et al., 2007) as well as on reservoir heterogeneity at all scales (MacMinn et al., 2011). For example, reservoir acidification could be extensive on short time-scales if significant channeling and fingering occurs, increasing the contact area. Acidification would continue as the radius of the CO<sub>2</sub> intrusion increases, allowing CO<sub>2</sub> to contact fresh, unsaturated brine instead of just pushing saturated brine ahead of it. Goodman et al (2013) estimated that up to 20% of the injected CO<sub>2</sub> could dissolve during the injection period.

In the medium term, CO<sub>2</sub> dissolution into underlying brine can be enhanced by convection (Lindeberg and Wesselberg, 1997; Ennis-King et al., 2005). CO<sub>2</sub>-saturated brine is denser by a few percent than the original brine and will slowly sink down and be replaced by fresh brine. High permeability reservoirs like the Utsira sands in the Sleipner GCS project favour the development of convection. Neufeld et al (2010) estimated that 10% of the CO<sub>2</sub> had dissolved at Sleipner after 6 years of injection. Numerical simulations predict total dissolution of CO<sub>2</sub> after hundreds to thousands of years (Benson and Cole, 2008). This is corroborated by observations made on natural reservoirs that contained CO<sub>2</sub> on geological timescales (Gilfillan et al., 2009).

Dissolution enhances reservoir sequestration capacity (MacMinn et al., 2011) because at GCS conditions the apparent molar volume of dissolved CO<sub>2</sub> is approximately half that of the gas phase (Bodnar et al., 2014). While it is clear that solubility trapping could greatly increase sequestration capacity, the overall rate of dissolution is difficult to predict. Reservoir management options to enhance CO<sub>2</sub> dissolution are under study (Leonenko and Keith, 2008; Buscheck et al., 2011). WAG injection can potentially increase fluid mixing (Qi et al, 2009). This could be associated with fluid

extraction and reinjection to control reservoir pressure and force CO<sub>2</sub>-brine mixing in the wellbore area (Hassanzadeh, 2009). The use of multiple horizontally dispersed wells is also a solution for low permeability reservoirs that can enhance dissolution, as in the In Sahla injection site (Michael et al., 2010).

Water dissolution in the CO<sub>2</sub> phase is generally less important than the reverse process, and ranges between 0.1 and 0.5 wt% under GCS conditions (King et al, 1992). This nevertheless has consequences for hydrodynamics and chemistry. Firstly, as the CO<sub>2</sub> keeps flowing in the well area, residually-trapped brine will gradually be evaporated, possibly leading to a complete “dry-out” of the formation (Pruess, 2009). This drying can result in the precipitation of halite and can produce mechanical instabilities (Giorgis et al., 2007) and a severe loss of injectivity (Pruess and Müller, 2009; Ott et al., 2011). The loss of injectivity could be even greater if the CO<sub>2</sub> injection was not continuous so that brine re-imbibition/desiccation cycles take place. On the other hand the loss of injectivity in the most permeable layers could lead to improved sweeping efficiency with fewer bypasses of low porosity regions (since the injection pressure must increase). The displacement efficiency is strongly influenced by small scale heterogeneities and is enhanced at high flow rates/pressures (Perrin et al., 2009).

On the chemical side, it has been noted that wet CO<sub>2</sub> is far more reactive than dry CO<sub>2</sub>; in experiments, wet CO<sub>2</sub> is fixed through carbonation of brucite (Schaefer et al., 2011), portlandite and anorthite (Regnault et al., 2005) and analogous reactions are known in nature.

The chemical and hydrodynamical impacts of water dissolution in CO<sub>2</sub> may be locally important during injection, but the main focus of this thesis is on the potential consequences of CO<sub>2</sub> dissolution in brine on the performance and integrity of the reservoir, this is introduced in the following section.

### **2.3.2 Fluid-rock interactions**

The presence of CO<sub>2</sub> as an immiscible phase is a constant source of acidity through dissolution to form carbonic acid, and this triggers fluid-rock interactions. The consequences of such interactions include dissolution and precipitation of minerals in the host reservoir and potentially in caprocks. It is safe to assume that these reactions will modify the rock properties, but can they affect sequestration efficiency and safety? To find out it is first

necessary to evaluate how much reaction will occur, how fast and at what sites, this is the main subject of Chapters 3 and 6.

The extent of reaction depends primarily on the amounts of reactive minerals present in the reservoir (which can be evaluated) and the CO<sub>2</sub> dissolution rate (which is partly controlled by hydrological parameters). The reaction rate depends on the rate limiting step, which may be dissolution-precipitation or fluid transport. The Peclet and Damköhler numbers are theoretical tools to evaluate the relative importance of those processes. The Peclet number (Pe) is the ratio of advection to diffusion rates of the reactants and products. The Damköhler numbers are either the ratio of reaction to advection rates (Da<sub>I</sub>) or reaction to diffusion rates (Da<sub>II</sub>).

These numbers are useful indicators for the localization of the reactions. At the edge of the advancing CO<sub>2</sub> plume, only fast reactions (high Da) can occur because the fast advection (high Pe) moves the acidified plume front rapidly through the rock. In contrast, transverse diffusion will dominate around high permeability zones, in those stagnant regions slow reactions can occur. Residually trapped water films, coating the grains after CO<sub>2</sub> invasion may however host some slow reactions (Shao et al 2010; Scheaf et al 2013). Overall the main uncertainty is in Damköhler numbers because of the uncertainties in the rates of sluggish reactions, the reactive surface areas and the possible competition between minerals.

With the general issues associated to fluid rock interactions being identified it is now useful to present a more detailed literature review. Dissolution and precipitation reactions will be treated first. Potential impacts on rock properties and knowledge gaps on this particular matter will be presented in a second part.

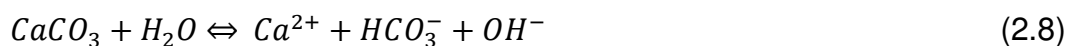
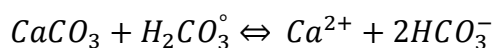
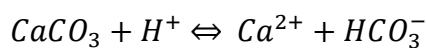
### **2.3.2.1 Mineral dissolution**

Brine acidification is most likely to lead initially to the dissolution of some specific rock-forming minerals, and may also be accompanied by the formation of secondary mineral precipitates. Mineral dissolution is triggered when the fluid becomes undersaturated due to drop in pH. The dissolution rate increases with distance from saturation (i.e. equilibrium) and with temperature, and may also be affected by other factors such as salinity. Reviews of the dissolution kinetics of various minerals at GCS conditions can be found in Palandri and Kharaka (2004), Kaszuba et al. (2013) and references therein. The dissolution rates of most rock-forming minerals are only poorly known at typical GCS reservoir temperatures because they are

slow and therefore difficult to measure. The overall dissolution rate depends on the dissolution kinetics and the accessible reactive surface area (Steeffel et al., 2005; Bickle et al., 2013). Image analysis of rocks reveals that the accessible reactive surface area of a given mineral can be a very small fraction (a few percent) of the total area due to mineral coatings (Peters, 2009), but for some minerals micro-porosity can lead to anomalously high surface areas. The reactive surface area is inevitably modified during dissolution, first increasing as dissolution increases the surface roughness but eventually declining to zero as the grain is totally dissolved. During simulations, reactive surface area modifications are often based on the work of Sonnenthal et al (2005) and use a cubic array of truncated spheres.

One more thing to consider is that where multiple mineral phases are present, they react at different rates. This means that fast reacting mineral can consume the brine acidity and thereby inhibit dissolution of slowly reacting minerals (Prigobbe et al., 2009). In addition many minerals dissolve incongruently: Carroll and Knauss (2005) studied labradorite dissolution rates and found that below 60°C, calcium was released three times faster than silica. Even if numerical sensitivity studies can partly circumvent these subtleties, more experimental investigation of dissolution rates under GCS conditions are needed. In particular, it is useful to study the dissolution rates of silicates as these likely provide the rate limiting step for CO<sub>2</sub> mineral trapping through CO<sub>2</sub> carbonation (Daval et al., 2010).

This study is principally focused on one mineral: calcite. At GCS conditions carbonate minerals and calcite in particular will dissolve orders of magnitude faster than other rock forming minerals (Palandri and Kharaka, 2004). Calcite dissolution has been extensively investigated, see for example Plummer et al (1978) and Pokrovsky et al (2009) which provide a synthesis and review of current thinking; it has been proposed that three parallel reactions can account for calcite dissolution (Equation 2.8).



At CO<sub>2</sub> pressures above 1 MPa calcite dissolution rate mainly depends on the pH but is weakly dependent on ionic strength and temperature. At fast transport rates calcite dissolution is typically transport limited at pH below 4 (Pokrovsky et al, 2005), hence the transport rate of acidity towards the calcite surface will most of the time be the rate limiting step for calcite

dissolution throughout the reservoir (Morse and Arvidson 2002). Calcite is present in most sedimentary reservoirs, and where present it will most likely dominate initial fluid-rock interactions and inhibit silicate dissolution, as observed in flow-through experiments (Kjolloer et al, 2011; Canal et al, 2012). Calcite dissolution does not directly participate to CO<sub>2</sub> trapping but it can modify reservoir properties over very short time scales.

In summary, the acidification of the brine will induce rapid and sustainable dissolution of the carbonate minerals in the vicinity of the CO<sub>2</sub> front. It will also lead to the slower dissolution of the other rock forming minerals. It is expected that dissolved carbonates will eventually re-precipitate either in stagnant microenvironments or further downstream as the CO<sub>2</sub> pressure diminishes and the pH increases. Additional calcite precipitation will occur if calcium ions have been released during silicate dissolution.

### **2.3.2.2 Mineral precipitation/trapping**

Numerous studies have focused on reaction paths that lead to the long term sequestration of CO<sub>2</sub> into carbonate minerals (Kaszuba et al., 2005; Rosenbauer et al., 2005; Hangx and Spiers, 2009). Mineral trapping is thought to be the most secure way to sequester CO<sub>2</sub>. Cations necessary for carbonate precipitation can be already present in the brine but most of the time as dissolved chlorides so that taking them out to form carbonates generates hydrochloric acid and stops further mineral growth. The most relevant mineral capture process is when the cations are provided by non-carbonate minerals such as silicates. Carbonate precipitation following feldspar dissolution has been demonstrated with batch reactor experiments, field observations and numerical simulations (Bénézech et al., 2009; Xu et al 2010; Kaszuba et al., 2005).

Classical theory states that the precipitation starts with nanoparticle nucleation when a critical supersaturation is reached (Giammar et al., 2005). Supersaturation can be brought about by change in brine composition, pCO<sub>2</sub>, pressure or temperature. In a flow-through reactor experiment trying to emulate a CO<sub>2</sub> injection scenario Bateman et al (2011) observed that calcite dissolved at the inlet and precipitated at the outlet. Along the flow path the reactions with other minerals and the decrease in pressure have led to the oversaturation of the fluid with respect to calcite. Extrapolating this result to the reservoir scale is not straightforward because heterogeneities may allow conditions for carbonate precipitation to develop in zones of slow flow throughout the reservoir.

The extent of mineral trapping depends on the availability of divalent cations and in practice will be kinetically limited by the silicate dissolution rate. Batch reaction modelling studies show that mineral trapping varies considerably with the rock types and CO<sub>2</sub> solubility. In detail, CO<sub>2</sub> carbonation depends on brine composition, pressure and temperature but the main control is mineralogical (Kaszuba et al., 2005, Knauss et al., 2005, Palandri and Kharaka, 2005). Audigane et al (2007) conducted reactive flow simulations and predicted that mineral trapping could account for only a few percent of the total sequestered CO<sub>2</sub> at Sleipner after a thousands of years. On the other hand Zhang et al (2009) estimated up to 80% mineral trapping for a far more reactive sandstone after 1000 years. This proportion could approach 100% in some reservoirs, effectively solving concerns about CO<sub>2</sub> leakage in the long term.

Secondary mineral precipitation is clearly documented in nature, especially where ultramafic rocks are available however carbonate precipitation is not always found. Hangx and Spiers (2009) studied the reaction of plagioclase feldspars (anorthite and albite) with CO<sub>2</sub> and brine; they observed clay precipitation (kaolinite, illite and smectite) rather than carbonate growth, and suggested that a carbonate substrate may be needed to promote precipitation. Similarly, Lu et al. (2011) only observed the precipitation of allophane (another clay) and the illitization of smectite. Kaszuba et al. (2005) used different chips of aquifer and caprock together and did observe magnesite and siderite (carbonate minerals less soluble than calcite) together with amorphous silica precipitation. Ketzer et al. (2009) observed some precipitation of calcite (accompanied by kaolinite) in experiments on Rio Bonito sandstone, but no carbon sink as it essentially consisted of re-precipitation. According to Soong et al. (2004) calcite precipitation can only be significant if the pH of the brine is buffered to values above 9.

The presence of minerals and pores affects carbonate precipitation in GCS context (De Yoreo et al., 2014). The presence of carbonate minerals can enhance carbonate precipitation as the precipitation energy barrier on their surface is lower. In fact the sole presence of any mineral surface can enhance the precipitation rate by 18 orders of magnitude compared to precipitation in the bulk fluid (Heges and Whitlam, 2012). Even an unreactive mineral like quartz can support calcite precipitation at ambient conditions: Fernandez et al (2013) observed the formation of 2 nm size spherical particles of calcite on quartz surfaces using small-angle scattering technique. Finally, the fact that the pore space is confined also enhances

precipitation (Heges and Whitlam, 2012). Those processes pose the question of how precipitation can affect rock properties in various topographical, mineralogical and chemical contexts. If homogeneous nucleation can happen, nuclei are likely to be transported and accumulate at the pore throats and block the flow. In the case of heterogeneous nucleation, the precipitation will occur at specific sites and affect fluid flow in an unpredictable way. Precipitation experiments in flow through reactors are very scarce, results of such an experiment are presented in Chapter 6.

### **2.3.2.3 Impurities in the injected gas phase**

To reduce the cost of GCS projects, it is likely that variable amounts of other gases will be co-injected. Several studies have focused on SO<sub>2</sub> and H<sub>2</sub>S. SO<sub>2</sub> injection may have the greater effect; 1% of SO<sub>2</sub> alone could sufficiently acidify the brine to prevent mineral trapping for tens or hundreds of years (Knauss et al., 2005); it would also dramatically enhance dissolution (Kummerow and Spangenberg, 2011). In some configurations, SO<sub>2</sub> dissolution and subsequent oxidation to sulfate could lead to anhydrite precipitation (Xiao et al., 2009). The slow diffusion of SO<sub>2</sub> in the CO<sub>2</sub> plume could mitigate these effects (Ellis et al., 2010). To a smaller extent H<sub>2</sub>S injection could also enhance mineral dissolution; in parallel its high solubility could provoke a lowering the interfacial tension and the capillary pressure (Bennion and Bachu, 2008). It is generally accepted that impurities will increase the reactivity of the system (Xu et al., 2007; Palandri and Kharaka 2005) however they are not addressed in this thesis.

### **2.3.2.4 Field evidence of fluid-rock interactions**

Fluid sampling in field tests such as Frio (Hovorka et al., 2006; Kharaka et al., 2006), Ketzin (Zimmer et al., 2011) or Cranfield (Lu et al., 2012) provides important information on the timing and progress of CO<sub>2</sub> dissolution and subsequent reactions. In their review paper, Kampman et al (2014) note that significant changes in fluid chemistry (pH, alkalinity, electrical conductivity and trace metal content) occur on short time scales ranging from days to weeks and can be attributed to fast CO<sub>2</sub> dissolution.

CO<sub>2</sub> concentration at observation wells increases gradually, and Kampman et al (2014) argue that this is due to CO<sub>2</sub> dispersion and reservoir heterogeneity. It is accompanied by evidence for gradual dissolution of calcite, when present, until it reaches saturation, over tens of days. Eventual carbonate precipitation may be inferred from fluid analyses on the time scale of weeks to months. Less soluble carbonate minerals precipitate first, for

example ankerite and siderite were inferred at the Frio project (Kharaka et al., 2006). As a consequence calcite can remain undersaturated and continue dissolving for an extended time.

Along with calcite dissolution, trace metal mobilization (Xu et al., 2010) related to Fe-oxyhydroxide dissolution (Kharaka et al., 2006) has been detected. Nevertheless, the system remains dominated by carbonates in both field trials one year after well completion (Lu et al., 2012) and after one year of CO<sub>2</sub> exposure in laboratory experiments (Kjoller et al., 2011).

Longer term reactions can be assessed with the aid of natural analogues. In reservoir sandstones from the Colorado Plateau, the dissolution of feldspars and phyllosilicates competed with the dissolution of carbonates (Bickle et al., 2014). Precipitation reactions mainly involved carbonates such as ankerite, siderite, dolomite and calcite (Zhu, 2005; Heinemann et al 2013).

## **2.4 Implications of fluid-rock interactions**

So far, a few tens of GCS projects have been carried out around the world (Michael et al. 2010). A striking feature is the variability in the fundamental properties of the aquifers chosen for injection. For instance, aquifers with permeabilities ranging from 5 mD (milliDarcy) at In Salah (Algeria) to 5000 mD at Sleipner (North Sea) are apparently both viable (1 mD =  $9.869233 \cdot 10^{-16}$  m<sup>2</sup>). This fact is encouraging given that thousands of GCS operations would be necessary to make a significant cut in CO<sub>2</sub> emissions. But it also represents a great challenge: trying to correctly predict CO<sub>2</sub> behaviour in any aquifer conditions. The case of the Utsira formation in Sleipner is “almost ideal” because the high porosity and permeability of the reservoir sandstone means that CO<sub>2</sub> injection has barely any impact on the mechanical and chemical stability of the reservoir. The situation is only slightly complicated by the presence of low permeability intra-reservoir mudstones (Boait et al., 2011; Johnson and Nitao, 2003). In this case, simple hydrogeological simulations (Audigane et al., 2007), or analytical solutions (Nordbotten and Celia., 2006) can predict the CO<sub>2</sub> fate. However in the general case, CO<sub>2</sub> sequestration will trigger a complex interplay between geochemistry, geomechanics and hydrogeology. Reactive transport codes such as NUFT (Hao et al., 2011) CRUNCH (Steeffel, 2006), PHAST (Parkhurst et al., 2005) or TOUGHREACT (Xu et al., 2011) aim at integrating geochemical and hydrogeological processes. Much fewer codes try to include geomechanics; examples are TOUGH-FLAC (Rutqvist et al., 2008b) or RCB (Kvamme and Liu, 2009). Reactive transport codes are essential tools for aquifer screening

and operation design. However, their increasing complexity is calling for more experimental validation.

Experiments provide relevant physical and chemical parameters, making it possible to study non-classical behaviour and to calibrate the models. Firstly however, fluid-rock interactions are not fully understood: clay swelling and clay precipitation mechanisms are still uncertain, and even where theories and models exist (Steefel and Van Cappellen, 1990) they are not integrated in the reactive transport codes. For dissolution, work continues to gather further kinetics data (Carroll and Knauss, 2005; Allan et al., 2011; Rösenqvist et al., 2012), but it is also important to ensure that rate-limiting steps are understood. Secondly, there is a poor understanding of the implications of fluid-rock interactions for the petrophysical properties of the rocks (Gaus et al., 2010). This is mainly because petrophysical properties are modified at the pore scale whereas continuum-scale models, by definition, do not explicitly account for pore-scale interactions. On the other hand it is difficult to introduce geochemical modelling into pore-scale models because of the computational expense.

It is easy to imagine that dissolution can have vastly different effects according to whether it is isolated detrital grains or their bonding cement that dissolves. Dissolution of pure carbonate rocks has been studied extensively because of the interest in Enhanced Oil Recovery (EOR) from carbonate reservoirs, and in particular the determination of flow regimes that would lead to the formation of wormholes. By comparison, calcite-cemented or more generally calcite-bearing sandstones have been little studied. On this subject, there are contradictory hypotheses. Will dissolution enhance permeability by opening new flow paths, or on the contrary, will it result in release of fines, re-precipitation and ultimately pore clogging? Can it result in a destabilization of the rock matrix, leading to grain rearrangement and compaction? It is particularly critical to understand how low permeability sandstones containing significant amounts of calcite will react to the injection of CO<sub>2</sub> in order to assess short term reservoir performance, and this is the topic of much of the work described in the following chapters.

#### **2.4.1 Impact on caprock petrophysical properties**

The potential of geochemical reactions to increase caprock transmissivity has been of primary interest when dealing with fluid-rock interactions. Several groups have tested various caprock samples but none found significant or adverse permeability changes (Rimmelé et al., 2010; Bachaud et al., 2011; Carey, 2013). The main reason for this is that the transport of

chemical components in caprocks matrix is diffusion limited which allows time for re-precipitation and self-healing. Geochemical profiles through exhumed reservoirs also show limited reaction with CO<sub>2</sub> over geological time scales, for example Wigley et al., (2013b) reported transport and re-deposition of dissolved trace metals over a few centimeters in bleached red sandstones at Green River, Utah (USA). In conclusion it is generally believed to be unlikely that geochemical reactions alone will create leakage paths (Gaus et al., 2010; Gherardi et al., 2007; Wollenweber et al., 2010). It is however possible that reactions will contribute to the enhancement of caprock defects such as fractures and faults, or of leakage paths along the well-well completion cement-reservoir interfaces (Carey et al., 2007) and these effects might lead to leakage.

Fracture dissolution is enhanced during WAG injection experiments with the formation of an acid layer at the fracture surface (Andreani et al., 2008). The initial aperture widening can be mitigated by secondary precipitation (Wigand et al., 2009); by an increase in fracture roughness and tortuosity (Deng et al., 2013; Noiriél et al., 2007); and by grain rearrangement (Ellis et al., 2013). Similar observations can be made for reactions with the wellbore cement. Dissolution of the cement is followed by a carbonation front (Gherardi et al., 2012) so that reaction over the whole length of the well is unlikely (Carey, 2014). More problematic are old abandoned wells that were not properly cemented. A final remark is that during leakage to the surface the pressure is reduced, and this will eventually lead to CO<sub>2</sub> coming out of solution in the form of poorly connected bubbles which would in turn reduce the permeability of the leakage pathway (Plampin et al., 2014).

#### **2.4.2 Impact on reservoir petrophysical properties**

If changes in caprocks properties are limited by the slow diffusion of reactants, this is a priori not the case for the reservoirs. Fluid-rock interaction impacts are twofold. Firstly, fluid-rock interactions can modify the properties of the minerals themselves, for example Kim et al (2012) noted that after CO<sub>2</sub> dissolution, the quartz surface was less water wet which resulted in an increase of the relative permeability to CO<sub>2</sub>. Secondly, reactions can change the rock framework because of dissolution and precipitation. Most studies have focused on carbonate reactions although silicate reactions could be significant at far from equilibrium conditions or over long time scales, and could affect permeability (Nelson et al 1994) and porosity (Soprai et al 2005). There is evidence from natural analogues that these parameters can change significantly, for example Watson et al (2004) inferred a doubling of

porosity and permeability due to albite, calcite and chlorite dissolution in the Ladbroke grove field, with re-precipitation of kaolinite, quartz and carbonates close to the CO<sub>2</sub> water contact.

Historically, permeability enhancement of carbonate rocks has been studied in the context of oil production (McCune et al., 1979). Specifically those studies were searching for the conditions of wormhole formation (Daccord et al., 1993). Wormholes can form in carbonate rocks when strong acids, like hydrochloric acid, are injected. They are meant to counteract the low permeability barrier generated by fines released during drilling. Luquot & Gouze (2009, 2010) performed percolation experiments on carbonate rock using CO<sub>2</sub>-charged brines. Even though carbonic acid is weak they observed a change in the dissolution regime from homogeneous (slow) to heterogeneous (fast) as the CO<sub>2</sub> partial pressure was increased. This was accompanied by a strong increase of the permeability of the sample as wormholes, a heterogeneous dissolution feature, were created.

Minor enhancement of permeability due to homogeneous carbonate dissolution has been reported from batch reactor experiments. For example (Radilla et al., 2010) studied the alteration of limestone from the Dogger Aquifer upon introduction of a dilute acid whereas Rimmele et al. (2010) exposed limestone samples to wet CO<sub>2</sub> and CO<sub>2</sub>-saturated water. Both these experiments represent an end-member in term of reactivity since the fluid is not constantly renewed and so approaches equilibrium as the reaction proceeds. To study pore-scale interactions during CO<sub>2</sub> injection, flow-through reactor experiments provide the other end-member: continuous replenishment of the reactive fluid.

In flow-through experiments the interpretation of the permeability evolution is complex because a range of competing effects are possible. Following dissolution of carbonate, fines may be released, secondary carbonates may precipitate, clay swelling/shrinking may take place and physical compaction can occur. Carbonate secondary precipitation is likely to have an adverse effect on the permeability (Bertier et al., 2006). Clay precipitation following feldspar dissolution could also significantly decrease permeability due to the particular intricate geometry of clay minerals. These complex competing effects may explain the varied and contradictory results in the literature (Bowker and Shuler, 1991; Izgec et al., 2008; Sayegh, 1990; Shiraki and Dunn, 2000).

## 2.5 Conclusion and knowledge gaps

In summary, CO<sub>2</sub> injection into reservoirs and its subsequent sequestration, are controlled by a combination of interdependent and time-dependent hydrological, geochemical and geomechanical processes, summarized in Figure 2.21. Each fundamental process taken individually is fairly well understood but it is clear that there are significant knowledge gaps at the interfaces between geochemistry, hydrology and geomechanics, where processes are modified by fluid-rock interactions. Some interactions are complex and subtle, for example changes in wettability or changes in pressure solution creep rate, while others are more obvious, for example enhancement of porosity by mineral dissolution. This chapter tried to demonstrate that effects due to the dissolution (and eventually re-precipitation) of carbonates and in particular calcite are likely to be particularly significant, at least during the early stages of GCS, and the work presented in the following chapters is designed to investigate them further.

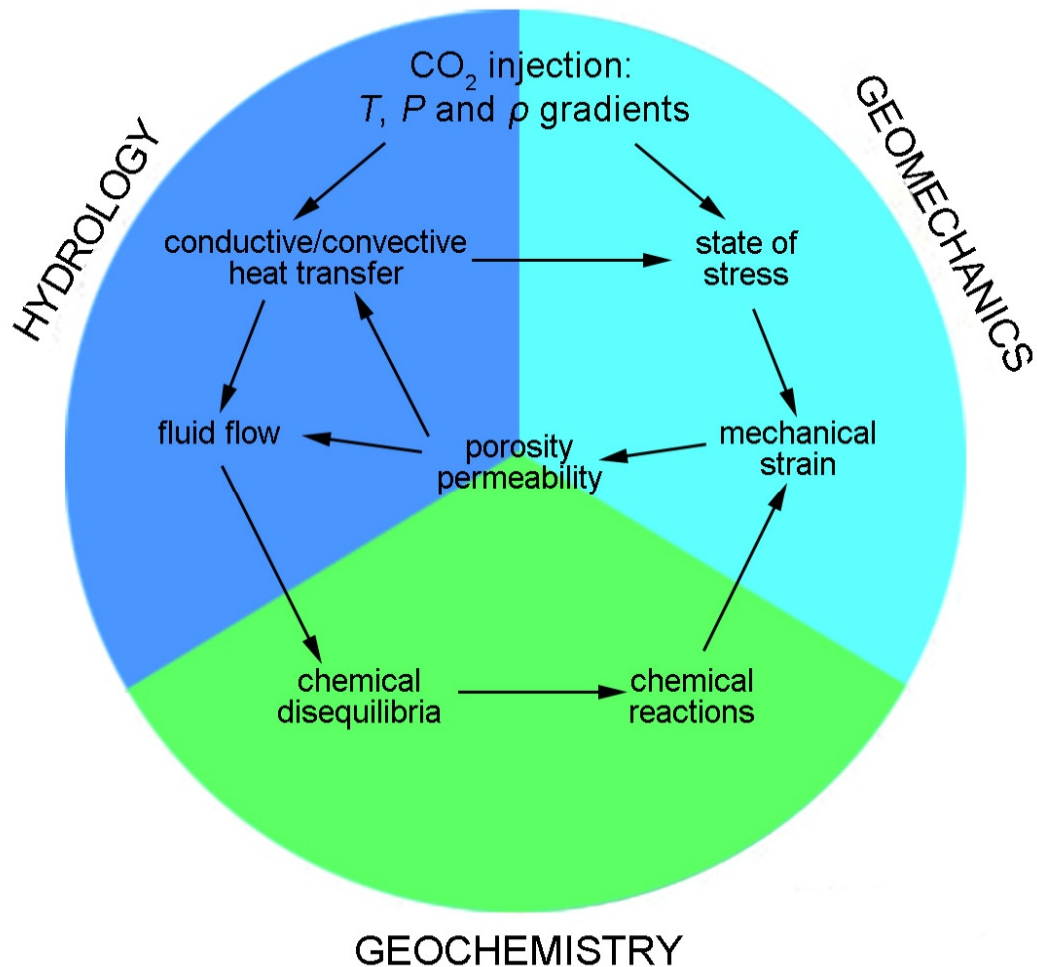


**Figure 2.21** Inter-relationships between the principal processes involved in GCS, from Johnson et al. (2004).

There has been relatively little work on the impact of calcite dissolution when calcite is only a minor rock component, although this is commonly the case in reservoir sandstones. In consequence, minor calcite dissolution is expected to be widespread. Reactive transport models are not very sensitive to the dissolution of 1-5% of a rock with a much larger initial porosity, however this thesis will show that the effect of calcite dissolution on rock properties may be much larger than allowed for in existing models. Equations to describe porosity-permeability relationships and other petrophysical properties need to be calibrated with experiments in the context of GCS. Below are arguments supporting this last point and a description of the project aims.

### **2.5.1 Scale problem**

In current simulations, the fluid flow is assumed to be only controlled by large scale characteristics, principally long range correlations of the permeability field and the boundary conditions. Flow parameters are averaged at the Darcy scale (the scale corresponding to the mathematical discretization of the transport equation). This averaging prevents the development of pore-scaled, chemically-induced heterogeneities. However, in highly reactive systems, chemical dissolution at the pore scale can be transport-limited, and this induces heterogeneous dissolution.

One possible outcome of this situation is the formation of highly conductive and spatially correlated flow channels, referred as wormholes (Daccord et al., 1986; Steefel and Maher, 2009). This phenomenon is characterized by a large permeability increase for a limited porosity change and is specific to carbonate rocks (limestones). However Ross (1982) made qualitatively similar observations with calcite cemented sandstones since the reactive minerals were “strategically” placed in the pore network. Carbonate bearing sandstones have been largely overlooked since then. Sandstones containing variable amounts of dispersed carbonates would de-facto host heterogeneous dissolution, inducing unpredictable permeability changes from the perspective of the continuum scale.

Another possible source of error in applying continuum models to natural rocks is the existence of microenvironments. This is nicely illustrated by the work of Andreani et al (2009). They performed flow-through reactor experiments on ultramafic rock samples (Dunite) and observed totally different features in places sometimes separated by only a few micrometres, with limited dissolution in the preferential flow zones and precipitation in dead-end or reduced flow zones. The permeability increased despite the fact

that overall the porosity was decreasing; because of the localization of the precipitates outside of the main flow paths, at the pore scale.

### **2.5.2 Porosity-permeability relationship**

Since reactive transport simulations yield porosity changes it is attractive to try to infer how permeability will change based on the evolution of porosity. To this end, reactive transport codes provide simple permeability-porosity relationships, such as the Verma-Pruess and the Kozeny-Carman equations. In these models the pore space is idealized by tubes in series or by tortuous capillaries respectively. The relationships are used to calculate permeability variations out of variations in the model pore dimensions, although they depart significantly from experimental data when large porosity variations are applied. To improve the predictive capability of their model over large porosity range Pape et al (1999, 2000) assumed that the pore space had a fractal structure.

The improved equations of Pape et al. work relatively well at reproducing porosity and permeability trends with depth for a given formation: typically the porosity and the permeability decrease with depth due to compaction. Nevertheless, during reactive transport other processes are also participating to the pore structure evolution and those relationships may not be readily applicable to non-classical problems where small scale effects modify the pore space.

Advances in our understanding of porosity and permeability evolution has been enabled by the use of time lapse computer tomography (CT) imaging (Wildenschild and Sheppard, 2013; Blunt et al, 2013). Today micro-CT scans allow a detailed quantification of the pore space distribution and the calculation of reactive surface area or tortuosity Noiriél et al (2009). It is then possible to extract models of the pore space and simulate their evolution. Nogues et al (2013) simulated reactive transport in a simplified representation (pore network model) of a carbonate rock. They found that the permeability scaled with the porosity to the power 4 to 10 depending on rock intrinsic properties (heterogeneity, connectivity and anisotropy) and on the Damköhler and Peclet numbers. This is an important step toward the quantitative interpretation of the porosity-permeability relationship. Another method using fluid flow simulations in real rock geometries and numerical calcite dissolution is presented in Chapter 4.

### **2.5.3 Geomechanics**

There are few publications on the effect of fluid-rock interactions on the mechanical properties of rocks in the context of GCS. Interest in this field is growing since knowledge of rock mechanical properties is essential to monitor CO<sub>2</sub> injection with seismic surveys or to evaluate risks associated with reservoir deformation. Recent investigation indicates that small amounts of carbonate dissolution in limestones and sandstones can significantly decrease sonic velocity (Vanorio et al, 2011; Canal et al, 2012). Much less has been done on the effects on long term rock deformation or failure and yield conditions. Hangx et al (2010) conducted creep test on a sandstone containing 0.3% calcite cement and did not observe any changes in rock strength. More experiments are needed to test rocks with higher carbonate content.

### **2.5.4 Aim, methods and limitations**

The principal hypothesis that motivated this research is that changes in the pore structure, triggered by the injection of CO<sub>2</sub> but ignored in continuum models, can have significant effects on the transport and mechanical properties of a reservoir. The aim is to contribute to better understanding of the coupling between geochemistry and hydrodynamics on two specific aspects: short term petrophysical modifications induced by calcite dissolution-precipitation, and long term capillary trapping.

How do large-scale, averaged properties such as permeability, diffusivity and reactivity depend on pore scale phenomena? Flow-through reactor experiments provides useful data to answer this question, but they have a limited application range due to the complexity and variability of natural rocks. Pore scale modelling provides a more versatile and direct method to evaluate how rock properties evolve. The biggest limitation of this approach is the computing power required which may render it difficult to create a model that is large enough to be representative. In this project, pore scale modelling and experimental approaches have been compared on similar rocks.

A second area of interest is the effect of reactivity on the fate of residually trapped CO<sub>2</sub>; long term simulations always assume this is perfectly immobile but Chapter 7's work tests the hypothesis that CO<sub>2</sub> diffusion in the aqueous phase may lead to an Ostwald ripening process with small trapped bubbles shrinking and feeding bigger bubbles. If this occurred, it may lead to the

reconnection of a continuous CO<sub>2</sub> phase in layers with higher porosity and the possibility of renewed flow.

In summary, the goal of this thesis is to study pore scale gas-fluid-rock interactions and their feedbacks to the macroscopic flow properties and mechanical properties of rocks, aspects which currently are not adequately considered in continuum scale simulators. Chapter 3 describes experimental studies of the effect of calcite dissolution on the flow properties of a potential host rock. Chapter 4 presents an approach to evaluate this effect by direct computation of fluid flow in rock geometries extracted from micro-CT scans of rock cores. Chapter 5 focusses on the potential modifications of the mechanical properties of the reservoir. Chapter 6 is an attempt to observe and quantify the effect of a fluid pressure drop on calcite re-precipitation and subsequent modifications of a host rock. Finally chapter 7 provides new arguments to assess the long term viability of capillary trapping of CO<sub>2</sub>.

## **Chapter 3**

### **The effect of CO<sub>2</sub>-enriched brine injection on the hydrological properties of sandstones.**

The experimental study presented in this chapter explores the effects of fluid rock interactions in response to CO<sub>2</sub> injection on the porosity and permeability of two sandstones. This Chapter is in part adapted from Lamy-Chappuis et al. (2014).

### **3.1 Samples**

#### **3.1.1 Cayton Bay sandstone**

A 40cmx40cmx40 cm<sup>3</sup> block was collected from a 20 meters thick bed of the Jurassic Lower Calcareous Gritstone formation at Cayton Bay, Scarborough (UK). A series of tests and observations were carried out to determine its mineralogical composition (with a special interest for calcite) and its petrophysical properties.

##### **3.1.1.1 Mineralogy**

Initial mineral composition was determined by quantitative X-ray diffraction (QXRD). This method has a nominal detection limit of 0.5% with relative standard deviation typically reaching 10-15% when the mineral fraction is lower than 2%. Results for two samples (mass: 2 g) are given in table 3.1. There is no guarantee that the two samples are fully representative of the bulk rock, but values for all components agree very closely except for the uncertainty in the assignments of sheet silicate peaks between “mica” and “illite/smectite”. Since the carbonate content is of primary importance, an additional four samples were sent for TIC (Total Inorganic Carbon) measurements. TIC values were between 0.62% and 0.70%. Assuming that the carbon comes from calcite and dolomite, the possible total carbonate content lies between 5.8% (for 100% Calcite and 0.70% TIC) and 4.8% (for 100% Dolomite and 0.62% TIC). Since the carbonate distribution is roughly 90% calcite and 10% dolomite (according to QXRD results), TIC values can be translated to calcite contents between 4.6% and 5.2%, and dolomite contents between 0.5% and 0.6%. This is in good agreement with QXRD results. In summary, about 5% of the rock mass (3.4% of its total volume) is calcite and could quickly dissolve in acid, giving rise to pore network modifications.

**Table 3.1** Mineralogy of two Cayton Bay sandstone samples acquired with QXRD technique.

Element	Quartz	Microcline	Mica	Calcite	
Mass fraction of solids (%)	75.8	6.4	4.9	4.8	
	75.6	6.7	7.9	4.2	
	Illite/ Smectite	Kaolinite	Dolomite	Albite	Total
	3.8	0.7	0.7	0.6	97.8
	0.0	0.8	0.6	1.2	97

### 3.1.1.2 Minerals distribution maps

To get some insights on how calcite dissolution may affect the pore network it is necessary to know the spatial distribution of calcite. Mineralogical maps were acquired using a Scanning Electron Microscope (SEM) mounted with an Energy Dispersive X-Ray Spectroscopy (EDS) microprobe on polished thin sections. Based on the mineralogical composition of the sample, maps were made of the following elements: Mg, Ca, Fe, Si, Al, S, K and Na. By applying simple arithmetic calculations to those maps it is possible to construct mineralogical maps (Figure 3.1, see Appendix A for details).

Mineralogical maps show that calcite is dispersed in the form of isolated bioclast fragments. This observation is fundamental for the pore structure evolution. Fluid-rock interactions in a calcite-cemented sandstone would give rise to different permeability evolution than in the present case.

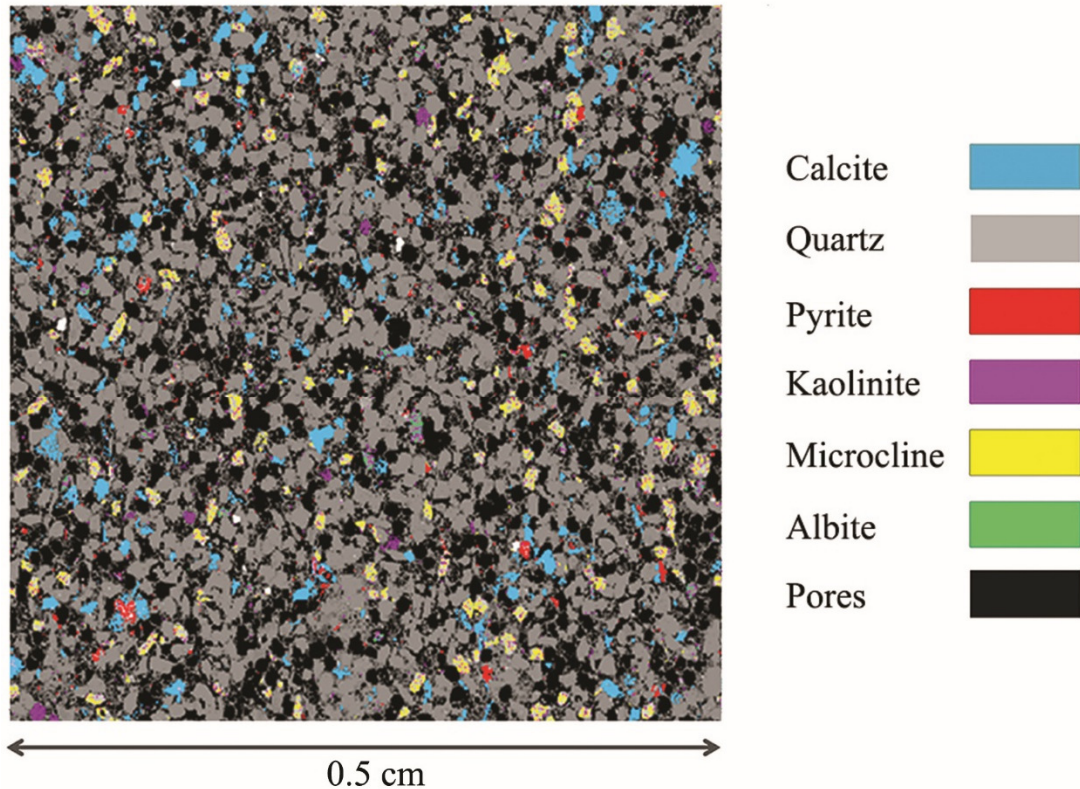


**Figure 3.1** Mineralogical map showing the minerals and pores distribution and size on a 2D section of Cayton Bay sandstone. It is expected that the calcite (in blue), representing about 5% of the rock mass can quickly dissolve in contact of CO<sub>2</sub> charged brines, giving rise to complex modifications of the rock permeability.

### 3.1.1.3 Petrophysical properties

High initial porosity of 30.5 to 35.5% was measured with both helium expansion and NMR methods. NMR analyses showed a bimodal pore size distribution with a main peak at  $T_2=200$  ms, corresponding approximately to a size of 100  $\mu\text{m}$  (Figure 3.2).  $T_2$  is the transverse relaxation time of polarized protons in the pore fluid, for water it depends principally on the pore sizes of the rock (Coates et al., 1999). SEM observations show that the rock contains numerous round pores 100  $\mu\text{m}$  in diameter, but these are connected by small pore throats, see Figure 3.3.

Initial permeability of the cores ranged from 8 to 12 mD (reminder: 1 mD =  $9.869233 \cdot 10^{-16} \text{ m}^2$ ). This is at the very low end of the permeabilities encountered in current injection projects (Michael et al., 2010). As a result this sample illustrates the importance in taking into account permeability change due to calcite dissolution: the high porosity would make this rock a good candidate for GCS in term of sequestration capacity however its relatively low permeability could disqualify it in terms of injectivity depending on fluid rock interactions effects.

The porosity, permeability and calcite content of this sample makes it a well-suited candidate to study the impact of fluid-rock interactions on rock petrophysical properties.

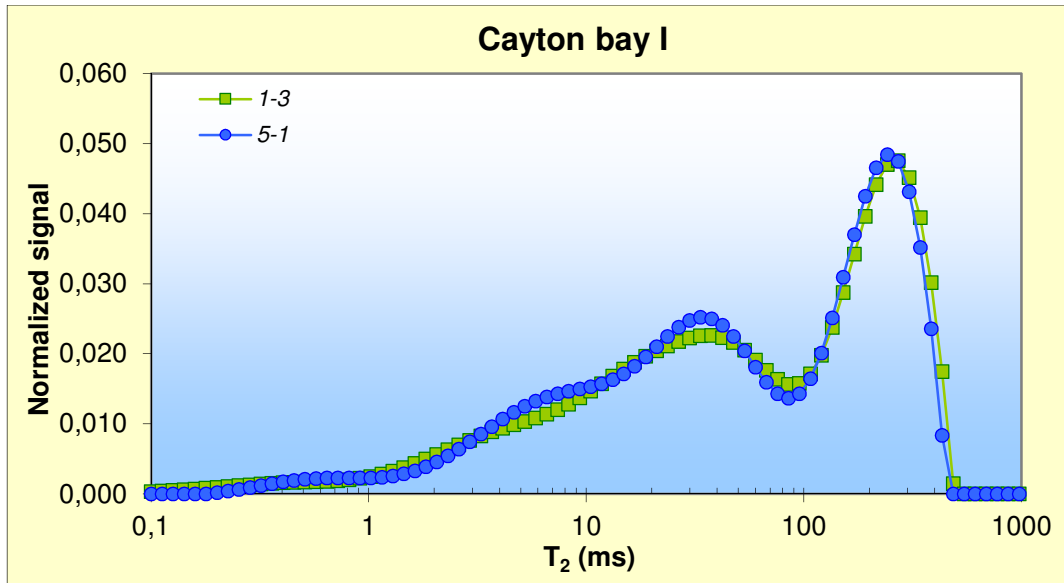


**Figure 3.2** NMR T<sub>2</sub> curves representing the pore size distributions of two Cayton Bay sandstone cores. There is a bimodal pore size distribution with a main peak corresponding to the larger pores (about 100  $\mu\text{m}$  in diameter, visible on Figure 3.1), and micro-pores (see Figure 3.3) of various sizes between T<sub>2</sub>= 1ms and T<sub>2</sub>=100ms.

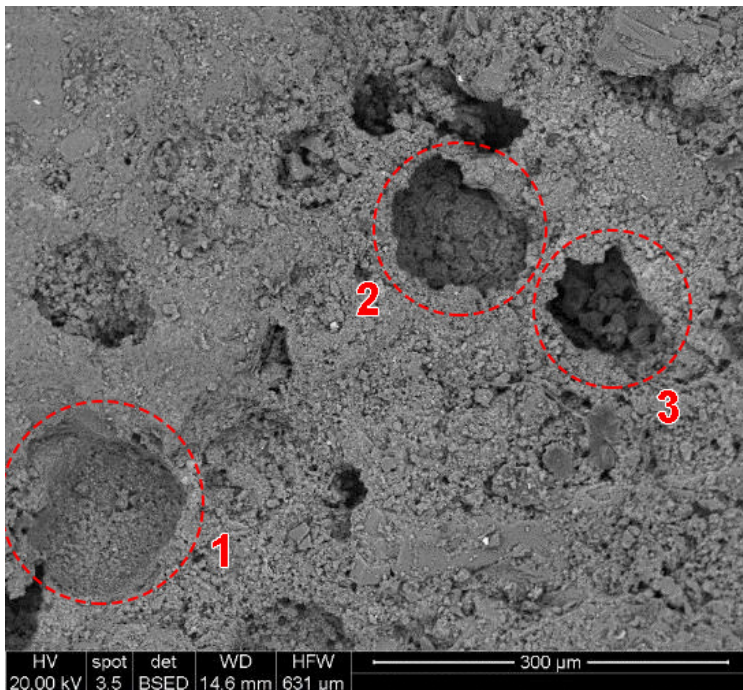


**Figure 3.3** SEM image of the bulk rock (Cayton Bay sandstone) showing 100  $\mu\text{m}$  large pores connected by micro-pores of various sizes. Compare for instance the walls of pores number 1, 2 and 3. This particular disposition of pores result in a large porosity and a small permeability.

### 3.1.2 Bramhope sandstone

A 10cmx10cmx50 cm<sup>3</sup> block of Bramhope sandstone was acquired in a quarry in Bramhope (near Leeds), UK. This sandstone contained less carbonate than the Cayton Bay sandstone (Table 3.2). It presented a porosity of 19±1% and a permeability of 50±10 mD. This sandstone was chosen to provide a less reactive and higher permeability case.

**Table 3.2** Mineralogy of Bramhope sandstone acquired with QXRD technique.

Element	Quartz	Microcline	Mica	Calcite	
Mass fraction of solids (%)	76.1	10.2	6.4	0.4	
	Illite/ Smectite	Kaolinite	Dolomite	Albite	Total
	2.9	1	0.5	0	101.9

## 3.2 Experimental conditions and protocol

### 3.2.1 Rock and fluid properties monitoring

Cylindrical rock cores (5 cm long, 3.75 cm diameter) were drilled parallel to bedding from a single sample block. The cores were initially saturated with 1M NaCl brine and stored for 2 days before being loaded into the core holder.

A flow through reactor set-up was constructed to inject different fluids into the rock cores while monitoring the porosity, permeability and fluid chemistry (Figure 3.4). These standards features were accompanied with special experimental capabilities such as the possibility to perform X-Ray scanning at any time and to directly monitor the fluid pH in-situ with a high pressure pH electrode.

#### 3.2.1.1 Permeability monitoring

The differential pressure across the core was monitored and changes in permeability during each run were calculated from Darcy's law, Darcy's law was applicable since the Reynolds number for our experiments was largely

inferior to 1 (see Table 3.2). Additional measurements of permeability were performed under pure brine saturated conditions before and after the experiments because of the possible permeability measurement errors caused by CO<sub>2</sub> degassing in the system during CO<sub>2</sub>-saturated brine injection.

### **3.2.1.2 Fluid chemistry monitoring**

Chemical analyses of the inlet and outlet fluid were performed to monitor the reactivity and the mass balance of the system. Samples of acidified brine were collected in a syringe under working pressure (1 MPa) at the inlet prior to injection. The syringe was mechanically controlled to retrieve fluids under pressure and avoid any CO<sub>2</sub> degassing in the sampling line. The samples were then titrated to verify the CO<sub>2</sub> concentration of the injected fluid against expected model values (Duan et al., 2006)

Outflow sampling was done at intervals of 15 minutes at the beginning of the experiment, then less frequently. The samples composition was then obtained by with a Agilent 7500ce inductively coupled plasma mass spectrometer in an external laboratory (University of Portsmouth, Dr. Gary Fones, Actlabs) and was checked principally for Ca using a ion-chromatograph (University of Leeds, Dr. Sam Allshorn). Standards were used to evaluate analytical errors, the relative standard deviation of the measurement was found to be lower than 2%. Additionally, the pH was continuously monitored at the outlet using a Unisense® pH electrode system described in Rösenqvist et al. (2012).

The pore pressure was set to 1 MPa because this is the maximum pressure for operation of the Unisense® pH electrode. Pore pressure control was achieved using a back pressure regulator (Figure 3.4). All experiments were carried out at room temperature and with a confining pressure of 10 MPa.

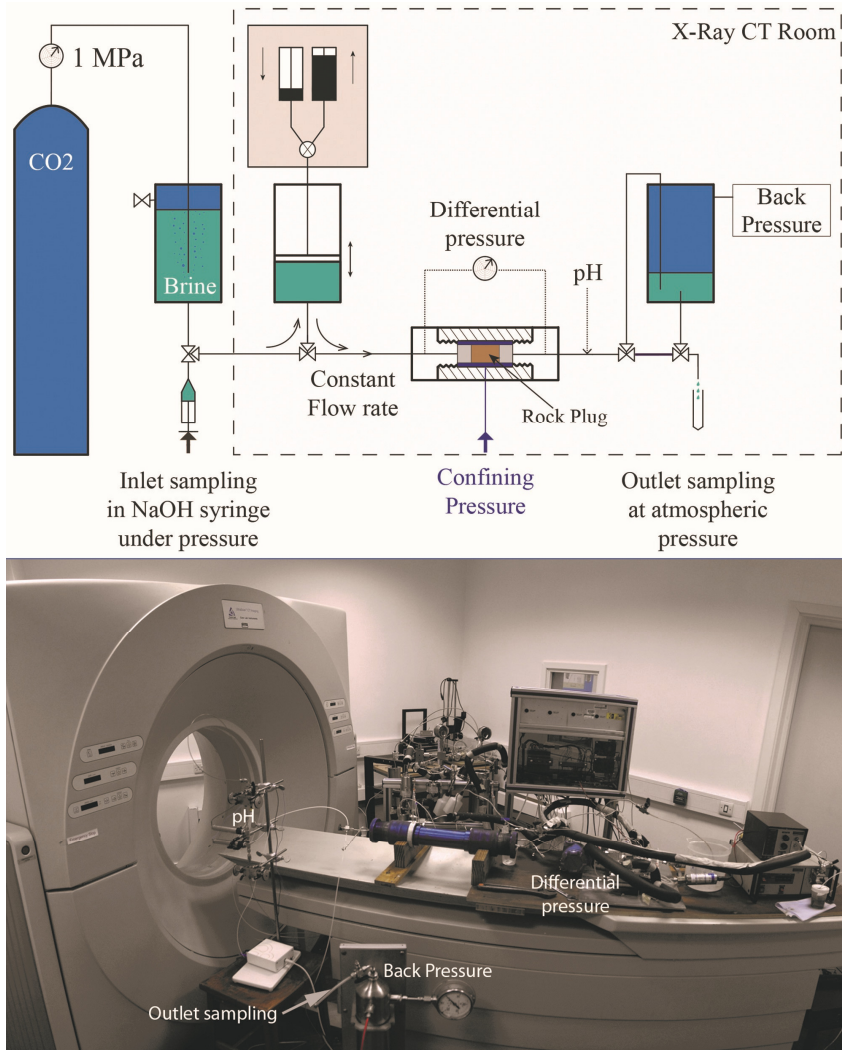


**Figure 3.4** Schematic overview and picture of the experimental setup. CO<sub>2</sub>-saturated brine was stored above a floating piston and injected into the rock sample via a Quizix® dual pump system (grey box). The core holder was placed in the CT scanner during the entire course of the experiment.

### 3.2.1.3 Porosity monitoring

Porosity evolution along the core was monitored periodically with time lapse CT scanning using a PICKER PQ 2000 medical CT scanner. This scanner offers only low pixel resolution (250  $\mu\text{m}$ ) but allows the entire volume of the core to be scanned. Figure 3.5 is a screenshot of the CT scanner monitor showing a cross section, or slice, of a rock core. There is a linear relationship between the grey scale value of each pixel on the image and the CT number of the material. The CT number is a function of the material density and atomic number, typically brighter parts of the image represent denser or less porous material. The CT number is an arbitrary measure of the material and is calibrated regularly against water and air, which by convention are assigned CT values of 0 and -1000 respectively.



**Figure 3.5** 2mm thick cross section of a Cayton Bay rock core as seen in the PICKER PQ 2000 medical CT scanner.

Porosity can be estimated by comparing two scans of the same rock region saturated with two different fluids; most commonly air and brine are contrasted because the large difference in density between them allows for a more accurate porosity determination. Porosity maps can be obtained with image analysis software like Matlab through Equation 3.1.

$$\varphi = (CT_{bs} - CT_{as}) / (CT_b - CT_a) \quad (3.1)$$

where  $\varphi$  is the porosity of a pixel comprising the slice,  $CT_{bs}$  and  $CT_{as}$  are the CT value of the pixel, under 100% brine saturation and 100% air saturation respectively.  $CT_b$  and  $CT_a$  are the CT values of pure brine and air [Withjack, 1988]. Due to errors of core placement in the CT scanner, the porosity cannot be evaluated on a pixel by pixel basis but the averaged porosity of the slice can be determined to within 1% of the porosity evaluated with standard methods (porosity by weight, helium expansion porosimetry), irrespective of the scanner resolution.

It is not practical to use this technique during the brine injection experiment since it would require drying the core at regular intervals to get the full set of CT scans required by Equation 3.1. However this technique is not necessary

if one can assume that a single mineral is dissolving (or multiple minerals with similar X-ray attenuation coefficients), in which case:

$$\delta_{CT} = \delta_{\phi} (CT_b - CT_{\text{mineral}}) \quad (3.2)$$

since  $CT_b - CT_{\text{mineral}}$  is a constant, the variation in porosity ( $\delta_{\phi}$ ) is directly proportional to the variation of the CT number ( $\delta_{CT}$ ). This constant was evaluated by calculating  $\frac{\delta_{CT}}{\delta_{\phi}}$  using two set of scans and Equation 3.1 at the start and end of the experiment. Equation 3.2 was then used to convert incremental CT number variations into porosity variation during the experiments, assuming that only calcite was dissolving.

Core porosity was evaluated on a slice by slice basis as shown in Figure 3.6. The porosity profile improves our understanding of the porosity-permeability relationship. It was possible to determine if the porosity variation was uniform across a sample or if it was localized. For example, it is possible that a similar permeability variation could be caused either by a moderate homogeneous dissolution across the core or a large dissolution at the inlet associated with precipitation at the outlet.

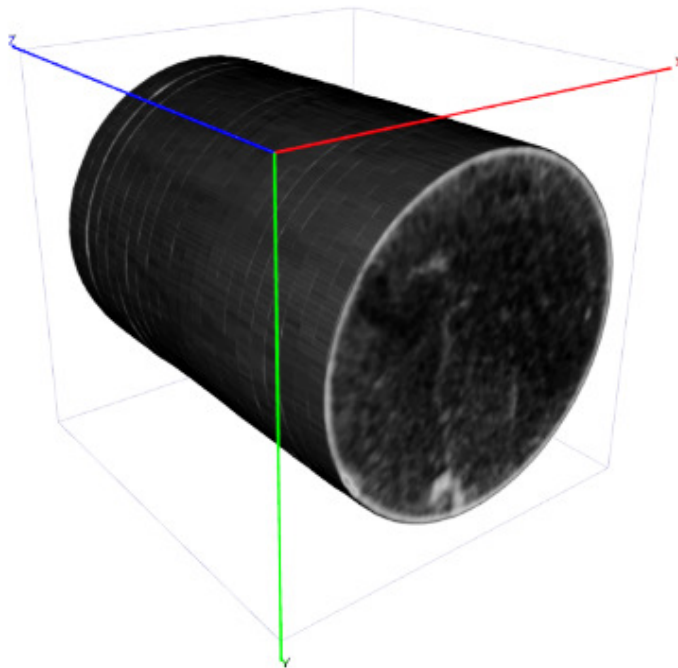


**Figure 3.6** 3D reconstruction of a rock core taken during a CO<sub>2</sub> injection experiment and composed of 24 slices on which the porosity is averaged. In practice the external part of the slices is not taken into account for the porosity calculation due to errors caused by beam hardening effects (bright external rim).

The resolution of the scanner (250  $\mu\text{m}$ ) is not sufficient for a pore scale understanding of pore network evolution and the porosity-permeability relationship. To help the interpretation of the results a comparative study was carried out using pore size distributions obtained by Nuclear Magnetic Resonance (NMR) and observations on thin sections of reacted and unreacted cores. Random walk simulations were also performed on higher resolution 3D models of the pore space reconstructed from separate sets of micro-CT scans (resolution: 2.5  $\mu\text{m}$ ) as described in Chapter 4 (section 4.2). Random walk simulations were used to calculate the tortuosity change of the pore network after calcite dissolution.

### **3.2.2 Injection fluid preparation**

For base-line “unreactive” experiments, the injected fluid was 1M NaCl brine that had been equilibrated with rock powder at room conditions for 1 week and then filtered with a 0.2  $\mu\text{m}$  filter. For the “reactive” experiments the injected fluid was 1 M NaCl brine saturated at 1 MPa  $\text{PCO}_2$  and room temperature resulting in a dissolved  $\text{CO}_2$  concentration of 0.3 mol/L and a pH of 3.3. During supercritical  $\text{CO}_2$  injection in deep saline aquifers, higher  $\text{PCO}_2$  can be achieved which means that  $\text{CO}_2$  solubility will typically be between 0.7 and 1.2 mol/L and the pH at the  $\text{CO}_2$ -brine interface could be as low as 2.8. Hence  $\text{CO}_2$  solubility in the experiments is 3-4 times smaller than could be achieved when injecting  $\text{CO}_2$  into deep reservoirs for GCS. However, the experiments provide a conservative estimate of the effect of  $\text{CO}_2$  and are also likely to reflect conditions in the brine behind the  $\text{CO}_2$  interface.

The  $\text{CO}_2$ -saturated brine was prepared in an accumulator prior to the experiments. A 2 L vessel was filled with 1M NaCl solution and air-vacuumed; the addition of  $\text{CO}_2$  was controlled by an Isco pump set to constant pressure. The accumulator was shaken regularly to enhance mixing. At any time samples could be collected in a high pressure syringe filled with a solution of 1M sodium hydroxide to trap the  $\text{CO}_2$ . The  $\text{CO}_2$  saturation was checked periodically by analyzing a sample and was normally reached after two days.

The volume of carbonated brine prepared for each experiment was in excess relative to the calculation of the volume of fluid required to dissolve all the calcite present in the core; assuming instantaneous dissolution and full accessibility of the calcite. Figure 3.7 present results from a PHREEQC simulation of the injection of  $\text{CO}_2$ -saturated brine at 1 MPa pressure into a rock core similar to the ones used in the experiments (i.e. porosity=30%,

calcite content=5%, length=5 cm, diameter=3.75 cm). PHREEQC (Parkhurst and Appelo, 2013) is a geochemical simulator that includes a simple one dimensional transport module. Figure 3.7 presents the outflow fluid chemistry (i.e. the composition once the fluid has travelled through the core to the last cell of the model; these plots are also known as breakthrough curves).

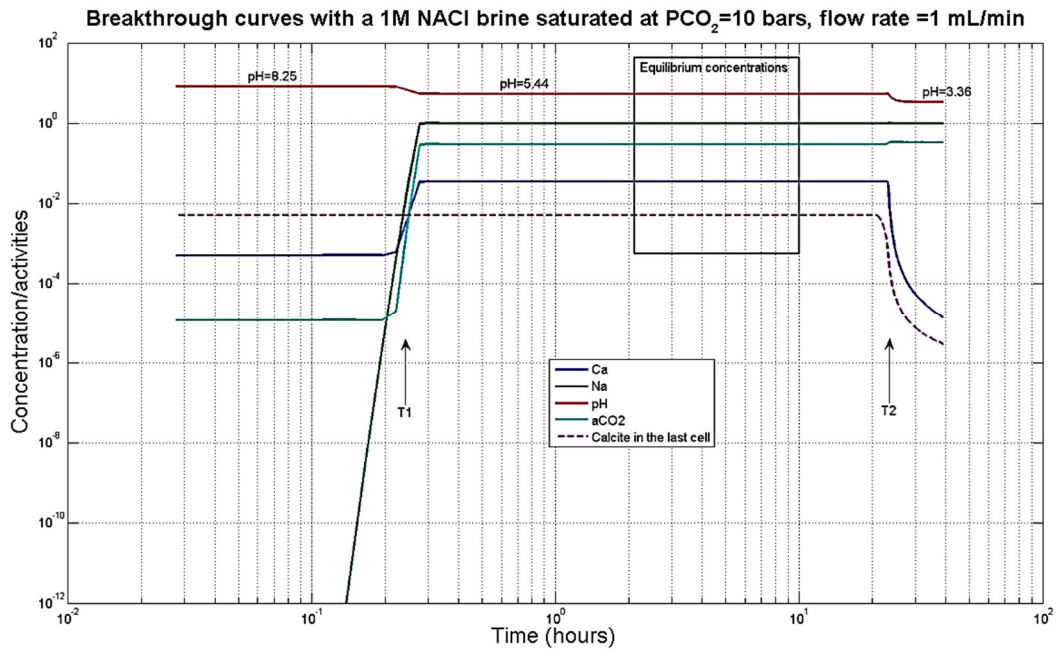


**Figure 3.7** Breakthrough curves resulting from a 1D reactive transport simulations performed with PHREEQC. The simulation consists of the injection of a 1 M NaCl brine saturated with CO<sub>2</sub> at 1 MPa into a rock core similar to the ones used in the Cayton Bay experiments (same size and petrophysical properties).

The initial composition of the pore fluid represents H<sub>2</sub>O-CO<sub>2</sub>-Calcite equilibrium with an atmospheric partial pressure of CO<sub>2</sub>. At time T<sub>1</sub>, one pore volume of acidified brine has been injected and starts exiting the core. At this point the fluid that reaches the outlet has equilibrated with calcite, having pH 5.4 and greatly enhanced calcium concentration. Between times T<sub>1</sub> and T<sub>2</sub> the outlet fluid composition remains constant and reflects equilibrium conditions. At time T<sub>2</sub>, all the calcite has dissolved from the core and so the pore fluid composition reverts towards the one of the injected fluid. Table 3.2 presents the number of pore volumes and time needed to theoretically dissolve all the calcite in a “standard” core in various conditions.

**Table 3.2** PHREEQC simulations results indicating the volume of fluid (in pore volumes) and time required to dissolve all the calcite present in a typical Cayton Bay sandstone core for a standard injection rate of 1 mL/min and variable salinity and CO<sub>2</sub> partial pressure conditions.

Flow rate Q (mL/min)	1	1	1	1
NaCl molality (mol/KgH <sub>2</sub> O)	0	1	0	1
Partial pressure of CO <sub>2</sub> (bar)	100	100	10	10
Pore volumes / Total time	46 pv 13 hours	35 pv 10 hours	125 pv 35 hours	84 pv 23 hours

At our experimental conditions the volume of fluid needed is expected to be 84 pore volumes (about 1.4 dm<sup>3</sup>) and the duration of the experiment 23 hours for a flow rate of 1 mL/min. It is interesting to remark that the presence of Na<sup>+</sup> and Cl<sup>-</sup> ions decreases the CO<sub>2</sub> solubility but on the other hand facilitates calcite dissolution (less pore volumes are needed). This is because the Na<sup>+</sup> forms NaHCO<sub>3</sub> and NaCO<sub>3</sub><sup>-</sup> complexes with carbonate ions and by doing so decreases the saturation index of calcite.

### 3.3 Experimental results

#### 3.3.1 Cayton Bay non-reactive baseline experiment

A first base-line experiment consisted of the injection of an inert fluid into a core of Cayton Bay sandstone. The goal of this experiment was to investigate whether injection of unreactive brine could influence permeability, for example through particle detachment. Porosity remained constant between the start and the end of the experiment but there was however a slight decrease of permeability possibly due to small fines present in the injected fluid or particles being detached inside the core. This is illustrated on Figure 3.8 which displays a slight and steady increase in the differential pressure in the first 25 hours.

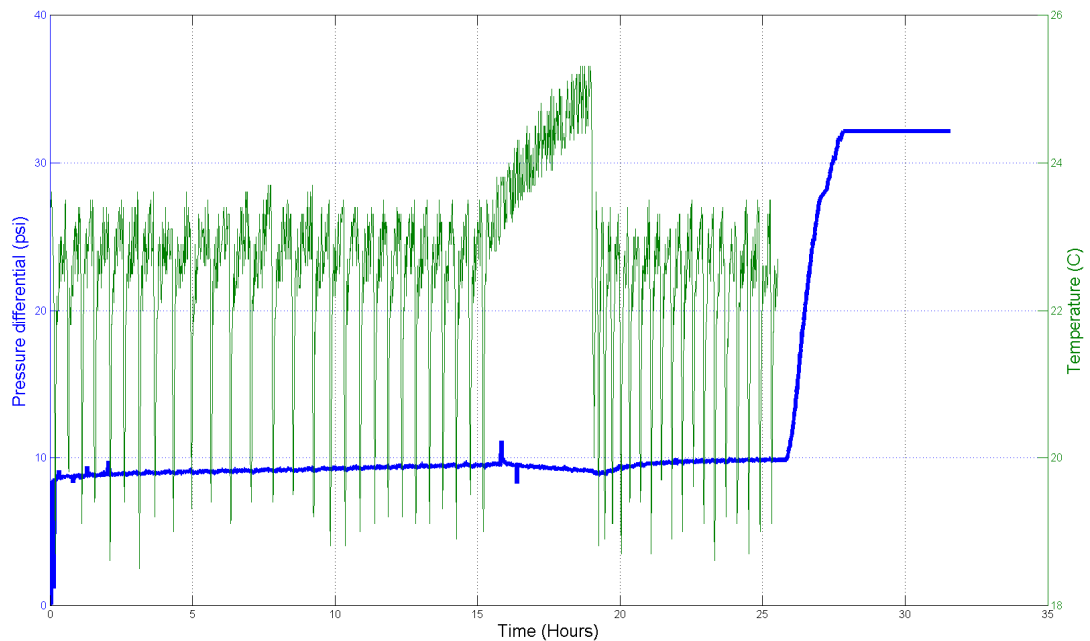


**Figure 3.8** Temperature and differential pressure traces from the Cayton Bay unreactive experiment.

The differential pressure is also responding to variations of the room temperature due to changes in brine viscosity (between 15 and 20 hours). The fluid composition recorded at the outlet of the core was comparable to that of the injected fluid and remained fairly constant (Figure 3.9).

Distilled water was injected after 25 hours in order to remove as much brine as possible before drying the core and measuring its porosity in a Helium expansion porosimeter. The permeability dropped by one order of magnitude during distilled water injection, likely because of clay swelling in response to changes in electrostatic forces. Later on the permeability reverted to initial

values once brine was injected through the core. Overall the main lesson from this experiment is that the injection of an unreactive fluid only has marginal impact on the permeability, and this provides a baseline for the CO<sub>2</sub>-saturated brine injection experiments.

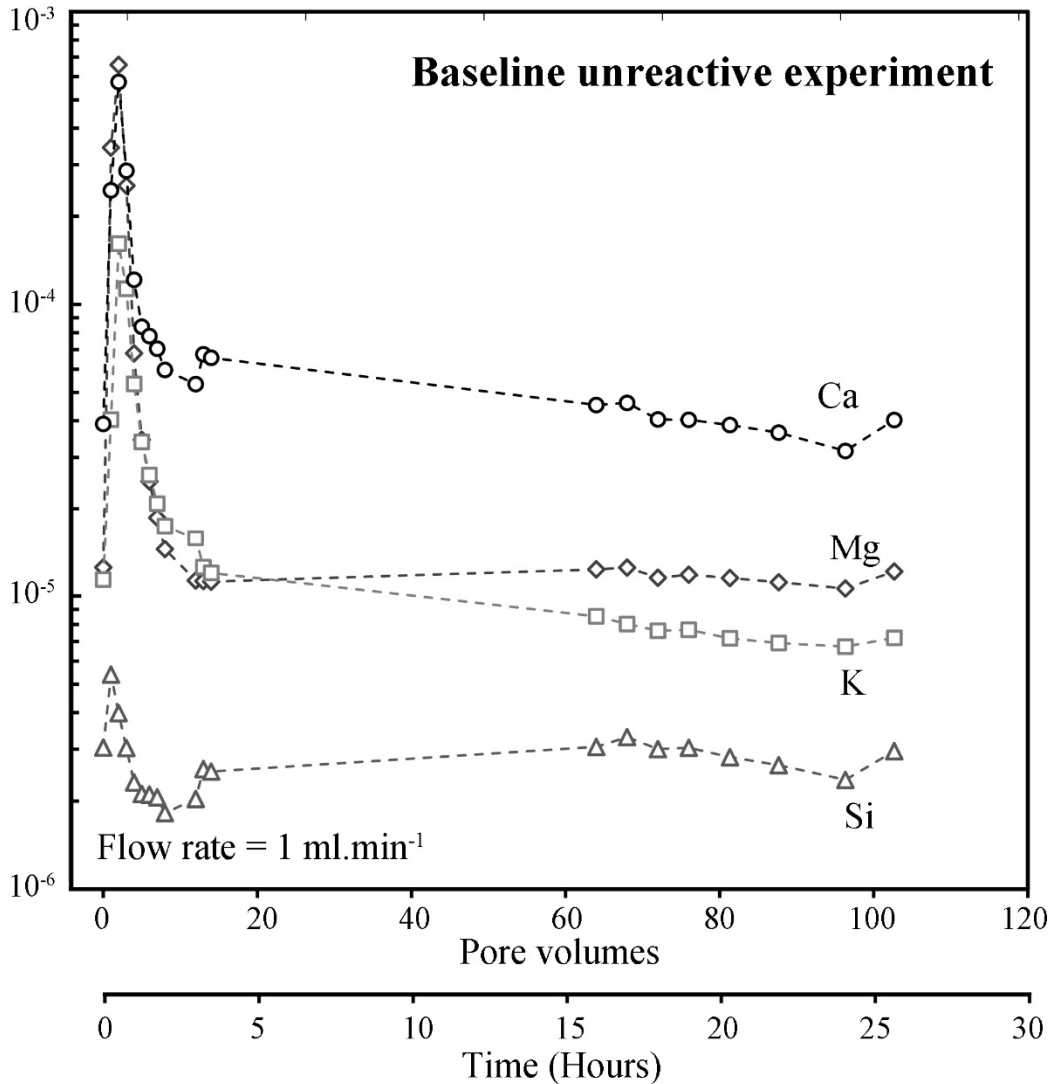


**Figure 3.9** Breakthrough curves from the Cayton Bay experiment displaying main cations concentrations. The cation concentrations are low and fairly constant over time apart from during the first hours of the injection. If the injected fluid was truly unreactive as suggested by the unchanged porosity then the initial peaks can be interpreted as the transport of fines produced during the rock core drilling. Even if the case this has only a minor influence on the results, especially for the reactive experiments where the cations concentrations are order of magnitude higher (see next section 3.3.2).

### 3.3.2 CO<sub>2</sub>-saturated brine injection experiments

In a further 6 experiments CO<sub>2</sub>-saturated brines were injected at constant flow rates (1, 2 or 3 mL/min) for 1 or 2 days. Table 3.3 presents the main characteristics and results of these experiments, details of the calculations can be found in Appendix B. The key results are the consistent increase in porosity and permeability in all experiments. Following are detailed observations and interpretations of these results.

**Table 3.3** Summary of experimental conditions and results, tabulated by experiment number

	1	2	3	4	5	6
Flow rate (mL/min)	2	1	1	2	3	2
Initial porosity (%)	35.5	33.1	30.4	34.0	32.5	32.2
Final porosity (%)	38.8	35.7	33.4	38.5	34.2	36.9
Relative porosity change (%)	9.3	7.9	9.9	13.2	5.2	14.6
Initial permeability (mD)	7.0	8.7	8.0	10.2	9.3	13.2
Final permeability (mD)	12.1	13.7	13.6	18.0	14.3	22.8
Relative change in permeability (%)	72.9	57.5	70.0	76.5	53.8	72.7
Interstitial velocity (cm/s)	0.008	0.004	0.005	0.008	0.014	0.009
Interstitial velocity (m/day)	7.0	3.8	4.1	7.2	11.7	7.5
Damköhler number	19	24	23	21	19	19
Péclet number	11	6	6	11	18	12
Reynolds number	0.002	0.001	0.001	0.002	0.004	0.002
[Ca] <sub>outlet</sub> (mol/L)	0.012	0.015	0.014	0.013	0.010	0.013

#### 3.3.2.1 Calcite dissolution at the core scale

A time series of CT profiles of the core (each comprising 24 slices perpendicular to the core axis) were used to track the dissolution front as it migrated during the course of each experiment (Figure 3.10).

Near the inlet, there was a rapid porosity increase at the start of the experiment; approximately half the porosity increase occurred in the first 5 hours. With time, the region of rapid dissolution propagated down the core, and extensive porosity increase at the outflow began only after 5 hours had elapsed.

This pattern of migration of the zone of dissolution is the signature that dissolution was transport-limited at the core scale even at the low CO<sub>2</sub> concentration and high flow velocities of these experiments (see Table 3.3).

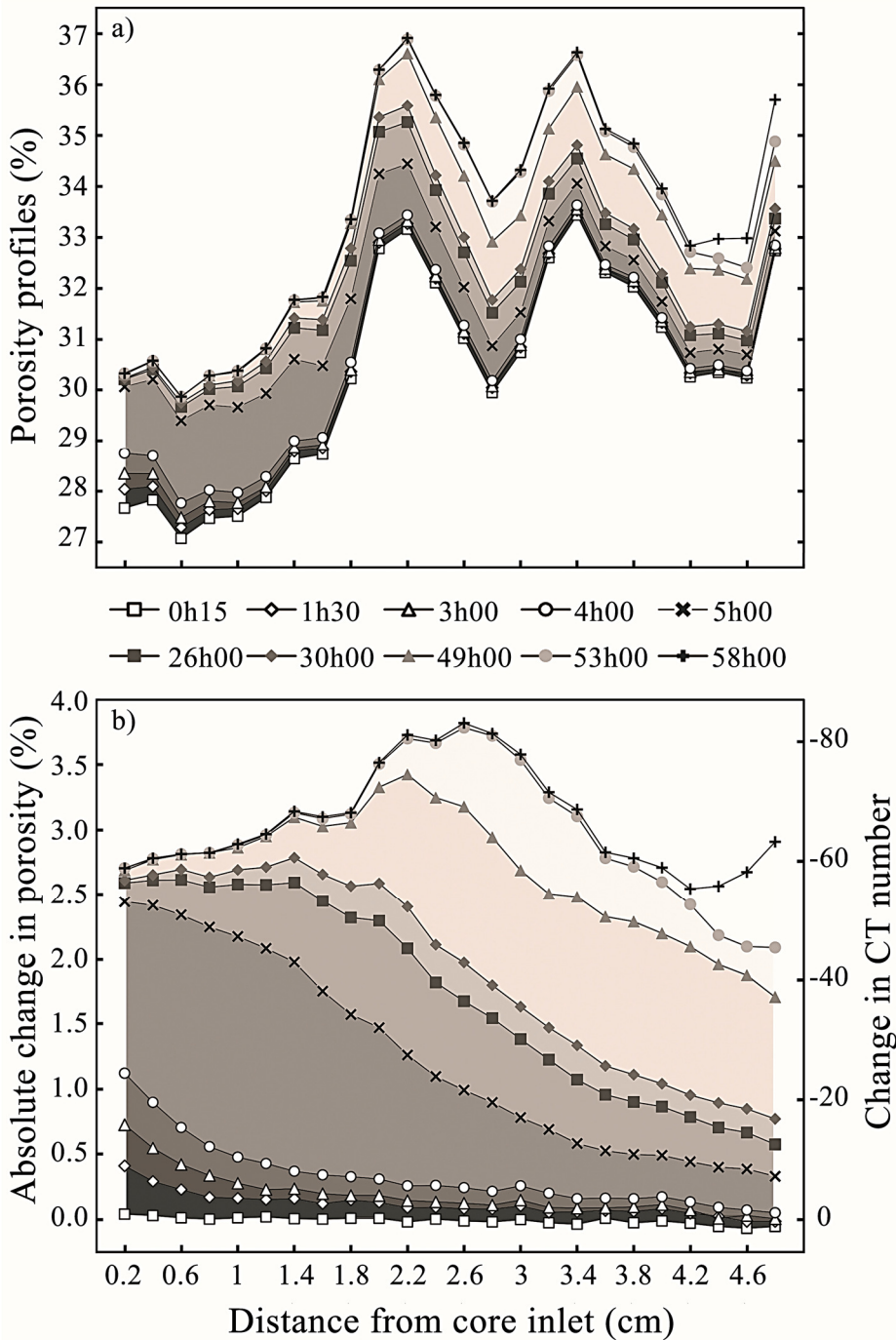


**Figure 3.10** Time series to demonstrate porosity evolution in experiment 3. Time-lapse porosity profiles are presented as surfaces of decreasing grey scale intensity in a). They have been normalized to the initial porosity profile in b). Equivalence with change in CT number (in Houndfield units (Houndfield, 1973)) is also shown. In b) the progressive shape of reaction front (as opposed to a sharp shape) seems to reflect the mixing of reacted and unreacted fluid at the pore scale as the fluid is flowing down the core (see section 3.3.2.2).

Analyses of the effluent fluids indicate that calcite dissolution dominated in each experiment (details of the chemical analyses can be found in Appendix C). Measured mass and volume changes were in good agreement with the ones calculated from fluid chemistry. For example, in experiment 3 (Figure 3.11), integration of the curves indicates leaching of 37.0, 1.0, 0.7 and 0.2 millimoles of Ca, Mg, K and Si respectively, corresponding to dissolution of 3.66 g calcite and 0.21 g dolomite with minor silicates. The equivalent volumes are 1.36 and 0.07 cm<sup>3</sup>, yielding a total of 1.43 cm<sup>3</sup> if there was no secondary precipitation. This is thought unlikely as calcium was steadily released throughout the experiments and pH dropped progressively. These changes calculated from effluent composition correspond well with the changes in core mass and pore volume measured by mass balance and Helium porosimetry of 4.24 g and 1.78 cm<sup>3</sup> respectively.

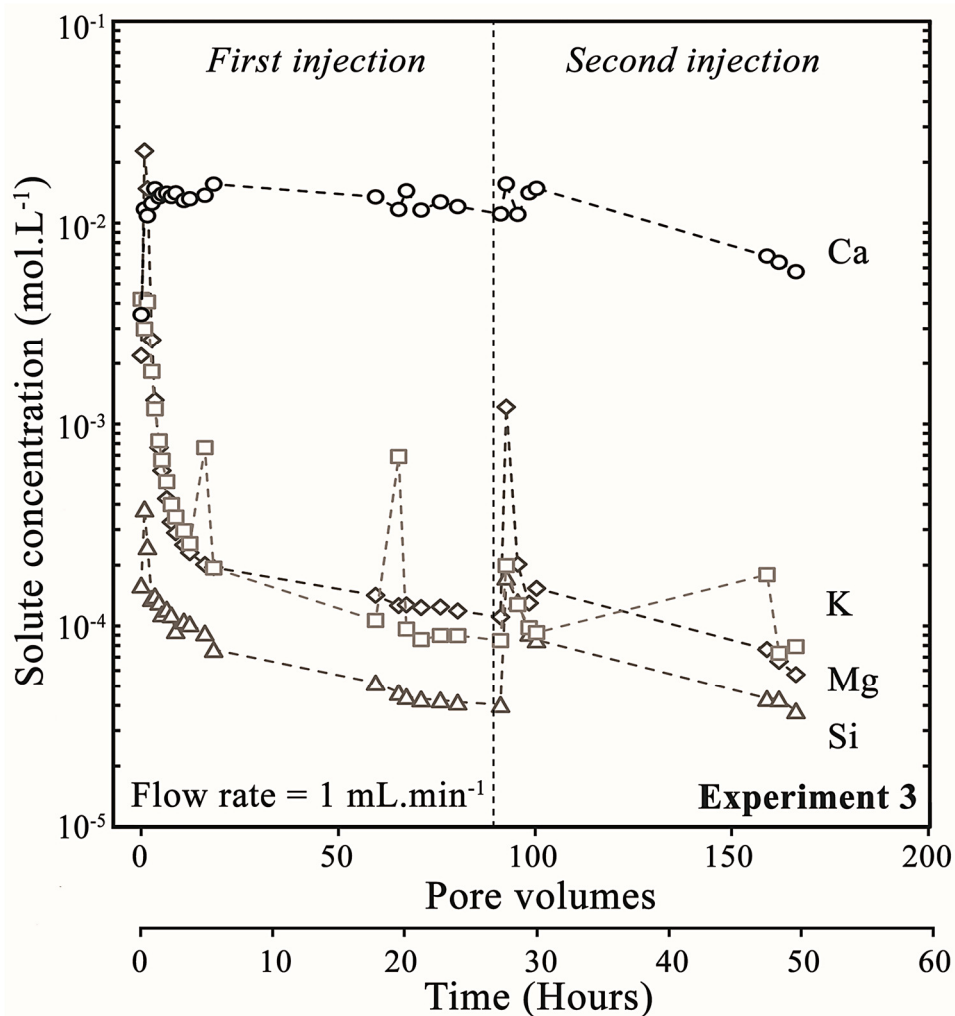


**Figure 3.11** Breakthrough curves from experiment 3. The separation line marks a 4 hour break between the first and the second injection of CO<sub>2</sub>-saturated brine. The concentrations of most elements drop due to dilution by newly-injected brine, but Ca concentrations remain quite stable due to sustained calcite dissolution.

QXRD analyses of sub-samples taken from the inlet and the centre of the core after experiment 3 showed total removal of calcite, indicating that calcite was fully accessible to the fluid. There were no other mineralogical changes detected. About 25% of the initial calcite remained at the far end of the core; hence outflow calcium concentrations remain significant, although falling, indicating that calcite dissolution was close to completion.

### **3.3.2.2 Calcite dissolution at the pore scale**

During the experiments the calcium concentration was about half that predicted by PHREEQC simulation so that twice as much fluid was injected than was required to dissolve all the calcite at 100% efficiency.

In PHREEQC simulations calcite dissolution was 100% efficient since it was at local equilibrium (transport limited), all the fluid was in contact with the calcite and all the calcite was accessible. The particular assumption that all the fluid come in contact with the calcite was not true in our experiments and the presence of calcite free flow paths at the pore scale can explain the observed decrease in calcite dissolution efficiency.

During all the experiments the pH gradually decreased while the permeability increased. The pH evolution is shown for experiment 3 in Figure 3.12. During the initial stages of the experiment the pH of the inlet fluid was 3.3 while the outlet pH was 7.5, reflecting extensive reaction of calcite and mixing with initial pore fluid (pH 9.0). The pH curve stabilized after 50 hours, close to the pH of the injected fluid. The gradual drop in pH is inferred to result from the development of the dissolution front and the presence of gradually longer calcite free flow paths through the core (as a result gradually increasing amount of unreacted brine mix with buffered brine).

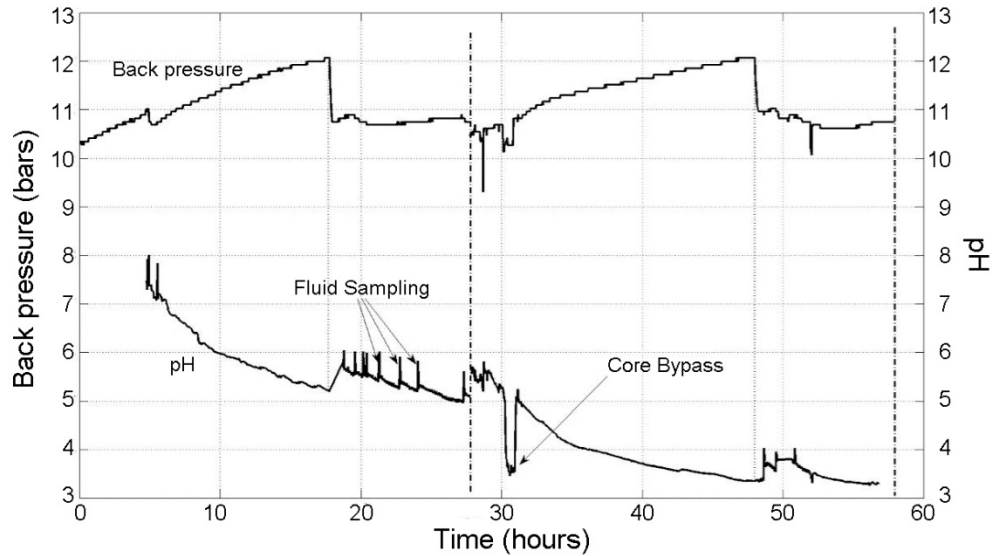


**Figure 3.12** Back pressure (same as pore pressure) and pH traces from experiment 3 showing the gradual decrease in pH and secondary effects such as the influence of fluid pressure on the pH measurement (pH tend to decrease) and minor artifacts due to fluid sampling (next to the pH electrode). Also shown is the pH of the injected fluid after 30 hours of injection (labelled as “core bypass”) as the rock core (or rock “plug”) was bypassed by the CO<sub>2</sub>-saturated brine for one hour shortly after the start of the second injection.

### 3.3.2.3 Transport-control of calcite dissolution

Some experiments were conducted at higher flow rates to evaluate the rate of transport controlling calcite dissolution (Table 3.3). The first evidence for transport controlled dissolution is that calcium concentration remained the same with a doubled flow rate. A flow rate of 2mL/min was used in experiments 1 and 6, the corresponding calcium breakthrough curves shown in Figure 3.13 are almost identical to the ones of experiment 3 (flow rate 1mL/min) shown in Figure 3.11.

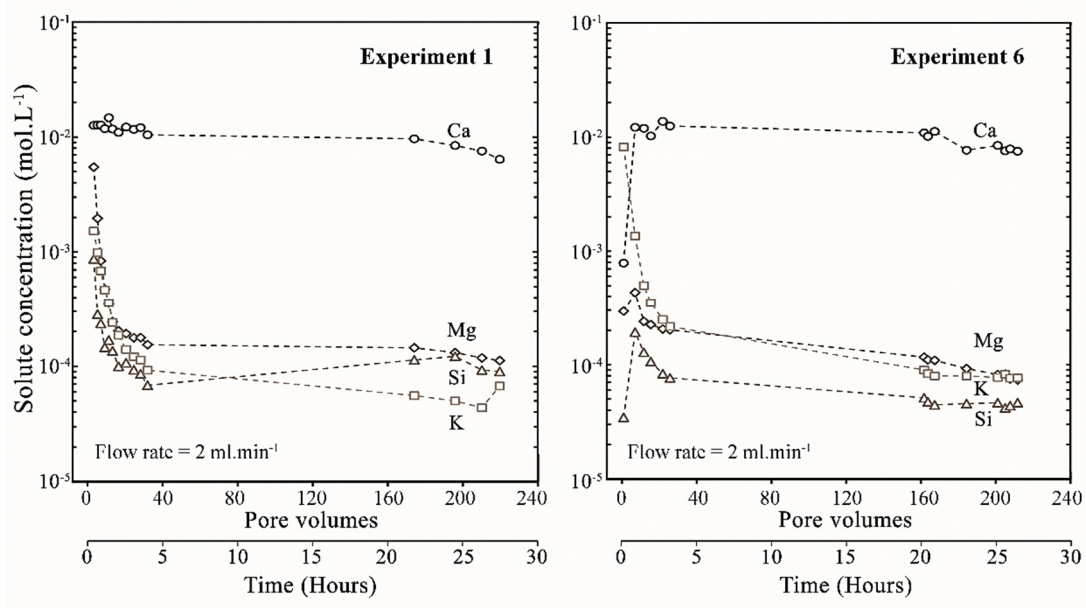


**Figure 3.13** Breakthrough curves from experiments 1 and 6 showing repeatable results and calcium concentrations similar with experiment 3 despite the fact that those experiments were carried at a doubled flow rate (i.e. calcite dissolution was in fact doubled). This indicate a transport control of the calcite dissolution.

Additional evidence is given by comparing pH and permeability curves for experiments 3, 4 and 5 where the flow rate used was 1, 2 and 3 mL/min respectively (Figure 3.14). The rock cores in these experiments had the same volume (Table 3.3) so that the amount of calcite in each of them was very similar. It appears that the time needed to stabilize both pH and permeability is directly proportional to the flow rate while the number of pore volumes injected remains broadly constant. These imply that the calcite dissolution was transport limited at least up to flow rates of 3 mL/min.

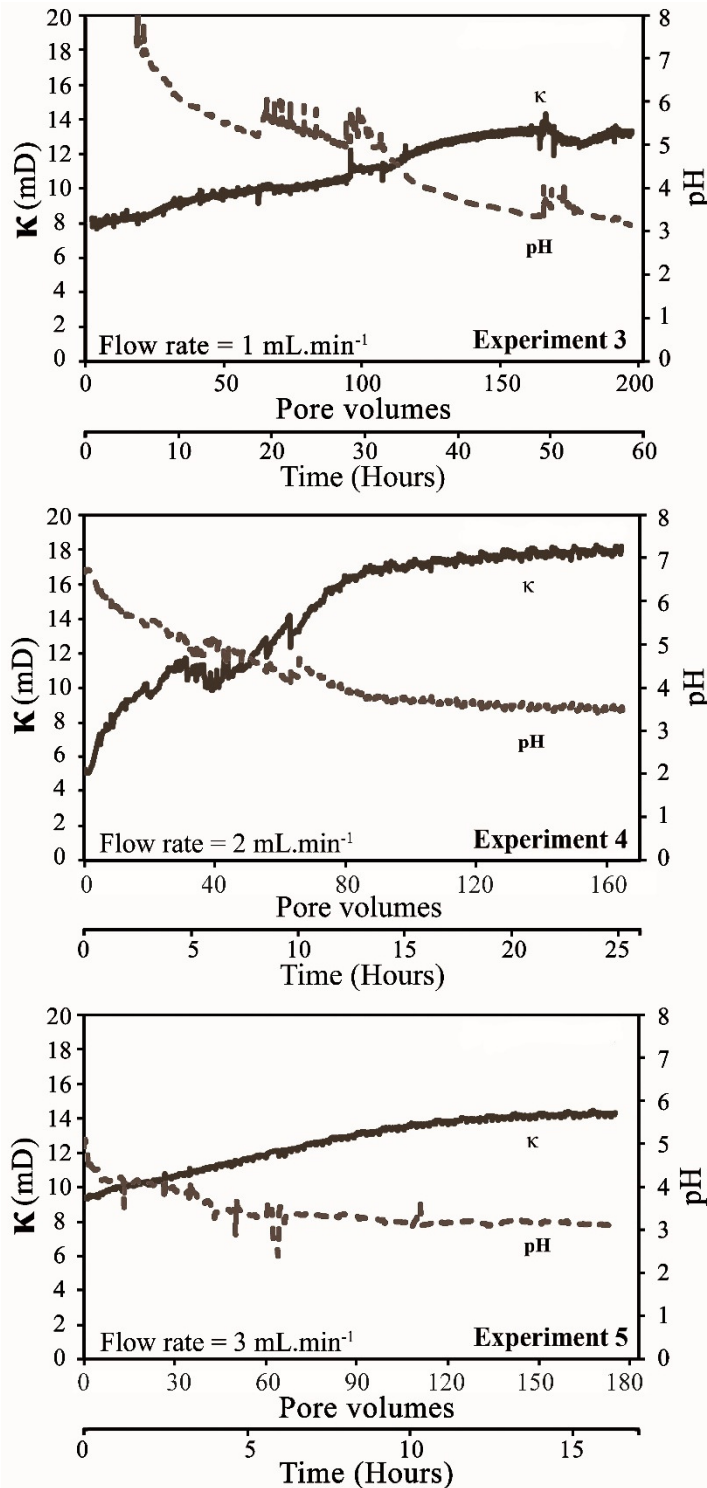


**Figure 3.14** Permeability and pH curves for experiments 3, 4 and 5. The time needed for the permeability and the pH to stabilize is strongly correlated to the flow rate, demonstrating that the rate of calcite dissolution is transport-limited. Note that the initial permeability for the core used in experiment 4 measured with pure brine was 10.2 mD, and this value was used for the calculation of permeability change in Figure 5. It differs from the value measured early in the run shown in this figure. This is the only inconsistency encountered in all six experiments, and is most likely due to the presence of gaseous CO<sub>2</sub> in the pipes at the start of the experiment.

Reactive transport is considered transport limited when  $Pe \times Da \gg 1$ . The advective Damköhler number calculated for calcite dissolution during flow and averaged over the core length ranged from 19 to 24, while the Péclet number was between 6 and 18, this means that averaged over the core length calcite dissolution can be considered transport limited even though not 100% efficient. Table 3.1 provides details of these numbers for all experiments, see Appendix B for details of the calculations. Table 3.1 shows that the experimental conditions were not designed to maximize calcite dissolution as high flow rates were achieved, such flow rates would only be anticipated close to the injection well.

In conclusion these results validate the use of the local equilibrium assumption for simulations of calcite dissolution at the reservoir scale and demonstrate that it is the physical introduction of acidity to calcite-bearing rocks that will dictate how much calcite dissolves, rather than surface reaction rates, as already shown for pure calcite by Pokrovsky et al. (2005). However they also emphasizes the need for experiments or transport simulations at the pore scale to properly evaluate the efficiency of dissolution.

### **3.3.3 Bramhope sandstone**

Two CO<sub>2</sub>-saturated brine injection experiments were carried out with Bramhope sandstone cores at 1 mL/min flow rates, the injected fluid chemistry was identical to the previous Cayton Bay experiments. Results of outlet fluid chemistry and porosity variation suggest marginal reactivity as initially intended. However large and contradicting variations in permeability were recorded. These results are unclear and difficult to interpret, they might be explained by fines migration and clay swelling/shrinking processes. These hypotheses would require further investigations.

### 3.4 Porosity-permeability relationship

#### 3.4.1 Model fitting of Cayton Bay sandstone results

The relative increase in porosity resulting from dissolution in the cores ranged from 5 to 15% (Table 3.1). However the resulting permeability change was between 50 and 75%. Figure 3.15 is a porosity-permeability plot showing the increase in porosity and permeability for each experiment. Porosity-permeability relationships are often described by the Kozeny-Carman (K-C) equation (Bear, 2013):

$$\kappa \propto \phi^n / (1 - \phi)^2 \quad (3.3)$$

where  $n$  ranges from 3 to 7,  $\kappa$  is permeability and  $\phi$  is porosity, or the modified Kozeny-Carman equation of Mavko et al. (2003):

$$\kappa \propto (\phi - \phi_{critical})^3 / (1 - \phi + \phi_{critical})^2 \quad (3.4)$$

which allows for the existence of a percolation threshold  $\phi_{critical}$ , the minimum porosity at which fluid can flow through a given porous assemblage (Sahimi, 1993). Figure 3.15 compares these fits with the experimental data. Given the high porosity of the sandstone,  $n = 3$  would be appropriate in Equation 3.3, but this leads to a large underestimation of the actual permeability increase with porosity increase. Using  $n = 5$  or  $n = 7$  narrows the gap between the model and the data, but there is no theoretical basis to justify this and the fit is still poor. The prediction is not improved if the percolation threshold is increased to 10% (Equation 3.4).

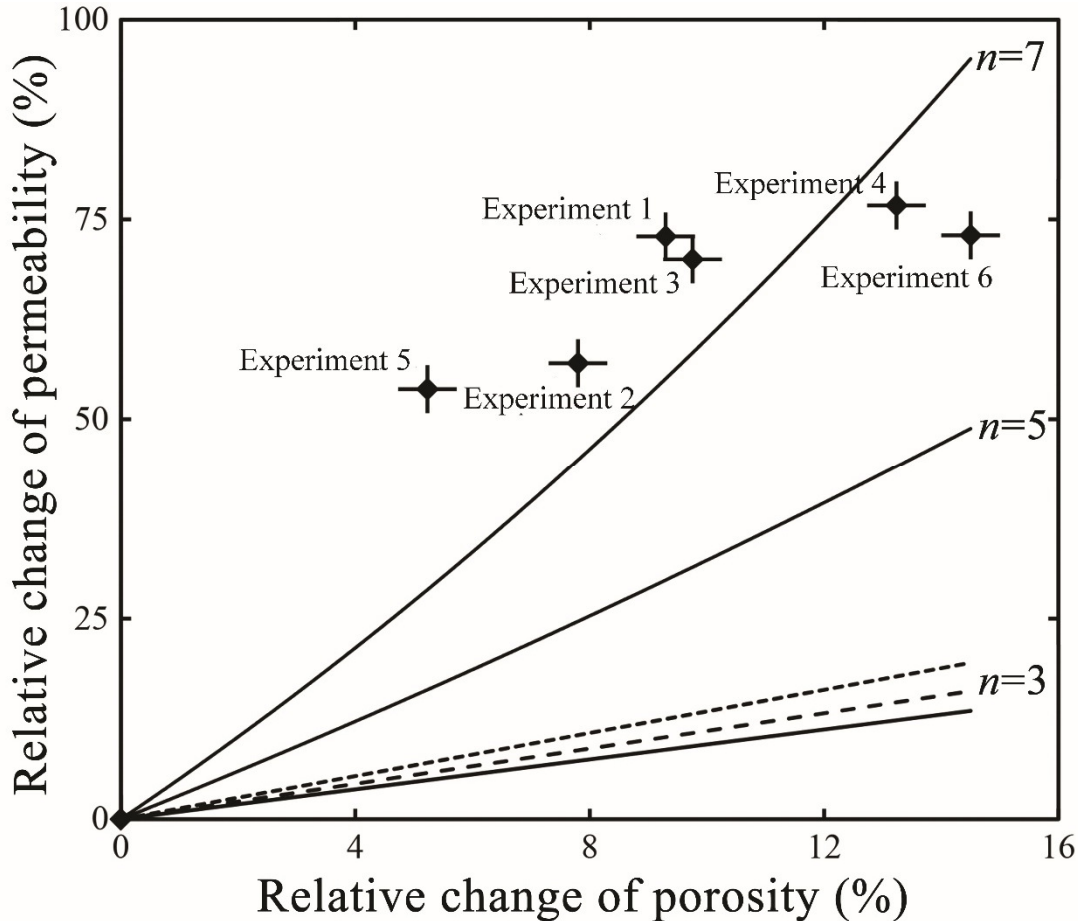


**Figure 3.15** Relative changes of porosity and permeability for 6 experiments (experiment numbers are displayed next to data points). Also shown is the calculated permeability change for each measured porosity change, based on different parameterizations ( $\phi_{critical}$  and  $n$ , see text) of the Kozeny-Carman equation. Solid lines:  $\phi_{critical} = 0\%$ , dashed line:  $\phi_{critical} = 5\%$ , dotted line:  $\phi_{critical} = 10\%$ . Each measurement was repeated at least 5 times and the error bars represent three standard deviations from the mean.

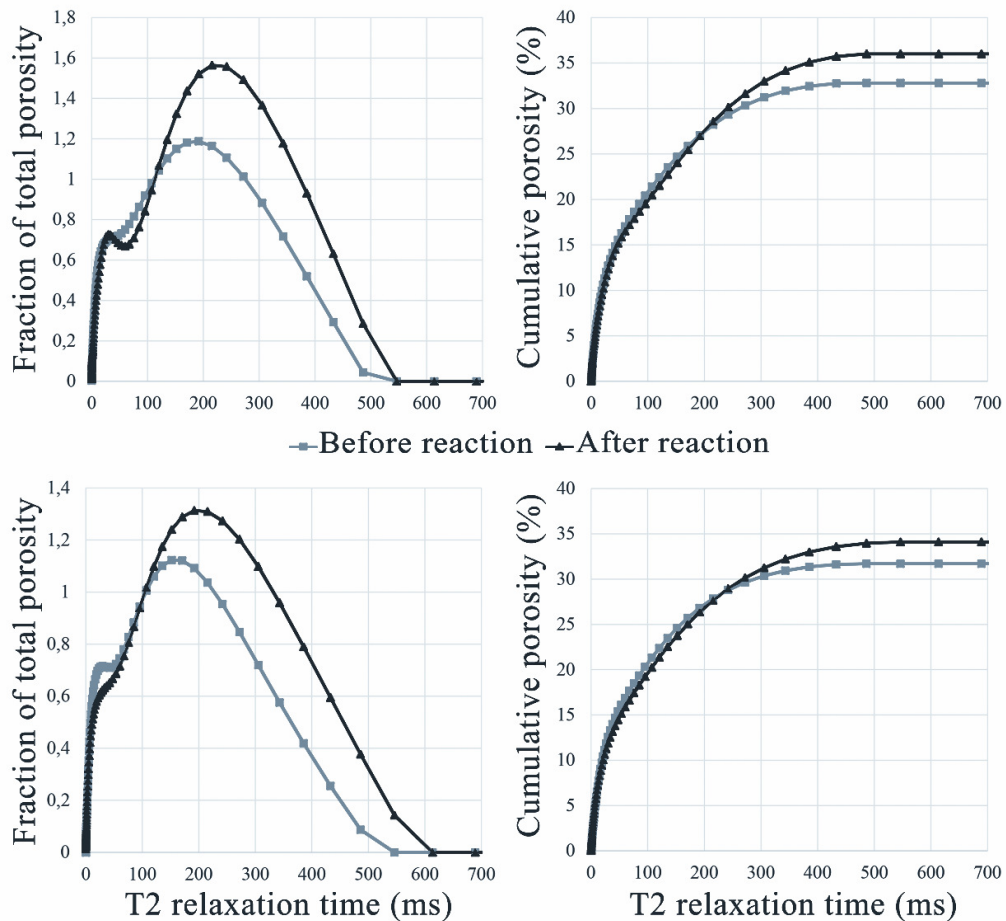
### 3.4.2 Hypotheses to explain model and experiments discrepancies

In summary, the observed large change in permeability for a small change in porosity is not predicted by the Kozeny-Carman approach. It may result from combination of increase in connectivity, focused dissolution at the pore throats and/or a reduction in tortuosity.

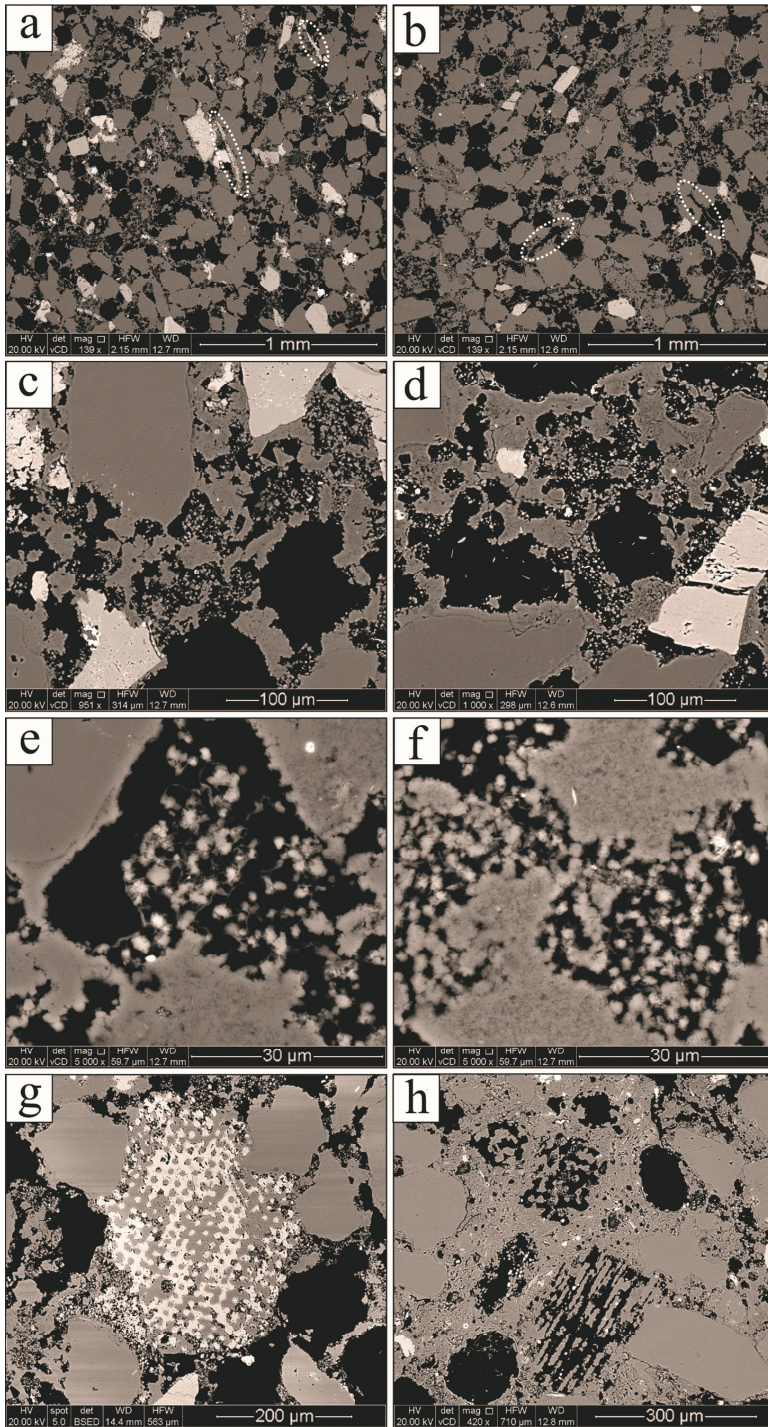
For connectivity, analysis of SEM images of unreacted sandstone and of micro-CT scans (Figures 3.17 and 3.18) suggest that the porosity is already totally connected through numerous small pore throats so that the dissolution of a few discrete calcite grains would have little effect on the connectivity of the existing pores.

Figure 3.17 contrasts observations made on thin sections of reacted and unreacted cores from the sample block. No calcite cement was observed at the pore throats (Figure 3.17 c, e) and NMR  $T_2$  curves indicate that it is mostly the creation of new large pores that contributed to the increase in porosity (see Figure 3.16). Some of the new pores are clearly calcite pseudomorphs of shell fragments (Figure 3.17 a, b). The main influence on permeability is the presence of small silicates fragments filling the pores, those were apparently not affected (Figure 3.17 e, f).

From these observations it is inferred that the marked increase in permeability aroused primarily from a decrease in tortuosity, as the dissolution of discrete grains opened new flow paths.



**Figure 3.16** Comparison of the pore size distribution and cumulative porosity curves before and after calcite dissolution for two side experiments, PSD1 (top) and PSD2 (bottom). They show that the increase in porosity results from the creation of large pores ( $T_2$  above 200 ms). An interesting secondary feature is the slight decrease in porosity for  $T_2$  below 100 ms. One possible interpretation is the disappearance of micro-pores present in calcite shells.



**Figure 3.17** SEM images of rock sample before experiment (left) and afterwards (right). a,b). Low magnification views showing the presence of elongated calcite shell fragments (a) matching pores created by the dissolution of such fragments (b). c,d). Detail of the pore throat structure showing silicate material coating grains and filling the pores. No significant difference can be detected after the experiments. e,f). Detail of pore fillings (quartz and clay particles) seen in c, d, confirming that they have been unaffected by the acid brine injection. g,h). Example of a partly silicified shell fragment (g) matched by a comparable pore shape in the reacted sample due to the dissolution of the calcite portion only (h).

### 3.4.3 Changes in tortuosity

To estimate the tortuosity change random walk simulations have been performed on 3D models of the pore space reconstructed from separate sets of micro-CT scans (Figure 3.18). Details about these models and the micro-CT methodology can be found in Chapter 4. Each cubic voxel is assigned a value of 1 or 0 depending on whether it is a solid or a pore part of the model. If the number of voxels is  $n^3$  then one can generate an  $n^3$  long vector composed of zeroes and ones by scanning successively the X, Y and Z coordinates. Initially random walkers are placed on this vector, then at every time step they can perform a jump to one of the 6 adjacent voxels, this means that they can jump by 1,  $n$  or  $n^2$  up or down on the vector depending on whether they jump in the X, Y or Z direction. If after a jump the walker is in a pore (voxel value=0) the jump is validated, otherwise the walker remain immobile for this time step. After a several times  $n^2$  time steps virtually all walkers had time to reach the external faces of the model. The cumulative flux of walkers exiting the model is recorded and fitted to an analytical solution of diffusion through a cube presented in Nakashima and Yamaguchi (2004). The random walk code can be found in Appendix C.

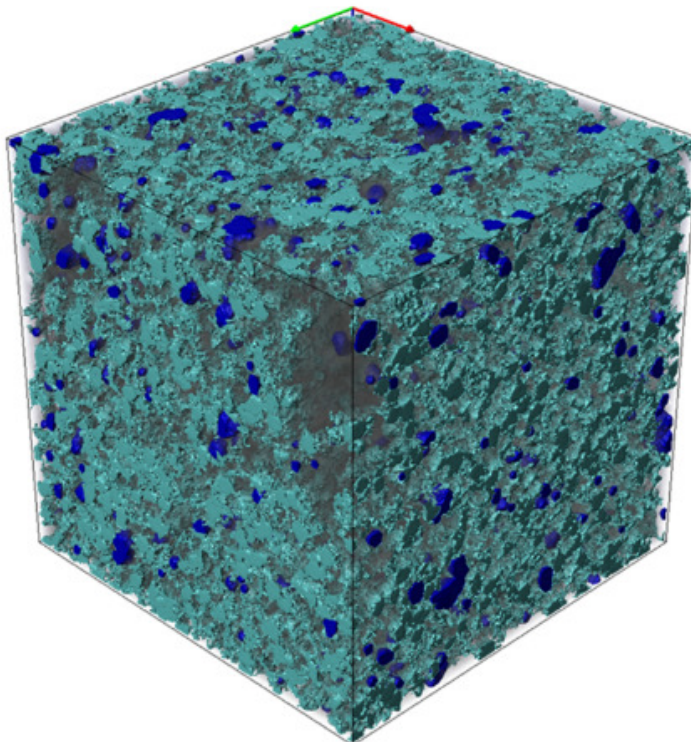


**Figure 3.18** 3D reconstruction from micro-CT scans representing a 9 mm<sup>3</sup> volume of Cayton Bay sandstone with pores in light blue, calcite in dark blue and other minerals in shades of grey. Three similar models have been used to run random walk simulations in order to determine the rock tortuosity before and after calcite dissolution.

Three simulations were conducted, one with 100% porosity, one with the initial rock porosity and a last one where calcite has been numerically removed and set as pores. The tortuosity is defined as the ratio of the bulk diffusion (when the porosity is 100%) to the effective diffusion in the rock geometry. Three sets of simulation have been performed with the three porosity conditions stated above in three different 9 mm<sup>3</sup> subsets of the rock, the result for one set of simulations is presented in Figure 3.19.

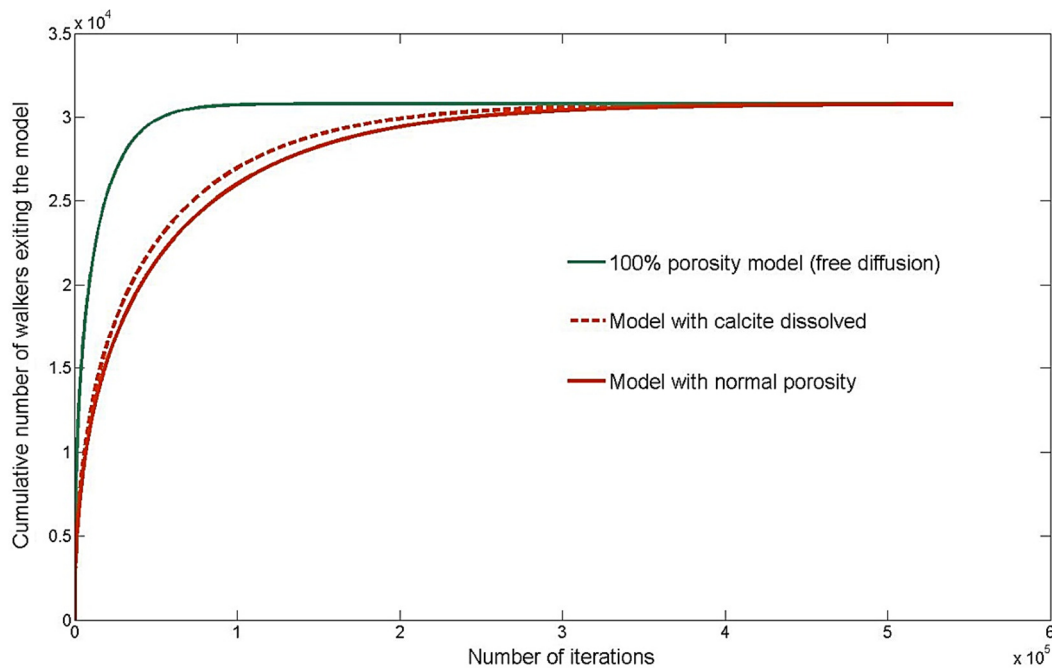


**Figure 3.19** Random walk simulation results presented as cumulative exit of about 30000 walkers randomly placed in the rock model. These curves can be fitted to analytical solutions in order to determine the model diffusivity. Tortuosity can then be calculated as the ratio of effective model diffusion to the free diffusion (Nakashima and Yamaguchi, 2004).

The simulations show a relatively modest tortuosity decrease from 2.00 to 1.85 due to calcite dissolution which cannot explain the change in permeability if permeability scales linearly with tortuosity. It is arguable that in these experiments, permeability is more sensitive to tortuosity change because this change results from the opening of new flow paths, not simply a change in sinuosity of existing ones. Therefore, the effect on permeability is fundamentally different from the capillary tube model used as the theoretical basis for K-C based models.

### 3.5 Conclusion

Brine acidification following CO<sub>2</sub> dissolution leads to fluid-rock interactions that alter porosity and permeability and therefore have the potential to affect reservoir sequestration capacity and injectivity. Thus, we determined how efficiently CO<sub>2</sub>-enriched brines could dissolve calcite in sandstone cores and how this affects petrophysical properties. During computerized tomography (CT) monitored flow-through reactor experiments, calcite dissolved at a rate largely determined by the rate of acid supply, even at high flow velocities which would be typical near an injection well.

In practice this means that the key parameters for calcite dissolution are the amount of mixing between CO<sub>2</sub> and brine, the local permeability distribution that delivers acidified brine through the rock and the local mineral accessibility. The experiments represent an end member of the conditions likely to be encountered in a steadily filling reservoir because the CO<sub>2</sub> and the brine were mixed prior to injection and the pore volume was refilled with unreacted fluid about two hundred times over the course of each experiment. Nevertheless, this reflects the conditions likely to be encountered in the case of WAG injection or CO<sub>2</sub> and brine co-injection scenarios. Such conditions would allow a modification of the permeability throughout the reservoir similar to the one occurring at the core scale during the experiments.

Dissolution of even small amounts of calcite can have a much larger effect on permeability than conventional models predict. The advance of acidified brine ahead of a CO<sub>2</sub> plume infiltrating permeable layers may cause significant changes to reservoir permeability, provided that unreacted brines are continually incorporated into the zone of acidification as it moves out from the injection well (as would be expected for radial rather than linear flow). Permeability may also be modified if confining beds above or below a CO<sub>2</sub> plume contain calcite. There are two key questions for evaluating changes in reservoir performance due to interactions of CO<sub>2</sub> enriched fluid with calcite-bearing rocks. Firstly, how effectively will CO<sub>2</sub> interact with brine causing acidification and reaction? Secondly, how effectively will reacted brine pushed ahead of the CO<sub>2</sub> front mix with unreacted brine, creating the potential for further calcite dissolution?

These results also show that it is advisable to evaluate changes in absolute permeability due to fluid rock interactions since these can lead to variations in effective permeability of similar magnitude to the ones due to phase

saturation change. Depending on the specific geological setting, enhanced permeability through calcite dissolution could be a threat to the integrity of injection schemes, or could be managed to make them more effective.

## **Chapter 4**

### **Pore scale simulation of fluid flow in original and modified rock models.**

The study presented in this chapter explores the effects of a porosity increase on the permeability of the Cayton Bay sandstone (presented in Chapter 3) using pore scale simulations of fluid flow.

#### **4.1 Introduction**

Macro-scale transport properties such as Darcy permeability are bulk parameters combining the contributions of various properties only properly defined at the pore scale (micro-scale). Since micro-scale processes are known to modify the rock properties it is legitimate to ask if constitutive equations based on macro scale properties (e.g. porosity, permeability, formation factor...) can properly describe their effect. Until recently the effect of pore scale modifications could only be studied by means of experiments or predicted with simple semi-empirical equations, for example the Kozeny-Carman (K-C) equation presented in Chapter 3. For these reasons there has been a move towards the evaluation of transport properties by direct fluid flow simulation at the pore scale over the past 20 years.

Developments of pore scale simulation methods have accompanied recent progress in X-ray CT imaging of material structures (Wildenschild and Sheppard, 2013). It is now possible to obtain 3D models (or images) of any material containing components of different densities to a micron (also referred as micro-CT) or even sub-micron resolution on a time scale of a few hours to days. CT scanning is non-destructive and produces very accurate and reproducible representations of the pore space. In parallel, the rise in computing capabilities has enabled more complex simulations (e.g. two phase flow and turbulent flow) in larger models while preserving high resolutions. The trade-off between resolution and model size is still an issue and in most cases it is unsure if the models are large enough to be representative. Most contemporary studies deal with model sizes not larger than a few millimeters.

First studies focused on small models only a few pores wide obtained at resolutions of tens of microns. Single phase flow was simulated by direct solving of the Stokes equation (Adler, 1992). In the last decade the Lattice-

Boltzmann (LB) method (Ferréol and Rothman, 1995; Zu and He, 2013) supplanted other pore flow modelling methods. This is firstly because LB codes are easy to implement and are not computationally intensive.

Secondly they are very versatile and easy to modify by adding modules to simulate additional processes. Thirdly they have been shown to be accurate for incompressible low Reynolds number (ratio of inertia to viscous forces) flows as they can recover Stokes equation in these conditions (Chen and Doolen, 1998; Nourgaliev et al., 2003; Raabe, 2004).

These studies were meant to serve as a proof that pore scale flow modelling in reconstructed real porous media was possible but already several authors claimed to have successfully recovered Darcy's permeability from CT images (Ferréol and Rothman, 1995; Chen and Doolen, 1998; Coles et al., 1998). As for two-phase flow simulations they were at least qualitatively successful as the predicted general features were observed (Ferréol and Rothman, 1995; Chen and Doolen, 1998; Hazi et al., 2002). Kang et al (2002) added a calcite dissolution module to their LB code and obtained a qualitative agreement with a wormholing dissolution experiment.

Some workers have tried to avoid brute force computations by using network models. Network models are made of simple geometric volumes such as tubes and are extracted from the CT images (Blunt and King, 1991; Sholokhova 2009). Pore network simulations are potentially orders of magnitude faster than simulations using the real rock geometry. This method can be as effective as more complex simulations in modelling macroscopic flow behavior because much larger models can be used (Vogel et al, 2005).

Instead of directly using 3D CT images for the construction of 3D models, Zhang et al (2005) used 2D SEM images to reconstruct 3D models based on the 2D image porosity variogram. The advantage is that the 2D images have a resolution orders of magnitude higher than the best CT scans, the disadvantage is that a single 2D image might not be representative or might not provide the most relevant statistics for the 3D flow as it is based on porosity alone.

The study presented here used high resolution 3D micro-CT images as a source for a 3D porosity model and used finite element code FLUENT to directly solve the Stokes equation. The porosity models were shared with project partners at Sheffield and Aberdeen universities where flow was simulated using Finite Volume (FV) and LB methods respectively.

## **4.2 Generation of a porosity model**

Micro-CT scanning followed by image processing has become a very popular method to obtain pore space morphology, see the review from Wildenschild and Sheppard (2013). The detailed steps to generate the finite element porosity models are explained in this section.

### **4.2.1 Micro-CT scans and mesh extraction**

A cylindrical sample from the same block of Cayton Bay sandstone sampled for experimental studies (Chapter 3) was scanned using a Scanco 100  $\mu\text{m}$  micro-CT scanner housed in the Department of Mechanical Engineering, University of Leeds. X-rays were generated with a fixed X-Ray source operated at 50 kV and 160  $\mu\text{A}$ , with a 0.1 mm copper filter to reduce noise and beam hardening and to increase image contrast. The volume of interest was a 5 mm long portion of the cylinder. This volume was reconstructed by stacking 2000 cross-sections of 5000x5000 pixels each so that the final volumetric pixel (voxel) shape was a 2.5  $\mu\text{m}$  large cube. A micro-CT scan example is shown in Figure 4.1.

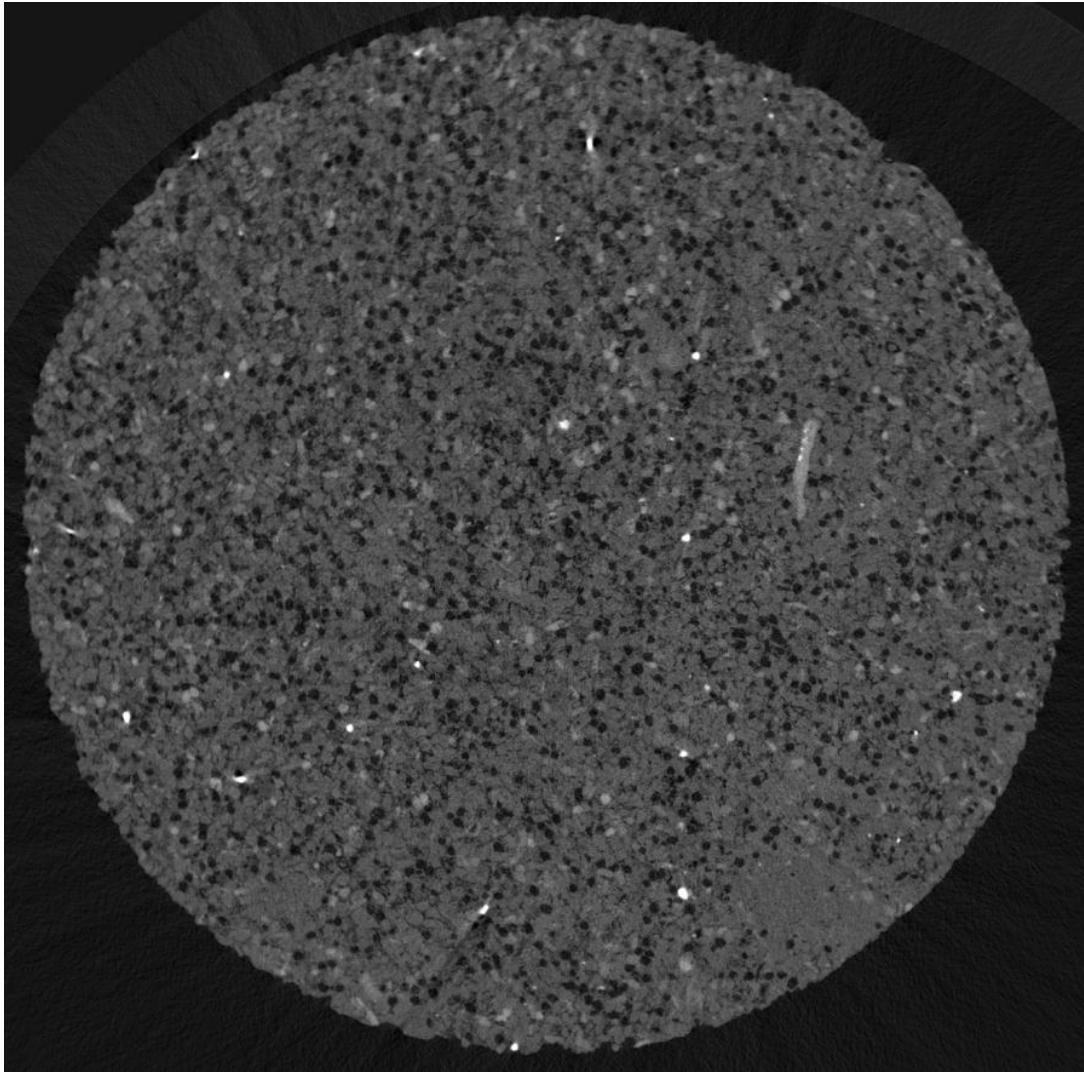


**Figure 4.1** CT scan cross section of a Cayton Bay cylindrical sample (diameter = 1.2 cm), black zones correspond to pores, grey zones correspond to minerals of variable density/atomic number. For instance very bright dots correspond to dense pyrite grains while very light grey zones correspond to calcite (visible on the largest feature of the image which is a calcite shell). Most of the image is composed of darker grey quartz.

Each voxel has a grey scale intensity that represents the mean X-Ray attenuation coefficient of the corresponding cubic volume in the sample; itself a function of the density and the atomic number of the material. The final result is a 3D image composed of 50 billion voxels. A  $8 \times 8 \times 3.5 \text{ mm}^3$  sub-volume of the image was extracted so that only the core of the rock sample was represented (Figure 4.2), this correspond to about 15 billion voxels.

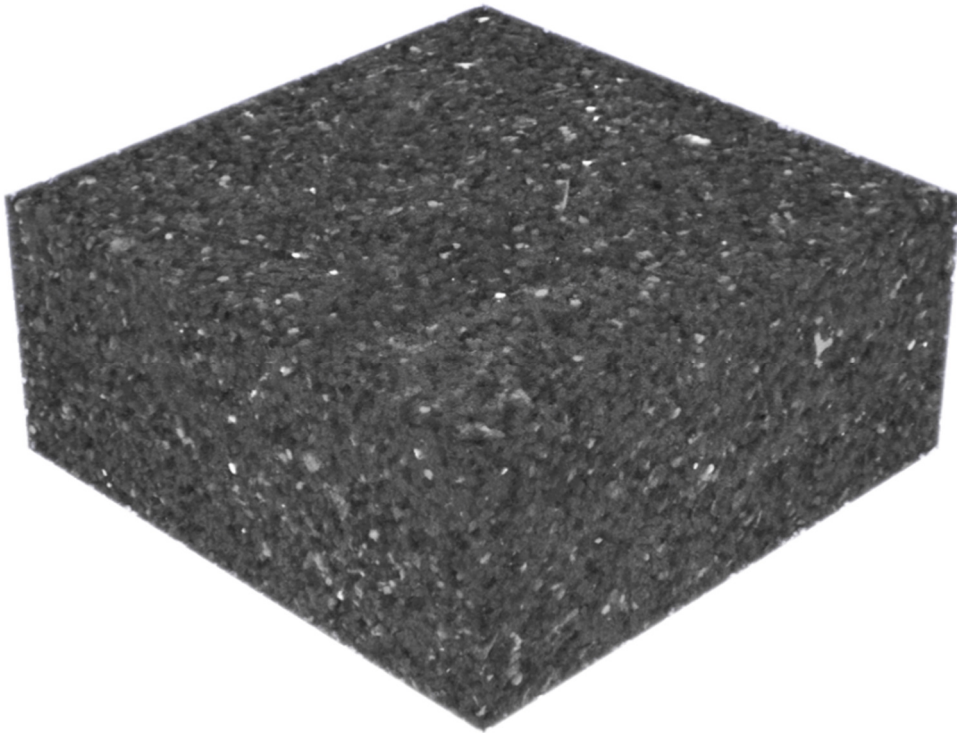


**Figure 4.2** 3D volume reconstruction composed of 1400 horizontal CT scans, the dimensions are  $8 \times 8 \times 3.5 \text{ mm}^3$ .

Direct segmentation was then applied to the image using a trial version of the purpose-built ScanIP software obtained online at "<http://www.simpleware.com/>". A first segmentation was done to isolate the pores by selecting the darkest voxels. For this selection the lower bound of the voxel intensity was zero and the upper bound was fixed so that the final porosity would correspond to the experimental porosity (porosity about 31%). A flooding (or burning) algorithm was also used with the same intensity bounds and resulted in a porosity of 30.9%; this implies that only 0.3% of the porosity was unconnected. A second segmentation was done following the same procedure to select the 4% brightest voxels after screening out pyrite; this corresponded to the experimental value of calcite content. Figure 4.3 presents the result of the segmentation process on a small portion of the model.

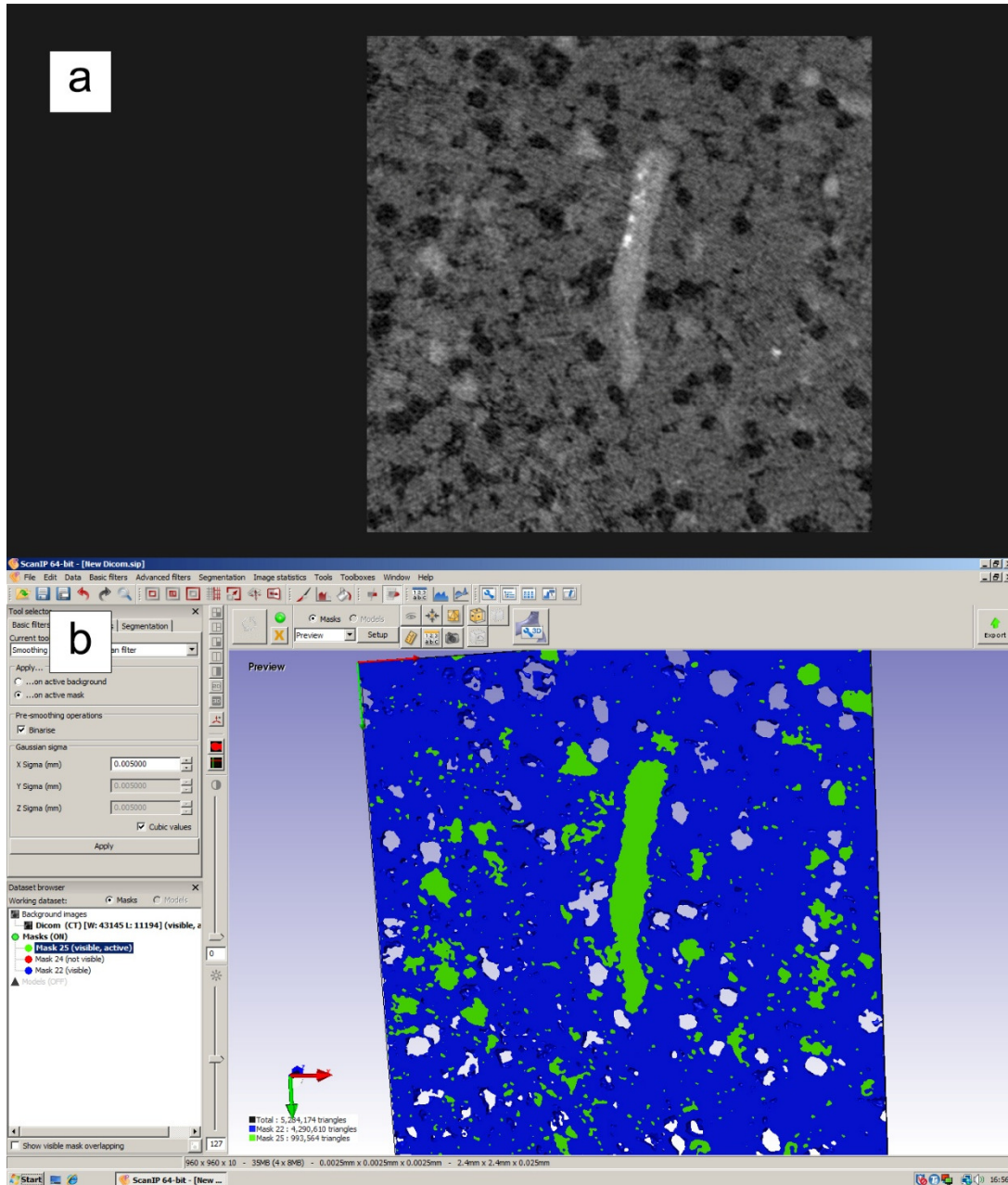


**Figure 4.3** Illustration of the segmentation process, a) is the micro-CT image from which the segmented image, b), has been derived. In the segmented image the pores are transparent, the calcite is green and other minerals are blue. Upon visual inspection it appears that the calcite is not connected to the pores. The pore size seems smaller in the segmented image. These two observations are discussed in the text.

The possibility of extracting mineralogical information from CT images is quite recent and is due to the improvement of scanning tools; in our study it was facilitated by the fact that the only mineral of interest was calcite which is significantly brighter than all the other minerals in the CT images (excluding pyrite which has a much smaller abundance). A final visual

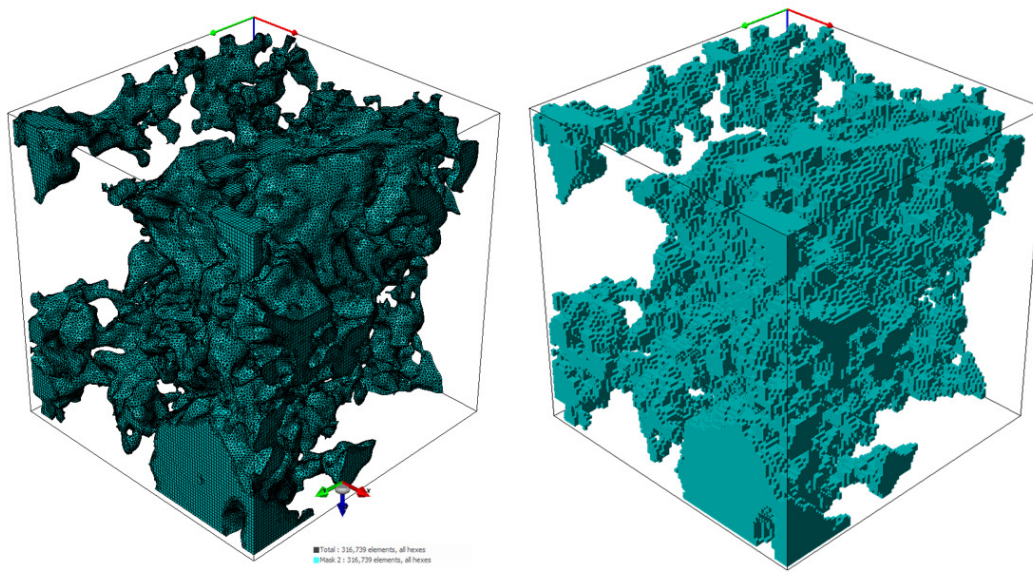
inspection was conducted to verify that the three different phases (pores, calcite and “other solids”) were correctly segmented.

Several sub-volumes were extracted from the initial volume to serve as rock models for fluid flow simulations and below are reported the results obtained for three of them: A1, B1 and B2. The basic properties of these models are shown in Table 4.1.

**Table 4.1** Porosity models properties

Model name	Size (mm <sup>3</sup> )	Resolution(μm)	Number of voxels	Connected porosity	Calcite content
A1	3x3x3	12	250 <sup>3</sup>	30.5	4.2
B1	1x1x1	2.5	400 <sup>3</sup>	30.9	4.7
B2	1x1x1	2.5	400 <sup>3</sup>	27.3	3.7
C1	2x2x2	5	400 <sup>3</sup>	30.2	4.0

The segmented volumes were converted into finite element meshes using the finite element module of the ScanIP software: ScanFE; this generated regular meshes in which all elements were forced to be cubes of the same size. The use of mesh adaptation techniques or of tetrahedral elements was avoided to facilitate the conversion of the models for FV and LB methods. As a test, an irregular mesh was obtained for a very small portion of the rock and simulations results were compared to those from a regular high resolution mesh (Figure 4.4). The irregular mesh used a much larger number of tetrahedral elements which provided a more accurate and smoother representation of the pores but also dramatically increased computing time. The difference in absolute permeability is quite significant in this example and it seems logical that the permeability would increase in the irregular mesh due to the pore walls being smoother. This example provides a word of caution and shows that there is space for improvement especially for absolute permeability predictions. The time and computing resources needed to solve for flow in the smoothed model are an order of magnitude larger than in the regular model. For this reason and because the focus of this study is changes in permeability (not absolute permeability) the regular meshes were taken as an adequate approximation.



Permeability 30% higher

**Figure 4.4** Comparison of a small sub-volume permeability (size  $0.75 \times 0.75 \times 0.75 \text{ mm}^3$ ). The model on the left uses a combination of hexahedral and tetrahedral elements (one hundred thousand and one million respectively). The model on the right only uses hexahedral elements (about three hundred thousand). The more complex model on the left has smoother interfaces and the permeability is higher. It is not known if this effect would persist in larger models.

#### 4.2.2 Mesh modification

For the models B1 and B2 a nearest neighbour resampling was used to reduce the number of voxels from  $400^3$  to  $350^3$ ,  $300^3$ ,  $250^3$  and  $200^3$  (see Figure 4.5). A comparative study was made to determine if the simulated permeabilities depended on the resolution. The ten resulting models were then modified to increase the porosity, either by numerically dissolving the calcite and reassigning it as pores or by dilating the existing pores.

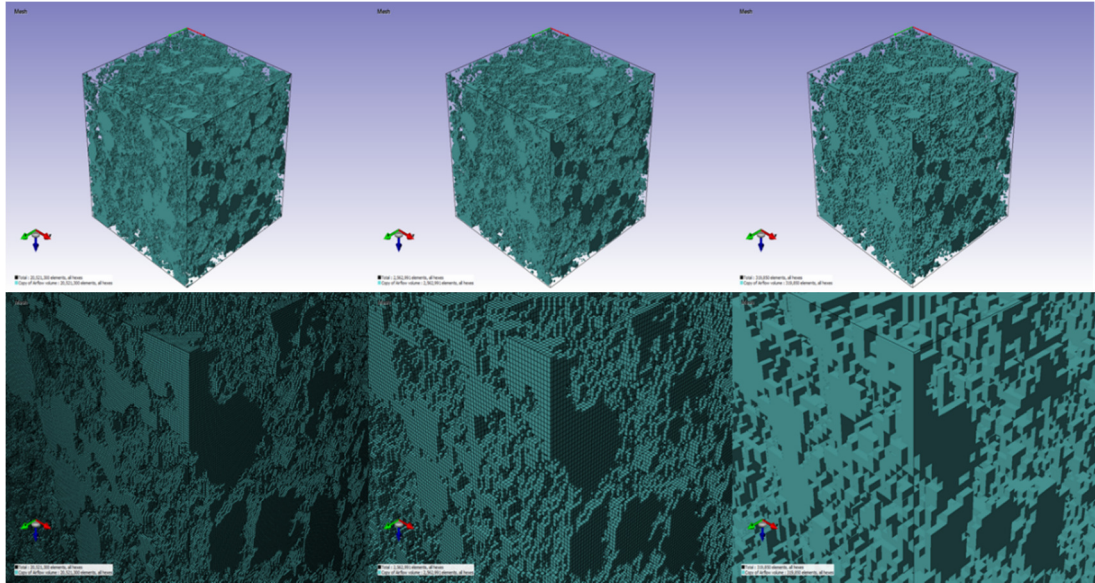


**Figure 4.5** Comparison of three models containing  $400^3$ ,  $300^3$  and  $200^3$  elements with a close up on the upper central corner. Coarser models originate from a nearest neighbor resampling of the  $400^3$  model.

The main issue that arose with the numerical calcite dissolution procedure is that the representation of the calcite-pore interface in the CT scans is not perfectly sharp. The interface frequently contains voxels of intermediate grey scale value, interpreted as “other solids” (Figure 4.3). This can make solid films that isolate calcite from pores so that when calcite is removed the increase in connected porosity is underestimated. To solve this problem erosion and dilatation operations were performed to remove smaller calcite elements and enlarge larger ones so that they were in direct contact with the pore elements. The choice of the structuring elements was done by trial and error to ensure that the calcite content was unchanged after these manipulations.

The structuring element size used for pore dilatation was also found by trial and error so that the variation in porosity in pairs of “dilatation” and “dissolution” cases was as close as possible. The rationale is to understand the different effects on permeability when two different processes modify the porosity and to make a direct comparison between the pore-scale modelling method, the Kozeny-Carman (K-C) relationship and the experimental results (from Chapter 3) for the relationship between porosity and permeability. The K-C approach assumes that pores can be represented as capillaries of a given radius and tortuosity; therefore it should be successful at predicting the model permeability increase for the dilatation case. In Chapter 3 the K-C approach did not predict the permeability change in the experimental “dissolution” case. Hence the objective is twofold: testing the predictive

capabilities of pore-scale simulations for permeability change due to dissolution and understanding why the K-C approach is ineffective.

#### **4.2.3 Estimation of the representative elementary volume**

It is first necessary to evaluate if the model sizes provide Representative Elementary Volumes (REV). For a given medium, the REV is the minimum volume at which parameters (porosity, permeability, calcite content...) become independent of the volume (Bear, 1990). Constitutive equations found by averaging porous media properties in a REV are by definition valid in a larger volume. The largest model size used at the highest micro-CT resolution (2.5  $\mu\text{m}$ ) was  $1\text{mm}^3$  and since the Cayton Bay sandstone is homogeneous with small pores and grains (about 100  $\mu\text{m}$  diameter) it was initially assumed that a  $1\text{mm}^3$  volume, containing about 125 pores, was likely to be representative. The REV for porosity was estimated by sequentially dividing the initial  $8\times 8\times 3.5\text{mm}^3$  volume imaged by CT in two or four and measuring the porosity of the resulting sub-volumes; one such sub-volume branch is shown in Figure 4.6 and the results for porosity convergence are shown in Figure 4.7. This approach is based solely on porosity and does not necessarily define the REV for permeability. Al-Raoush (2010) estimated the REVs for porosity and permeability of a range of computer-generated porous media, and concluded that in some case the permeability REV might be smaller than the porosity one. Therefore the porosity REV has been taken as a guideline but not a definite evaluation of the permeability REV. It is apparent on Figure 4.7 that the  $1\text{mm}^3$  size is not perfectly representative of the porosity of the  $8\times 8\times 3.5\text{mm}^3$  initial volume; however the porosity dispersion is comparable to the one found experimentally comparing rock cores (see Table 3.3). For this reason two  $1\text{mm}^3$  high resolution sub-volumes with different porosities (B1 and B2) were used in the following study, together with a  $27\text{mm}^3$  low resolution volume (A1).

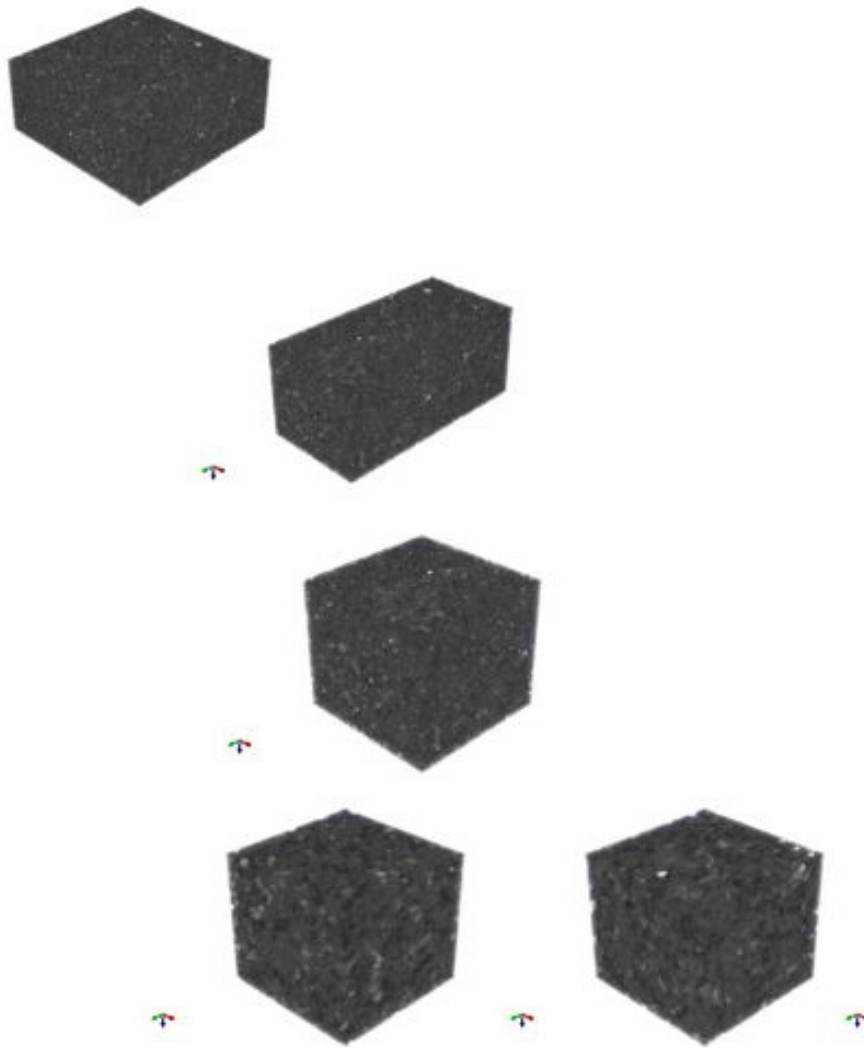


**Figure 4.6** Example of subdivision branch used to evaluate porosity convergence with model volume presented in Figure 4.7 starting from the largest volume ( $8 \times 8 \times 3.5 \text{ mm}^3$ ) volume on top. The smaller models presented here have a volume of approximately  $0.9 \text{ mm}^3$  which is close to the volume of the B1 and B2 models.

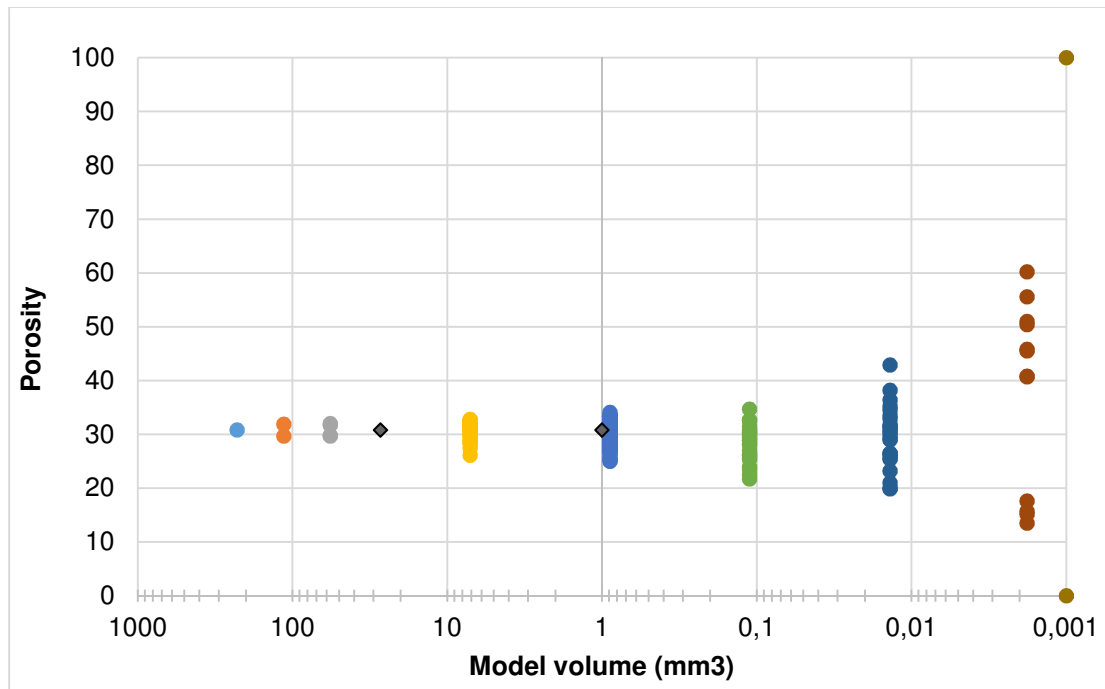


**Figure 4.7** Porosity convergence with model volume. Grey diamonds represent actual model sizes used in this study. It is likely that models larger than 10 mm<sup>3</sup> will provide an excellent porosity REV of the initial volume. Below 10 mm<sup>3</sup> the models are less representative, but the porosity distribution at 1 mm<sup>3</sup> is still consistent with the porosity distribution of 40 cm<sup>3</sup> rock cores (Table 3.3).

### 4.3 Absolute permeability predictions from original and modified models

#### 4.3.1 Simulations setup and parameters

Fluid flow simulations were conducted in all models using FLUENT code to simulate single phase laminar flow with constant pressure boundary conditions at the inlet and outlet faces and wall conditions on the four remaining faces. A constant inlet pressure condition was found to be better for stability and convergence compared to constant velocity, especially in the presence of disconnected pores at the inlet face. The use of wall conditions on the faces parallel to the flow lead to an underestimation of the permeability compared to periodic conditions (Figure 4.8). Wall conditions however allowed for shorter computing times and were consistent with the experiments where the flow was constrained by a rubber sleeve around the cores.

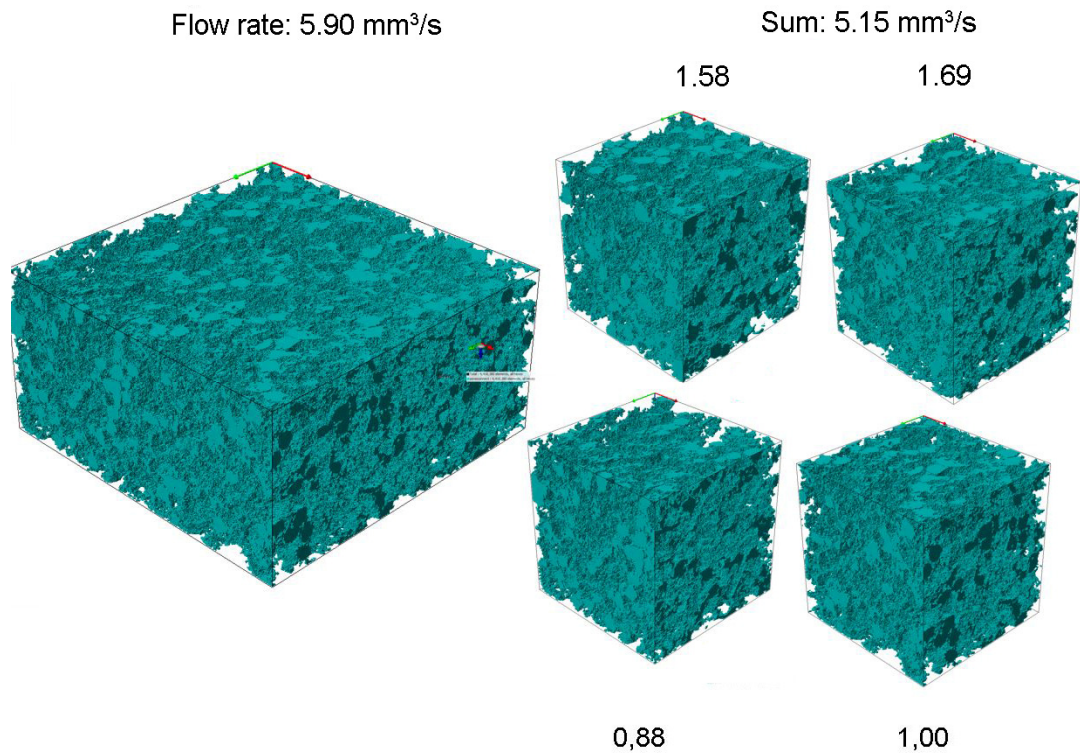


**Figure 4.8** Test of the wall boundary conditions. The flow is directed from bottom to top. A large volume (2.5x2.5x1.25mm) has been divided into four parts. In all cases the four lateral faces were set as walls. The integrated flow rate of the four sub-volumes is less than the flow rate computed for the large volume. This implies that the chosen wall conditions reduce the likelihood of a volume acting as a REV in term of permeability.

Initial simulations were conducted on the lower resolution (200<sup>3</sup> voxels) B1 and B2 models. The solution was considered to have converged when the velocity and continuity residuals had reached a value of 10<sup>-4</sup>. This solution was then used to initiate the simulation in the higher resolution B1 and B2 models. With this method, the calculation time at the higher resolution was about 1 hour with 50 CPU and 100 GB memory. For each simulation the difference in mass flow rate between the inlet and outlet was less than 0.1%. The average of the mass flow rate was used to compute permeability using Darcy's law.

Two series of simulations were also conducted on A1 and B1 with constant velocity inlet conditions instead of constant pressure; this was done to investigate changes in pressure gradient inside the models as a result of porosity change.

### 4.3.2 Qualitative observations

Several qualitative observations can be made to evaluate the quality of the simulations and their relevance in term of REV. Figure 4.9 presents the results obtained with the low resolution A1 model using constant velocity inlet and constant back pressure boundary conditions. The figure shows that the pressure gradient in the flow direction is fairly linear across the whole volume indicating that the pore distribution is homogeneous. The variation in pressure gradient for flow simulations in the three orthogonal directions does not exceed 5% indicating that the model is also isotropic. These are two strong arguments in favor of the model being a REV since the rock is homogeneous and isotropic at the core size.

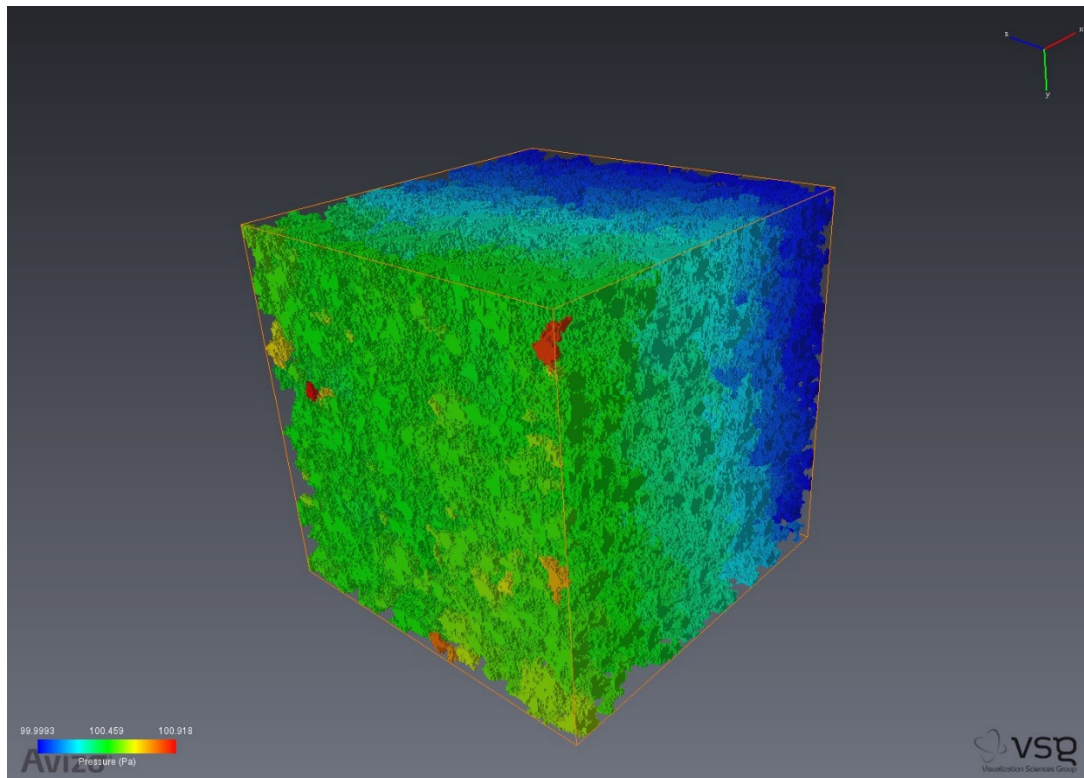


**Figure 4.9** Pressure drop in the A1 model with constant velocity condition at the inlet. Red zones correspond to isolated pores at the inlet which can lead to problem in solution convergence.

Figures 4.10, 4.12 and 4.13 present the flow paths, coloured according to the magnitude of the velocity, for the A1 model in three different cases: original pores, dilated pores and calcite removed. There is no clear pattern of fluid flow through the original pores; the flow is composed of a large number of streamlines and is apparently homogeneous. The flow features at the pore scale are qualitatively consistent with a constant velocity inlet

condition: higher flow velocities are found in constrictions and at the center of the pores: (Figure 4.11).

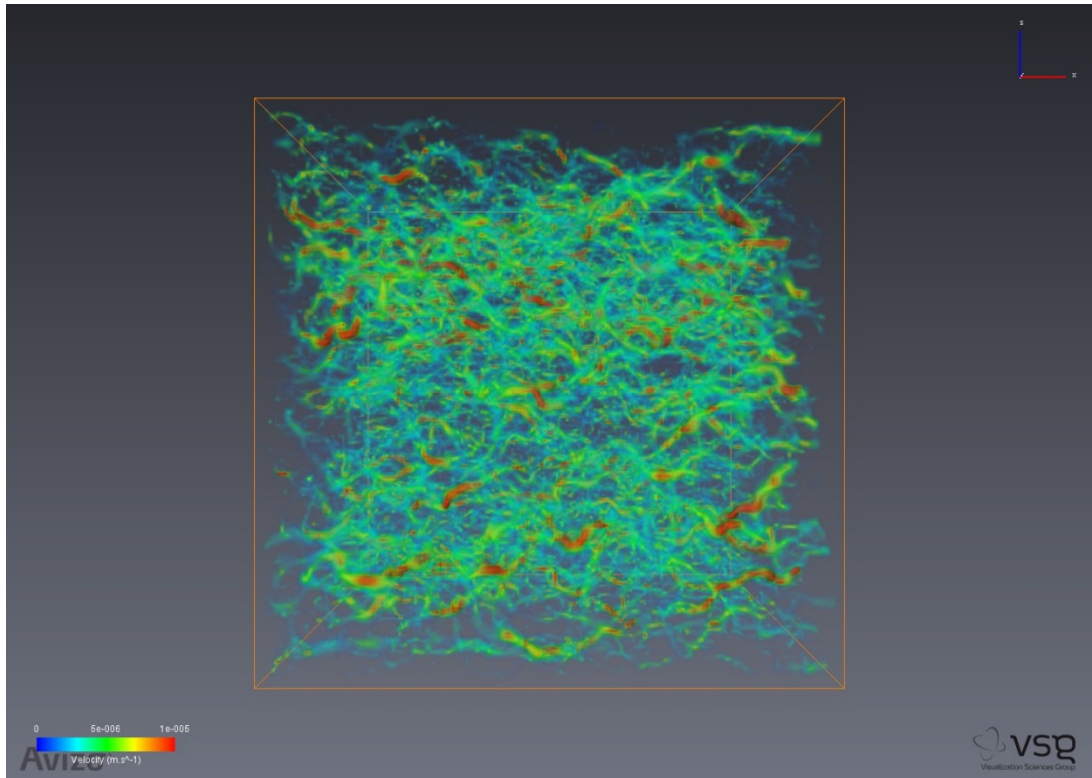


**Figure 4.10** Flow paths colored by velocity magnitude in the initial A1 model with constant pressure conditions on the left and right faces.

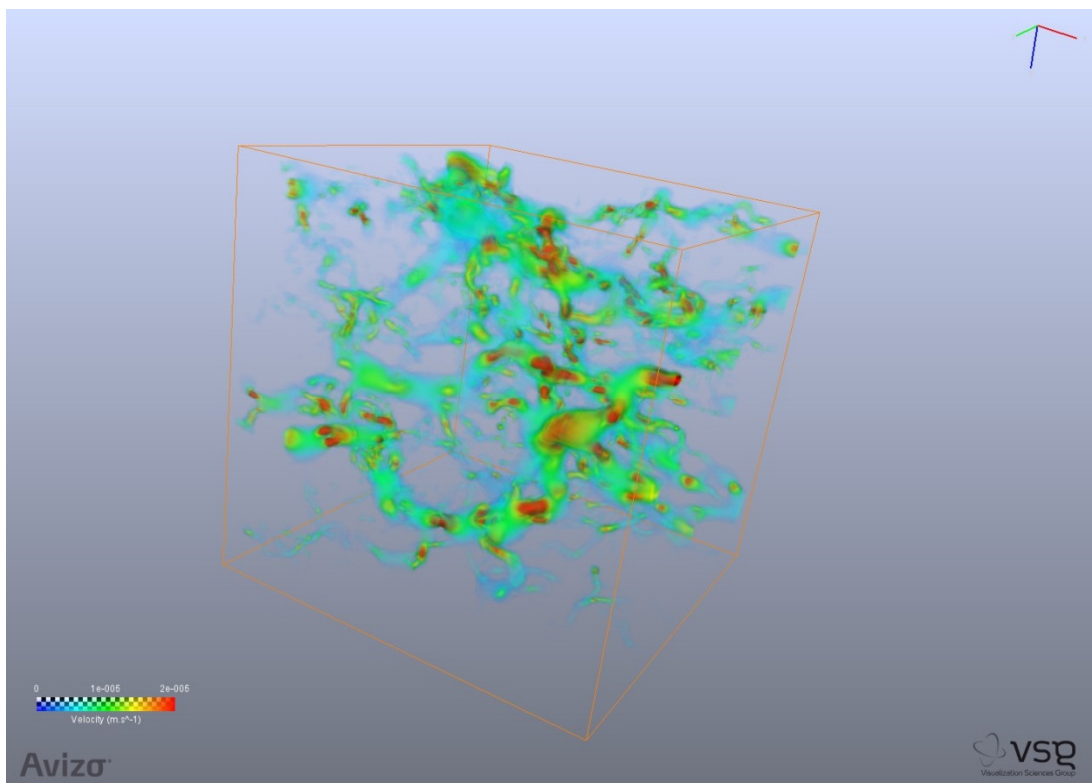


**Figure 4.11** Close up on the Figure 4.10 ( $0.5 \times 0.5 \times 0.5 \text{ mm}^3$  sub-volume) showing flow velocity dependence on the pore geometry.

As expected, pore dilatation did not change the general pattern of flow significantly (Figure 4.12) even though some connections might have been created during the process. On the other hand calcite dissolution led to the creation of new streamlines in addition to the original flow (Figure 4.13). Some of those new streamlines are relatively large with respect to the model size but are sufficiently well disseminated that the homogeneity of the flow and the linearity of the pressure gradient are preserved. This stems from the fact that calcite is quite homogeneously distributed in the rock (Figure 4.14).

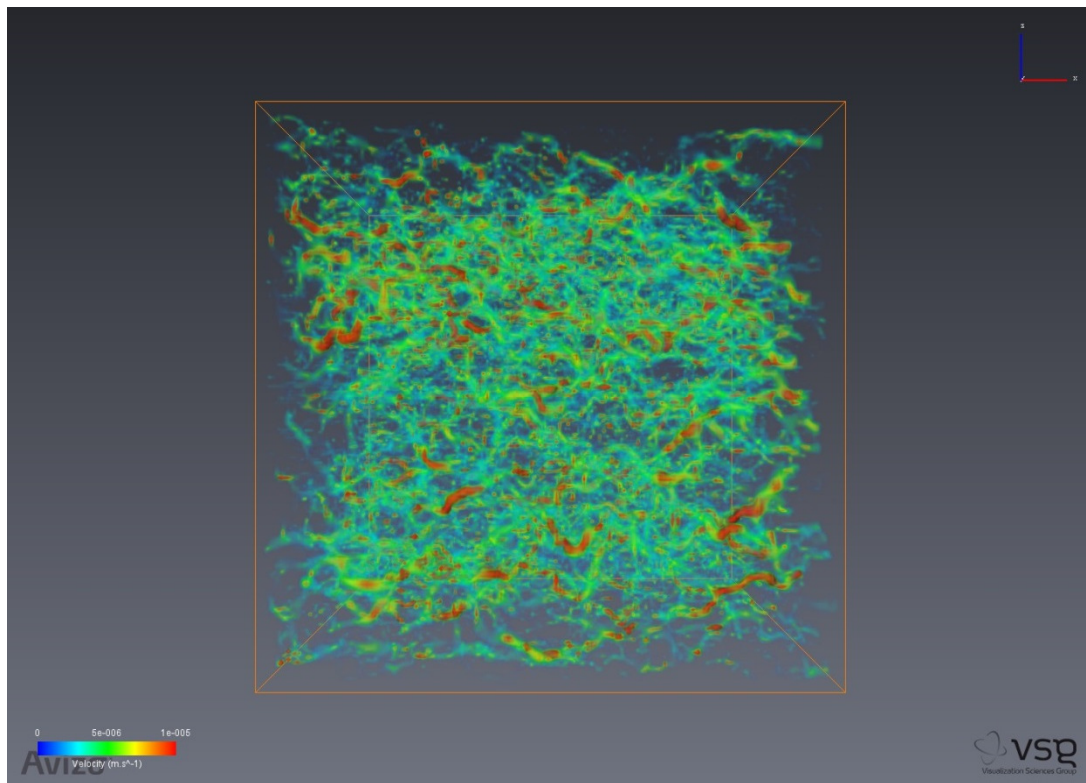


**Figure 4.12** Flow paths colored by velocity magnitude in the A1 model with dilated pores.

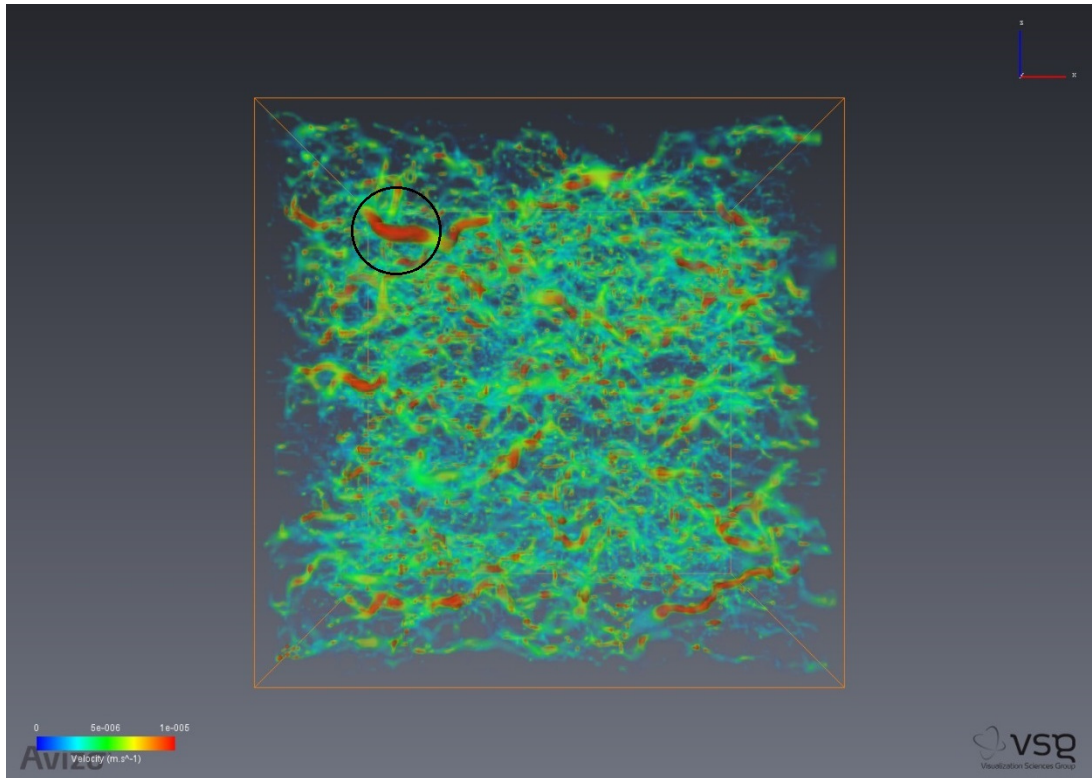


**Figure 4.13** Flow paths colored by velocity magnitude in the A1 model with calcite dissolved. A new streamline has been circled for illustration.

Fast visualization | Quality: 10

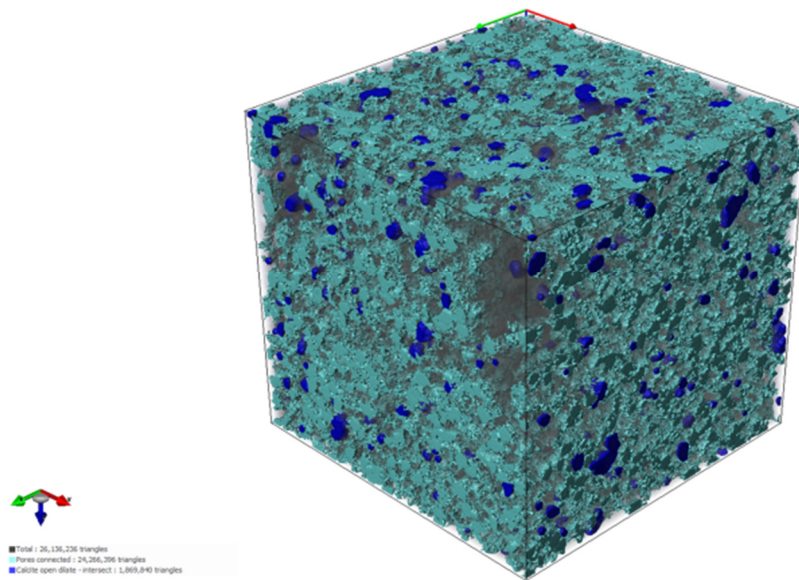


**Figure 4.14** Pores (light blue) and calcite (blue) distribution in the A1 model.

From these preliminary observations it is clear that the A1 model and the modified A1 models are effectively REV. The A1 model size was unfortunately only attained by trading off the resolution and applying a coarse voxel size of 12  $\mu\text{m}$ . To use the highest resolution of 2.5  $\mu\text{m}$  the volume had to be reduced to 1  $\text{mm}^3$  for the B1 and B2 models. Figure 4.15

shows that the pressure gradient is visually less linear for the B1 model meaning that 1 mm<sup>3</sup> volumes are not as representative.

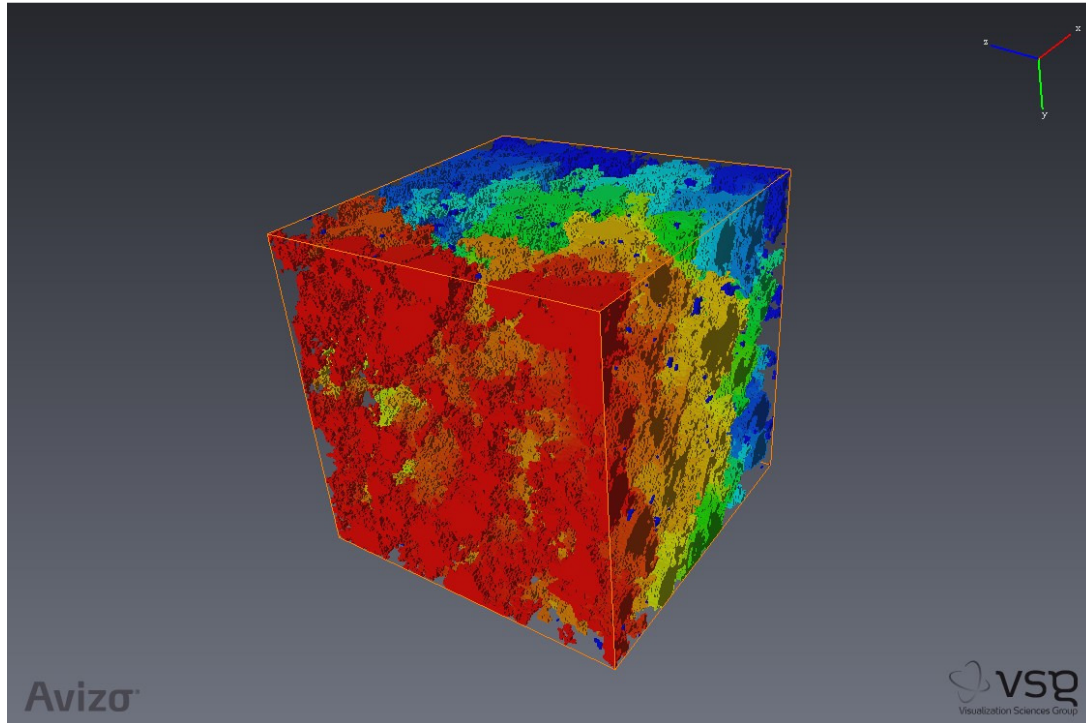


**Figure 4.15** Pressure drop visualization in the B1 model.

Figure 4.16 shows a lateral view of the pressure drop in the B1 model for initial pores, dilated pores and after calcite dissolution. The fluid enters on the left at constant velocity while the outlet pressure on the right is kept constant. Even though the pressure gradient is not as linear as in the larger A1 model there are no major heterogeneities. The effect of pore dilatation or calcite removal is explicit: the pressure gradient retains the same geometry but its magnitude is linearly decreased. Surprisingly the pressure gradient is slightly smaller in the pore dilatation case meaning that the permeability increase is even more important in conditions for which the K-C approach should be valid.

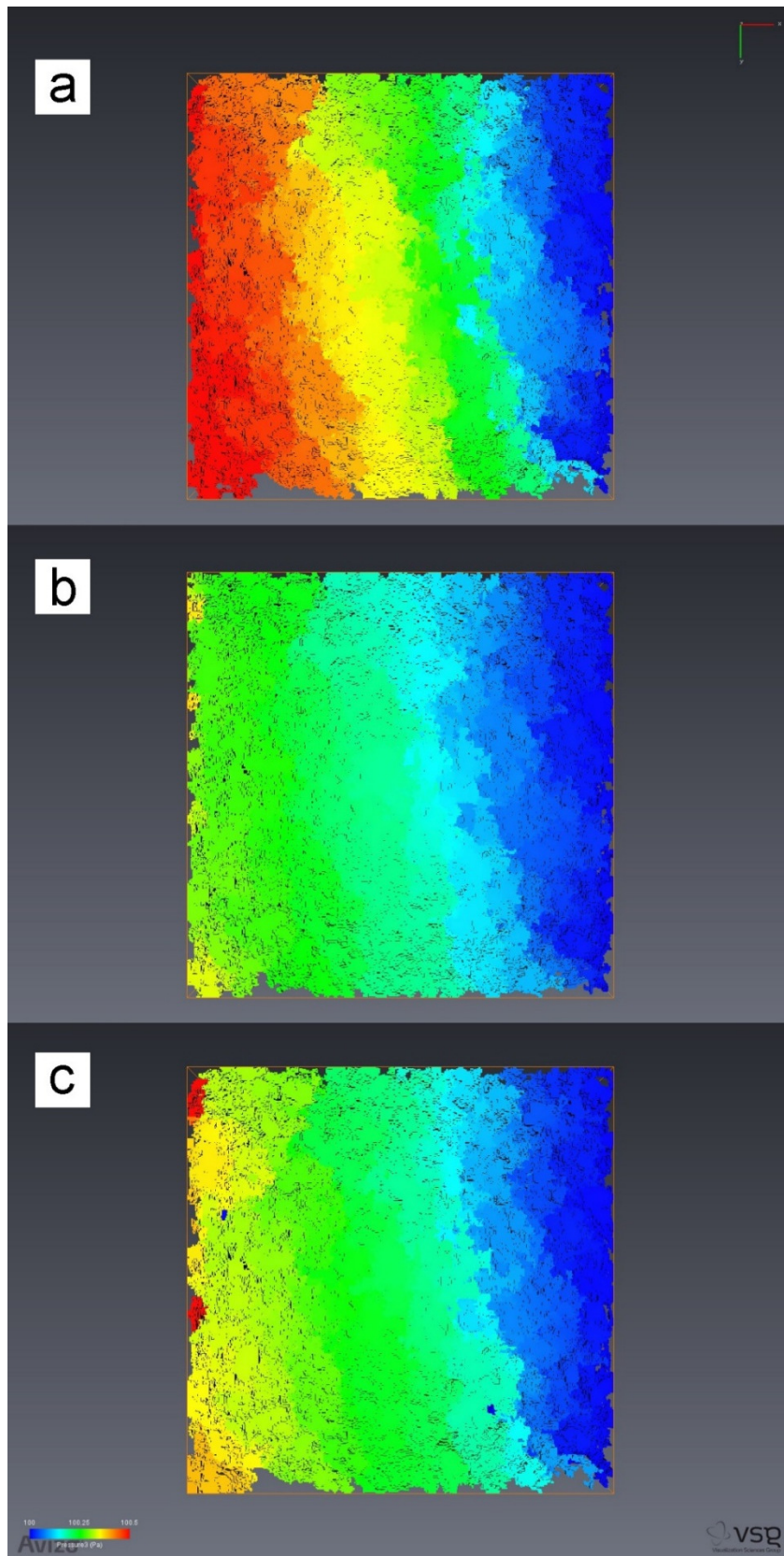


**Figure 4.16** Comparison of the pressure drop in A1 model with constant velocity inlet (left) and constant outlet pressure in the A1 model in three different cases. Initial pores in a), dilated pores in b) and calcite dissolved in c).

### 4.3.3 Statistics of fluid flow

The analysis of fluid flow statistics can provide additional insights on the effects of resolution, pore modifications and model physical size on the calculated permeability. The velocity magnitude distribution along the main flow path (Figure 4.17) and the velocity distribution in transverse directions (Figure 4.18) are consistent with the hypothesis that the medium is homogeneous and isotropic, they are also in agreement with particle image velocimetry experimental observations (Cenedese and Viotti, 1996; Moroni and Cushman 2001). On Figure 4.17 it is apparent that up to 20% of the pore space is filled with stagnant water which does not participate in the flow.

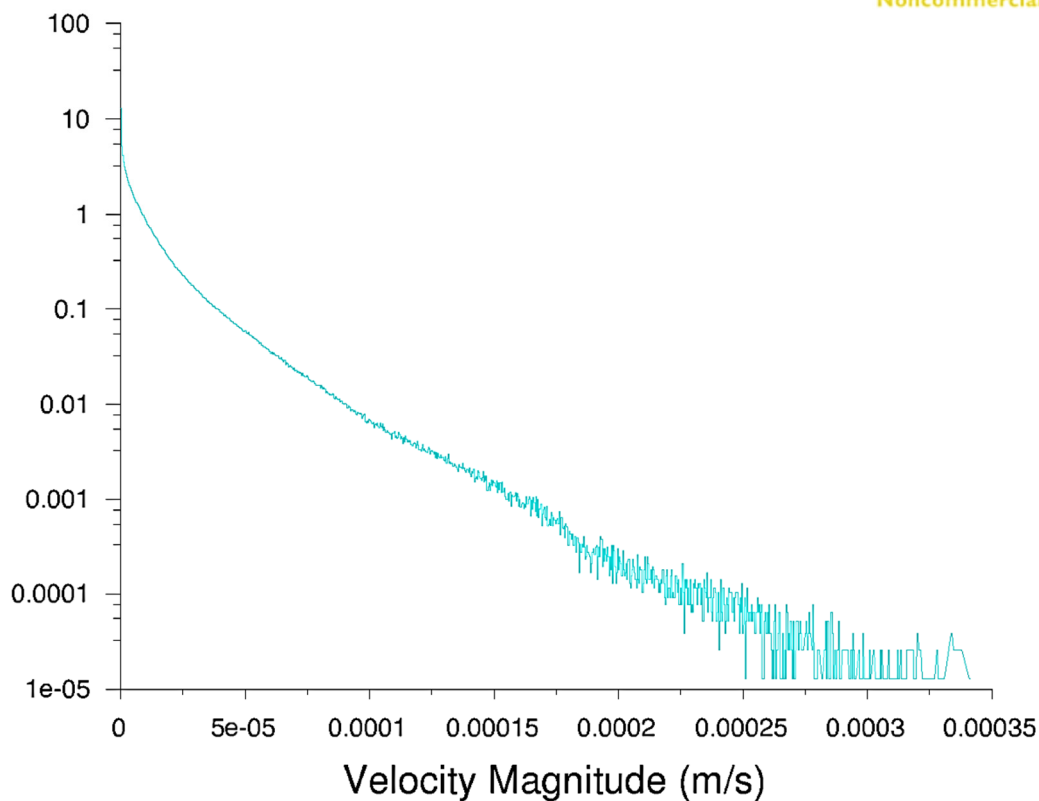


**Figure 4.17** Example of velocity magnitude histogram in the initial A1 model. This shows the percentage of voxels for each velocity magnitude value of the fluid present in the pores.

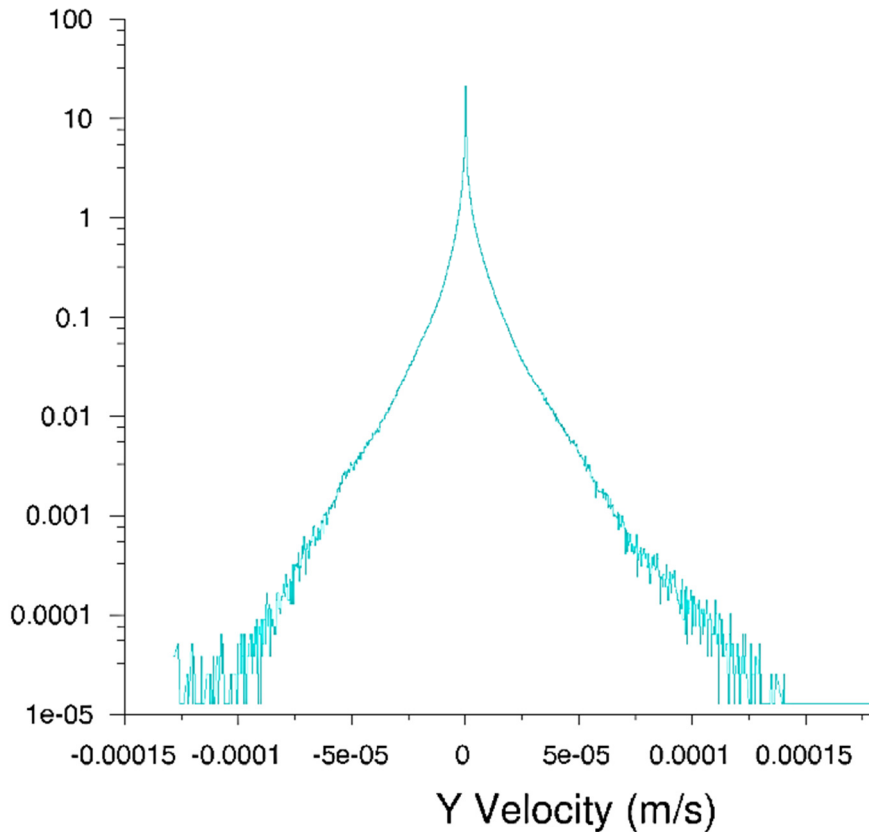


**Figure 4.18** Example of transverse velocity histogram in the initial B1 model. This shows the percentage of voxels for each velocity value of the fluid in the Y direction. The main flow direction is in the X axis so that Y and Z axis are referred as transverse directions. The symmetry of the curve indicates that the model is homogeneous. Similarity of the Z velocity curve (not shown) indicates model isotropy.

Typical velocity distributions for the main flow direction component are skewed forward and display a peak at zero velocity. Visually, coarsening the models has a minor impact. Figure 4.19 presents velocity distributions for B1 at all five resolutions (2.5  $\mu\text{m}$ , 2.9  $\mu\text{m}$ , 3.3  $\mu\text{m}$ , 4  $\mu\text{m}$  and 5  $\mu\text{m}$ ); the height of the zero velocity peak is not modified and there is no clear effect on the backflow part of the distribution. The only sensible effect is a small velocity increase of the forward flow part which is slightly heterogeneously distributed with higher velocity increase in high velocity regions. Overall the effect on the permeability is negligible, and hence permeability is resolution independent as well as independent of fluid viscosity; although this result is a priori only valid over the resolution range available for B1 and B2 models and does not indicate if the resolution is sufficient to correctly represent the real pore space geometry.

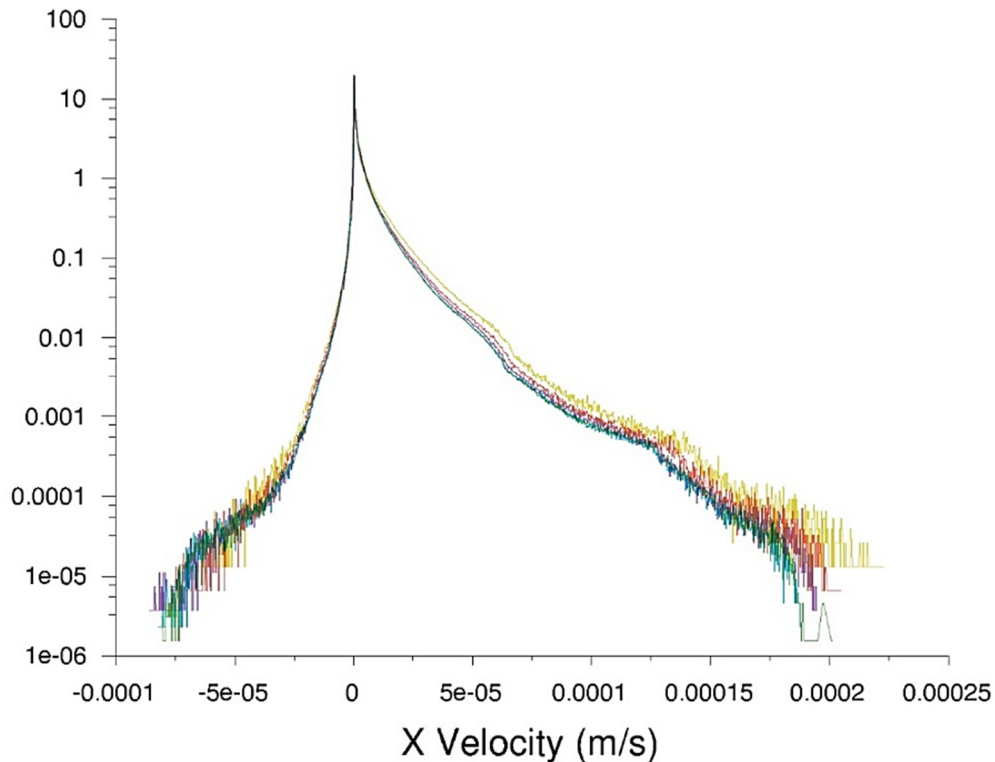


**Figure 4.19** Comparison of the flow velocity histogram (in the main flow direction) for the B1 model at various resolutions. The result for the lower resolution is in yellow and for the highest resolution in green.

Figures 4.20 and 4.21 present results for B1 at the highest and lowest resolution for the three different porosity scenarios used earlier (initial pores, dilated pores, calcite dissolved). In the low resolution model the effect of pore dilatation is a widening of the distribution for both forward flow and backwards flow. The zero velocity peak decreases from 20 to 10%. This is an expected result as all flow paths are accelerated, especially the high velocity ones. The reduction in the zero velocity peak is probably an artifact of the pore dilatation creating some new connections between the pores; this is illustrated in Figure 4.22. Calcite dissolution also widens the velocity distribution in a similar fashion albeit with a small distortion indicating that the calcite is not perfectly homogeneously distributed. The zero velocity peak decreases from 20 to 15%.

Most comments made on the low resolution case are valid for the high resolution one. The only difference is that, for reasons that are unclear, the zero velocity peak is not changed at high resolution. An interesting second order observation is that calcite dissolution also created some relatively high velocity backflow paths. This counter intuitive result is illustrated in Figure 4.22.

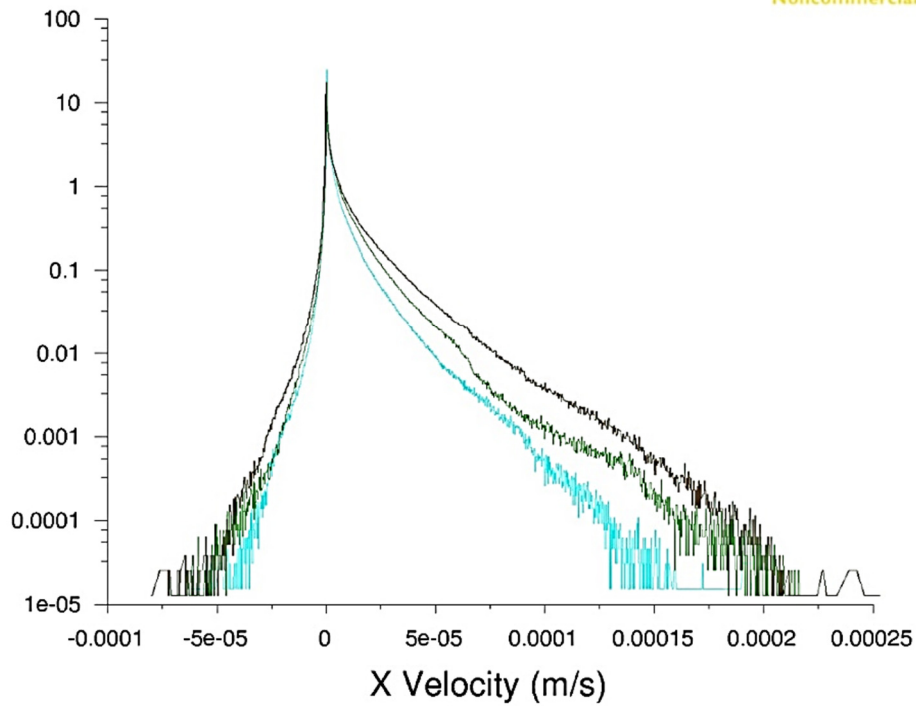


**Figure 4.20** Comparison of velocity histogram (in the main flow direction) for A1 at the lowest resolution and in the three different porosity cases.

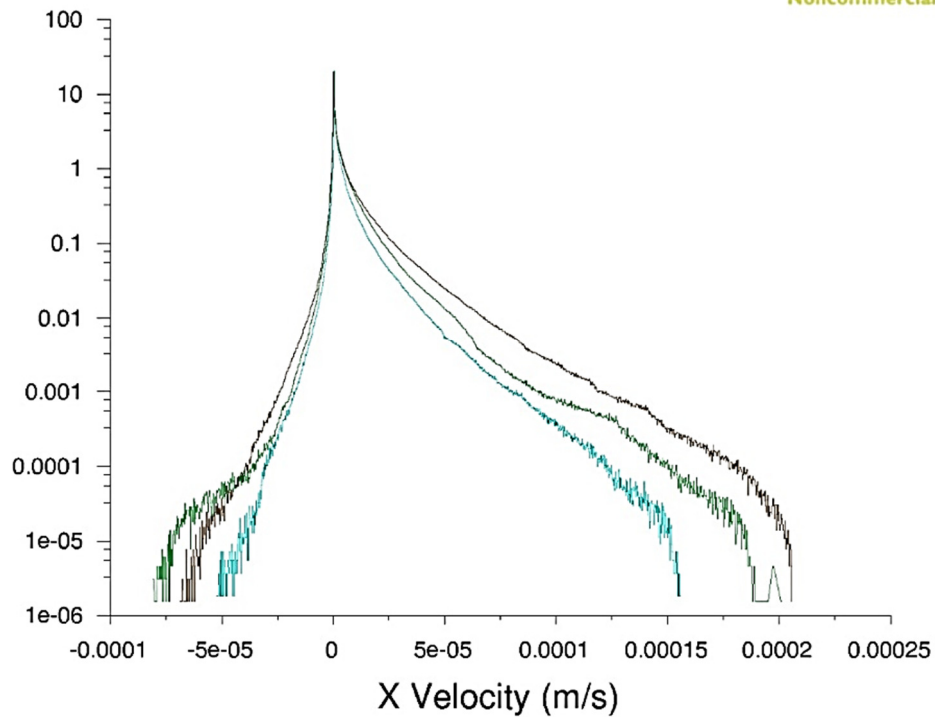


**Figure 4.21** Comparison of velocity histogram (in the main flow direction) for A1 at the highest resolution and in the three different porosity cases.

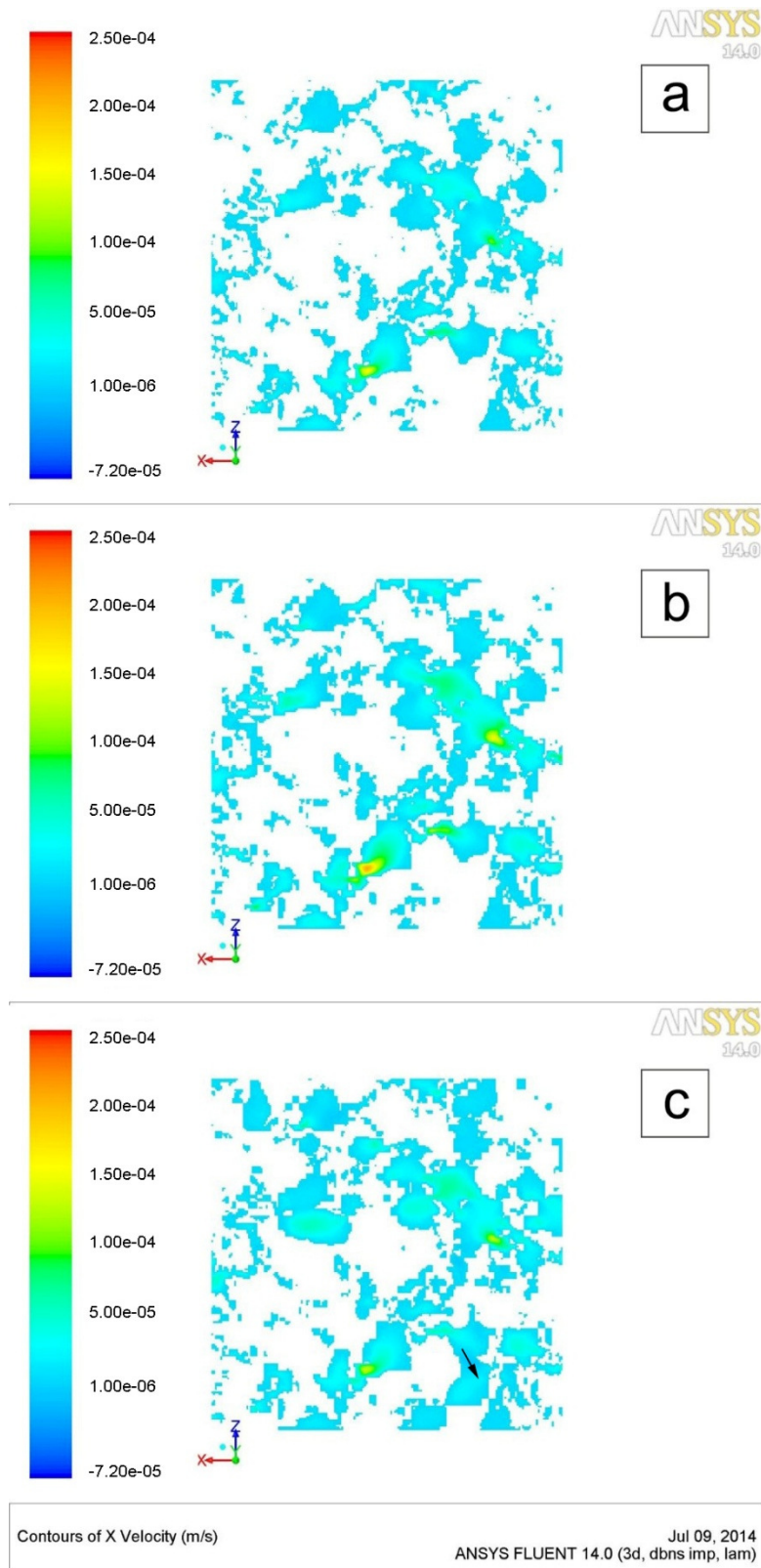


**Figure 4.22** Comparison of the velocity magnitude in the main flow direction on cross sections of the A1 model in the three different porosity cases, initial pores in a), pores dilated in b), calcite dissolved in c). This illustrates the flow velocity increase and the creation of new pores connections when the pores are dilated. It is also apparent that calcite dissolution can generate some backflow (dark blue zone and black illustrative arrow) in c).

Finally the effects of model size and resolution on the pressure gradient (in the main flow direction) were evaluated and results are shown in Figure 4.23. This figure represents the pressure gradient for the initial B1 model at high and low resolution. The increase in resolution has no visible effect on the pressure gradient apart from the fact that it is slightly more continuous at higher resolution. Discontinuities in the pressure gradient are interpreted as backflow regions, dead end pores or isolated pores. The pressure seems mostly linear although there is some significant dispersion. The pressure dispersion is an indicator of the model heterogeneity at the pore scale, all flow paths are not equivalent. The dispersion in itself is not necessarily an issue for the model to be homogeneous or representative at the millimeter scale, once all flow paths are averaged. Dispersion also exists at the core scale. However it might be expected that the dispersion amplitude will decrease and eventually reach a minimum as the physical size of the model increases. Figure 4.23 presents a comparison between models B1 and C1 (C1 has a resolution of 5  $\mu\text{m}$  and a volume of 8  $\text{mm}^3$ ). Clearly the dispersion is less in the larger model, and this means that model C1 is more representative from the Darcy permeability point of view. It would be useful to continue increasing the model size but this would come at great computational cost. This result reinforces the earlier word of caution concerning the B1 and B2 model sizes that were used in this study. Those models cannot be fully considered as REV for the absolute permeability.

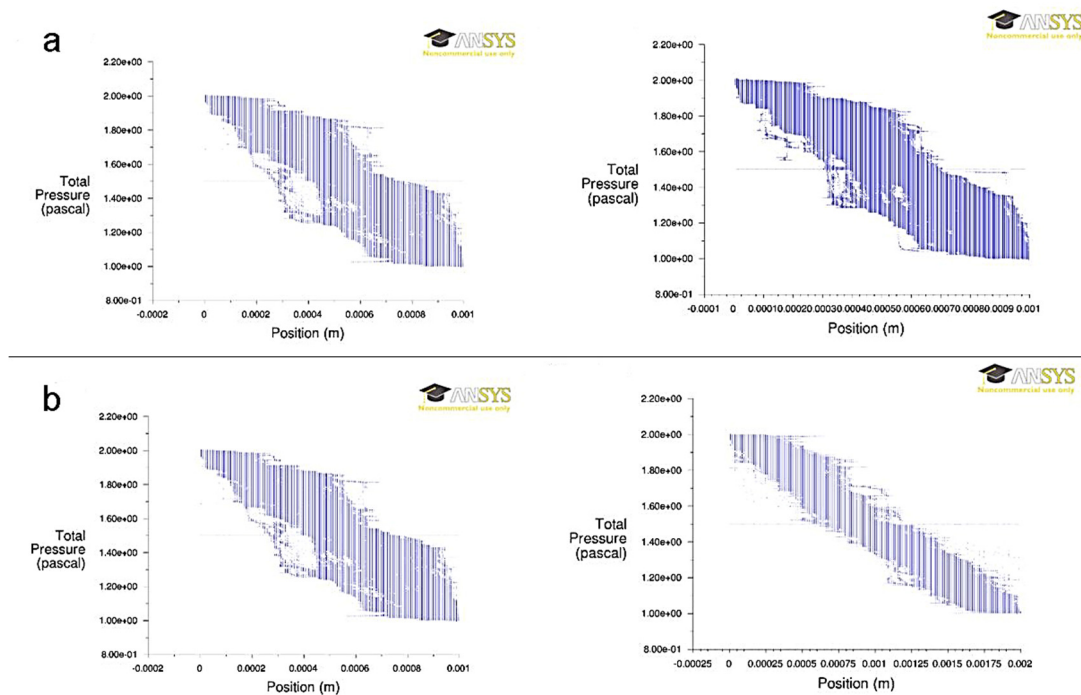


**Figure 4.23** Visualization of pressure gradient at lowest and highest resolution (Top part) and comparison at low resolution between the B1 and C1 models (lower part).

## 4.4 Comparison of results from modelling and experiments

### 4.4.1 FLUENT permeability predictions compared with a simple capillary tube model

Following is an analysis of the absolute permeability predictions made with FLUENT simulations and a verification of their consistency with simple constitutive equations relating the mean hydraulic radius or the resolution of the models with their permeability. The mean hydraulic radius is easily available through model analysis as it is related to porosity and wetted area through Equation 4.1. This is also the occasion to investigate further the effect of model resolution on the results.

This analysis starts with the porosity of models B1 and B2 at various resolutions: Figure 4.24 is a plot of the porosity of the two series of models; the porosity changes from pores dilatation or calcite dissolution are almost equivalent by construction. The porosity of the models are constant over the all resolution range. The porosity increase after pore dilatation or calcite removal is about 15% for B1 and 14% for B2.

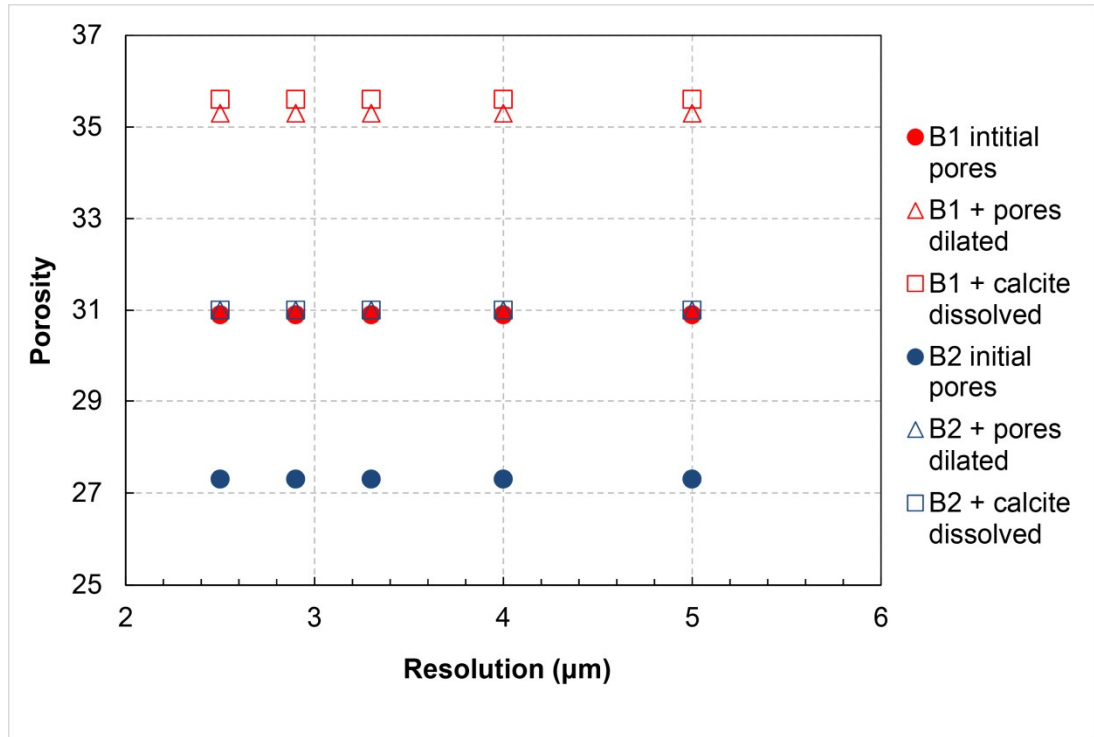


**Figure 4.24** Porosity of the B1 and B2 models at various resolutions.

One other property available from model analysis is the wetted area (which in this context means the surface area of the interconnected pore walls). Figure 4.25 is a plot of the wetted area for all the models. The wetted areas of B1 and B2 are very similar but the value for B2 is always lower at any resolution because it has a lower porosity. As expected, the wetted area increases with finer resolution since the grain roughness increases. In the pore dilatation case the wetted area should slightly increase with respect to the initial value. This is only partially true as it tends to decrease at high resolution and increase at lower resolution, this is probably due to a competition between surface increase and surface smoothing during the dilatation procedure. This effect is slightly more important for B2 which is the low porosity model. Comparatively the dissolution of calcite always gives rise to a marked increase in the wetted area of about 2 mm<sup>2</sup>. The increase is marginally higher for B1 since the calcite content is higher. The increase in wetted area caused by calcite removal is fairly independent of resolution although a slight augmentation is visible at high resolutions. This is because the calcite identification procedure explained earlier tends to generate smooth (large wetted area) calcite grains at high resolution.

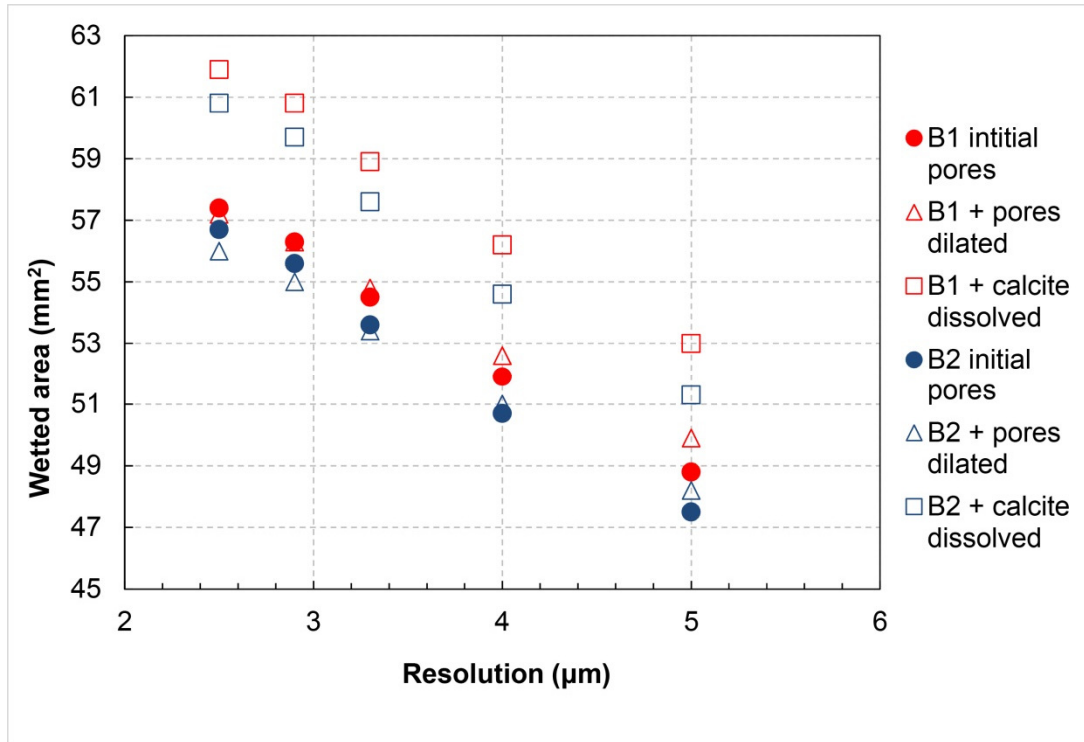


**Figure 4.25** Wetted area of the B1 and B2 models.

At this stage it is possible to calculate the mean hydraulic radius of the pore space using Equation 4.1.

$$R_h = V/S \quad (4.1)$$

where  $R_h$  is the mean hydraulic radius,  $V$  is the pore volume and  $S$  is the wetted area.

The mean hydraulic radius is increased by about 1 µm with calcite dissolution and is higher for B1. The increase in mean hydraulic radius in the pore dilatation case is higher, by about 0.5-1 µm, and is slightly higher for B2. The increase reaches a maximum in the pore dilatation case as the change in volume is associated with a minimum change in wetted area.

Remarks made on the relative changes in wetted area and their dependence on resolution are also valid for the mean hydraulic radius since the porosity does not depend on resolution. In the pore dilatation case the increase in mean hydraulic radius increase slightly at finer resolution. In the calcite dissolution case the increase in mean hydraulic radius is almost resolution independent.

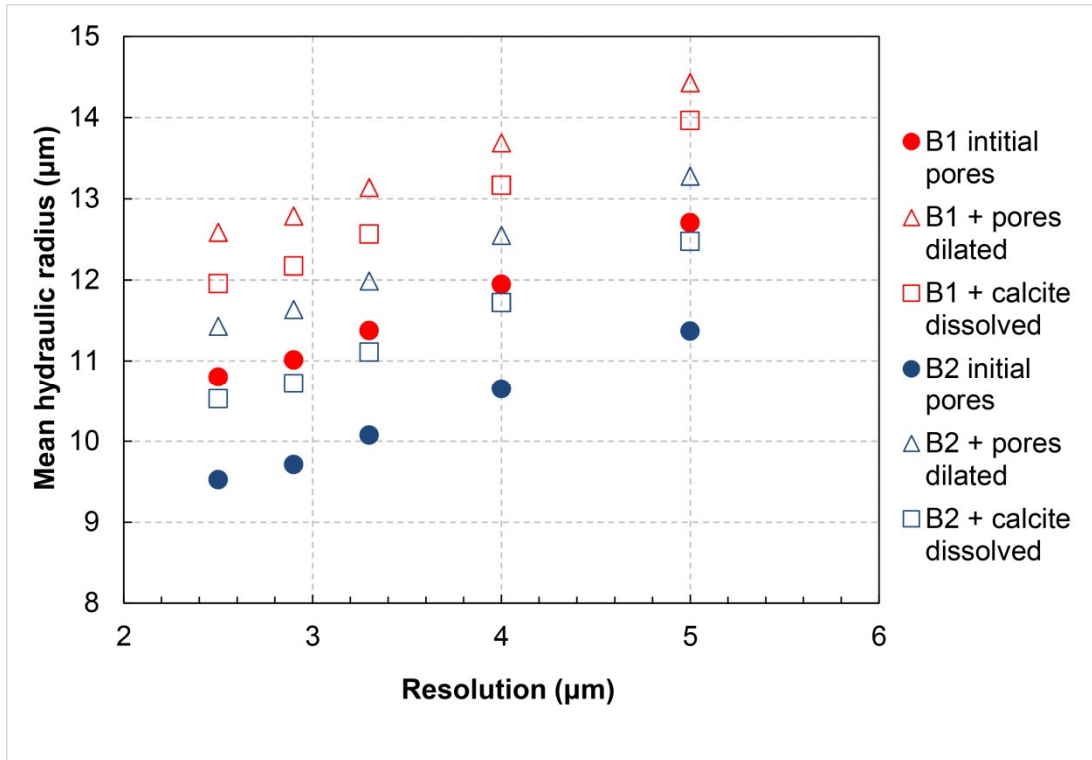


**Figure 4.26** Mean hydraulic radius of the various B1 and B2 models.

Overall, the model sets B1 and B2 display similar changes in mean hydraulic radius. For all models the mean hydraulic radius decrease with resolution. The hydraulic radius increase more in the pore dilatation case. The relative change in hydraulic radius depends on resolution but is only a second order effect, it is almost insignificant in the calcite dissolution case.

Assuming again that the pore space can be represented as straight capillaries of constant radius the permeability can be derived using the newly determined mean hydraulic radius (Equation 4.2).

$$\kappa = \frac{\phi R_h^2}{2} \quad (4.2)$$

where  $\kappa$  is the permeability, and  $\phi$  the porosity.

In this model the permeability depends principally on the mean hydraulic radius therefore all observations made on this property comparing B1 and B2 and the various sets of models at different resolutions is visible in the permeability data.

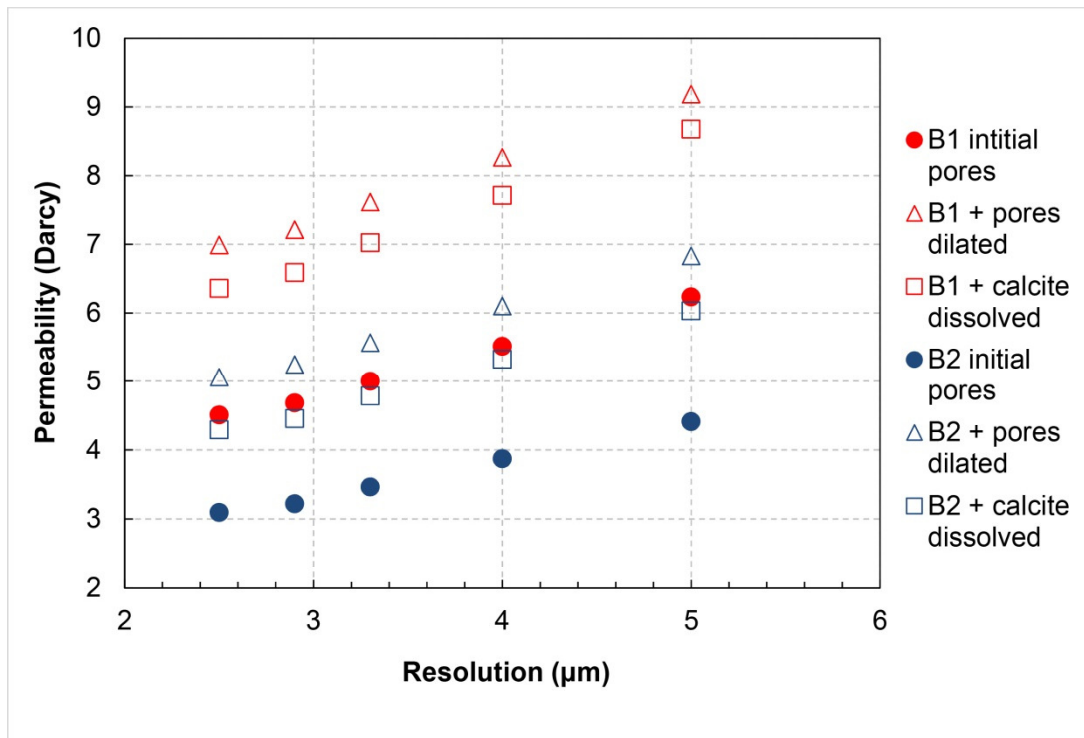


**Figure 4.27** Permeability calculated with Equation 4.2 of the B1 and B2 models.

The next step of this analysis is to compare the prediction of the simplified model explicated above with the FLUENT results. Figure 4.28 compare absolute permeability predictions. On first visual inspection the absolute permeability predictions do not seem to be in agreement. The permeability ranges between 0.5 and 10 Darcy which is one to two order of magnitude higher than the experimental values. One noticeable difference is that the permeability of the initial models calculated with FLUENT is less dependent on the resolution. In contrast, coarsening of the modified models lead to a permeability increase similar to the one obtained by the simple capillary tube model. The FLUENT permeability is systematically lower for all models: this is likely due to the fact that the mean hydraulic radius parameter does not capture correctly the influence of small pore throats on the permeability and because it does not take into account the pore network tortuosity. Overall the absolute permeability overestimation with FLUENT is consistent with the mean hydraulic radius which is an intrinsic property of the models.

The absolute permeability is supposed to depend on resolution since the minimum possible mean hydraulic radius is limited by the voxel size (if all flow streams were one voxel wide). The resolution effect is evident when considering the results from model A1 which resolution is 12  $\mu\text{m}$ . Figure 4.29 shows the FLUENT results for A1, B1 and B2 in initial models and models with calcite removed, on the graph is also shown the typical experimental

results at the origin of the resolution axis. The black dotted curve indicate the smallest possible permeability expected with a porosity of 30% and straight capillaries one voxel wide. There is a some correspondence between this curve and the FLUENT results when changing the resolution from 12  $\mu\text{m}$  to 5  $\mu\text{m}$ . Going from 5 to 2.5  $\mu\text{m}$  resolution the permeability convergence towards the experimental values is much slower with FLUENT. In conclusion: there must be flow paths significantly smaller than 2.5  $\mu\text{m}$  in the real rock that have a determinant control on the permeability and that are not properly resolved in the models. Given the theoretical curve a minimum resolution of 1  $\mu\text{m}$  is necessary to obtain permeability values in the same order of magnitude as the experimental ones (about 10 mD). In practice one would need an even finer resolution so that the mean hydraulic radius would effectively be 2  $\mu\text{m}$ .

Taking into consideration the tortuosity, the minimum theoretical resolution needed to achieve a given permeability would be multiplied by the tortuosity. For example tortuous capillaries of radius 2  $\mu\text{m}$  and tortuosity 2 would also give a permeability of 10 mD.

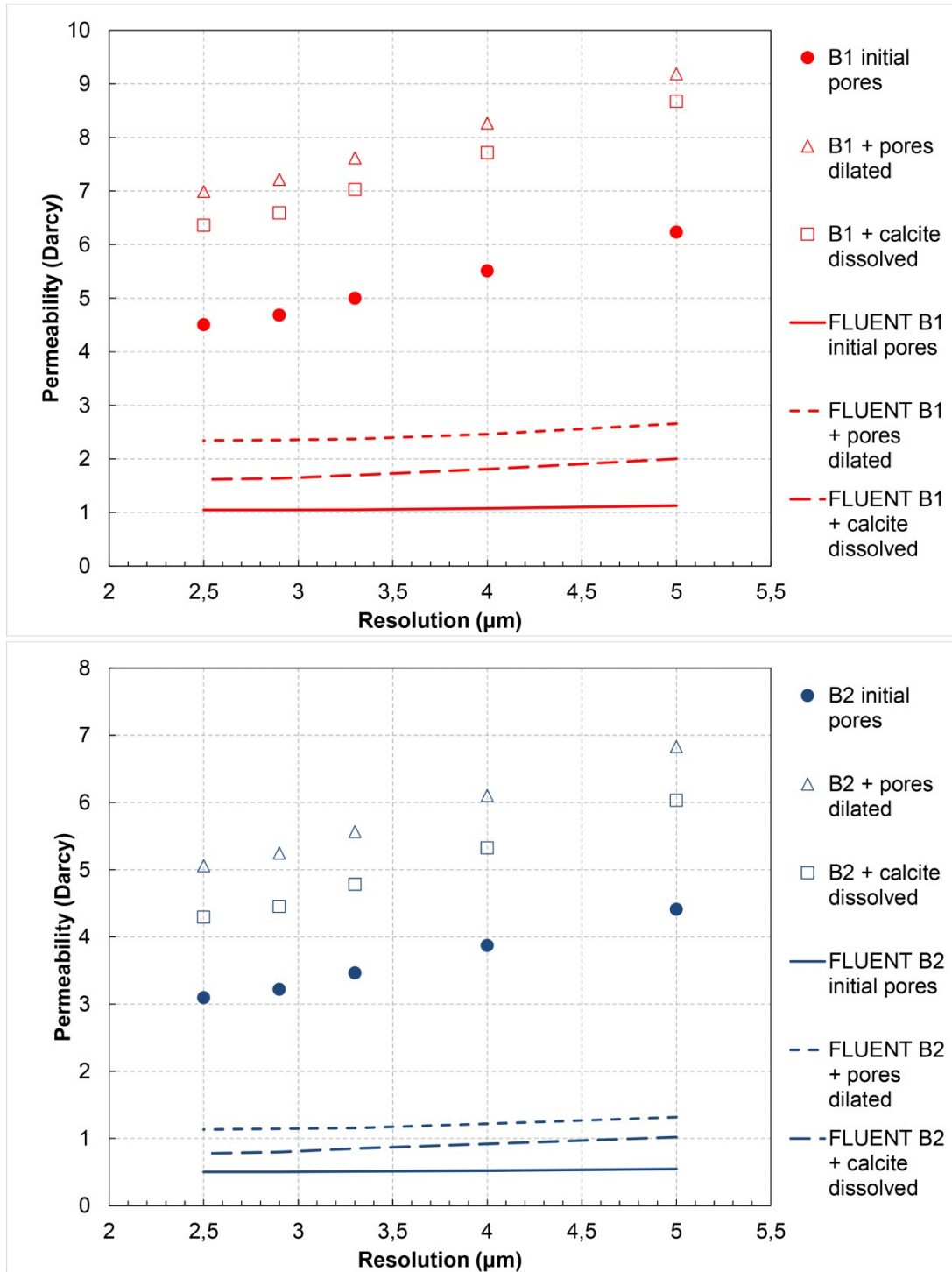


**Figure 4.28** Comparison between FLUENT permeability calculations and Equation 4.1 for the B1 and B2 model.

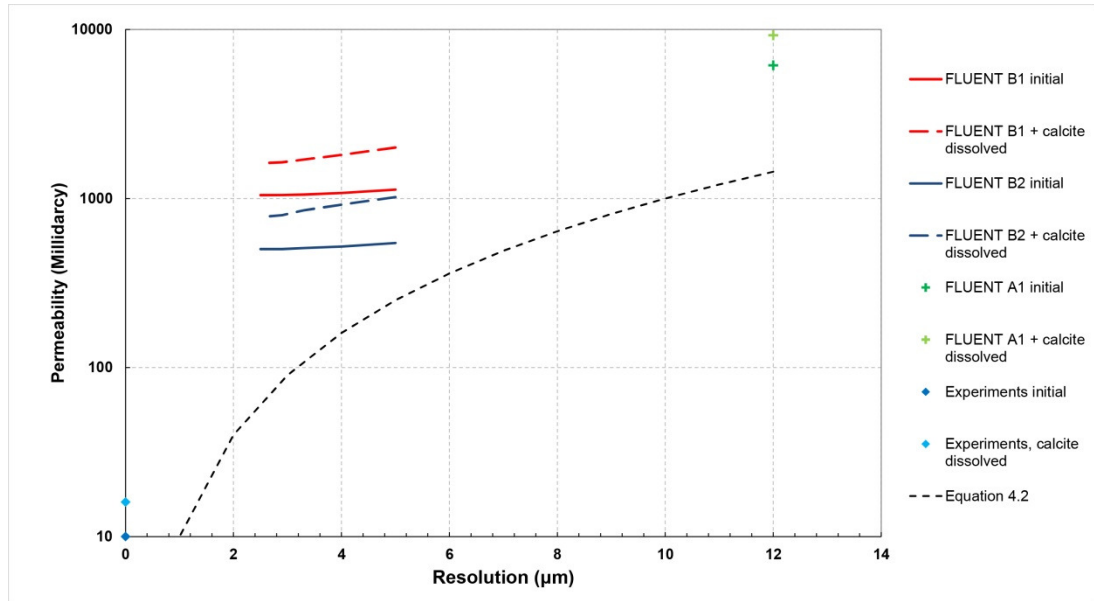


**Figure 4.29** Comparison between FLUENT results for A1, B1 and B2 with experimental results (on the vertical axis) and Equation 4.2 where  $R_h$ =voxel size was used.

In conclusion of this first analysis of the absolute permeability results it appears that the FLUENT results seems trustworthy and logical but that the models do not provide an accurate representation of the pore space. The cause of this inaccuracy is the insufficient model resolution and the consequence is an overestimation of the absolute permeability. Despite these discrepancies, do FLUENT simulations provide meaningful and useable values for the relative changes in permeability upon a given porosity change?

First consider a network of identical tubes crossing each other's randomly so that the tortuosity of the network is 2.  $N1\_2$  would be a network of tubes 1  $\mu\text{m}$  wide with a tortuosity of 2 and  $N10\_2$  would be a network with the exact same structure but with 10  $\mu\text{m}$  wide tubes. It is clear from Equation 4.1 that the same relative increase in porosity, for example 10%, would lead to the same relative change in tube radius (10% too) and therefore the same relative change in permeability(21% increase). The addition of a connection to  $N1\_2$  so that the tortuosity decreases to 1.9 would produce the network  $N1\_1.9$ . The same connection addition to the network  $N10\_2$  would necessarily create the network  $N10\_1.9$  assuming that the orthogonal flow in the tubes is negligible compared to the longitudinal flow. In this case the relative change in permeability would be identical.

In this framework the tortuosity and the mean hydraulic radius are two independent parameters defining the permeability completely. As a result, if the model is inaccurate for the absolute values of the mean hydraulic radius

and tortuosity but is accurate for the relative changes of those parameters then it will be accurate for the relative change in permeability.

It is possible to test these hypotheses with the results available. First it is possible to test the relevance of the mean hydraulic radius parameter by looking at the initial B1 and B2 models and the respective dilated pores models. The changes in mean hydraulic radius were shown earlier in Figure 4.26. Changes in tortuosity caused by a small pore dilatation can be neglected; in that case the results from Equation 4.2 and FLUENT should be the same. It is clear on Figure 4.30 that this is not the case. In a real rock geometry the mean hydraulic radius is not very relevant since a real rock cannot be represented as a network of tubes of identical sizes. There are an infinity of tube network sets with variable tube sizes that would give the same mean hydraulic radius but different permeability. For example three tubes of radius 10 and length 10 in series or two tubes of radius 10.5 and length 10 plus one tube of radius 1 and length 10 have the same mean hydraulic radius. In the second case a pore dilatation would give rise to a larger permeability increase. This probably explains the discrepancy in Figure 4.30 since there are many narrow flow paths in the rock. If the model is inaccurate, for example by representing numerous small flow paths by one single large flow path then the model results in term of relative permeability change will be inaccurate.

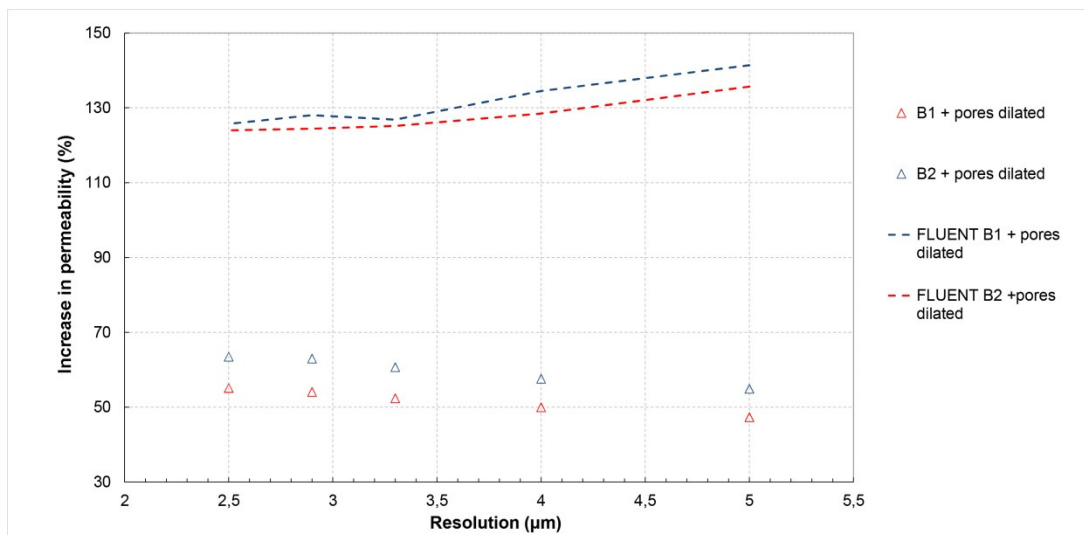


**Figure 4.30** Increase in permeability after pore dilatation calculated with FLUENT (dotted lines) and Equation 4.2 (symbols).

The calcite dissolution case is more complex. In this study calcite is present as large grains a priori accurately represented in the model. The calcite once set as pores represent about 4% of the final pore volume. Narrow flow paths are not affected by calcite removal thus there is not the same issue as

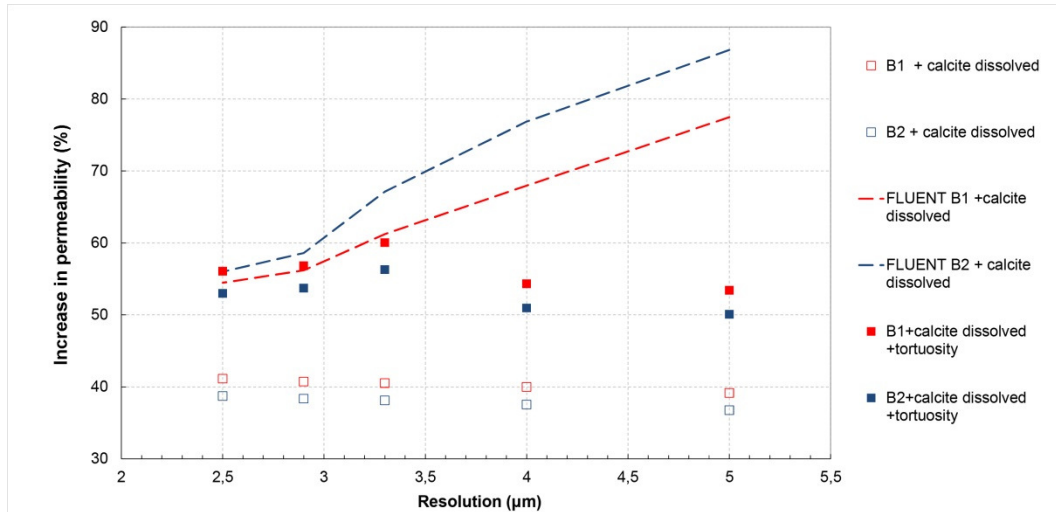
above. The relative change of mean hydraulic radius is practically the same when flow paths are created in various permeability backgrounds as long as  $\frac{\alpha R1}{R_{calcite}} \ll 1$ , where alpha is the relative increase in pore volume when calcite is dissolved,  $R1$  is the radius of the tubes composing the initial pore network and  $R_{calcite}$  is the equivalent radius of the calcite grains. This equation is verified in the models since the calcite grains are large relative to the mean hydraulic radius and the calcite content is small. It is safe to assume that the mean hydraulic radius contribution to the permeability change in the models is only slightly underestimated compared to the real rock. The pure tortuosity contribution should also be accurate given the hypothesis described earlier (with the networks N1\_2, N1\_1.9, N10\_2 and N10\_1.9). The tortuosity change after calcite dissolution has been calculated using random walk simulations in the models (Chapter 3). The tortuosity change in the models is approximately an 8% decrease with calcite dissolution.

Figure 4.31 compares the relative permeability change after calcite dissolution found with FLUENT and with Equations 4.2 and 4.3 which account for mean hydraulic radius contribution alone or on both mean hydraulic radius and tortuosity.

$$\kappa = \frac{\phi R_h^2}{2\tau}, \quad (4.3)$$

where  $\tau$  is the tortuosity (this equation is an extension of Equation 4.2)

Accounting for the contribution of both parameters there is a good agreement between the capillary tube model and FLUENT at high resolution. All results converge towards about 55% permeability increase at the highest resolution. The relative change in permeability tends to decrease with finer resolution. This is partly explained as the opening of new flow paths should have less influence on the permeability if the background permeability is lower. However the magnitude of this effect is surprisingly high. Naturally it is expected that the results obtained at the finer resolution would be more accurate, thus for the rest of the study were only considered the relative change in permeability obtained with FLUENT at the finest resolution. These results were compared with the experimental values.



**Figure 4.31** Increase in permeability after calcite dissolution calculated with FLUENT (dashed lines), Equation 4.2 (empty symbols) and Equation 4.3 (filled symbols).

#### 4.4.2 Comparison of the calcite dissolution case with experimental observations

The comparison of the simulation results with the experiments showed that the numerical approach was only partially successful. First the accuracy of the permeability prediction in term of absolute value was poor as it was found that the permeability was overestimated by several orders of magnitude. This seemed to be related to the model resolution and the fact that some property of the pore space likely expressed itself at a length scale smaller than 2.5 μm and had a major impact on the permeability. Based on SEM observations it seems likely to be the small silica fragments filling the pore throats. On average the silica fragments brighten the pore space slightly at the resolution of the CT scans. This is however not enough to make them distinguishable from the background and as a result they were simply counted as pores during the segmentation process. In reality those fragments would largely impeach the flow. Looking back at Figure 4.3 that present the pore segmentation process it is clear that the pores seems to be filled with salt-pepper noise on the original images but then appear as clean voids in the segmented image. On a side note, since the final porosity was manually enforced, neglecting those fragments lead to slightly thinner pores on the segmented image.

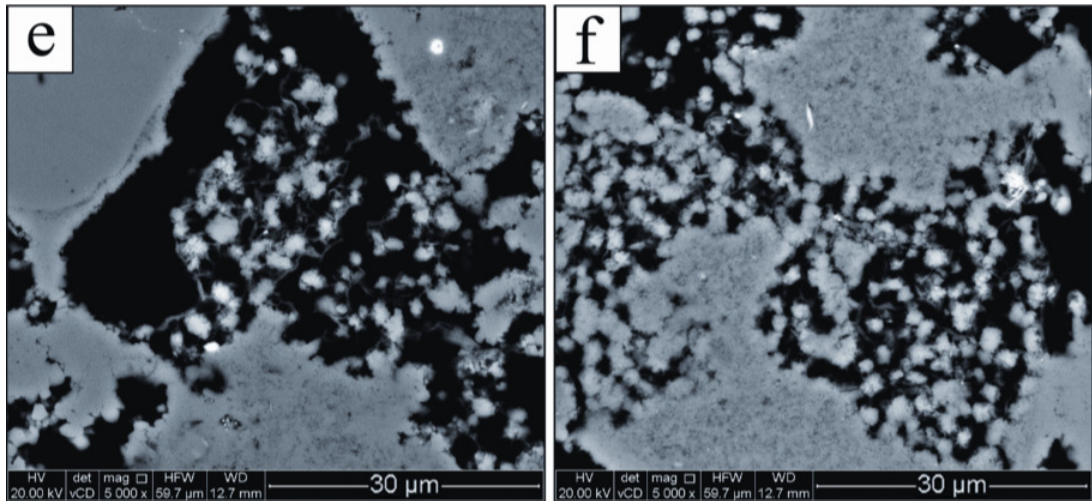


**Figure 4.32** SEM images (Lower part of Figure 3.3) presenting silica fragments filling the pores before and after calcite dissolution experiments (left and right).

Comparing the relative change in porosity with calcite dissolution the agreement is much better. Some arguments were developed in favor of the numerical approach to simulate calcite dissolution effect on permeability and indeed it seems to provide some meaningful information. It appeared during this study that there is a second order effect depending on the resolution that affects the prediction. Taking the higher resolution result for all models as a best guess the agreement with the experimental results is certainly much better than the one using K-C equations (presented in Chapter 3).

This is somehow unfortunate that the K-C equation underestimate the permeability increase by such a large amount for  $n=3$  since this is this exponent value that would be used by default for a sandstone with a porosity of 30%. The FLUENT results for A1, B1 and B2 in the pore dilatation case are an increase in permeability by 100%, 123% and 125% respectively (not on the plot). A power exponent above 7 could potentially agree with these results however a large set of experiments would be necessary to determine this value. The alternative method presented here would consist in determining the model tortuosity and mean hydraulic radius therefore going back to the root of the K-C theoretical framework before these parameters are lumped into the  $n$  exponent parameter. However this method also has its limits mainly due to the fact that the mean hydraulic radius is not a very meaningful parameter. In definitive, even the pore dilatation case which is most suited to the K-C equation it appears that the FLUENT approach is fundamentally better. For the calcite dissolution case the K-C theory is not at all adapted since it considers that the pores can be represented as fixed tortuous capillaries that can vary in width and tortuosity. In reality new

“capillaries” are created when calcite dissolves. Despite the agreement with Equation 4.3 and FLUENT results (Figure 4.31), doubts remain on the validity of this equation. The analysis conducted above concluded in a net contribution of the mean hydraulic radius and the tortuosity of about 40% and 10% respectively to the total permeability increase. But is it meaningful to consider the increase in the mean hydraulic radius when isolated calcite fragments dissolve? Given the pore network configuration it seems more likely that some tortuosity contribution was mistaken as a mean hydraulic radius one. If calcite grains were twice thinner, the permeability of the voids created by the calcite removal would still be orders of magnitude higher than the other flow paths leading to an almost identical permeability increase. It is definitely possible that in case of heterogeneous dissolution the permeability does not scale linearly with the tortuosity. For example a permeability dependence on the tortuosity power 4 would fit the FLUENT results as well. Again it seems that the FLUENT approach is fundamentally better as it makes direct use of the complex pore network instead on relying on possibly erroneous constitutive equations. Moreover those constitutive equations rely on parameters only available through 3D model analysis hence supposing that models are available for pore scale simulations. Finally this study showed that the pore scale simulation approach was successful despite the inaccuracy of the models and there is ground to believe that this was not a mere lucky coincidence. This is due to the fact that the permeability change depends more on the creation of large isolated flow paths (well resolved) than on the absolute permeability (poorly resolved). This idea is explicated in Figure 4.34.

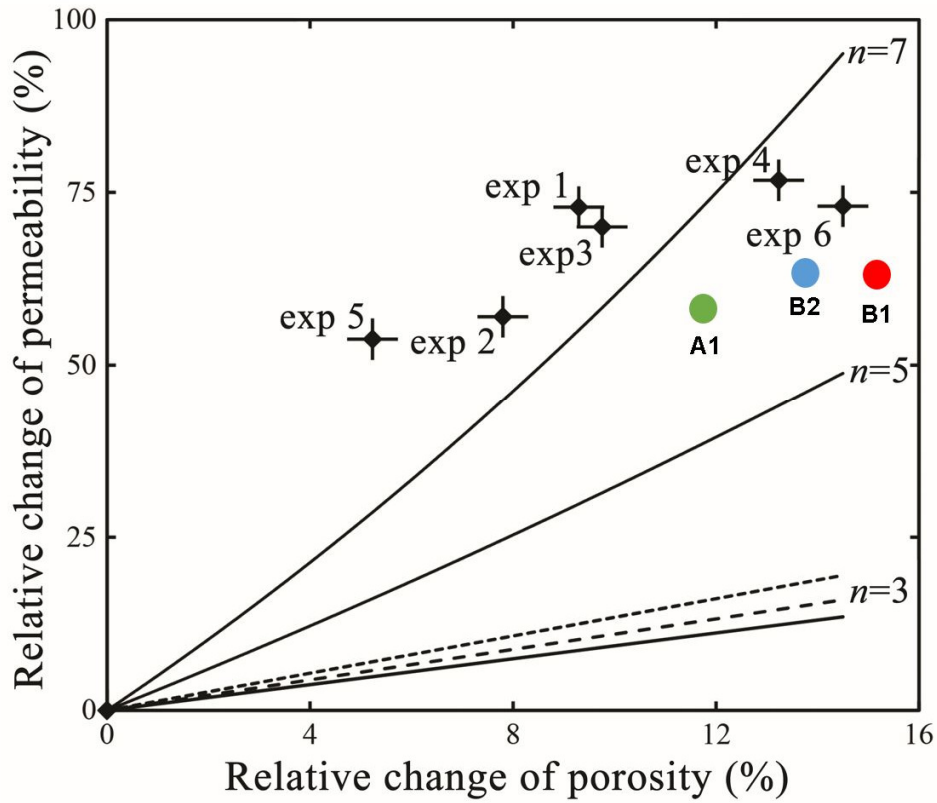


**Figure 4.33** Comparison of the change in permeability after calcite dissolution determined with core scale experiments (6 crosses), FLUENT simulations (disk symbols) and K-C equation (curves)

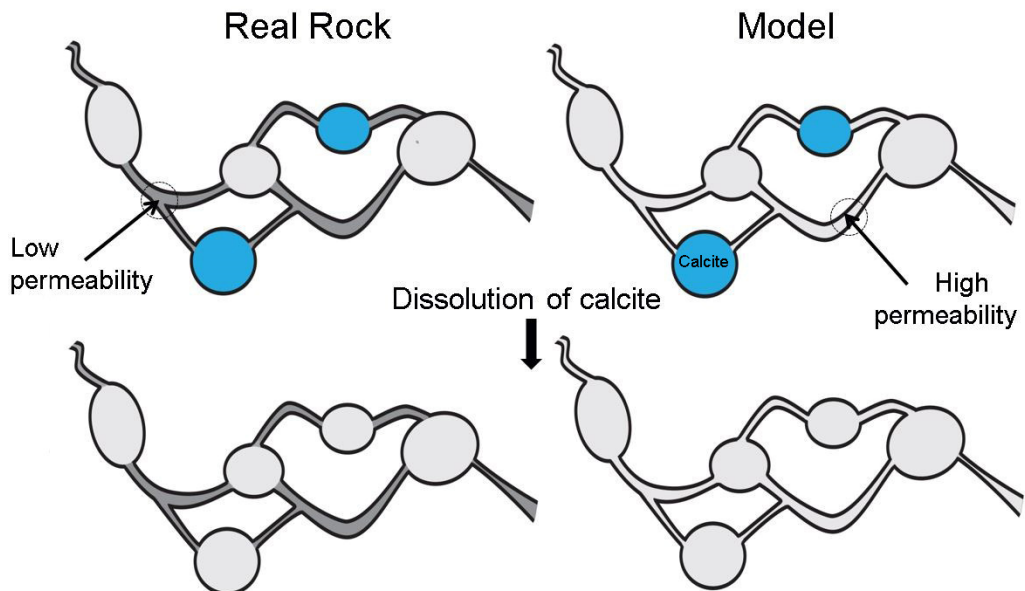


**Figure 4.34** Conceptual rock model summarizing observations made on the model ability to correctly capture calcite dissolution features but overestimating absolute permeability. When large, well resolved dissolution features are created the model can capture the relative change in permeability. However the model cannot capture small features controlling the absolute permeability (dark grey paths).

## 4.5 Conclusions

A new methodology to calculate the permeability of a calcite bearing sandstone before and after calcite dissolution has been evaluated. The first order result of this study is that it is possible to successfully evaluate the relative changes in permeability that arise when there are changes to the porosity and pore network induced by CO<sub>2</sub> injection. This approach proved to be much more reliable than general equations such as the Kozeny-Carman relationship that are widely used today. This method is also very versatile as one can manipulate the models and test different variations of the initial pore network without having to perform time consuming experiments. At this stage experiments are however still necessary for validation. Computational power is an issue and even though a powerful HPC system was used, trading off the model size and simulation complexity was necessary in order to run about a hundred simulations in a reasonable time lapse (about 20 days).

The very large overestimation of the absolute permeability initially came as a surprise given the numerous claims made in previous publications about successful attempts to predict permeability from CT images at even coarser resolutions and with smaller models. Upon closer examination it seems very likely that these success were due to the fact that the rocks under study had very large permeability and were very clean sandstones such as the popular Fontainebleau sandstone when they were not simply synthetic materials (see review from Blunt (2013) and references herein). One way to solve this anomaly in this study could be to perform multi-scale analysis where low permeability material would be imaged separately at the nanoscale resolution for example using FIB-SEM technique. For instance the low intensity regions in the CT scans could be labeled as “silica fragments” and attributed a very low permeability evaluated separately.

Several areas would profit from an increase in brute force computing power. First maybe an increase in model size, mainly because of REV considerations. The larger model was composed of 400<sup>3</sup> voxels and model sizes of 1000<sup>3</sup> are at reach; although this would not lead to a significant increase in the physical size if we were to use adaptive mesh refinement. One other improvement would be to use periodic boundary conditions instead of wall conditions on the faces orthogonal to the inlet and outlet faces: this necessitate to simulate the flow in four additional mirrored meshes. Other directions of improvements could be the complexification of the simulated processes. Some examples are non-laminar single phase flow,

multiphase flow or reactive flow. Mechanical and thermal effects could also be taken into consideration.

The method presented here allows the upscaling of the calcite dissolution effect on permeability from the micron to the millimeter scale and by extension to the core scale given the very homogeneous nature of the rock studied. Further implications of calcite dissolution at the reservoir scale have been discussed in the conclusions of Chapter 3. One advantage of this method over experiments presented in Chapter 3 is the possibility to quickly evaluate the effect of dissolving slower reacting minerals such as silicates.

## **Chapter 5**

### **The effect of CO<sub>2</sub>-enriched brine injection on the mechanical properties of calcite bearing sandstone.**

#### **5.1 Introduction**

It is essential to understand the mechanical properties of reservoirs and the surrounding rocks to plan and conduct GCS operations. This is because mechanical properties affect various aspects of the injection such as seismic monitoring surveys, maximum safe injection pressure, reservoir deformation, and so on. In this context two properties of interest are the rock sonic velocity and the rock strength (yield and peak strengths). These rock properties have been extensively studied on various occasions but there is very little literature on the impact of CO<sub>2</sub> injection and possible fluid-rock interactions on these properties.

First, basic concepts of rock mechanics and their relevance to GCS operations are reviewed. In a second section, results obtained with Cayton Bay sandstone cores are used to illustrate some actual effects of fluid rock interactions on mechanical properties. This sandstone, and the calcite dissolution experiments conducted on it have been introduced in previous chapters. The same technique was used to dissolve calcite from cores that were then subjected to series of sonic velocity and strength experiments.

The initial aim of the study was to investigate the impact of pore fluids alone on the P and S wave velocities ( $V_p$  and  $V_s$ ) and to test the applicability of the Gassmann theory (Gassmann, 1951) for the influence of fluids on sonic velocity. The effect of calcite dissolution on sonic velocity is then compared with the effect of CO<sub>2</sub> replacing brine. This is particularly useful to evaluate the reliability of seismic surveys taking only into account fluid substitution but not geochemical effects. Finally the effect of calcite dissolution on rock strength is investigated.

#### **5.2 Sonic velocity measurements**

##### **5.2.1 Basic concepts**

Seismic exploration aims to identify and quantify pore fluids, porosity and the lithology of reservoirs from their seismic velocity and impedance. Seismic exploration techniques are varied: bright spot evaluation, amplitude versus

offset (AVO) analysis, log interpretation, travel time analysis, phase variations analysis, 4D monitoring and others (Sheriff and Geldart, 1995).

V<sub>p</sub> and V<sub>s</sub> velocities of target reservoirs can be of great interest for exploration purposes. For instance Murphy et al., (1993) found that quartz sands always displayed a V<sub>p</sub>/V<sub>s</sub> ratio close to 1.5; this property can then be used as a primary lithology indicator (Domenico, 1984; Castagna and Backus, 1993). Other correlations between rock sonic velocity and specific petrophysical parameters like porosity are sometimes used to correlate lithological with geophysical data.

More advanced techniques such as AVO are well suited for mapping of reservoir fluids (Ostrander, 1984) while time-lapse seismology (i.e. 4D monitoring) is the most relevant technique to observe changes in fluid distributions during reservoir production (Calvert, 2005). 4D monitoring is based on the observation of changes in seismic properties and the results are displayed as difference maps compared to baseline values. Changes may be attributed to modifications of the fluid saturation and pressure, changes in the reservoir stress state or reservoir compaction. 4D seismic technology has progressed to become an essential tool for hydrocarbon reservoir monitoring (Meyer, 2001). Great improvements have been made in term of data acquisition and interpretation (Lumley, 2001). This progress makes the technology a potential tool to monitor CO<sub>2</sub> injection and displacement (Langan et al., 1997) for GCS, as CO<sub>2</sub> injection in underground reservoirs should in most cases trigger changes in seismic properties. Fine interpretation of 4D seismic surveys could provide additional information such as the change in reservoir pore pressure (Chadwick et al., 2012). The use or potential use of time lapse seismic monitoring for GCS is in fact well documented (Chapman et al., 2000; Arts et al., 2004; Brown et al., 2002; Li, 2003; Miller et al., 2004).

As for most physical properties, seismic properties in natural systems are affected by many factors. Rock frame properties such as porosity, mineralogy, pore type, clay content and grain size are the main rock intrinsic factors (Mavko et al., 2009). Statistically, porosity is the most important parameter affecting sonic velocity (Wang et al., 1991). There is also a very good correlation between velocity and rock density, see for instance Gardner's law (Gardner et al., 1974).

Beyond intrinsic rock properties, the most important parameter for sonic velocity is the pore fluid content. Pore fluids found in reservoirs have very variable seismic properties (Batzie and Wang, 1992; Vargaftik, 1975). Pore

fluids influence the seismic response of the fluid-rock system by modifying its density and bulk modulus. An important additional note is that rock and fluid seismic properties can both vary greatly with temperature and pressure.

For GCS, neglecting modifications of the rock frame and assuming stable pressure/temperature conditions the most important process modifying the seismic response is fluid substitution due to the injection of CO<sub>2</sub>. The effect of the fluid substitution on the seismic properties of the rocks will primarily depend on the porosity and on the compliance of the pores. As a general rule, rocks with higher porosity or softer rocks will show higher contrast in seismic properties during fluid substitution. The effect of fluid properties on the seismic properties of reservoir rocks can be modelled using the Gassmann and Biot equations (Gassmann, 1951; Biot, 1956a, b; Mavko and Jizba, 1991; Han and Batzle, 2004). However, these equations only address the mechanical aspect of the fluid substitution process and neglect the effects that fluids could have on the rock frame behavior, for example lubrication of grain joints when the rock becomes water saturated and the possible modifications of the rock frame, for example calcite dissolution upon CO<sub>2</sub> injection.

### **5.2.2 Experimental design and sample preparation**

A series of measurements have been made of the sonic velocities ( $V_p$  and  $V_s$ ) of cores of Cayton Bay sandstone. The experimental setup consisted of a universal triaxial cell instrumented for ultrasonic velocity measurement under variable fluid saturation conditions (Figures 5.1 and 5.2).

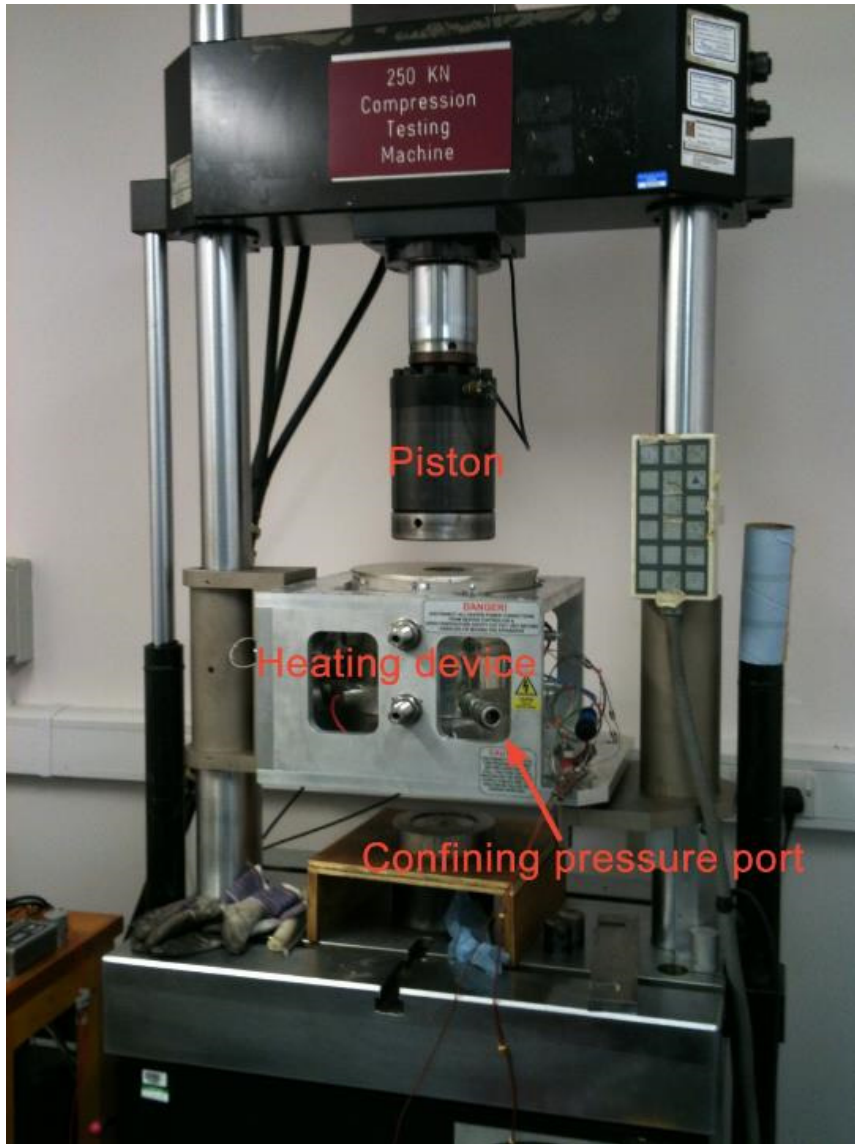


**Figure 5.1** Triaxial cell equipped with sample heater used for sonic velocity determination. The pump used to apply confining pressure had a large manual control valve (not on the picture).

The vertical press was programmed to perform an axial loading and unloading cycle while the lateral pressure was manually controlled with an external pump. A rubber sleeve was used to isolate the core samples from the pressurizing fluid. Isostatic conditions were maintained during all experiments and fluid pressure was changed between each measurement series to modify the effective pressure (effective pressure = confining pressure - pore pressure). Experiments were done at a temperature of  $50 \pm 2^\circ\text{C}$  (above the critical temperature of  $\text{CO}_2$ ) or at room temperature (about  $20^\circ\text{C}$ ). Pressure conditions were chosen to span a large range of relevant in-situ reservoir conditions.



**Figure 5.2** Steel platens placed on both sides of the sample inside the heater and used to generate sonic waves and to inject fluids.

Piezoelectric crystals mounted at the ends of steel platens (Figure 5.2) were used to generate P and S waves of 1 MHz and 0.7 MHz frequency respectively. A lead foil was used to improve the contact between the transducers and the samples. The transducers generated a compressional wave and two orthogonally polarized S waves that propagated in the vicinity of the core axis. The received signal was amplified, filtered and sent to a digital oscilloscope. The digitized signal was then sent to a personal computer where signal processing operations could be performed. The results presented here were obtained by collecting travel time data and converting it into velocity data. Travel time was determined manually on screen for the first peak (Figure 5.3) corresponding to the sonic wave arrival. Travel times were zeroed by doing a measurement with no rock core.

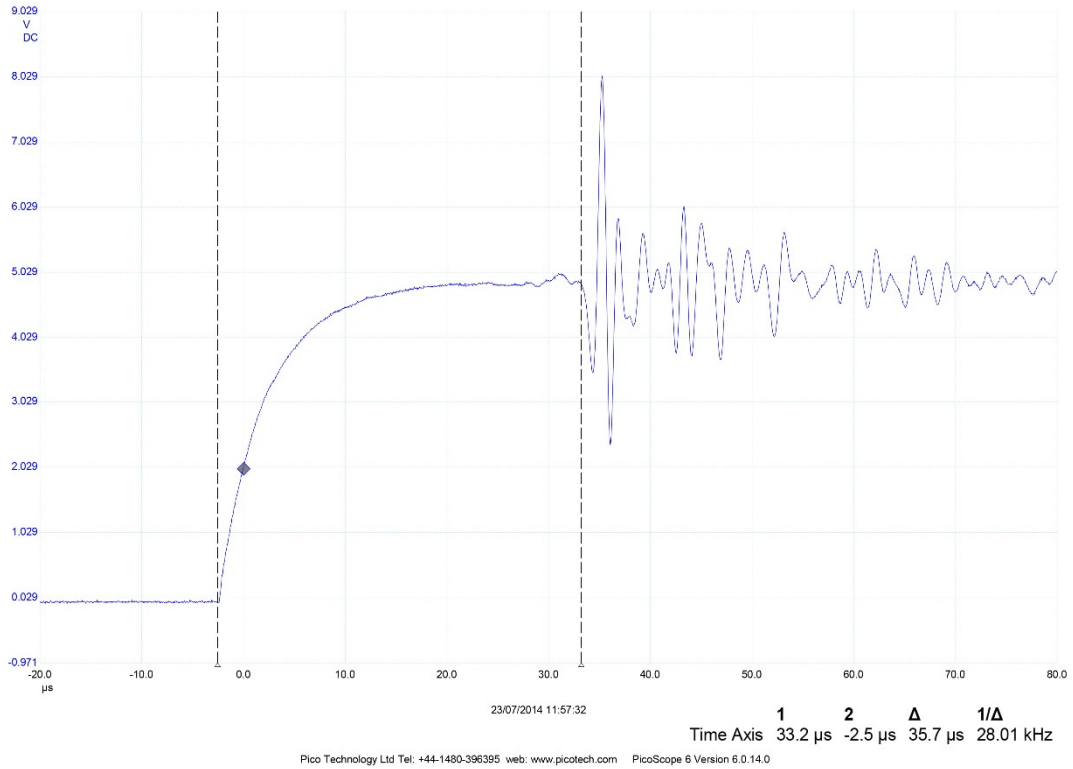


**Figure 5.3** Example of S wave manual travel time measurement.

As a general rule, the precision of the velocity measurement depends on the quality of the core preparation and on the velocity of the samples. Sharp and clear peaks are generally obtained for high velocity rocks and at high effective pressures. In the experiments, the effective pressure was chosen to be high enough to allow good signal transmission but low enough to prevent sample damage.

Cores were drilled with a diameter of 3.75 cm and cut to a length of 7.30 to 7.80 cm. The end surfaces were verified to be flat and parallel to enhance seismic signal quality. Cores were dried in an oven at 60°C for 48 hours before the first set of experiments. In some experiments the samples were saturated with CO<sub>2</sub> or brine under vacuum, the saturating fluids were then pressurized with an external pump and heated in the sonic velocity measurement apparatus (see Figure 5.1). All experiments were done in drained conditions (i.e. the system was not closed and the fluids were allowed to move in and out of the sample).

The pore pressure was varied between 500 and 4000 psi (3.4 and 27.5 MPa), 1 psi (pound per square inch) is equal to 6894.76 Pa which is approximately 0.069 bar. The confining pressure and axial load were varied between 1000 and 10000 psi (6.9 and 69 MPa) and were kept isostatic. The resulting effective pressure for each experiment was ranging between 500 and 6000 psi (3.4 and 41MPa). Table 5.1 present the experimental conditions

used to examine the effect of fluids, temperature and calcite dissolution on the sonic velocity.

**Table 5.1** Summary of sonic velocity experiments. All cores were drilled from the same sample block. Some cores were obtained by cutting a longer initial core in two (in that case they were numbered N.1 and N.2). Some cores were used for multiple experiments at various fluid saturation and fluid pressure conditions.

Core number	Porosity before calcite dissolution	Porosity after calcite dissolution	Saturation conditions	Experiments before and after calcite dissolution	Pore pressure range (psi)
2.1	32.8	36	Dry at T=20°C and 50°C	yes	N/A
3.1	32.5	34.2	Dry/CO <sub>2</sub> /Brine at T=50°C	yes	500-2000
3.2	34	38.5	Dry at T=50°C	yes	N/A
4.1	32.5	34.2	Dry/CO <sub>2</sub> at T=50°C	yes	2000-4000
4.2	35.5	N/A	Dry at T=20°C and 50°C	no	N/A

Differences in S1 and S2 shear waves are an indicator of rock anisotropy. The difference for Cayton bay sandstone is less than 0.3% meaning that the rock samples were fairly isotropic even though they were drilled parallel to the bedding (not orthogonal to rock layers). For simplicity, in the remainder of this chapter the average S wave velocity is reported. Similarly only the results obtained at a temperature of 50°C are reported, the effect of the temperature increase from 20°C to 50°C on dry rocks (experiments made on cores 4.2 and 2.1) have been found to be negligible.

### 5.2.3 Rock and fluid controls on velocity

A first series of measurements were done on sample 3.1 to evaluate the effect of effective pressure, pore pressure and fluid composition (either 1M NaCl brine or CO<sub>2</sub>) on sonic velocity.

The stress dependence of the rock sonic velocity is generally attributed to micro-cracks closing or opening and to interactions at the grain boundaries. Figures 5.4 and 5.5 present sonic velocity measurements made at various effective stress conditions through a confining pressure loading and unloading cycle and at various fluid saturation conditions. Those figures display the clear influence of the effective pressure on the sonic velocity with a consistent increase in velocity with effective pressure at all saturation conditions, tending to converge at the maximum confining/effective pressures. This effect is reversible since the velocity paths are the same during the loading and unloading cycles. In detail some transient hysteresis can be observed on the unloading paths which display slightly higher velocities. The low amount of hysteresis is a good indication that the samples were not damaged during loading and thus could be re-used for further experiments.

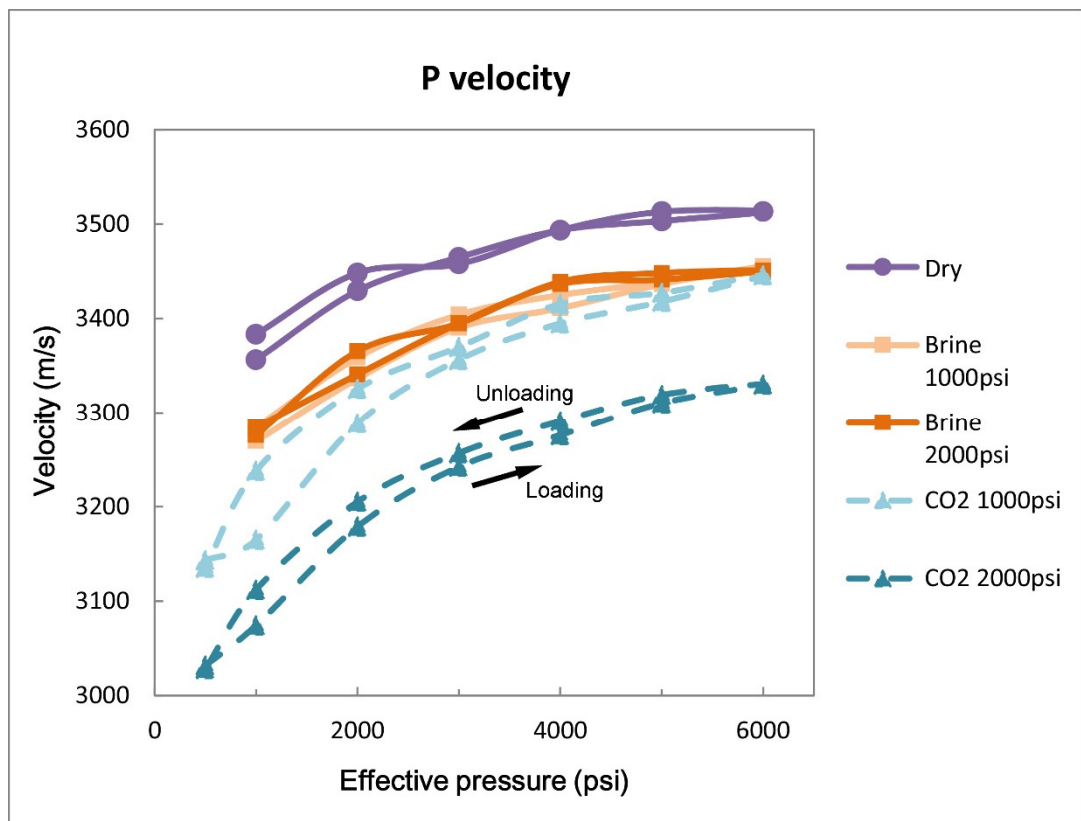


**Figure 5.4** Effect of fluid composition and pressure on the P wave velocity of sample 3.1.

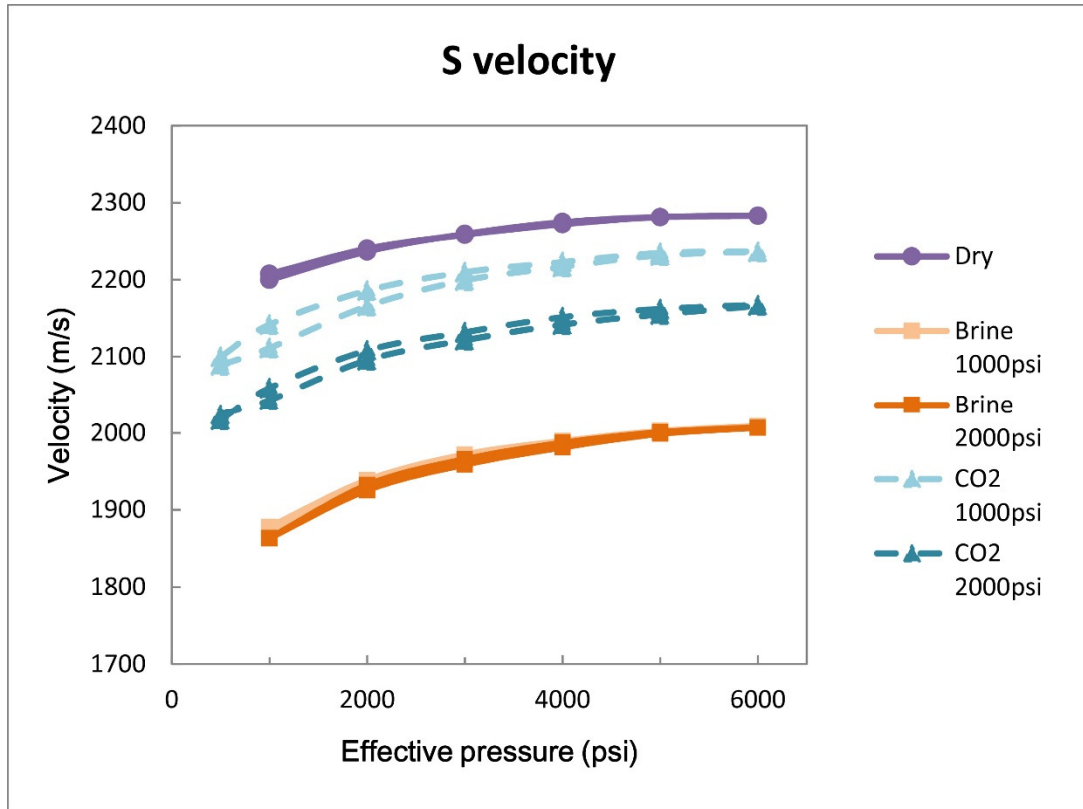


**Figure 5.5** Effect of fluid composition and pressure on the S wave velocity of sample 3.1.

On Figures 5.4 and 5.5 the effect of different fluids on seismic velocities is very clear although the interpretation can be ambiguous for the P wave since two opposite effects act on the rock-fluid system. First the fluid increases the system density  $\rho$  with regard to the dry rock baseline value thereby reducing P and S wave velocities (Equation 5.1). Secondly the fluid increases the bulk modulus  $K$  of the system thereby increasing the P wave velocity. The effect of fluid on the shear modulus  $M$  of the system should be limited or even absent assuming that Gassmann theory assumptions are valid. Variation in fluid pressure (at a given effective pressure) only influences the seismic velocity in the CO<sub>2</sub>-saturated case. This is expected since CO<sub>2</sub> properties such as bulk modulus and density are highly dependent on pressure in the experimental temperature-pressure range while brine properties are not.

$$V_p = \sqrt{\frac{K + \frac{4}{3}M}{\rho}}$$

$$V_s = \sqrt{\frac{M}{\rho}} \quad (5.1)$$

For this set of experiments, the fluid effect on the system density dominates and all velocities under fluid saturated conditions are lower than in the dry

case. The effect of increasing fluid density on  $V_s$  is particularly visible since the shear modulus is only slightly affected by the different fluids.  $\text{CO}_2$  density increases with pressure while brine density is almost unchanged and as a result  $V_s$  in  $\text{CO}_2$ -saturated cores decreases gradually with increasing  $\text{CO}_2$  pressure and is predicted to reach a lower limit at the value for brine saturation, which is effectively independent of fluid pressure (Figure 5.5).

The pattern is different for the P wave velocity where the velocity decrease does not follow the density trend. This is due to the fact that the bulk modulus of brine is several orders of magnitude higher than that of  $\text{CO}_2$  and is sufficient to counterbalance the effect of density on the velocity (Figure 5.4).

The  $\text{CO}_2$  effect is similar for both the P and S wave velocities and results from the density change of the system. The bulk and shear moduli remain dominated by the rock. As a result the ratio of  $V_p/V_s$  is very close to the dry case and does not vary for different  $\text{CO}_2$  pressure conditions. In contrast, saturation with brine not only affects the density of the core but also the bulk modulus so that the P wave velocity decreases by less than the S wave velocity. As a result the  $V_p/V_s$  ratio is significantly higher when the rock is brine saturated and this can be a very good indicator of fluid substitution (Figure 5.6).

In a  $\text{CO}_2$  injection scenario, the reservoir would be initially filled with brine and  $\text{CO}_2$  saturation would progressively increase. Additionally, in regions close to the well the pore pressure could increase slightly which would reduce the effective pressure. In this scenario,  $V_p$  would decrease with increasing  $\text{CO}_2$  saturation,  $V_s$  would increase and  $V_p/V_s$  would therefore decrease.  $V_p/V_s$  is a less ambiguous indicator of the fluid substitution since it does not depend on the density change (Equation 5.1) and is relatively insensitive to changes in effective pressure (Figure 5.6).

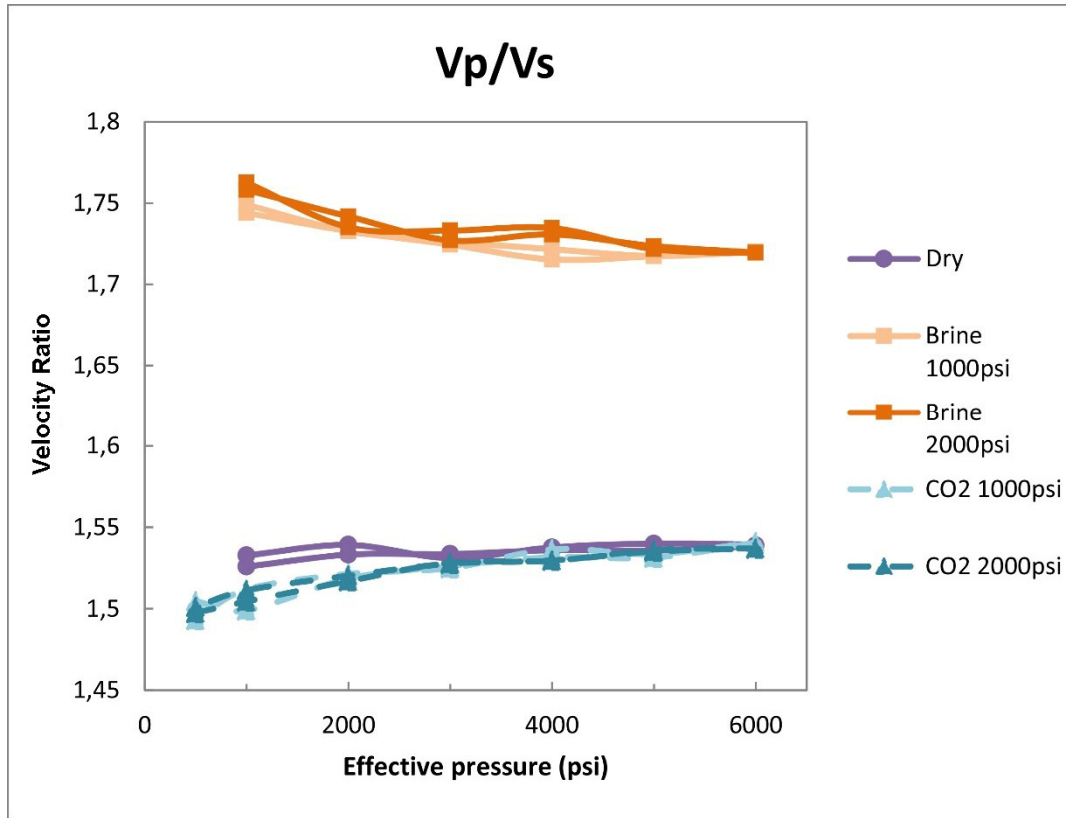


**Figure 5.6** Fluid saturation and pressure effect on the Vp/Vs ratio of sample 3.1.

Having evaluated the effect of a fluid substitution for the Cayton Bay sandstone it is possible to determine whether the Gassmann model can make accurate predictions since it is often cited as the reference model used to monitor fluids saturation underground. Care should be taken during this analysis as the wave frequency domain of application of the Gassmann theory is as close to 0 as possible and high frequency measurements were done in this study.

#### 5.2.4 Gassmann modelling of fluid substitution.

The Gassmann equation has been used to predict the change in sonic velocity caused by changes in fluid saturation. According to these equations the bulk and shear moduli of a fluid saturated rock can be calculated with the separate mechanical properties of the dry rock and fluid:

$$K_{sat} = K_{dry} + \frac{\left(1 - \frac{K_{dry}}{K_m}\right)^2}{\frac{\phi}{K_{fl}} + \frac{1-\phi}{K_m} - \frac{K_{dry}}{K_m^2}}$$

$$M_{sat} = M_{dry}, \tag{5.2}$$

where  $K_{sat}$ ,  $K_{dry}$ ,  $K_m$ , and  $K_{fl}$  are the bulk moduli of the saturated rock, dry rock, mineral composing the rock and saturating fluid respectively;  $M_{sat}$  and

$M_{dry}$  are the shear moduli of the saturated and dry rock;  $\phi$  is the rock porosity.

For  $K_{dry}$  the experimental data obtained on sample 3.1 was employed,  $K_m$  was calculated using the Voight-Reuss-Hill average (Hill, 1952) from the data shown in table 5.2.

**Table 5.2** Mineral bulk moduli and volume fraction used for the calculation of the  $K_m$  parameter.

Mineral Name	Volume fraction%	Bulk Modulus (GPa)
Quartz	76	37
Microcline	6	37
Mica	6	50
Calcite	5	77
Smectite	4	20
Kaolinite	1	1.5
Dolomite	1	95
Albite	1	76
<b>Voigt Average</b>		<b>30</b>
<b>Reuss Average</b>		<b>39</b>
<b>VRH Average</b>		<b>34.5</b>

$K_{fl}$  for CO<sub>2</sub> and brine were calculated from speed of sound equations of Span and Wagner (1996) and Batzle and Wang (1992) for CO<sub>2</sub> and brine respectively. For the Gassmann modelling the rock density was taken as 1780 Kg/m<sup>3</sup>, porosity as 32.5% and  $K_m$  as 34.5 MPa (these are averages over all Cayton Bay rock cores); other parameters used for the modelling are shown in table 5.3. The shear modulus of the fluid-rock system is assumed to be equal to that of the dry rock frame since CO<sub>2</sub> and brine have no shear strength under liquid and supercritical conditions (Equation 5.2).

**Table 5.3** Fluid properties used for the Gassmann modelling

Fluid saturation	Pore pressure (psi)	Fluid density (Kg/m <sup>3</sup> )	System density	Fluid bulk modulus (GPa)
CO <sub>2</sub>	1000	168	1835	0.009
CO <sub>2</sub>	2000	666	1996	0.073
CO <sub>2</sub>	3000	793	2038	0.176
Brine	1000	1026	2113	2.65
Brine	2000	1026	2113	2.69
Brine	3000	1026	2113	2.72

Figures 5.7 and 5.8 present both experimental and theoretical values for the bulk and shear moduli. Equation 5.3 was used to derive the experimental values, this set of equations is obtained by rearranging Equation 5.1.

$$K = \rho \left( V_p^2 - \frac{4}{3} V_s^2 \right)$$

$$M = \rho V_s^2 \tag{5.3}$$

The agreement is remarkably good, although in detail the calculated bulk and shear moduli are constantly higher than the experimental ones. It is often claimed that incorrect use of the Gassmann theory would lead to an underestimation of the bulk modulus, either because the theory does not take into account ultrasonic viscous fluid effects or because the  $K_{dry}$  input parameter was not obtained under irreducible water saturation but under “over-dried” and thus stiffer rock conditions. Here high frequency or “over-drying” effects probably did not affect the bulk modulus significantly since the theoretical values are higher than the experimental ones and that experimental velocities are higher in dry conditions (Figures 5.4 and 5.5)

One likely explanation for the overestimation of the bulk modulus is that the fluids had a weakening effect on the rock frame, sometimes referred as “lubrication”. Weakening of the rock due to “lubrication” is a particularly strong hypothesis to explain the overestimation of the shear modulus and the fact that the saturated shear modulus is lower than the dry one, especially in the brine case which has higher wettability than the CO<sub>2</sub>. Further observations are that the “lubrication” effect is somehow mitigated for the bulk modulus in the brine case (probably due to the especially high

brine bulk modulus) but that it does not seem to depend a lot on the fluid pressure under our experimental conditions.

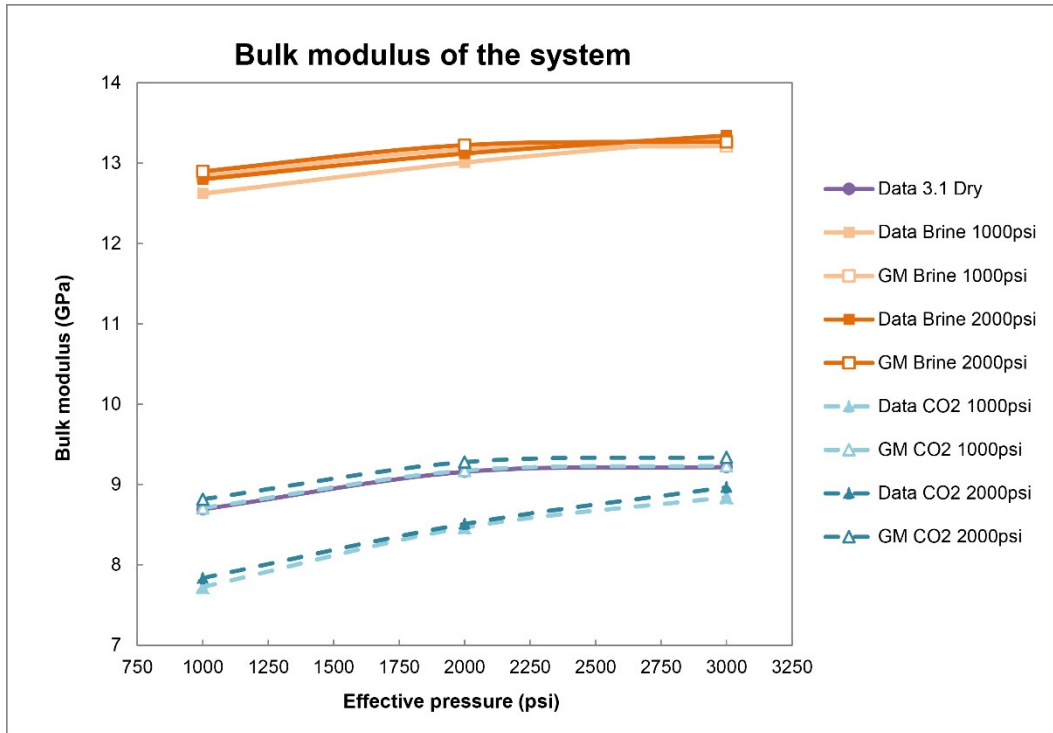


Figure 5.7 Comparison between Gassmann prediction (GM) and experimental data for the bulk modulus of sample 3.1.

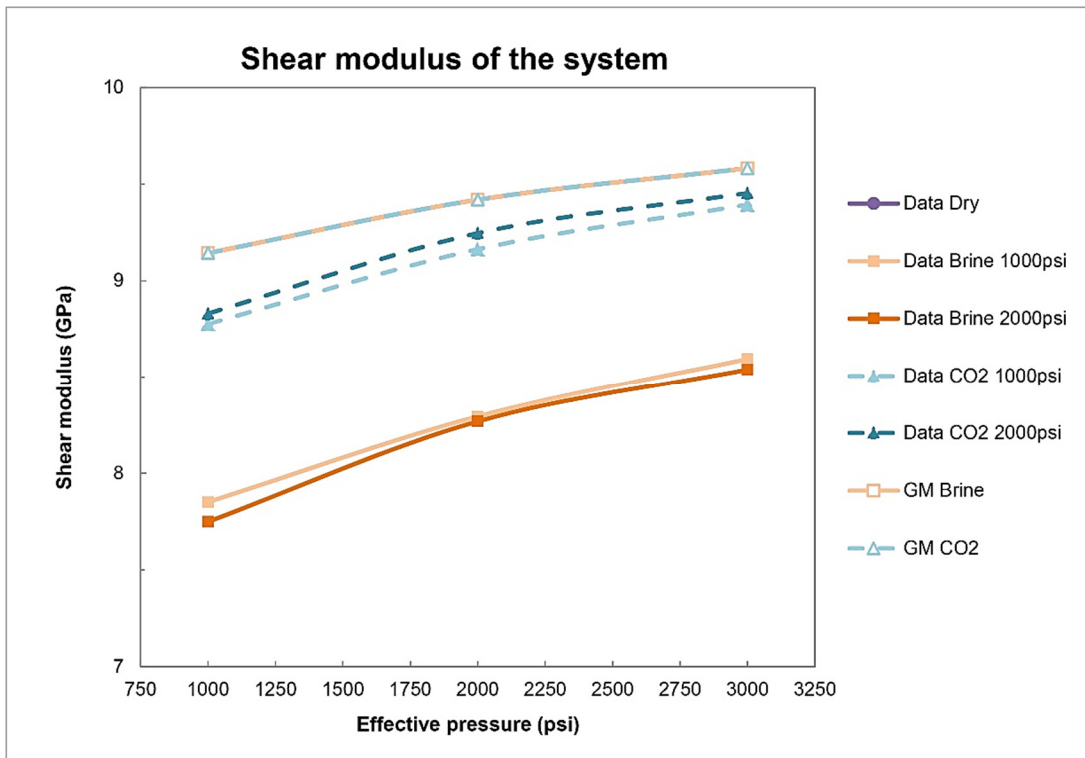
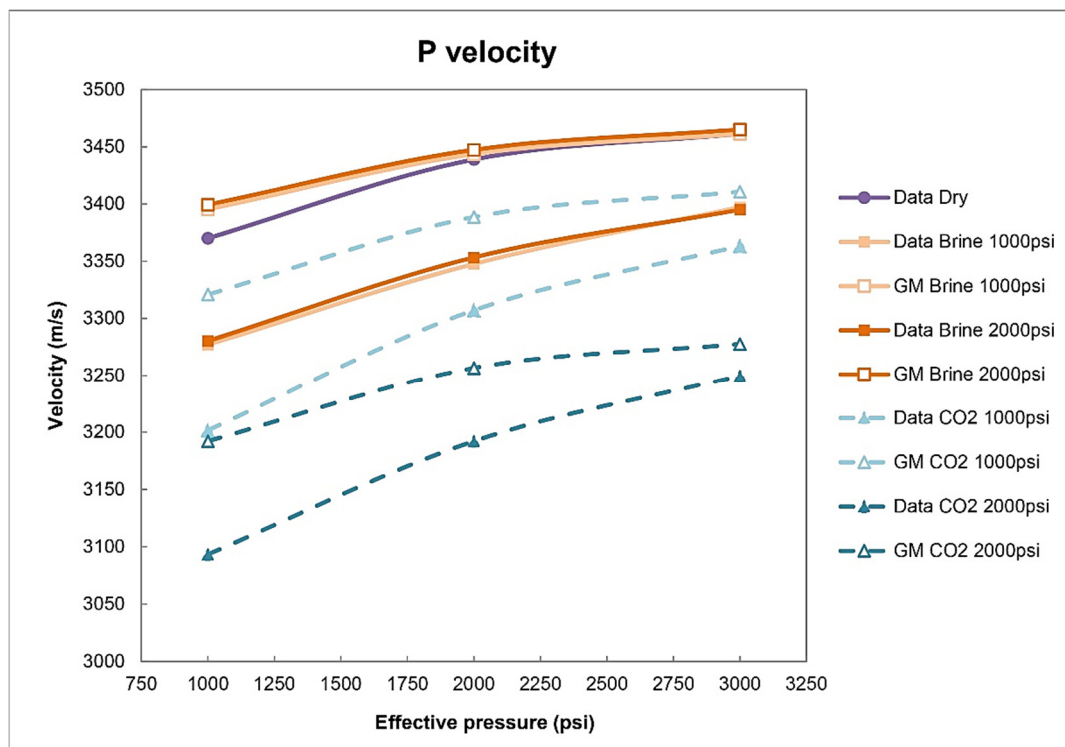


Figure 5.8 Comparison between Gassmann prediction (GM) and experimental data for the shear modulus of sample 3.1.

The difference between the experimental and theoretical values of the bulk and shear moduli probably account for discrepancies between theoretical and experimental Vp and Vs data (Figures 5.9 and 5.10).

P wave velocity is overestimated by about 3%, which is a direct consequence of the bulk and shear moduli overestimation. Similarly, the S wave velocity is also overestimated by a few percent. The agreement is generally good for the S wave data since the only source of error is the “lubrication” effect that has a relatively low impact on the shear modulus in the CO<sub>2</sub>-saturated case and a moderate impact in the brine saturated case. Overall the agreement is very good for the CO<sub>2</sub> case, less good for the brine case due to more significant lubrication of the rock frame.

Also visible is a small difference in stress sensitivity (curves slope) between theory and experimental data (Figures 5.9 and 5.10). The theoretical stress sensitivity is almost the same under fluid saturation and dry. The experimental data however show a slight increase in stress sensitivity as fluids are introduced. One possible reason for this is that the experiments were done in drained conditions rather than in a closed system and more importantly they were done at ultrasonic frequencies, hence violating two of the Gassmann theory assumptions. In these conditions it is possible that rock stiffening due to high frequency viscous fluid effects would increase with effective pressure since the rock framework would become tighter, thereby increasing the velocity sensitivity to effective stress.



**Figure 5.9** Comparison between Gassmann prediction (GM) and experimental data for the P wave velocity of sample 3.1.

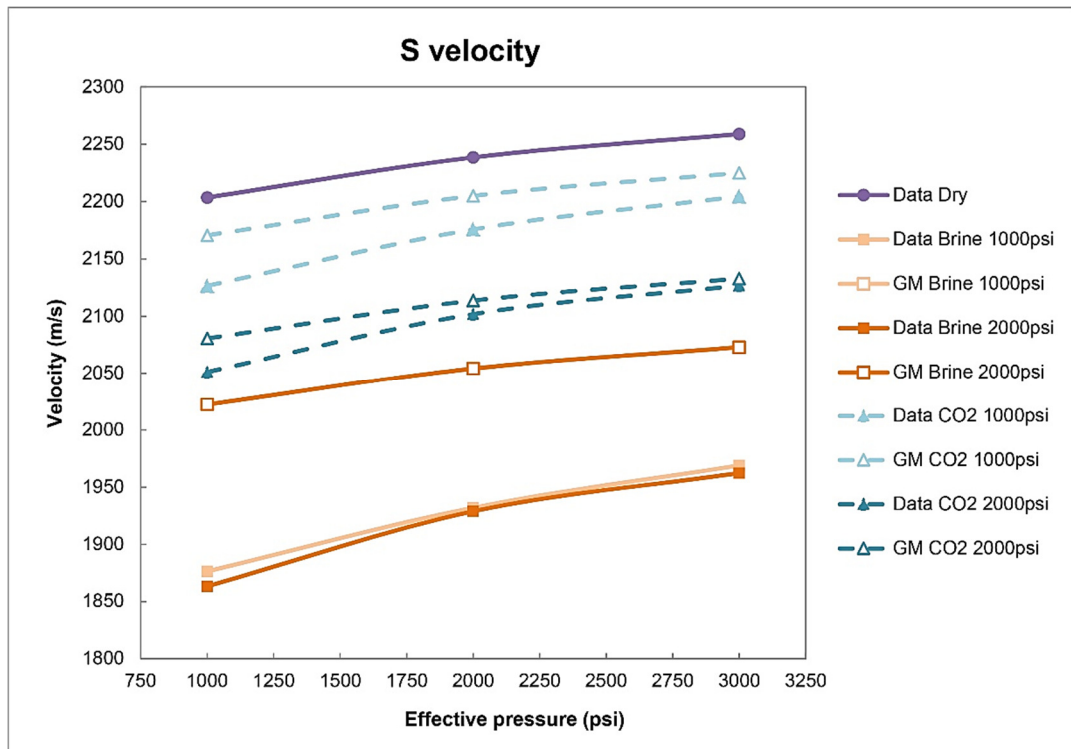


**Figure 5.10** Comparison between Gassmann prediction (GM) and experimental data for the S wave velocity of sample 3.1. Note: Gassmann predictions are almost identical for brine saturation at 1000 and 2000 psi.

The value of the calculated  $V_p/V_s$  ratio as an indicator of fluid substitution is retained using theoretical predictions (Figure 5.11) since the shear and bulk moduli are both overestimated in a similar fashion. In detail, the theoretical  $V_p/V_s$  ratio for the brine case is underestimated since  $V_p$  is less underestimated than  $V_s$ . This is due to the fact that the “lubrication error” has a smaller effect on the system bulk modulus compared to the shear modulus (because brine has a high bulk modulus). This is not true in the  $CO_2$  case where the error on the bulk modulus is larger than on the shear modulus, the theoretical  $V_p/V_s$  ratio in the  $CO_2$  case is therefore slightly overestimated. These errors do not compensate each other but are small with respect to the uncertainty on some of the parameters used in this analysis. For instance using a larger  $K_m$  of 55 MPa would reduce the underestimation of  $V_p$  and would significantly improve the fit between the Gassmann equation and the experimental data. Generally  $K_m$  is the least known parameter and is often used as a fitting variable.

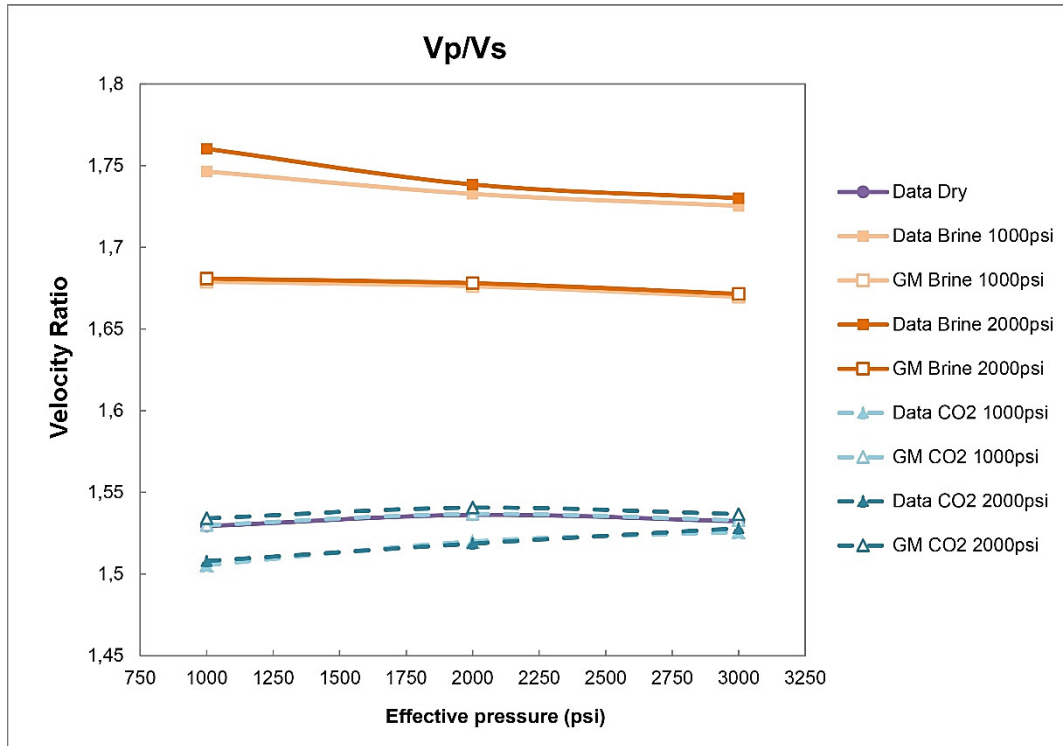


**Figure 5.11** Comparison between Gassmann prediction (GM) and experimental data for the  $V_p/V_s$  ratio of sample 3.1.

In conclusion this analysis justifies the use of the Gassmann theory while illustrating its limitations. The main source of error is the lubrication effect that reduce both the rock incompressibility and shear strength. This should not compromise a  $CO_2$  monitoring operation since the error in velocity is both on  $V_p$  and  $V_s$  so that the ratio  $V_p/V_s$  is still a very good indicator of the fluid saturation.

At this point it is essential to evaluate another potential source of uncertainty that was not addressed in this analysis: the effect on velocity interpretation introduced when fluid-rock reactions modify the rock framework. The following section considers the calcite dissolution effect on sonic velocity for the Cayton Bay sandstone.

### 5.3 Sonic velocity measurements on reacted and unreacted cores

#### 5.3.1 Fluid-rock reaction effects on sonic velocity

Fluid rock interactions can modify various physical properties of rocks. For example carbonate velocity data shows that diagenetic processes can modify mechanical properties in complex and various ways (Anselmeti and Eberli, 1993). The large variations observed cannot be explained simply by mechanical processes like compaction and hence classical correlation

equations like the “time average equation” (Wyllie et al., 1962) that link  $V_p$  to the absolute value of the porosity alone, cannot be valid. These processes can occur on relatively long time scales and so far geochemical interactions have largely been neglected in mechanical analysis of reservoirs in the context of GCS.

Recently, Vanorio et al. (2011) studied salt precipitation and carbonate dissolution effects in limestone and concluded that they were significant for modelling and interpreting 4D seismic signals. Vanorio and Mavko (2011) also found that calcite dissolution enhanced porosity and softened grain contacts but that the resulting rock compaction can mitigate this effect by closing low aspect ratio pores and compressing cement present at grain contacts, resulting in a decrease in the calcite reactive surface area and hence the dissolution rate.

The hypothesis that geochemical effects could be significant is appealing since some inconsistencies between measured and predicted velocities have been observed at GCS sites. For example, a larger than expected velocity decrease upon  $\text{CO}_2$  injection was observed at Frio (Daley et al., 2008). In particular the S wave velocity decrease could indicate a change in the rock frame as this parameter is relatively insensitive to changes in pore fluids.

Irrespective of fluid flow and heterogeneity control on the amount of fluid rock reactions, a change in baseline transport and mechanical properties is very likely in reservoirs containing carbonates (see Chapter 3). More experiments are necessary to evaluate the impact on seismic properties to calibrate models and help correct interpretation of time-lapse seismic surveys.

### **5.3.2 Calcite dissolution effect for the Cayton Bay sandstone**

Four experiments have been conducted on dry cores to evaluate the change in sonic velocity after calcite dissolution. The cores were drilled in the same Cayton Bay sandstone block used for permeability experiments described in Chapter 3. As previously described, this rock contained shell fragments accounting for about 5% of the rock grain volume. Once calcite dissolution was shown to have a significant effect on the transport properties of the rock the study was extended to the mechanical properties.

All samples were initially dried and a sonic velocity measurement was taken. The samples were then placed in a flow-through reactor apparatus and flushed with  $\text{CO}_2$  -enriched water until all calcite was removed. The amount of acidified fluid necessary for this operation had been evaluated in the

previous permeability studies (Chapter 3). Water instead of brine was used to avoid salt precipitation at the next drying step. After the dissolution, the samples' porosity was measured and a new sonic velocity measurement was performed. Changes in absolute sonic velocity of the samples are shown in Figures 5.12 and 5.13.

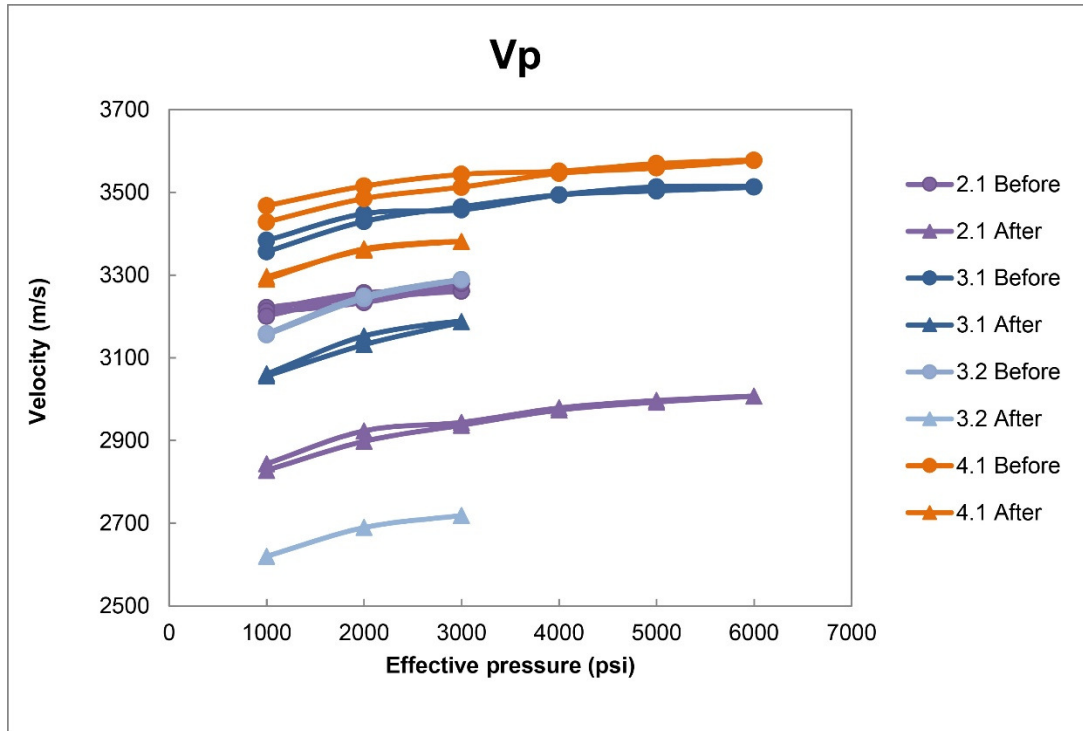


**Figure 5.12** Comparison of P wave velocity before and after calcite dissolution for 4 samples.

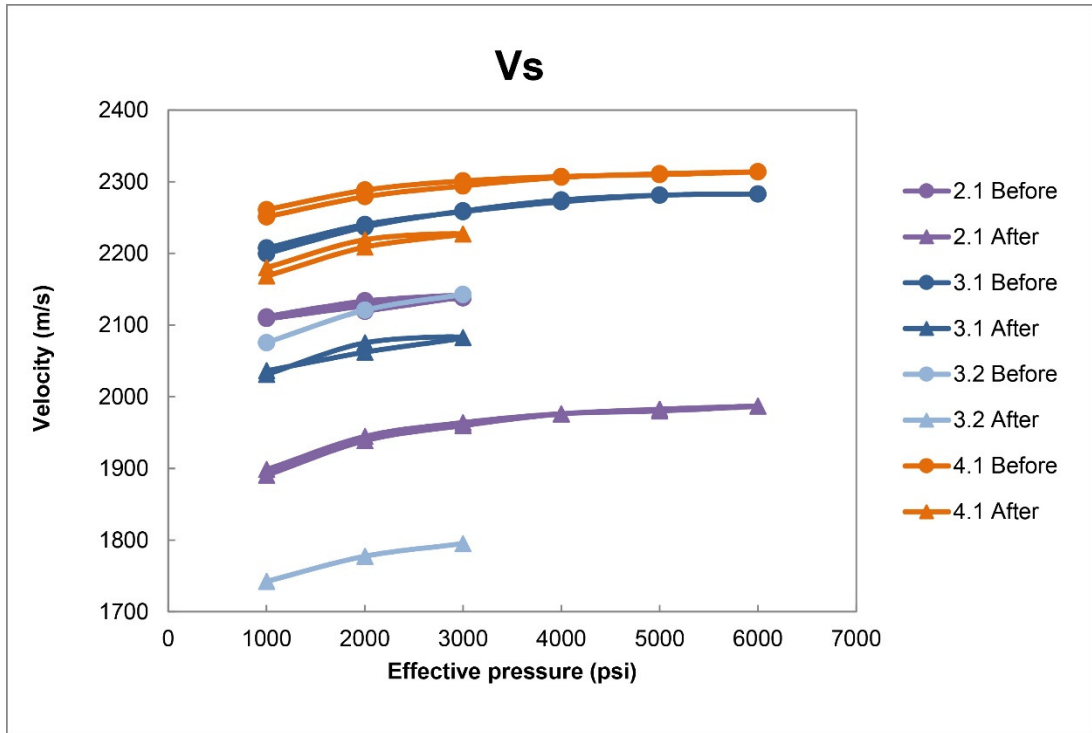


**Figure 5.13** Comparison of S wave velocity before and after calcite dissolution for 4 samples.

The first striking feature is the large variability in initial sonic velocities. A second observation is that all samples display a significant velocity decrease after calcite dissolution. This decrease in sonic velocity applied to  $V_p$  as well as to  $V_s$  so that the ratio  $V_p/V_s$  was left relatively unchanged (Figure 5.14).

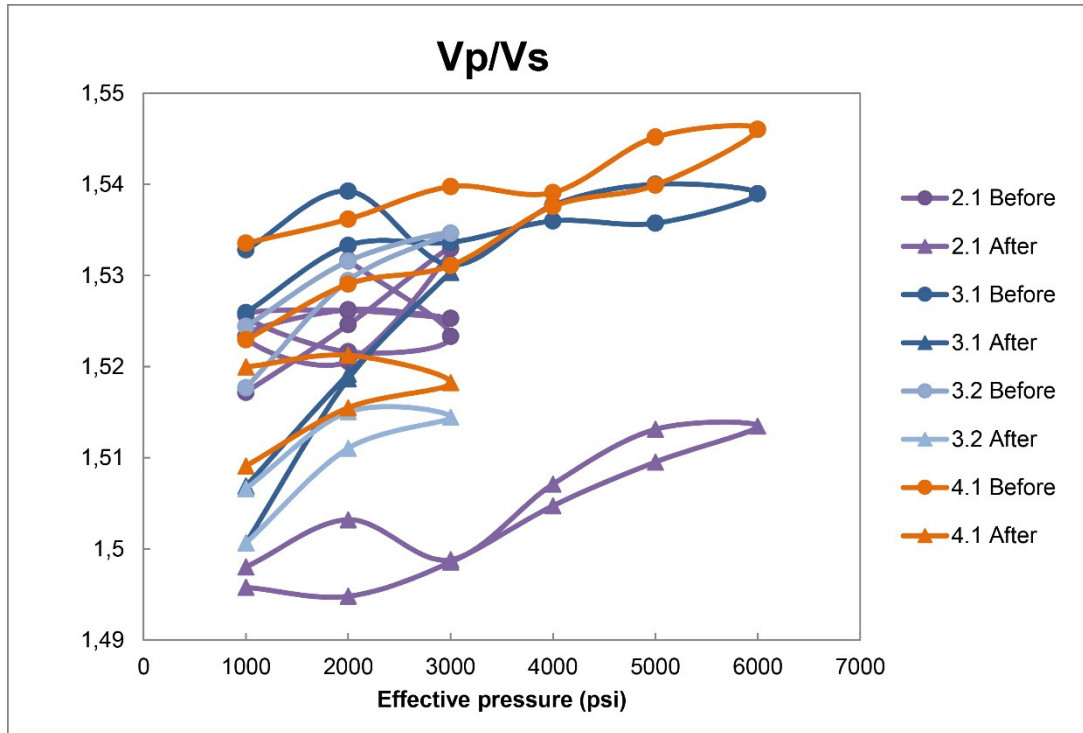


**Figure 5.14** Comparison of Vp/Vs ratio before and after calcite dissolution for 4 samples.

The analysis of the change in bulk and shear moduli calculated from sonic velocity data reveal that both parameters were reduced to 80% of their initial value on average. Variations in the dissolution effect can be observed: firstly it appears that the dissolution effect can be mitigated if the effective pressure is increased (Figures 5.15 and 5.17). Secondly, the dissolution effect at constant effective pressure can be reduced if the effective pressure is increased (Figures 5.16 and 5.18); this seems logical as the newly-created voids are likely to be more compliant and therefore be prone to closing when the confining pressure increases. Thirdly, the magnitude of the decrease in the rock moduli varies from one sample to another.

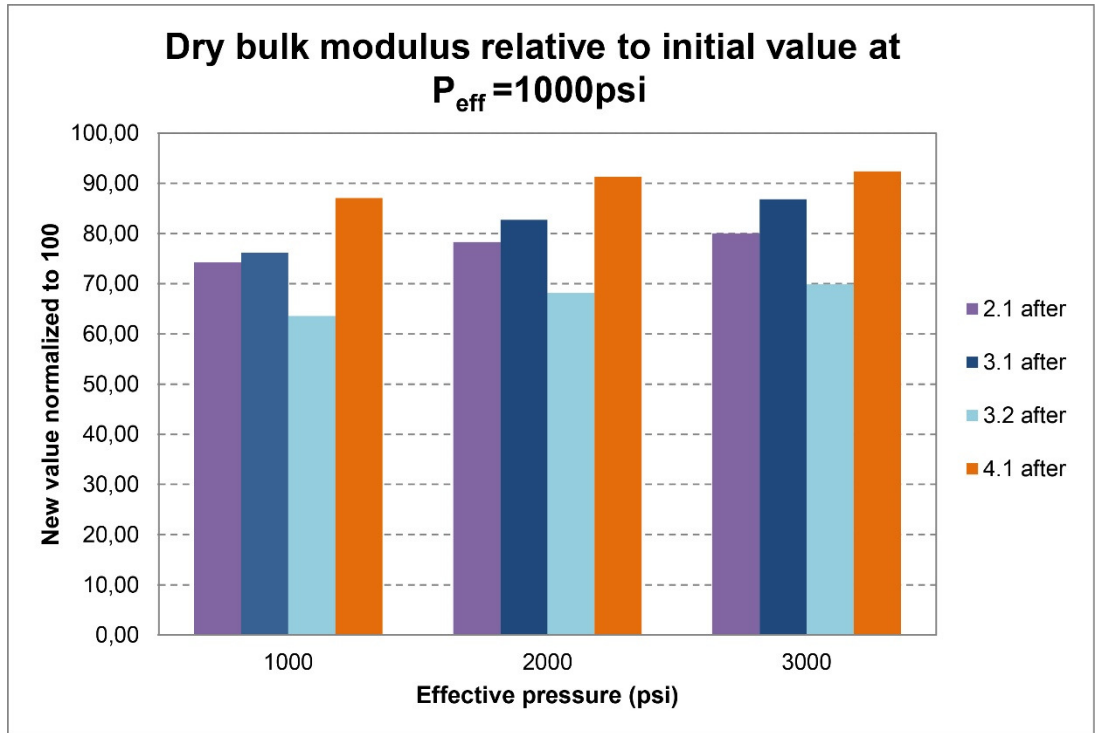


**Figure 5.15** Change in bulk modulus caused by calcite dissolution and increase in effective pressure ( $P_{eff}$ ).

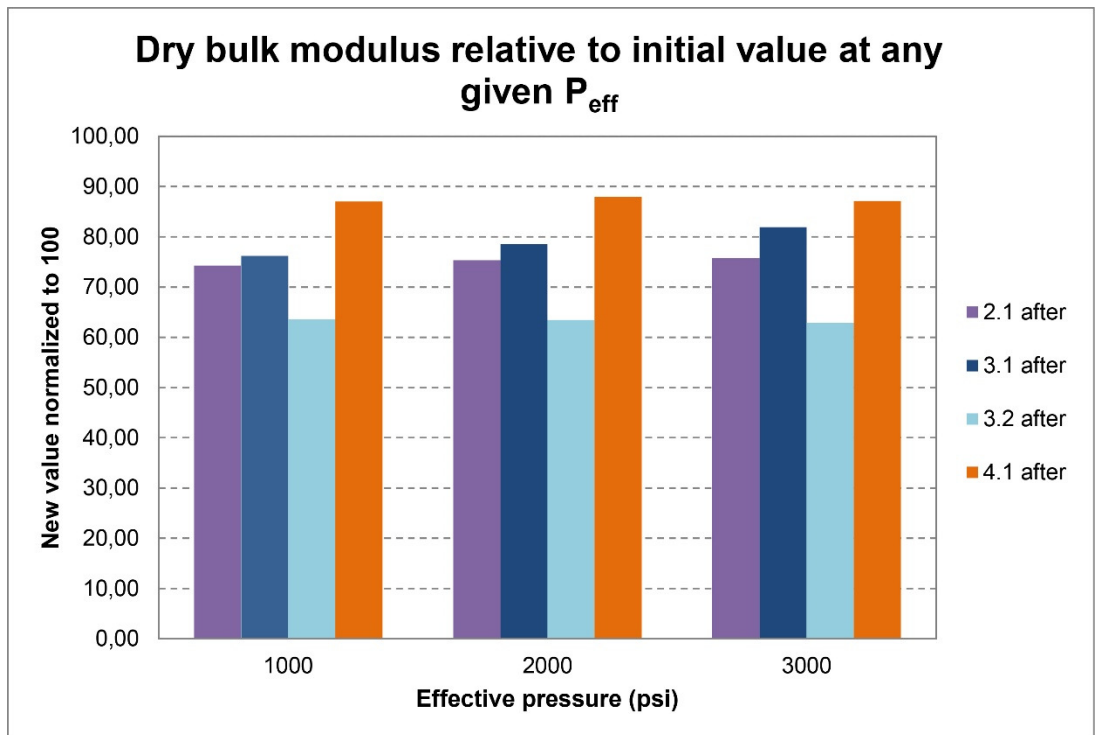


**Figure 5.16** Change in bulk modulus caused by calcite dissolution at constant effective pressure.

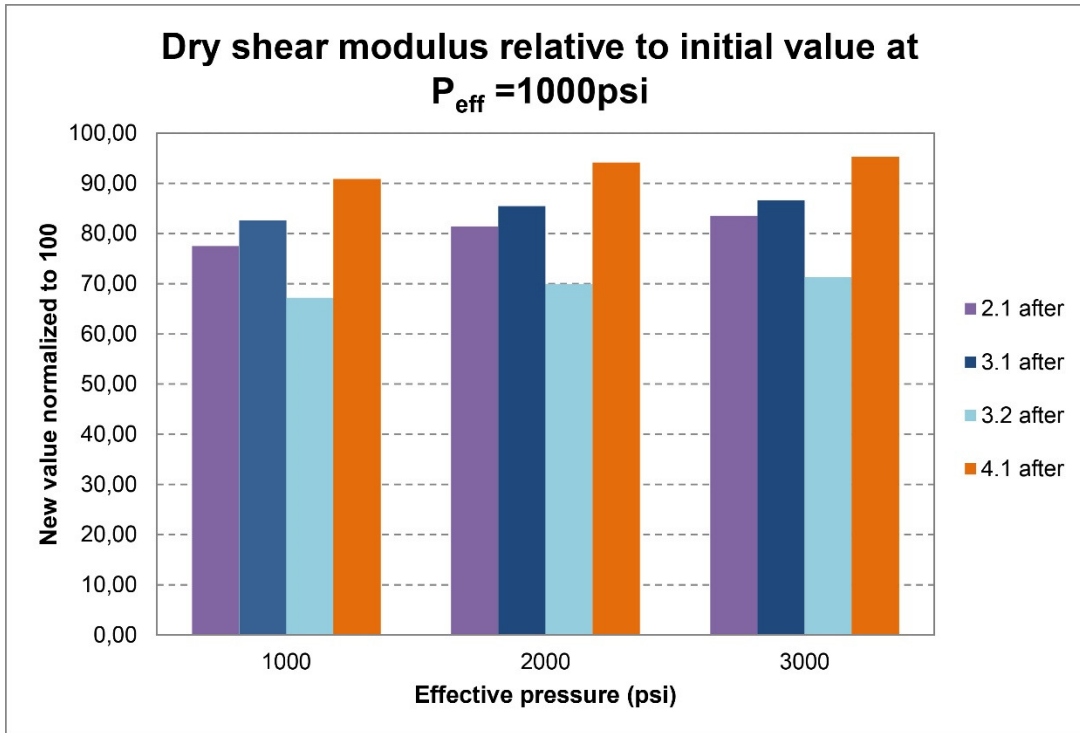


**Figure 5.17** Change in shear modulus caused by calcite dissolution and increase in effective pressure ( $P_{eff}$ ).

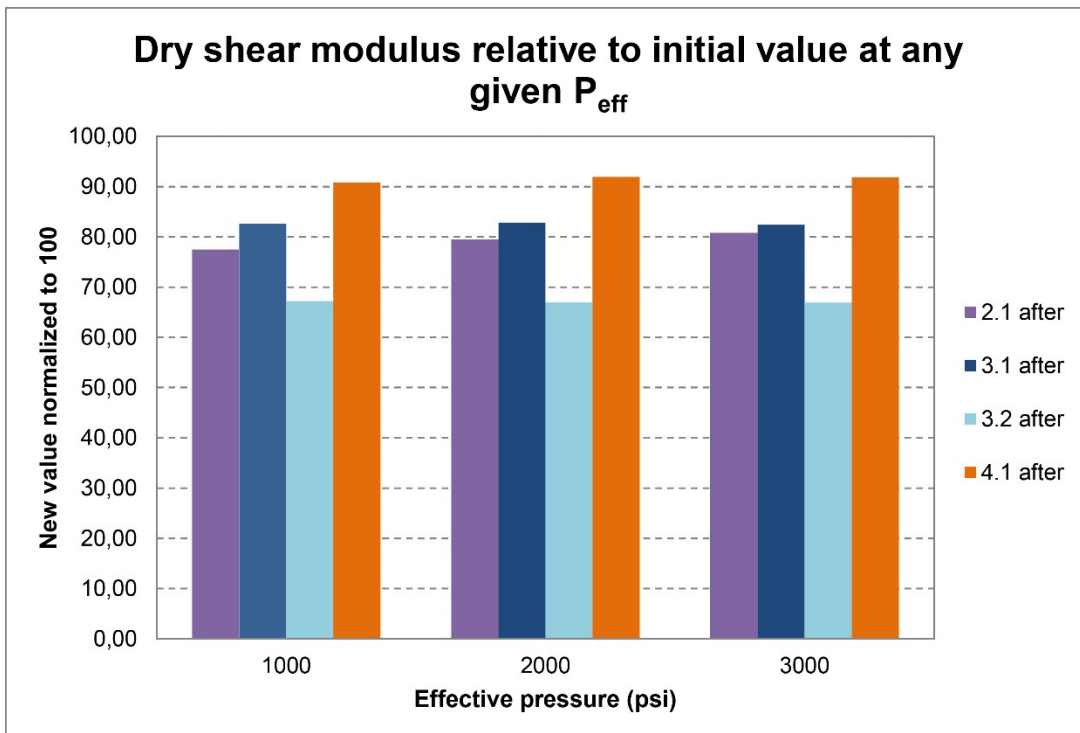


**Figure 5.18** Change in shear modulus caused by calcite dissolution at constant effective pressure.

The dissolution effect is closely correlated to the porosity change. It is interesting to observe that the natural variation in porosity of the initial samples produces the same trends on the plot of velocities against porosity

as the samples after calcite dissolution (Figure 5.19). This supports the idea that for a given rock texture the absolute value of the porosity is the primary variable upon which sonic velocity depends. This is the idea behind classical velocity-porosity correlations such as the “time average equation” or more advanced empirical correlations (Raymer et al., 1980; Han et al., 1986; Tosaya and Nur, 1982; Castagna et al., 1985). The experimental correlation from Han is very accurate in term of absolute velocity prediction based solely on porosity and clay content although the velocity gradient with porosity is lower than in the present experiments. Other correlations are less good in term of predicting absolute velocity but are better at predicting the changes in velocity after calcite dissolution (Figure 5.20). All the equations for these correlations can be found in Mavko et al. (2009).

These results show that a relatively good first order prediction of the velocity decrease upon calcite dissolution can be achieved by using simple correlations found in the literature. Care should be taken before generalizing this result since this study only tackled the effect of a small amount of calcite dissolution in the form of isolated grains. It is also worth noting that these calcite grains had relatively similar volumes to the pre-existing pores. It is possible that different sandstone textures would produce different results depending on the nature of the reactive minerals, their proportion in the rock and their placement in the rock frame. For example calcite cement dissolution from grain contacts might have a larger effect on sonic velocity and rock strength.

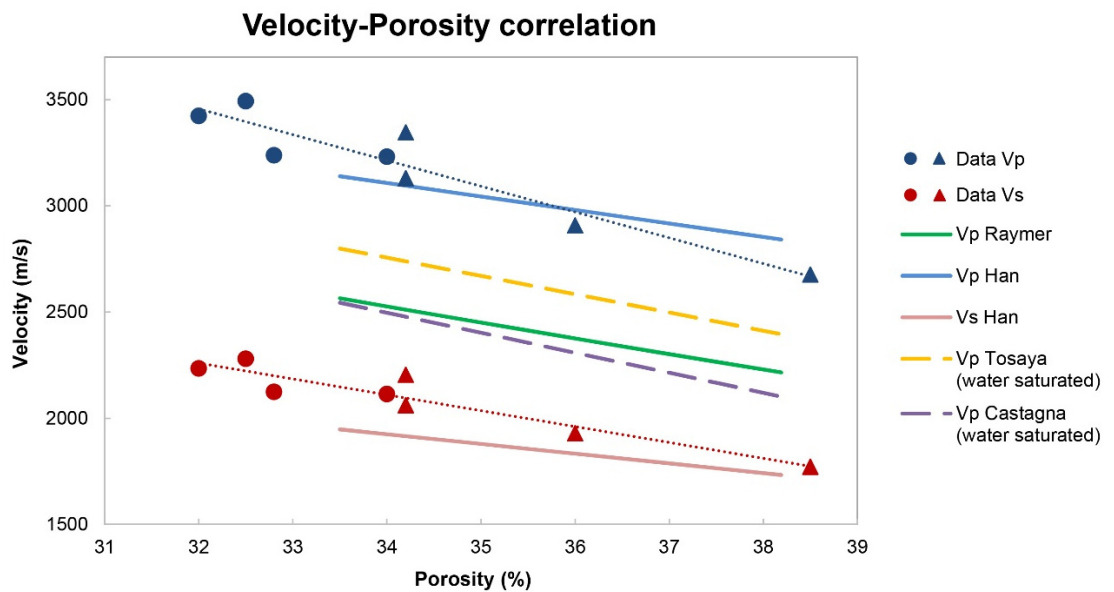


**Figure 5.19** Comparison between empirical velocity-porosity correlations and experimental data. Unreacted core data is represented with circles and reacted core data is represented with triangles.

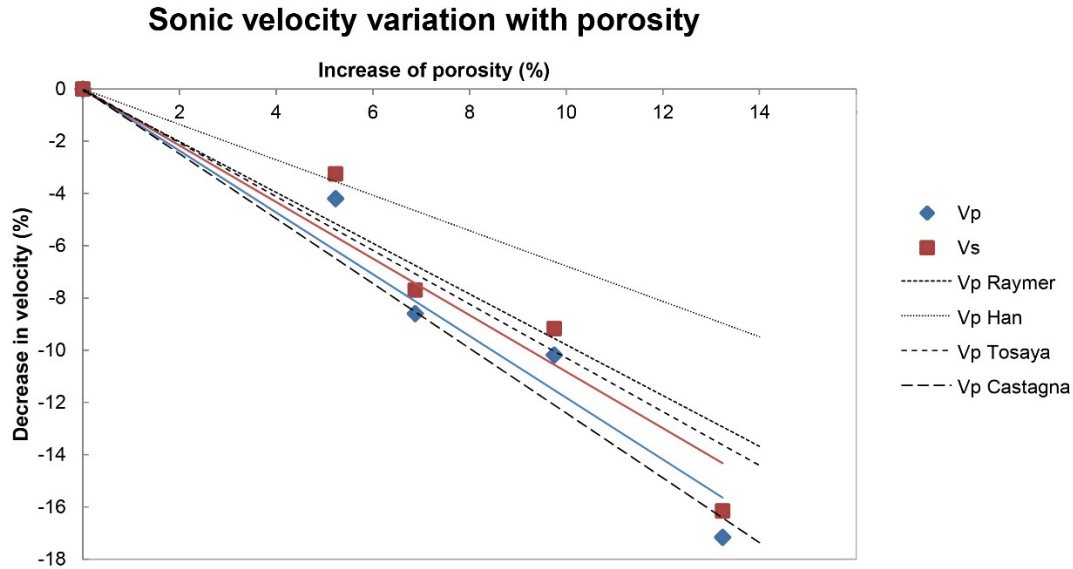


**Figure 5.20** Comparison between empirical and experimental variation in velocity with porosity. Linear fit of the experimental data is also shown.

### 5.3.3 Significance for 4D seismic monitoring of GCS

By using the experimental data it is possible to reconstruct a possible CO<sub>2</sub> injection scenario to identify the best indicators for tracking fluid substitution and calcite dissolution. It is necessary to identify both processes to correctly evaluate CO<sub>2</sub> saturation and to gain information on possible reservoir damage (due to dissolution). Figures 5.21 and 5.22 show sonic velocities for the brine saturated, CO<sub>2</sub>-saturated and CO<sub>2</sub>-saturated + calcite dissolution cases at different pore pressures and effective pressures calculated from the experimental dry moduli of the reacted and unreacted sample 2.1 and the saturated moduli from the Gassmann equations using Equation 5.2. In the next figures the following color code was used: orange colour stands for brine saturated and blue for CO<sub>2</sub>-saturated rock. Darker colours means higher fluid pressure. Calcite dissolution is represented as white dots.

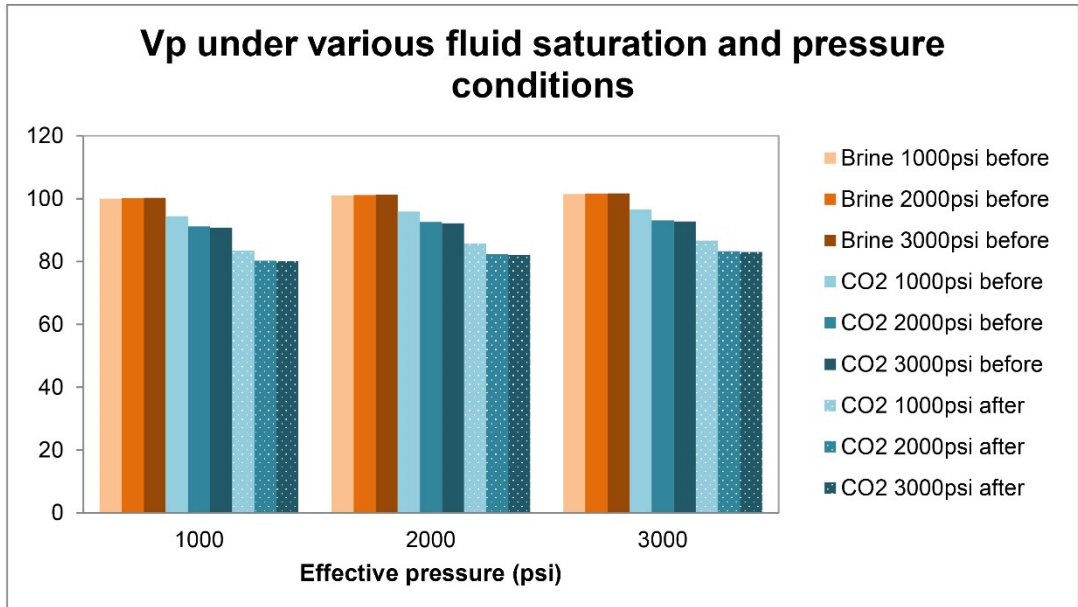


**Figure 5.21** Normalized Gassmann prediction of  $V_p$  under brine saturation conditions and under  $CO_2$  saturation conditions before and after calcite dissolution.

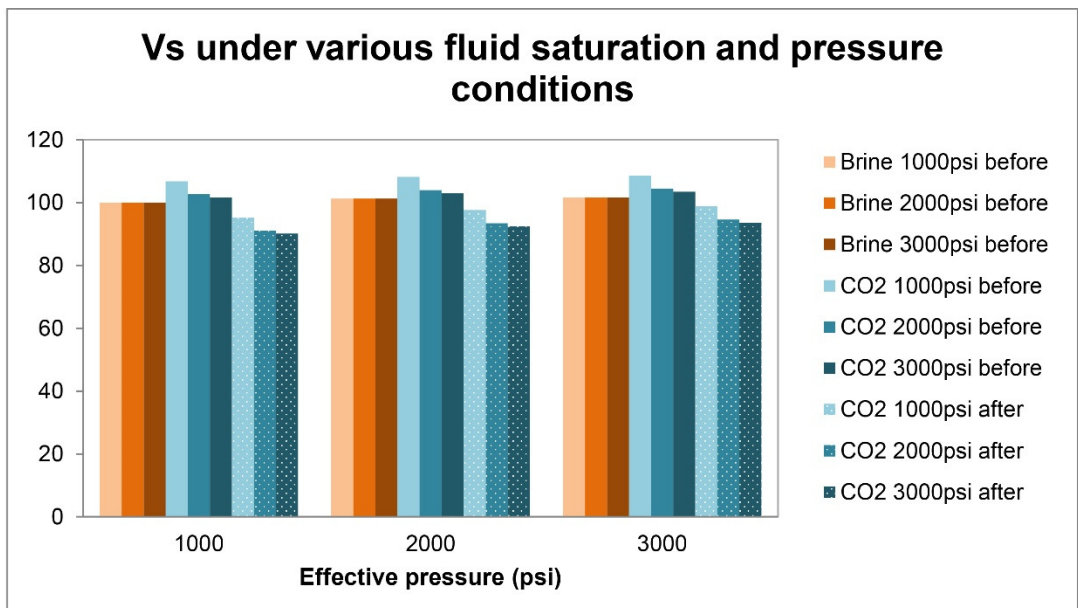


**Figure 5.22** Normalized Gassmann prediction of  $V_s$  under brine saturation conditions and under  $CO_2$  saturation conditions before and after calcite dissolution.

These sonic velocities were used to evaluate the potential for monitoring a simplified injection scenario involving initial pressurization of the reservoir at constant fluid saturation followed by fluid substitution. Figures 5.23 and 5.24 show a time sequence from left to right where the initial state is 100% brine saturation with a pore pressure of 2000 psi and an effective pressure of 2000 psi, the second stage retains the same fluid saturation but the brine pore pressure has been increased to 3000 psi which reduces the effective

pressure to 1000 psi. In the third stage the brine has been replaced by CO<sub>2</sub> at constant pressure. The last column is an end-member case including both fluid substitution and calcite dissolution effects on the bulk and shear moduli (note that calcite dissolution must have happened before or during fluid substitution as it requires the presence of water). As stated previously, the absolute values of the sonic velocity are slightly overestimated by the Gassmann equation but this makes only a marginal difference for the relative change in velocity. On the figures, all velocities are normalized to an initial velocity which value as been set arbitrarily to 100.

For the P wave velocity, the change in fluid pressure has a very small effect, whereas fluid substitution reduces the velocity by roughly 10% and calcite dissolution reduces the velocity by another 10%. Calcite dissolution and fluid substitution have very similar effect on V<sub>p</sub>.

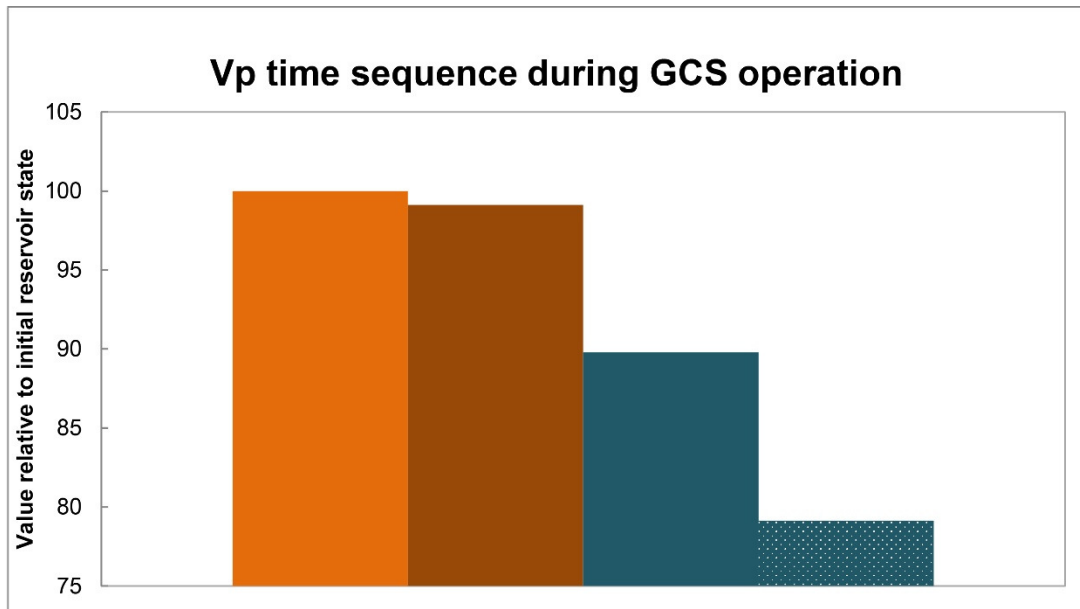


**Figure 5.23** Normalized V<sub>p</sub> evolution after brine pressurization, CO<sub>2</sub> invasion and calcite dissolution.

Following the same sequence of stages, the S wave velocity decreases slightly during brine pressurization but increases slightly after CO<sub>2</sub> injection. These V<sub>s</sub> changes might be below detection limits but calcite dissolution causes a significant decrease in V<sub>s</sub> by about 10% (Figure 5.24).

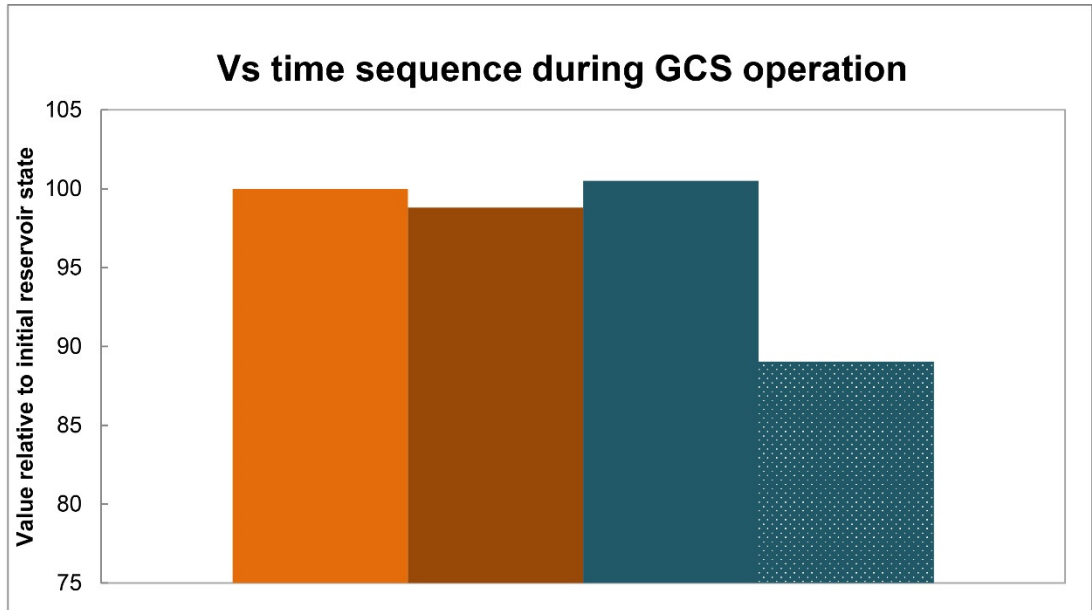


**Figure 5.24** Normalized Vs evolution after brine pressurization, CO<sub>2</sub> invasion and calcite dissolution.

The ratio Vp/Vs is essentially constant during reservoir pressurization and calcite dissolution, but responds strongly to fluid substitution (Figure 5.25).

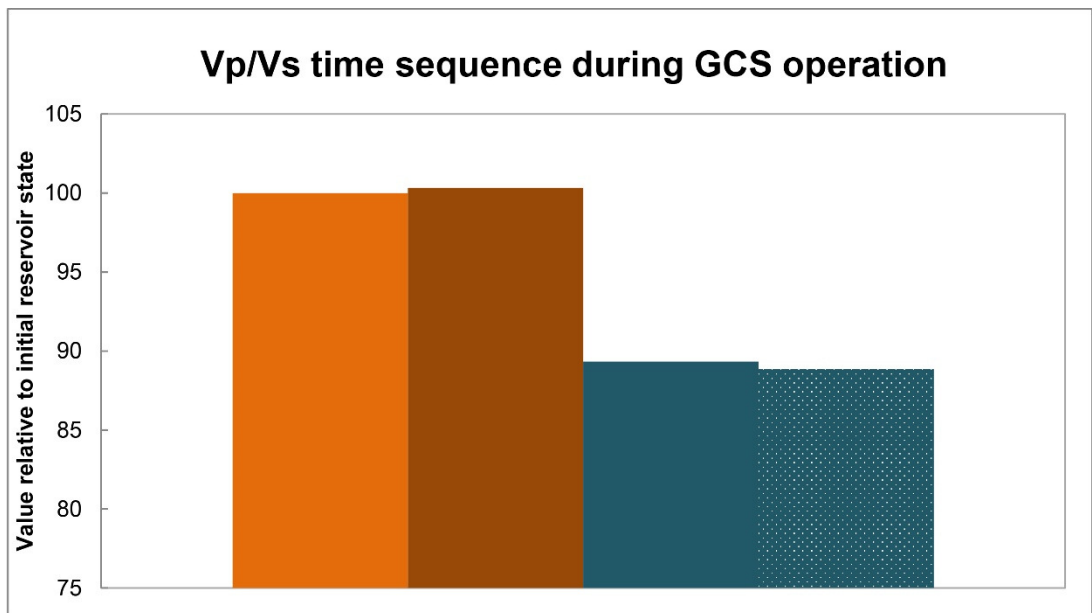


**Figure 5.25** Normalized Vp/Vs evolution after brine pressurization, CO<sub>2</sub> invasion and calcite dissolution.

The recommendations stemming from this analysis is that Vp/Vs should be used to detect replacement of formation water by CO<sub>2</sub> and Vs alone should be used to detect changes in the rock frame due to mineral dissolution.

This analysis only considered end-member values steps of fluid substitution and calcite dissolution. In reality the fluid saturations are going to slowly change and calcite dissolution is going to occur progressively. The difficulty

at this stage is the possible misinterpretation of the P wave velocity. Figure 5.26 shows the evolution of the P wave velocity calculated with Gassmann equation when CO<sub>2</sub> (gas) saturation gradually increases. The bulk modulus of the brine-CO<sub>2</sub> mixture was calculated with Wood's equation (Wood, 1941). From this figure it is evident that a few percent of CO<sub>2</sub> saturation associated with calcite dissolution (lower curve) could be misinterpreted as 100% CO<sub>2</sub> infiltration (upper curves). In practice the true V<sub>p</sub>-Saturation curve will lie between the two end-member curves as calcite dissolution and CO<sub>2</sub> invasion happen simultaneously.

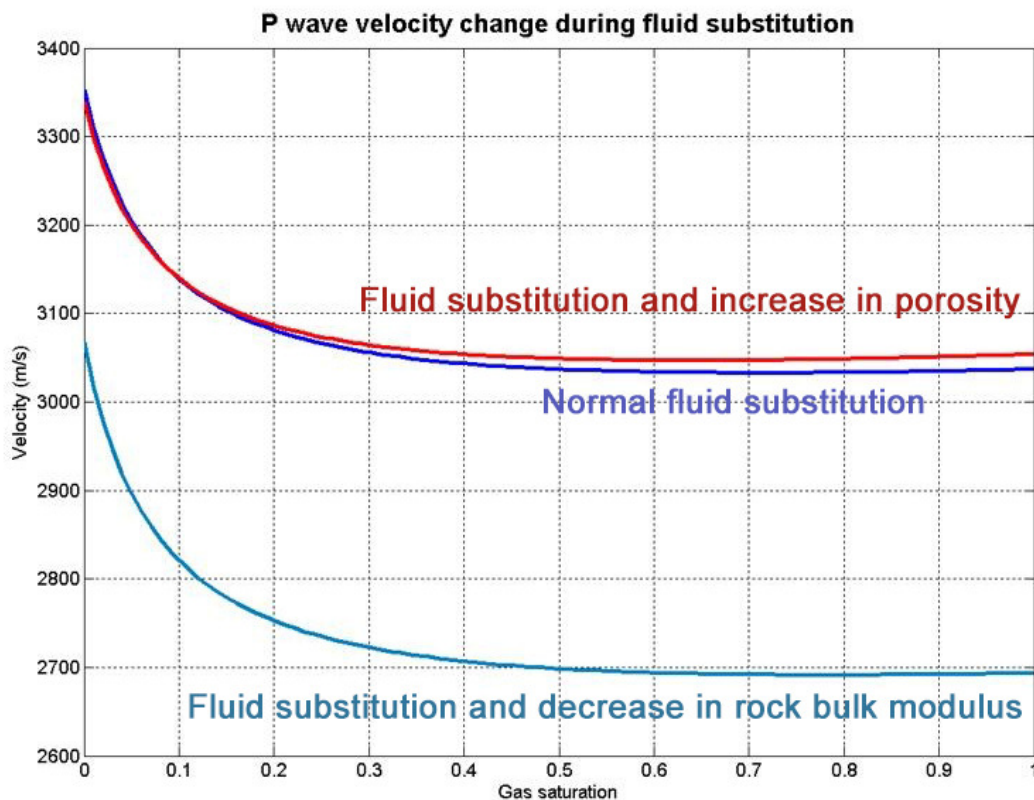


**Figure 5.26** Fluid substitution effects on V<sub>p</sub> according to Gassmann theory including the effect of a porosity change and the effect of a  $K_{dry}$  change. All curves were calculated using Equation 5.2. For the “Normal fluid substitution” curve only the CO<sub>2</sub> saturation was varied. For the “Fluid substitution and increase in porosity” curve the fluid rock interactions were incorrectly taken into account by simply increasing the porosity parameter in Equation 5.2. The last curve is the most accurate as it takes into account fluid-rock interaction effects on both porosity and  $K_{dry}$  parameters (as evaluated in the present experiments).

In conclusion, a detailed analysis of the sonic velocity changes is necessary to discriminate between the effects of fluid substitution and rock frame modification. This analysis is probably not necessary if the 4D monitoring is

simply intended to detect CO<sub>2</sub> leaks into the overlying geological layers. It is however necessary if the purpose is to track accurately the CO<sub>2</sub> advance in the reservoir or is to detect and quantify fluid-rock interactions in the reservoir or in surrounding layers. Detection and localization of fluid rock interactions could be useful to understand or even prevent reservoir and well damage. The following section specifically addresses the consequences of calcite dissolution for the peak and yield strength properties of the Cayton Bay sandstone.

## **5.4 Peak and Yield strength**

### **5.4.1 Basic concepts**

Peak and yield strength are material properties referring to the stress state at which rocks start to fail or to yield. Rocks stressed beyond a certain point stop behaving elastically and start to deform plastically. Plastic deformation is irreversible and larger than the elastic deformation for a given increment of stress. Plastic deformation, here referred as yielding, starts with compaction of the rock due to a loss of porosity and grain rearrangement. As deformation continues, shear stress increases and strain starts to localize on a failure plane. This process continues until rock failure occurs at the rock peak strength (or ultimate stress). It is important to know if, for a given reservoir stress state, calcite dissolution can trigger rock yielding or rock failure by changing peak strength. Yielding or failure could compromise both wellbore stability and formation stability and could also compromise GCS operation by reducing the reservoir permeability.

In general, rock strength and its resistance to differential stress increases with confining pressure. It is thus necessary to conduct tests at a range of confining pressures to establish a rock strength law. In basic triaxial tests cylindrical samples are introduced into a pressure vessel and an isostatic pressure is applied. The axial stress is then increased steadily by means of a hydraulic press and the confining lateral pressure is kept constant. The deformation of the sample is recorded with LVDT and strain gauges until it yields or fail. The result is a strain-stress relationship where yield and failure points for a given confining pressure can be established. An example of such a relationship is shown in Figure 5.27.

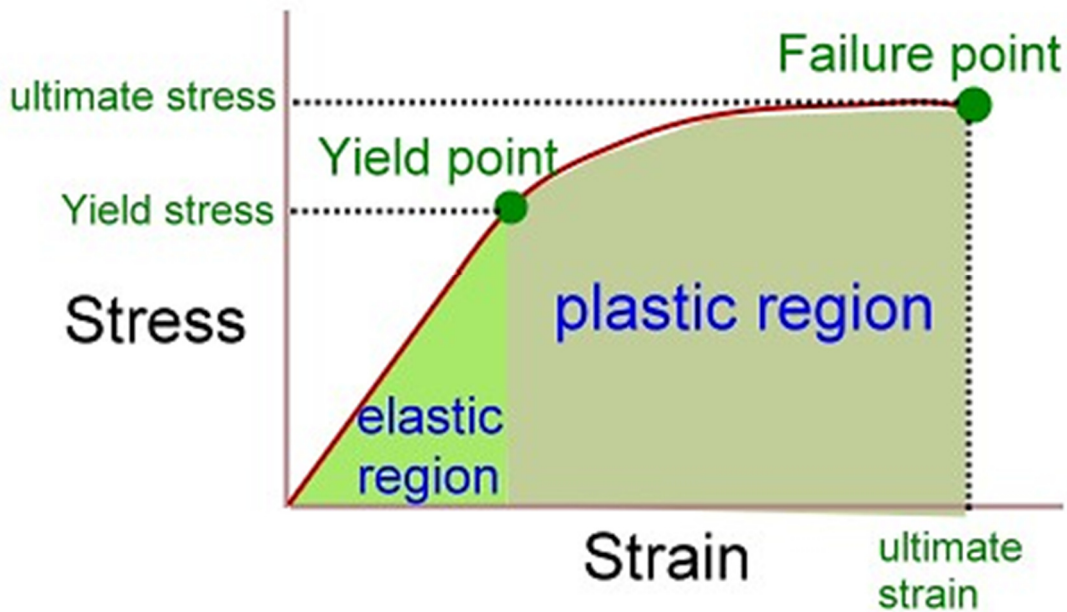


**Figure 5.27** Typical rock strain stress curve obtained during a triaxial test.

Source: <http://www.pt.ntu.edu.tw/hmchai/Biomechanics/BMmeasure/Stress Measure.htm>. Accessed on 08/12/2014.

Single triaxial tests running until sample failure are destructive by definition. A large number of samples are necessary to gather strain-stress relationships at various confining pressures. One alternative is to conduct multiple failure experiments. This kind of experiment proceeds as series of single tests where the confining pressure is quickly increased to reestablish isostatic pressure when the sample start to fail. At this point the axial stress is increased again until the next failure point is reached. Usually strength results from multistage tests are systematically lower than results from single stage tests. This is because the sample gets weaker as it becomes slightly damaged by incipient yielding and fracturing at each stage. This technique is however less time consuming and works very well on relatively plastic rocks where failure does not occur dramatically and confining pressure can be increased on time.

Initial tests on Cayton Bay sandstone indicated that the multiple failure test was well suited to this quite plastic rock. This method is destructive and so a statistical approach was adopted with two sets of samples, one unreacted and the other one where the calcite had been dissolved. In total nine strength experiments were performed.

#### **5.4.2 Strength measurements on reacted and unreacted cores**

Nine multiple failure tests were conducted on brine saturated cores in drained conditions. The pore pressure was atmospheric and so negligible relative to confining and axial pressure. This should not influence the results compared to relevant reservoir pore pressure conditions since brine properties are pressure independent in this pressure range. Another difference from reservoir conditions is that the experiments were conducted at room temperature. In summary, the experimental conditions are sufficiently close to reservoir conditions to provide meaningful insights onto the effect of calcite dissolution but may not provide absolute strength values.

A triaxial testing machine similar to the one used for the sonic velocity measurements was equipped with LVDT (Linear Variable Displacement Transducer) to record the axial strain. Rock cores were also instrumented with strain gages but these did not function; hence the following analyses are founded on the LVDT data only. The LVDT result from one experiment is shown in Figure 5.28. After each confining pressure increase, axial loading unloading cycle was performed, allowing the rock to return into the elastic domain. The yield points are defined as the points where the curve departs from the linear elastic trend. The confining pressure is increased in 7 stages at 5, 10, 20, 30, 40, 50 and 60 MPa. After the last stage was reached the confining pressure was gradually reduced to evaluate the residual strength of the rock. Because the samples were extremely plastic it was not always possible to reach the failure point since this is marked by the onset of a sharp decrease in the axial stress. In general the onset of rock failure occurred at 10MPa above the yield point.

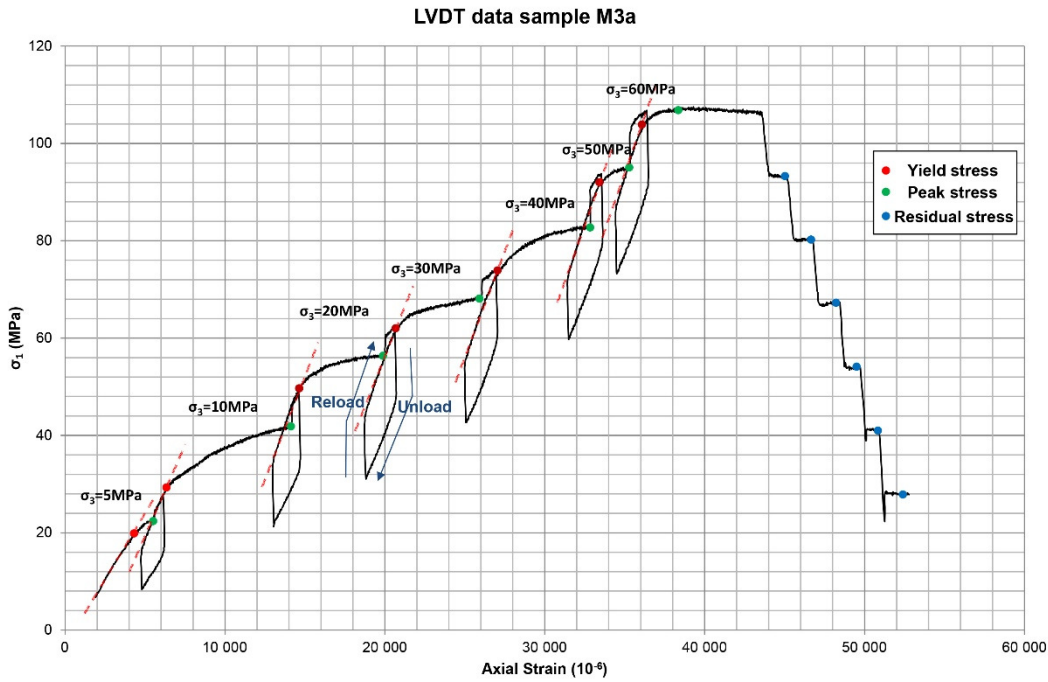


**Figure 5.28** Example of multiple failure test data. The values of interest have been highlighted with dotted red guidelines to illustrate the yield stress determination. The unloading and reloading paths at the start of new confining pressure stage is also illustrated.

It is possible to construct the yield envelope by plotting all yield points on a  $P$ - $Q$  or  $\sigma_1$ - $\sigma_3$  graph where  $P$  is the mean effective compressive stress  $P = \frac{(\sigma_1 + 2\sigma_3)}{3} - P_f$  and  $Q$  the differential stress  $Q = \sigma_1 - \sigma_3$ . The results demonstrate that calcite dissolution effectively decreased the strength of the rock (Figures 5.29 and 5.30).

For illustration the  $P$ - $Q$  state for a hypothetical reservoir where faults with a friction coefficient of 0.85 constrain the stress state is shown in Figures 5.29 and 5.30. The calculation used a continuous underground rock density of  $2800 \text{Kg.m}^{-3}$  (largely higher than the Cayton Bay sandstone density) and assumed that the pore pressure was hydrostatic. Three points are shown, corresponding to the  $P$ - $Q$  state in the reservoir at depths of 1000, 2000 and 3000m. In the ideal case, (Jeager and Cook, 1979) the ratio of  $\sigma_1 - P_f$  to  $\sigma_3 - P_f$  is a function of the fault friction coefficient  $\mu$  as follows:

$$\frac{\sigma_1 - P_f}{\sigma_3 - P_f} = \left( \sqrt{\mu^2 + 1} + \mu \right)^2 \quad (5.3)$$

Where  $P_f$  is the pore pressure. For a normal faulting regime  $\sigma_1$  is the vertical stress, equal to  $\rho g z$ , then at 1000 m  $\sigma_1 - P_f = 18 \text{ MPa}$ ,  $\sigma_3 - P_f = 4 \text{ MPa}$  which corresponds to a differential stress  $Q = 14 \text{ MPa}$  and a mean effective compressive stress  $P = 8.5 \text{ MPa}$ . Similarly for 2000 m  $Q = 28 \text{ MPa}$  and  $P = 17 \text{ MPa}$ ; for 3000 m,  $Q = 42 \text{ MPa}$  and  $P = 25.5 \text{ MPa}$ .

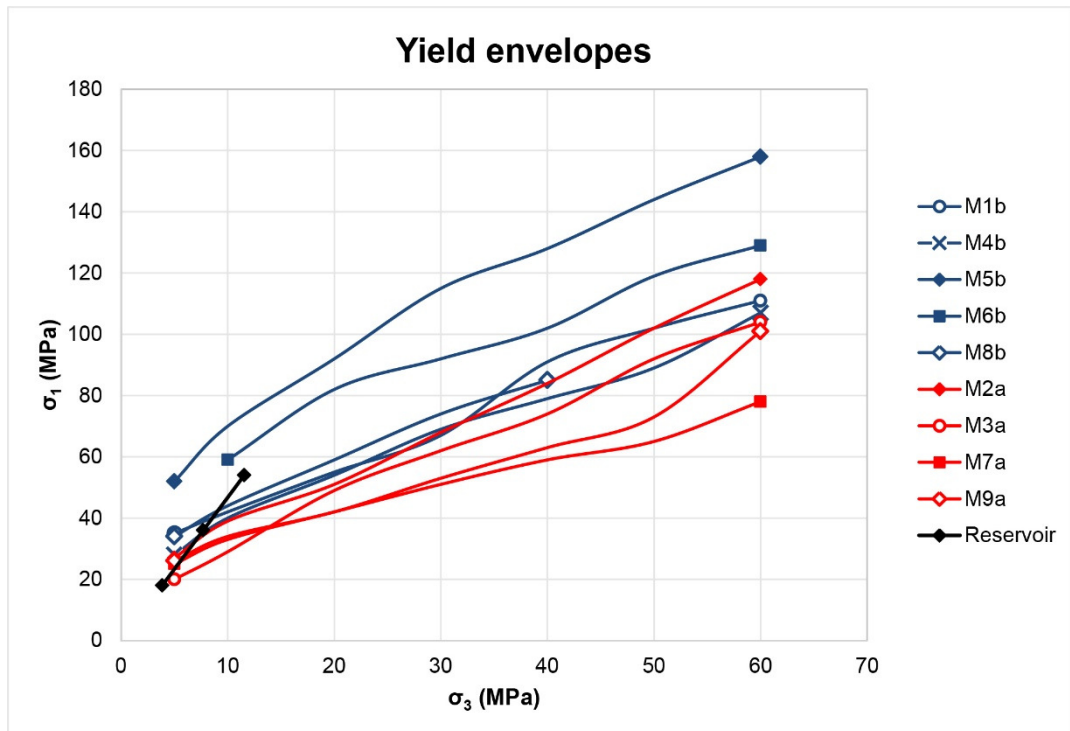


**Figure 5.29** Yield envelopes for all samples and possible reservoir stress state at increasing depths of 1000, 2000 and 3000 meters.

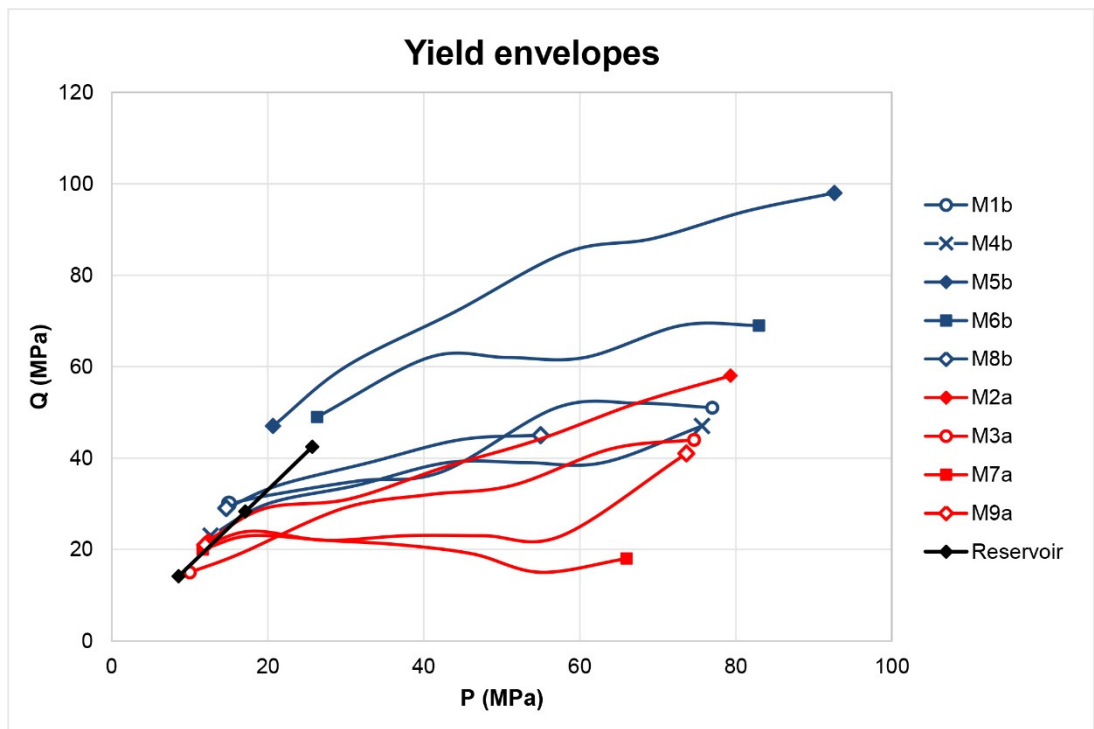


**Figure 5.30** Same yield envelope representation as Figure 5.29 shown in P-Q space.

The curves in Figure 5.29 and 5.30 indicate that it is possible for calcite dissolution to trigger ductile yielding in the hypothetical reservoir at a depth

of about 2000 m. At 1000 m none of the samples would yield while at 3000m only two unreacted samples did not yield.

The decrease in rock strength is likely due to a decrease in rock cohesion and in the angle of internal friction. Rewriting the Coulomb law of failure as:

$$\sigma_1 = \frac{2\tau_0 \cos \varphi}{1 - \sin \varphi} + \sigma_3 \frac{1 + \sin \varphi}{1 - \sin \varphi} \quad (5.4)$$

where  $\tau_0$  is the rock cohesion and  $\varphi$  is the angle of internal friction. Linear fits to average peak envelopes before and after calcite dissolution (Figure 5.31) gives  $\tau_0 = 14.5$  and  $10.5$  MPa and  $\varphi = 16.0$  and  $8.3^\circ$  respectively. This corresponds to an opening of the failure plane angle from  $37^\circ$  to  $41^\circ$  which agrees qualitatively well with the failure plane observed on some of the samples after the experiment (Figure 5.32), although clear determination of the failure planes angle was not always possible.

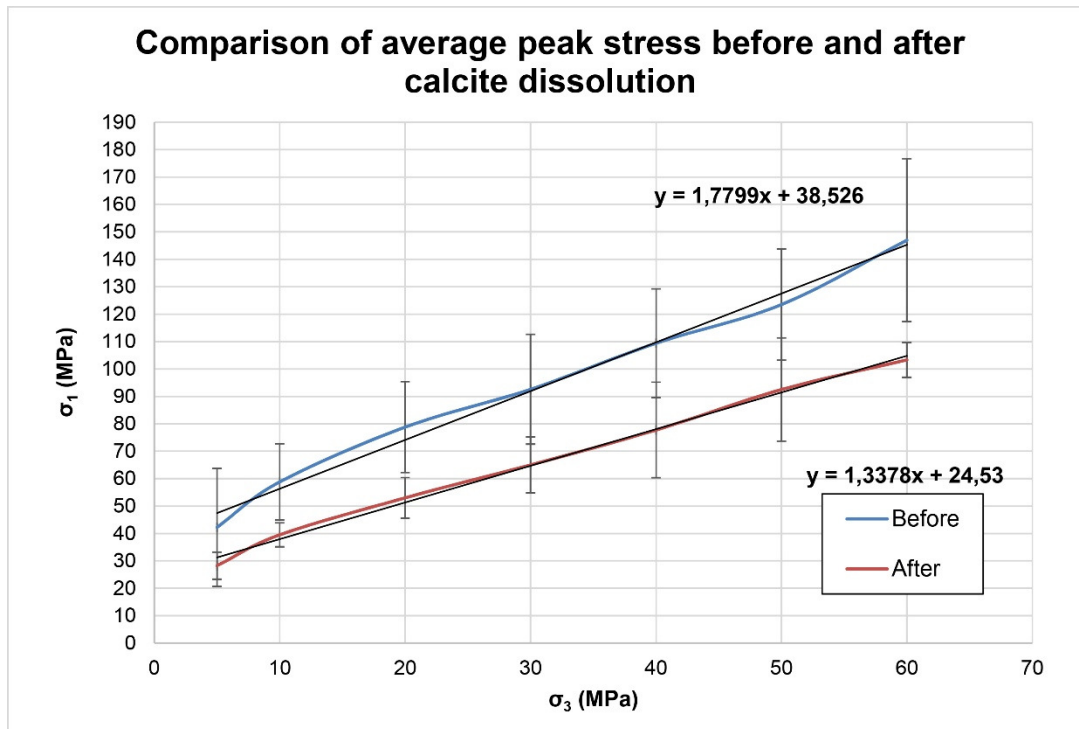


**Figure 5.31** Linear fit of the average peak envelopes before and after dissolution. The effect of calcite dissolution on the rock cohesion ( $\tau_0$ ) is obvious (downward translation of the curve) while its effect on the angle of internal friction is more subtle (change in slope).

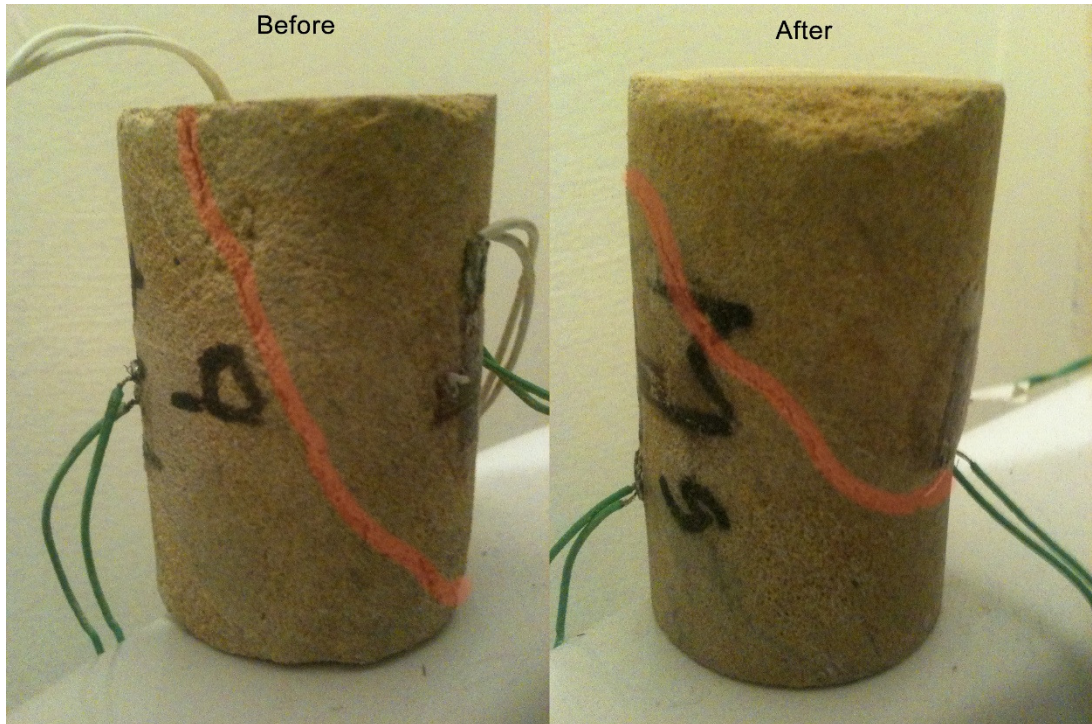


**Figure 5.32** Failure plane on two samples before and after calcite dissolution with visually steeper failure plane before calcite dissolution (Cores are the same size). This observation is consistent with the calculations concerning the increase in the angle of internal friction upon calcite dissolution (Figure 5.31 and Equation 5.4) but not conclusive on its own as those two samples are not statistically representative and the angles were not properly measured.

There is no clear break between results for reacted and unreacted cores. The yield and peak stress curves are shown as a function of porosity in Figures 5.33 and 5.34 and demonstrate that the decrease in strength is a strong function of porosity, irrespective of whether it is primary or secondary. This result is analogous to the one obtained on sonic velocity: porosity is the primary parameter on which velocity depends, irrespective of the presence of calcite or not.

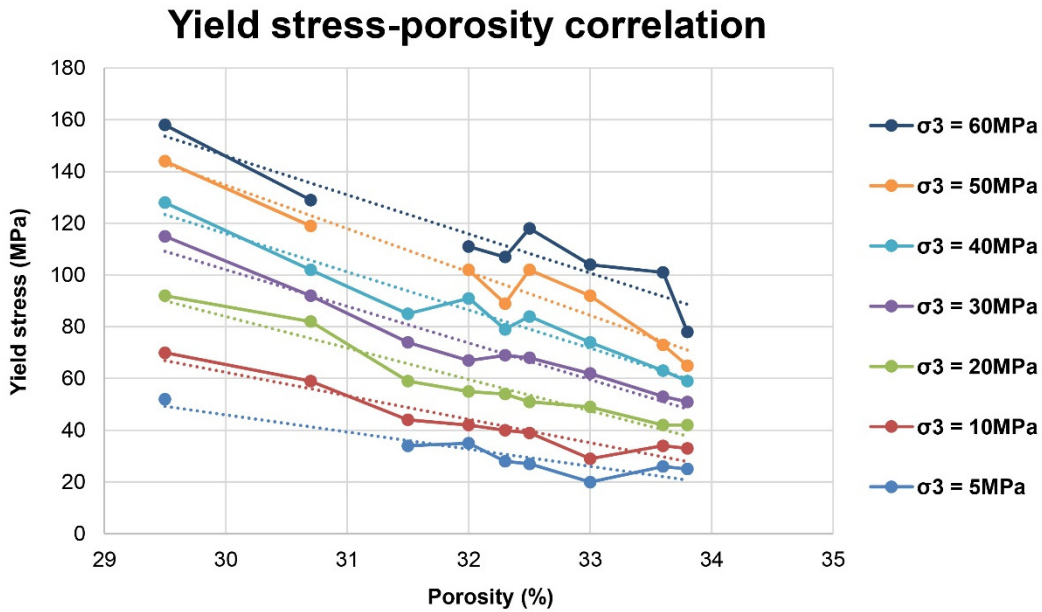


**Figure 5.33** Experimental data showing the yield stress-porosity correlation. This figure represent all experimental data, every data points column for a given porosity represent one sample experiment. From left to right is presented the data from samples M5b, M6b, M8b, M1b, M4b, M2a, M3a, M9a and M7a where “a” and “b” signifies “after” and “before” calcite dissolution.

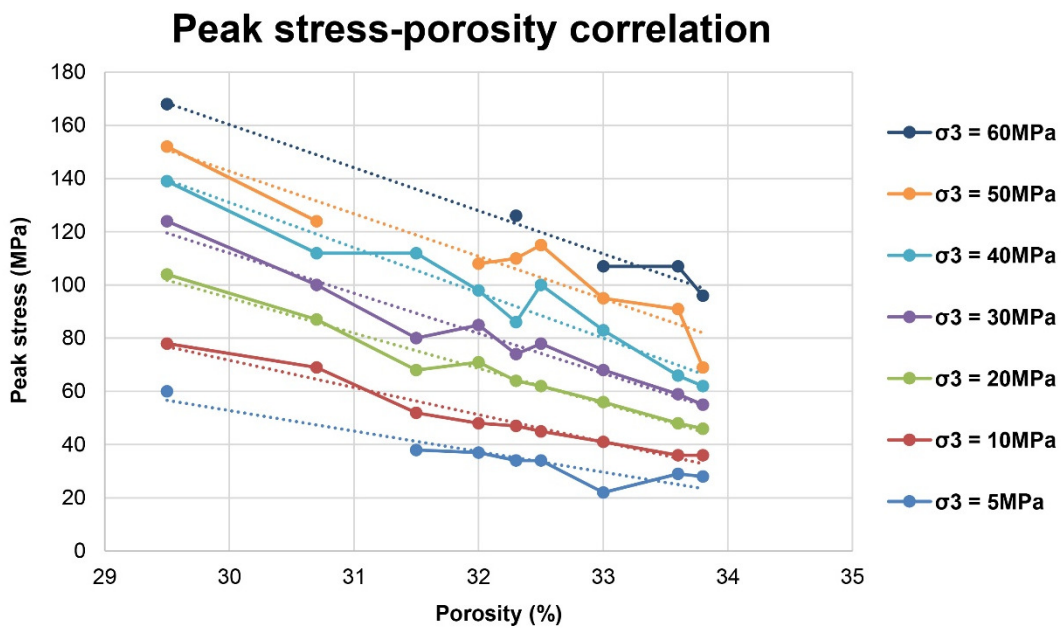


**Figure 5.34** Experimental data showing the peak stress-porosity correlation.

## 5.5 Conclusion

The experimental results presented here provide very strong evidence that fluid rock interactions cannot be neglected when dealing with the mechanical properties of calcite bearing reservoirs in the context of GCS. They show

large modifications of the sonic velocity and rock strength parameters. The exact implications of this work at the reservoir scale will depend on the extent and localization of calcite dissolution as discussed in Chapter 3.

At the reservoir scale the implications of this study are twofold. Firstly the work conducted on sonic velocity demonstrates the fluid-rock reactions must be accounted for to properly interpret seismic data in terms of fluid saturation. Secondly the study of the yield and peak envelopes demonstrates that fluid-rock interactions can in some circumstances be a threat to reservoir and/or well integrity by reducing rock strength and triggering irreversible plastic deformation. Note that rock compaction after yielding could mitigate this effect by increasing rock strength.

The changes in porosity and rock properties associated with fluid-rock reactions could be calculated and localized with time-lapse seismic surveys of P and S wave components. This could provide a means to assess the reservoir and well instability risk and would necessitate an integrated reservoir mechanical modelling that is out of the scope of this study.

The correlation between porosity and rock mechanical properties is very strong in our experiments, such that the effect of natural porosity variations is almost independent of whether porosity is original or created experimentally by calcite dissolution. This conclusion is very different from the one reached for the transport properties in Chapter 3. In the study of the Cayton Bay sandstone, the changes in transport properties depend on the change in pore network morphology rather than on the absolute change in pore volume, but this is the opposite for the sonic velocity and rock strength properties. Nevertheless it is not possible to generalize this result to all calcite bearing sandstones as it seems logical that in some conditions the pore morphology would have a larger influence.

It is evident that laboratory measurements directly relate to only a small portion of a given target reservoir. Still, such measurements are essential to provide meaningful input parameters into rock mechanics models and can serve to calibrate observations. Such experiments are time consuming and for this reason very few studies have been published on the subject. A possible way forward would be to perform mechanical simulations on real rock geometry models in a similar fashion to the method presented in Chapter 4 for the permeability change calculation.

## **Chapter 6**

### **Experimental study of calcite precipitation triggered by fluid depressurization and CO<sub>2</sub> degassing.**

#### **6.1 Introduction**

Chapters 3, 4 and 5 presented studies of calcite dissolution and its potential effects on rock. As discussed on the GCS geochemistry section of Chapter 2, calcite dissolution in one part of the reservoir is bound to trigger calcite re-precipitation elsewhere. On short length and time scales, calcite precipitation could happen in “dead-ends” or reduced flow regions of the pore space. On longer time scales, calcite precipitation could occur once silicate dissolution has introduced sufficient calcium into solution. This thesis is mainly focused on processes which have a short term impact on CO<sub>2</sub> injection into saline aquifers and so the focus here is on the effect of pore fluid depressurization as a trigger for precipitating calcite.

Variations in pore fluid pressure will always occur as fluids flow from the injection well into the reservoir but larger drops in fluid pressure are possible when CO<sub>2</sub> injection is stopped, if the fluid breaks through low permeability barriers compartmentalizing the reservoir or if the fluid leaks into overlying formations. In these cases the depressurization of the fluid phases will reduce the CO<sub>2</sub> partial pressure and in turn reduce the CO<sub>2</sub> solubility. The resulting degassing of CO<sub>2</sub> from saturated brine may trigger calcite precipitation, as with the formation of kettle scale.

Calcite precipitation is a complex process and even though it is thermodynamically favored by CO<sub>2</sub> degassing, many parameters can modify the kinetics and the localization of the calcite precipitates. For instance, for small oversteps precipitation may be localized where pre-existing grains are present. Pore space morphology may also play an important role since small pores are prone to clogging.

Many aspects of calcite precipitation phenomena have been studied in batch experiments. Most flow experiments involved fluid mixing to induce precipitation (e.g. Tartakovsky et al. 2008). Here the intent was to simulate reservoir processes more closely and therefore develop an experimental design where a flowing CO<sub>2</sub> and calcite saturated fluid would experience a sudden pressure drop before entering a rock sample. The aim of the

experiments was to study a two-step process: CO<sub>2</sub> coming out of solution followed by calcite precipitation.

The addition of the CO<sub>2</sub> degassing process hides many complications concerning the exact thermodynamics and kinetics of the degassing and precipitation processes and the way they influence each other. Does CO<sub>2</sub> degassing occurrence and magnitude depend on rock petrophysical properties, such as pore size? If calcite precipitation happens at the interface between the brine and the degassed CO<sub>2</sub> bubbles then will calcite nuclei be transported along with them?

The original goal was to conduct calcite precipitation experiments on different rock samples to try to decipher the correlations between petrophysical properties and calcite precipitation. For each rock sample, two experiments were planned, one with a normal core and one where a groove was cut in the core to promote CO<sub>2</sub> degassing (Figure 6.1).

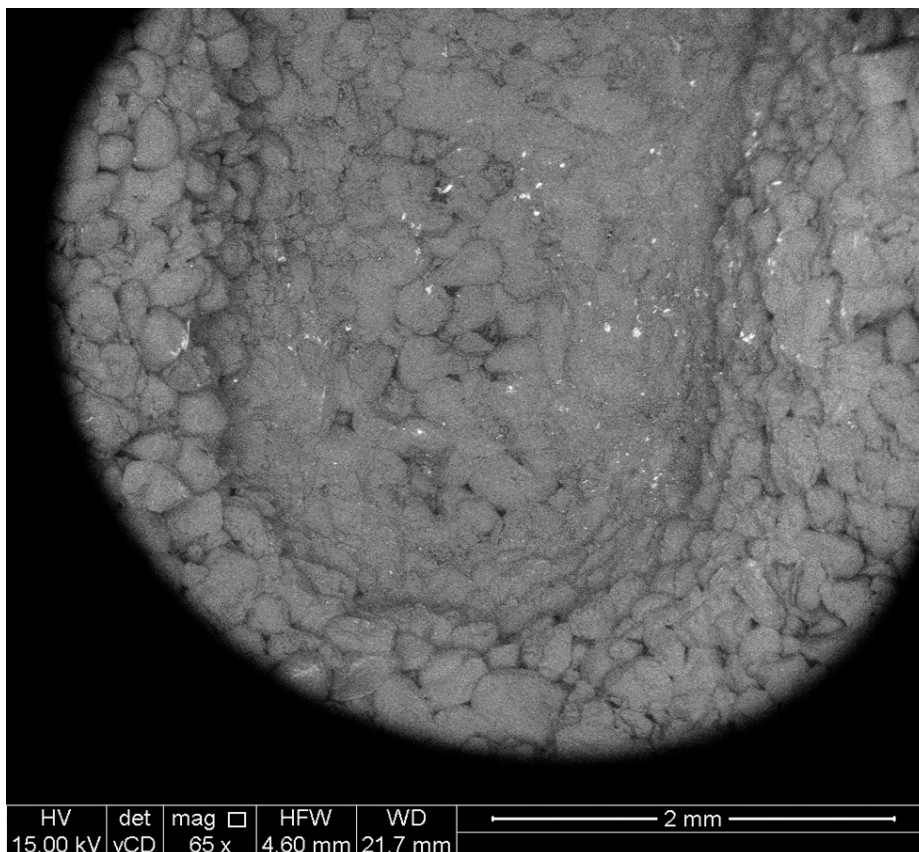


**Figure 6.1** SEM images of the groove cut in a Lochaline sandstone core at the outlet end of the core and in the flow direction.

In the event, time constraints meant that only one series of experiments concerning a single sample type (Lochaline sandstone) has been completed.

## 6.2 Experiment description

### 6.2.1 Experimental system and methodology

The experimental flow system is presented in Figures 6.2 and 6.3. On the left (inflow) side, water is initially equilibrated with CO<sub>2</sub> at room temperature and at a pressure of 4 MPa for two days. Similarly the small volume (0.3 L) calcite-saturation cell is filled with water and small grains of calcite (5mm grains, 99.9% pure calcite) and a 4 MPa CO<sub>2</sub> pressure is applied. During the run, CO<sub>2</sub>-saturated water is extracted from the bottom of the large tank with a high pressure pump. The high pressure line (blue) is slowly brought up to pressure and purged of remaining air bubbles. The pump is then set on constant pressure mode (4 MPa) to inject CO<sub>2</sub>-saturated water through the calcite saturation cell. Given the height of the calcite grain column in the cell (about 10 cm) and the low flow rates achieved during the experiment (0.4 mL/min at most), it is considered that the CO<sub>2</sub>-saturated water has time largely in excess to equilibrate with the calcite. The final calcite- and CO<sub>2</sub>-saturated water passes through a 1.2 µm filter before reaching the first sampling line and entering the core holder.

The core holder contains a very low permeability disk upstream of the rock core. A manually controlled back pressure of 1 MPa was used and the largest variations in back pressure never surpassed 0.06 MPa. Because of the very large permeability difference between the disc and the sample, the entire pressure drop occurred in the disc. The disc material and thickness (see section 6.2.2) were chosen by trial and error until a fixed pressure drop of 3 MPa would produce a flow rate sufficiently low to leave time for the calcite precipitation to take place and sufficiently large to allow the injection of 1 liter of solution in a reasonable time (4 days). During the main experiment the flow rate decreased from 0.4 to 0.2 mL per minute corresponding to one pore volume in 40 or 80 minutes respectively. Additional constraints were that the disc thickness had to be large enough so that it would not break once the confining pressure of 10 MPa was applied. On the other hand it had to be as small as possible to limit the amount of calcite precipitation occurring in the disc as this would quickly block the flow given its very low initial permeability. At the outlet of the core holder was placed a second fluid sampling line in order to measure the change in calcium concentration of the fluid between the two ends of the core holder and hence calculate the amount of calcite precipitation.

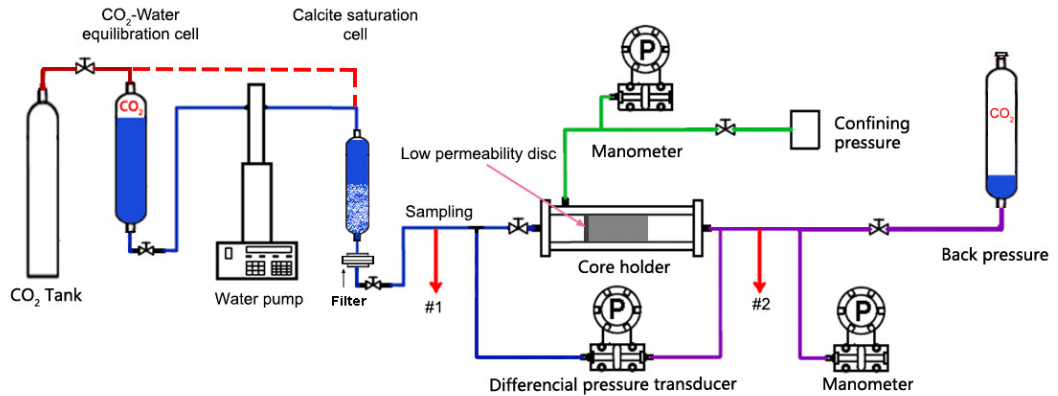


**Figure 6.2** Schematic representation of the calcite precipitation experiment.

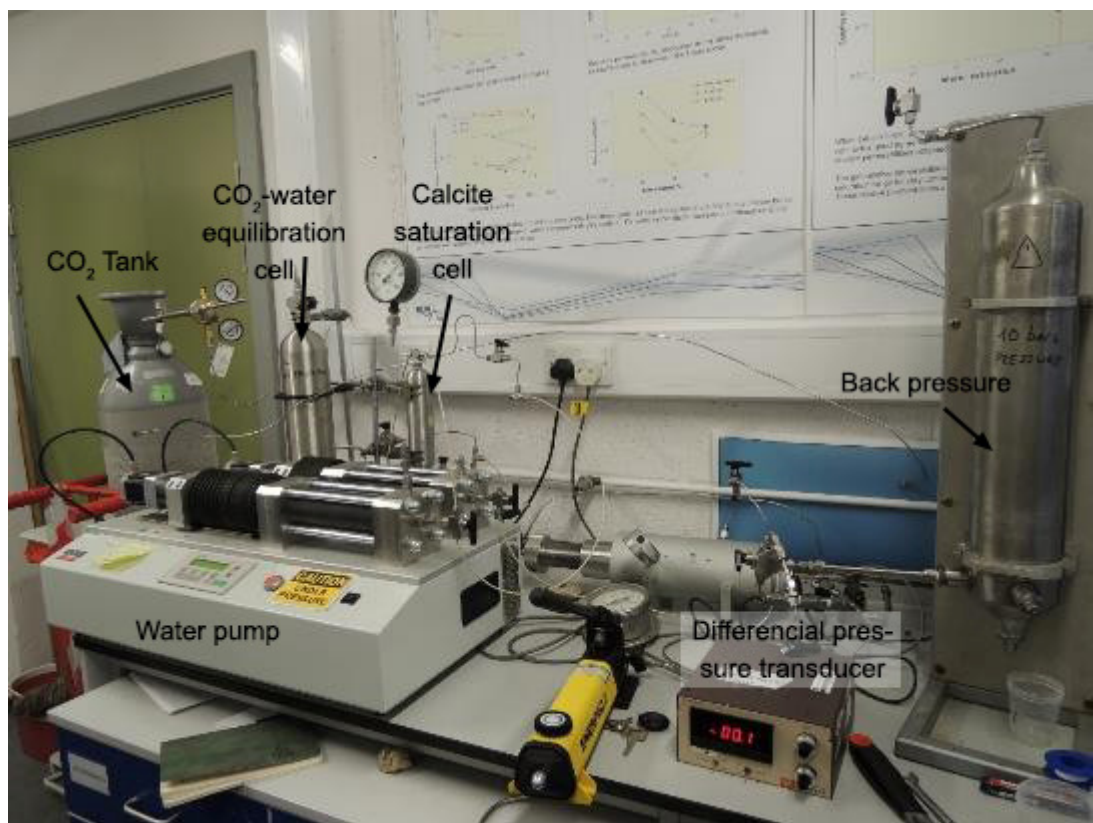


**Figure 6.3** Picture of the experimental assembly corresponding to Figure 6.2 with fluid preparation and injection on the left.

A preliminary test was conducted to evaluate CO<sub>2</sub> degassing in the core. A medical CT scanner was used to calculate the CO<sub>2</sub> saturation in the core using the same facility and methodology described in Chapter 3. The test exact protocol was as follow:

- (1) In order to calculate CO<sub>2</sub> saturation, the sample was first saturated with CO<sub>2</sub> and a series of 5 mm thick CT scans were taken. The pore pressure used was 1 MPa, similar to the pressure that would be achieved later on in the main experiment.

(2) The system was evacuated and saturated with water for two days at a pressure of 1 MPa. An identical series of CT scans of the water saturated sample was taken, ensuring the core holder occupied an identical position in the scanner.

(3) The back pressure tank was prepared by filling it with CO<sub>2</sub> at 1 MPa.

(4) CO<sub>2</sub>-saturated water was prepared at a pressure of 4 MPa and injected through the disc and sample. Soon after the start of the injection series of CT scans was initiated to monitor the CO<sub>2</sub> saturation evolution at regular intervals. Ten scans were taken over a period of two hours.

The main experiment protocol was as follow:

(1) The core and low permeability filter were saturated with brine and introduced in the core holder.

(2) The system was pressurized to 4 MPa on the core inlet end and to 1 MPa on the core outlet end.

(3) About one liter of CO<sub>2</sub> and calcite saturated brine was injected at constant pressure (4 MPa), first through the filter, then through the core.

(4) The permeability of the core/filter system and the fluid chemistry on both ends of the core holder was monitored at regular intervals.

(5) At the end of the experiment the core was taken to a SEM to observe potential calcite precipitates.

### **6.2.2 Sample description**

The experiment employed a cylindrical core (37.23 mm in diameter, 91.27 mm in length) of Lochaline sandstone. This sandstone is particularly pure, with 99.5% of 0.2-0.3 mm rounded quartz grains (Highley, 1977; Lowden et al., 1992); it has a permeability of 1.2 D and a porosity of 16%. The rationale for using this rock type in the experiment was firstly to provide a chemically neutral pore space for CO<sub>2</sub> degassing and calcite precipitation, thereby facilitating the interpretation of the fluid chemistry data and the observation of any calcite products in the core. Secondly, the very high permeability of this sandstone makes the pressure variation in the core negligible compared to the pressure drop achieved in the low permeability disc. This allows a better control on the experimental pressure and pressure homogeneity in the sample.

The low permeability disk (3.41 mm thick) was cut from a fairly unreactive sandstone (Hopeman sandstone), this sandstone is mainly composed of

quartz (83%), the remaining of the rock comprising various feldspars and clays. It has a permeability of 1 to 6  $\mu\text{D}$  and a porosity of 10%. The disk was placed at the inlet to provide the appropriate pressure drop. The core and the disk were wrapped in lead foil in order to stop diffusion of the  $\text{CO}_2$  into the rubber sleeve used to apply the confining pressure. The complete assembly is shown in Figure 6.4.

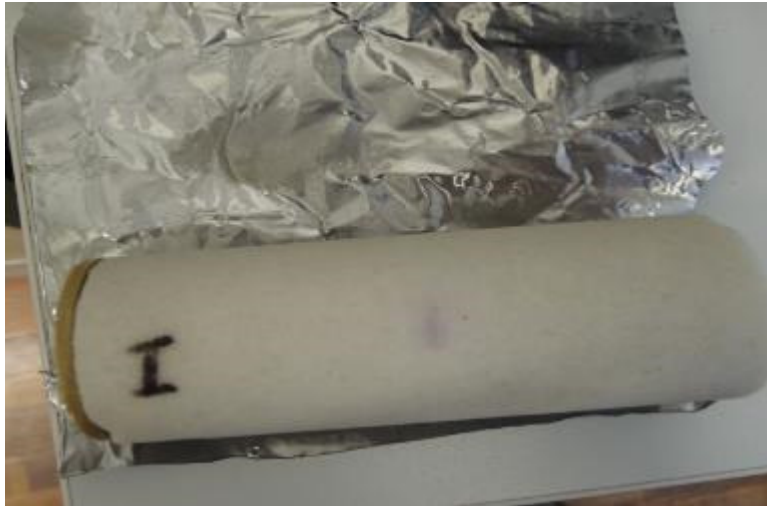


**Figure 6.4** Hopeman sandstone disc and Lochaline core montage (with the lead foil unwrapped) used in the experiment.

### **6.2.3 Injected fluid description**

The preparation of the reactive fluid was achieved in two steps. The first step was identical to the one used for  $\text{CO}_2$  saturation of brine in Chapter 3. For this experiment deionized water was saturated with 4 MPa  $\text{CO}_2$  pressure at room temperature. The product of this operation is  $\text{CO}_2$ -saturated water with a  $\text{CO}_2$  concentration of 1.37 mol/L and a pH of 3.1 (Calculations made with PHREEQC version 2.18.3).

The second step was specific to the experiments described here and consisted in the flow of this acidified water into a smaller high pressure vessel filled with 300 grams of pure industrial calcite in the form of small rounded grains (5 mm diameter). At this stage equilibrium was reached between the water, the  $\text{CO}_2$  and the calcite. The theoretical solubility of calcite and  $\text{CO}_2$  under these conditions are 0.06 and 1.43 mol/L respectively. At the outlet of this pressure vessel was placed a 1.2  $\mu\text{m}$  filter in order to limit the contamination of the system with large calcite fragments that could quickly clog the low permeability filter.

As shown in Figure 6.5, calcite solubility varies with CO<sub>2</sub> partial pressure and temperature. In this experiment, calcite solubility was about 0.06 mol/L at the point where fluid entered the low permeability disk (4 MPa, 25°C) and 0.036 mol/L at the outlet from the core (1 MPa, 25°C). Assuming that the fluid re-establishes equilibrium with calcite when the pressure is decreased, this corresponds to precipitation of about 2.5 g of calcite per liter of fluid. The corresponding volume change is 1 cm<sup>3</sup> which would decrease the porosity of the core from 16 to 15%. Possible variations in the core's permeability were expected.

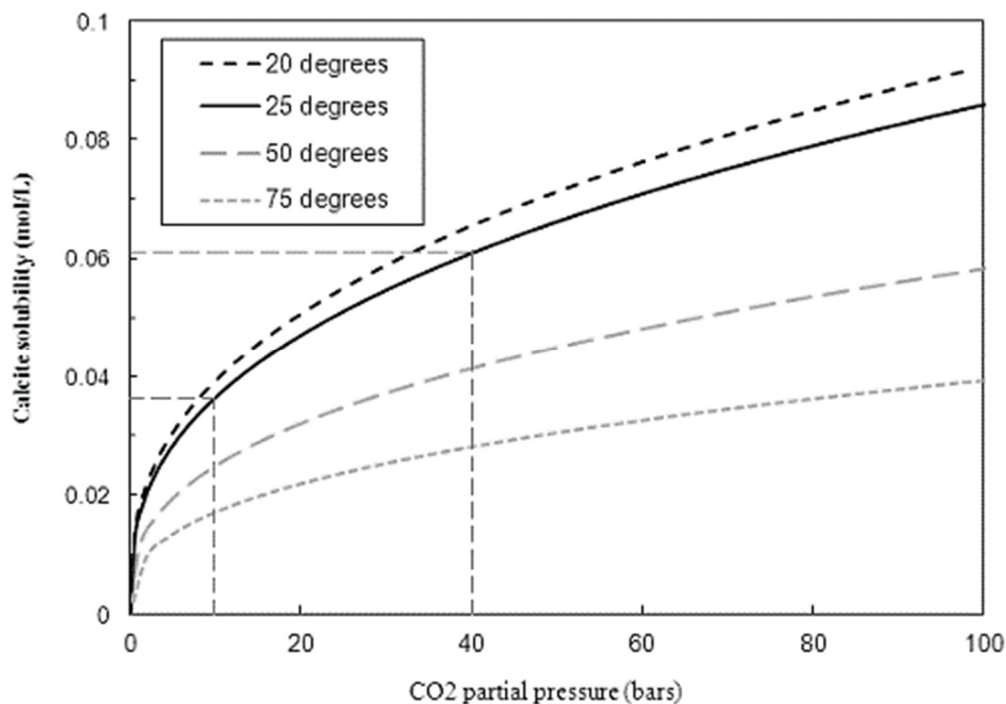


**Figure 6.5** The curves represent calcite solubility variations with CO<sub>2</sub> partial pressure in pure water along various isotherms. Assuming a constant temperature of 25°C the continuous curve indicates that a CO<sub>2</sub> depressurization from 40 bars (4 MPa) to 10 bars (1 MPa) would shift calcite solubility from 0.06 to about 0.035 mol/L. This means that 0.025 moles of calcite per liter of fluid can potentially precipitate.

## 6.3 Experimental results

### 6.3.1 CO<sub>2</sub> degassing preliminary test

Before the main experiment an initial test was performed by injecting CO<sub>2</sub>-saturated water (no calcite) through the disc and sample for 2 hours. This was done to verify that the CO<sub>2</sub> was effectively degassing in the sample when the 3 MPa pressure drop was applied. The degassing of CO<sub>2</sub> is a precondition for the calcite precipitation and it was uncertain how efficient it

could be depending on the pore space properties. The second goal of this test was to identify precisely the localization of the gaseous CO<sub>2</sub> phase to examine its relation with calcite precipitation in the subsequent experiment. Another purpose of this test was to flush the system with acidic water in order to get rid of any traces of reactive minerals, including original calcite, in the core. No change in permeability was detected hence confirming our initial assessment of the Hopeman sandstone as having low reactivity.

The scans conducted during the degassing experiment indicate that the CO<sub>2</sub> was effectively degassing within the Lochaline sandstone core with gaseous CO<sub>2</sub> saturation reaching 25% at the inlet and 5% at the outlet (Figure 6.6). These low saturations values indicate that the fluid remained oversaturated with CO<sub>2</sub> since the depressurization could have created about two liters of gaseous CO<sub>2</sub> per liter of water in an open volume, this would correspond to a CO<sub>2</sub> saturation of 66%.

Even though evidence for CO<sub>2</sub> presence was found, the exact dynamics of the CO<sub>2</sub> phase are unclear. The CT scans shows that the CO<sub>2</sub> saturation profile is achieved after only one pore volume and remains stable over the course of the entire experiment which lasted for 4 days (corresponds to the injection of 60 pore volumes). Another visible feature is the decrease in CO<sub>2</sub> saturation from inlet to outlet. What CO<sub>2</sub> degassing process can explain this almost instantaneous and stable CO<sub>2</sub> saturation gradient? Several hypothesis have been considered:

If CO<sub>2</sub> bubbles were formed and uniformly transported in the fluid one could expect the CO<sub>2</sub> saturation to quickly reach a stable value and the CO<sub>2</sub> bubbles to be uniformly spread across the sample. This hypothesis is thus contrary to the observed CO<sub>2</sub> saturation gradient. One explanation would be that the newly formed CO<sub>2</sub> bubbles dissolve back in water as they flow down the core, however this seems highly unlikely since the water should always remain oversaturated with CO<sub>2</sub>. Another explanation could be that CO<sub>2</sub> bubbles get trapped when flowing down the core, this could create the CO<sub>2</sub> gradient observed in the experiment but should also lead to a saturation build up near the source as more bubbles get trapped.

If the bubbles were not transported but rather directly trapped in the pore space after they are formed then a CO<sub>2</sub> saturation gradient in the early stages of the experiment could be expected. The decreasing CO<sub>2</sub> saturation away from the inlet could be explained by the decrease in new bubble formation along the way as CO<sub>2</sub> oversaturation of the water decreased.

However if this hypothesis were true the CO<sub>2</sub> saturation should continue to increase uniformly as fresh fluid is injected.

One last possibility is that the fluid remained oversaturated with CO<sub>2</sub> due to space constraints effectively stopping the nucleation of gas bubbles. In that case CO<sub>2</sub> bubbles could still be formed in the space at the interface between the low permeability disk and the core. They could then flow from this source and get trapped along the way. The source of gaseous CO<sub>2</sub> would stop once new bubbles could not physically enter the core and thus there would be no renewal of the CO<sub>2</sub> as well as no change in saturation. This hypothesis is in agreement with the stable CO<sub>2</sub> saturation and the decrease in saturation from the inlet to the outlet. This process was not observed since the CO<sub>2</sub> saturation gradient was already established at the time of the first CT scans (after 5 minutes). Also notable is that if this hypothesis were true there would be a very limited amount of CO<sub>2</sub> degassing and thus calcite precipitation.

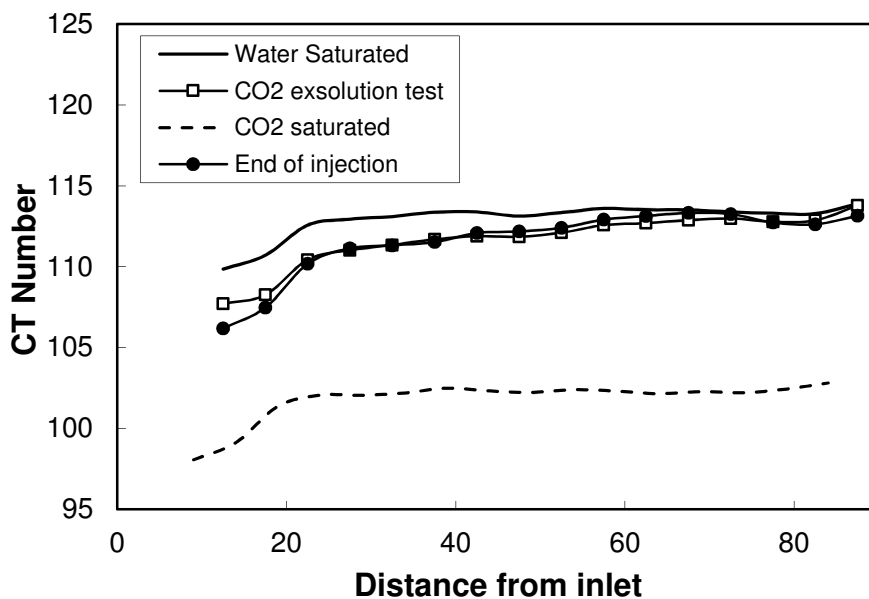


**Figure 6.6** CT value profiles under 100% water, 100% CO<sub>2</sub> and experimental conditions. The intermediate values at experimental conditions correspond to a CO<sub>2</sub> saturation of approximately 25% at the inlet and 5% at the outlet.

In summary this test demonstrated that the conditions for calcite precipitation would exist in the system at least at the point where fluid was flowing into the core.

### 6.3.2 Calcite precipitation main experiment.

Following the initial CO<sub>2</sub> degassing test the main calcite precipitation experiment was carried out. The precipitation experiment was similar in all

points to the previous test apart from the fact that the injected fluid was not only saturated with CO<sub>2</sub> but also with calcite and the duration of the injection was much longer.

The first evidences of calcite precipitation looked for were variations in the core porosity and permeability between starting and final values. There were no detectable changes of these parameters indicating at most only limited calcite precipitation.

This conclusion accords with the calcium concentration data for the inlet and outlet fluids (Figure 6.7). There is no significant change in calcium concentration between the inlet and the outlet fluids after the initial establishment of the experiment during the first 10 hours. This implies that calcite precipitation must have been very limited. Both inlet and outlet curves follow the same trend with an initial increase in Ca due to the fact that the core was initially saturated with pure water and a stable plateau around the expected calcium concentration at calcite saturation levels for equilibrium with a fluid at 1 MPa CO<sub>2</sub> pressure (24 mg/L). There is a notable scatter in the data which may be due to an error in sample preparation: the samples were not analyzed immediately which may have led to evaporation of some of them. Since all samples were treated the same way this error should not change the interpretation of the data overall.

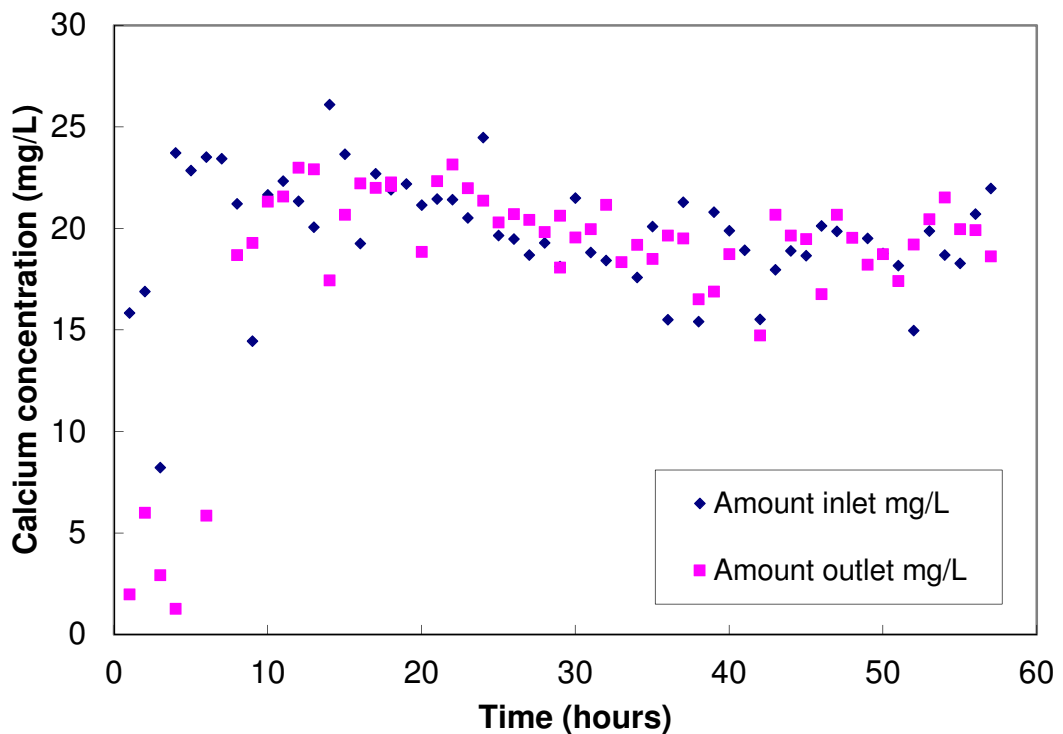


**Figure 6.7** Comparison of calcium concentrations at the inlet and outlet of the core holder during the main experiment.

A thorough SEM and EDS study was carried out on the core to search for carbonates and for calcite in particular. Infinitesimal trace amounts of calcite were found between the inlet and the center of the core. Some were formed on quartz others were found grown on trace amounts of undefined clays (Figure 6.8).

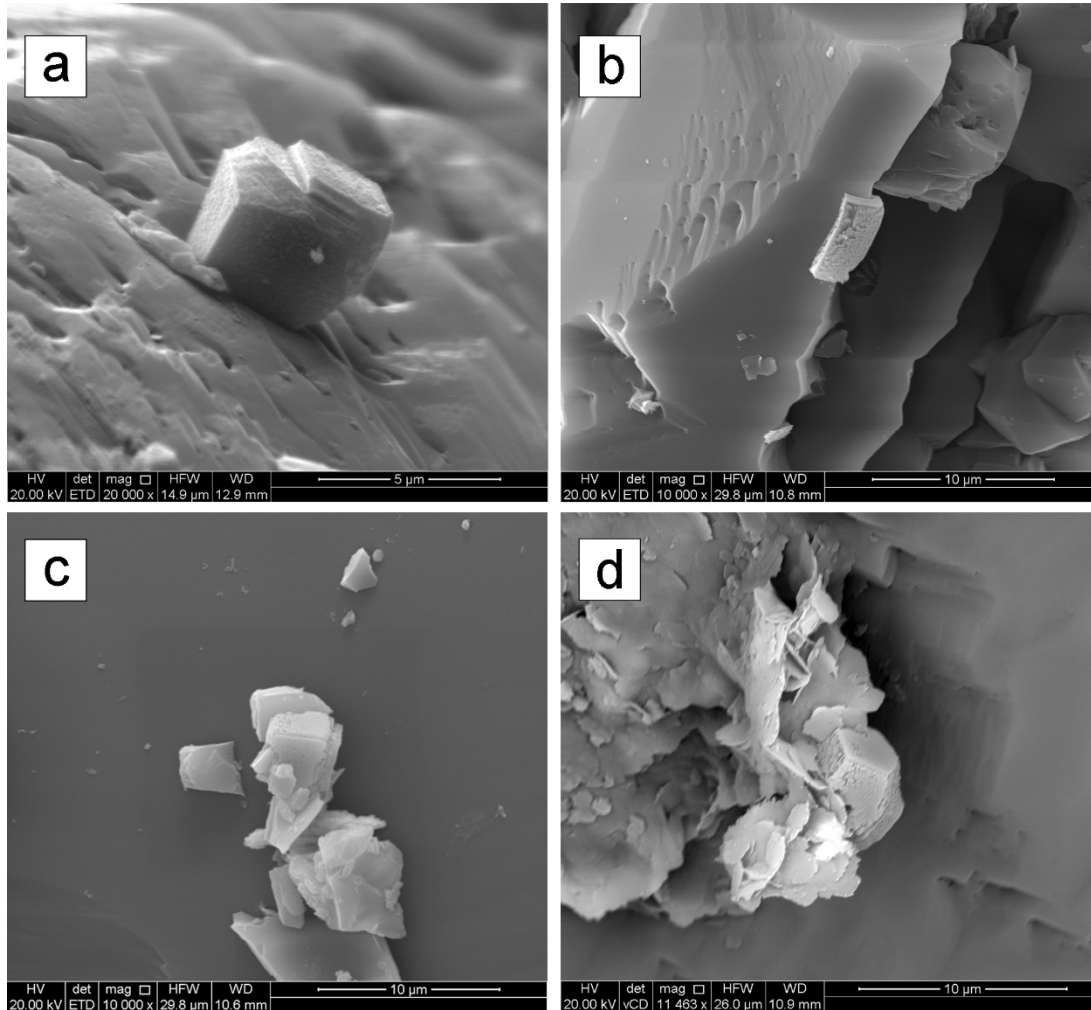


**Figure 6.8** Calcite grains, about 5 $\mu$ m in size, present at the inlet and middle of the core. Calcite crystals were extremely hard to find. Slightly irregular rhombohedral shapes typical of growing calcite crystals were found, this is particularly visible in a). On very rare occasions calcite was found on quartz grains as in a) and b). More frequently calcite was found on unidentified clays as in c) and d), although such clays were present in negligible amounts.

The results are significantly different at the outlet even though no carbonates can be observed at low magnification (Figure 6.9). Carbonate structures (possibly ankerite from the morphology) a few tens of microns across occur on individual quartz grains. Also visible is a thin film covering the grains. Upon closer inspection this film appears to be related to small carbonate

spheres with the morphology of Amorphous Calcium Carbonate (ACC) nanoparticles (Rodriguez-Blanco et al., 2011). It is unclear if the accumulation and homogenization of ACC spheres on the quartz surface generated this carbonate film or if this is the result of a carbonate concentrated solution covering the grains and drying out during sample preparation for SEM.

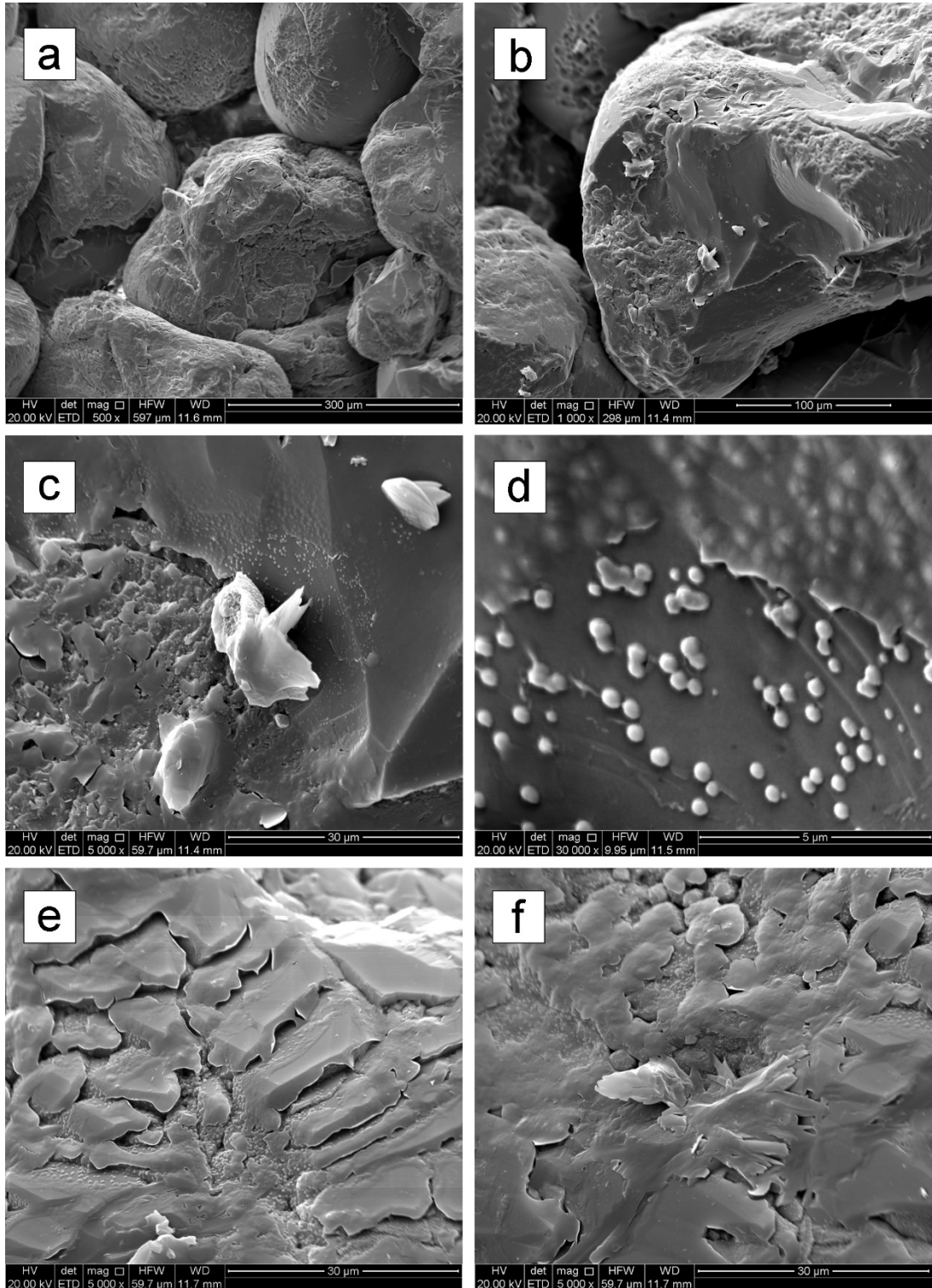


**Figure 6.9** Views of carbonate structures present at the outlet of the core at increasing magnification (a, b, c, d). Complementary views of carbonate spheres and film coating the quartz grains (e, f) and their relation to larger carbonate structures (f).

In summary, small amounts of carbonates did precipitate and accumulate near the outlet of the core. It was not possible to determine if the carbonates precipitated in situ or were transported. If ACC did form in the fluid and was transported this could mean that calcite precipitation could have occurred in large quantities but have been flushed away. Since all fluid samples were acidified to avoid calcite precipitation it is impossible to tell if ACC was present or not in the outlet fluid.

Another issue is the transition from very few large crystals of calcite at the inlet to abundant ACC a few centimeters away. Is it due to an abrupt spatial transition in the fluid chemistry or is it the result of a transport phenomenon? One possibility is that both crystals and ACC could form at the disk sample interface, lighter ACC spheres would be transported down the core while rarer calcite crystals would grow slowly; although it seems unlikely that two morphologies would grow at the same time and same place.

Boundary conditions such as the presence of CO<sub>2</sub> bubbles at the inlet and outlet faces of the core could be significant and it would be beneficial to conduct the same experiment on a core of different length.

The effect of boundary conditions is quite evident when looking at SEM images taken from the Hopeman sandstone disc. While no carbonates can be found on the inlet face there is a massive amount of precipitation 3mm further in, on the face in contact with the inlet of the Lochaline sandstone core (Figure 6.10). This precipitation probably explains the permeability trend of the Hopeman disk, which steadily decreased over the course of the experiment before it was eventually halved. This observation could be in agreement with the hypothesis of CO<sub>2</sub> degassing and calcite precipitation occurring in the space between the disk and the sample, but precipitation may have begun within the disc.

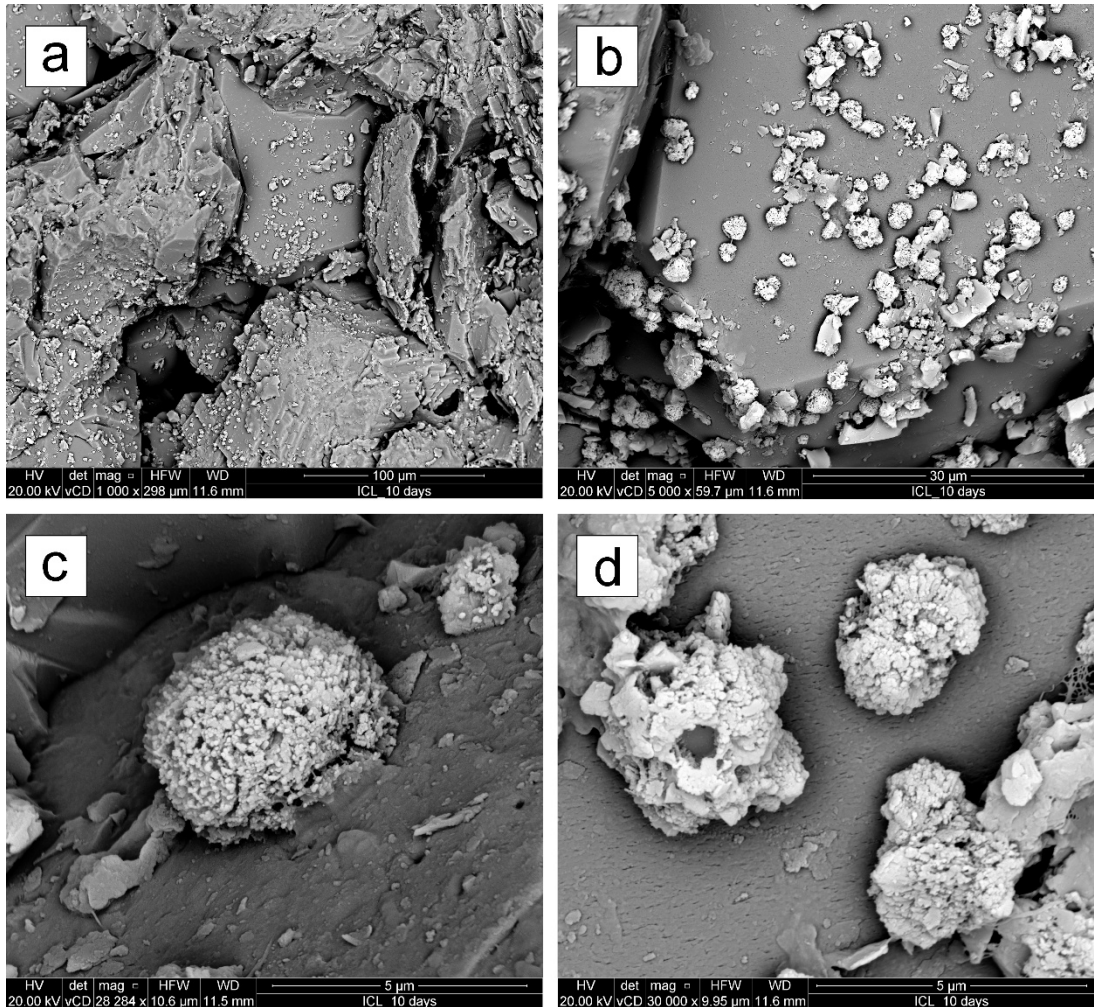


**Figure 6.10** Carbonates present at the outlet of the Hopeman sandstone disc at increasing magnification (a, b, c) and detail of these structures (c, d). The proliferation of these carbonate assemblages on quartz grains could be an indicator of fast and homogeneous carbonate nucleation during the experiment in this area.

Examination of the sample with a groove to enhance CO<sub>2</sub> degassing did not provide any evidences of calcite precipitation. Since the CO<sub>2</sub> bubbles could travel freely in the groove towards the outlet of the core it is possible that calcite precipitates, if present in the form of micron size ACC spheres, have been flushed out of the system.

## 6.4 Conclusions

This chapter has presented an original method to investigate the conditions of calcite precipitation and its possible effects on the rock properties. The experimental protocol was inspired by a realistic GCS scenario and was designed to follow a likely sequence of events with CO<sub>2</sub>-saturated water flowing through rock samples and undergoing a pressure drop.

The experiment demonstrated the occurrence of CO<sub>2</sub> degassing followed by calcite precipitation in a chemically inert medium once a moderate, albeit abrupt, pressure drop is applied. It is however unclear if calcite precipitation happened throughout the core and at all times. If it did then most of the precipitation products must have been flushed out of the core (although no traces remained). Alternatively, calcite precipitation might have happened at only one location (the disk - core inlet interface) or at only one time (e.g. the start of the experiment). Both scenarios could explain the relatively low amount of calcite precipitation observed.

This study has demonstrated the possibility of investigating calcite precipitation in GCS experimentally, but raises many questions that require a comprehensive experimental program beyond the scope of the present study. Additional experiments are necessary to evaluate the hypotheses and provide a definitive interpretation of the results. For instance it would be beneficial to conduct an analysis to detect possible particles of calcite in suspension flushed at the outlet of the core. It would also be beneficial to vary the experimental parameters such as pressure drop, sample dimension, sample nature or experimental time to determine the main parameters upon which the observed CO<sub>2</sub> degassing and calcite precipitation depends.

Despite these uncertainties it appears that the effect of calcite precipitation on the permeability of the thin Hopeman sandstone disc was very large even though it happened mainly at the outlet. This is particularly relevant for issues of CO<sub>2</sub> leakage through low permeability caprocks where the pressure drop could be significant. It is likely that the large oversaturation index of calcite might have promoted homogeneous nucleation of ACC in the fluid and thereby allowed subsequent transport of the products. This should increase the effect on low permeability rocks as precipitates are more likely to block the pore throats in this situation.

Implications of this work at the reservoir scale are hard to foresee since it will depend on a large number of parameters controlling both fluid rock interactions and fluid pressure. Also it is likely that precipitates escaped the core and this should not happen at the reservoir scale. The broad significance of this work from a reservoir scale perspective is that low permeability barriers and paths to the surface will become more impermeable if CO<sub>2</sub> and calcite saturated fluids flow through them and experience a pressure drop.

## **Chapter 7**

### **Long term evolution of capillary trapped CO<sub>2</sub> bubbles, experiments and simulations.**

#### **7.1 Introduction**

The experiment presented in this chapter constitutes the first attempt to study the long term evolution of capillary-trapped CO<sub>2</sub> bubbles. The capillary trapping (or residual trapping) mechanism was introduced in Chapter 2; in recent years it has been studied to evaluate the extent of capillary trapping possible, as it is seen as a very efficient way to immobilize CO<sub>2</sub>. Capillary trapping experiments to date have run for short time scales of a few hours or days (Krevor et al., 2011; Pentland et al, 2011; Iglauer et al, 2011). These experiments were aimed at observing and quantifying the trapped CO<sub>2</sub> bubbles and studying the effect of rock heterogeneity.

On longer term capillary trapping may however not be stable for CO<sub>2</sub> in brine. This is because CO<sub>2</sub> solubility in brine may give rise to an Ostwald ripening process whereby small CO<sub>2</sub> bubbles would dissolve while large CO<sub>2</sub> bubbles would grow at their expense; this is analogous to ice crystal ripening and growth leading to frost rock damage (Everett, 1961). The sole driving force behind this is the capillary pressure (see Chapter 2 section 2.2.3.2) which is higher for smaller bubbles and controls the CO<sub>2</sub> solubility at the CO<sub>2</sub>-brine bubble interface. This could enhance small bubbles dissolution up to a point where the aqueous CO<sub>2</sub> concentration reaches a high enough level to drive growth of larger bubbles. At this point capillary trapping could enter into a transient unstable phase with large bubbles constantly consuming the excess dissolved CO<sub>2</sub> and smaller bubbles constantly dissolving until only large bubbles remain. This process once started would be self-accelerated since a reduction or augmentation in bubble radius during dissolution and growth should give rise to an increase or decrease in the bubble capillary pressure respectively.

Significant CO<sub>2</sub> migration on the time scale of months or years could imply that capillary trapping is not such a secure mechanism for carbon sequestration. This chapter presents an experimental test of the hypothesis that small CO<sub>2</sub> bubbles will dissolve due to their higher capillary pressure and that the dissolved CO<sub>2</sub> will migrate into larger CO<sub>2</sub> bubbles. The second part of the chapter presents a numerical simulation of the transfer of CO<sub>2</sub>

from small bubbles to large ones via the aqueous phase, carried out using a Matlab code developed for this purpose.

## 7.2 Experimental design

Cores were drilled parallel to layering in a sample block of Cenomanian (Upper Cretaceous) sandstone collected near the city of Orange in France. This rock is known for its important cataclastic deformation bands associated with thrust faults movements caused by the Pyrenean compression (Wibberley et al, 2000). It is made of 95% quartz and 5% feldspar and the average grain size is 650  $\mu\text{m}$  (Soliva et al, 2013). Cataclastic bands present in the rock are small scale structures, not visible with large scale sonic velocity surveys, that can be efficient barriers to fluid migration since they are associated with a drastic reduction in the porosity and grain size (Ogilvie and Glover, 2001), see Figure 7.1.

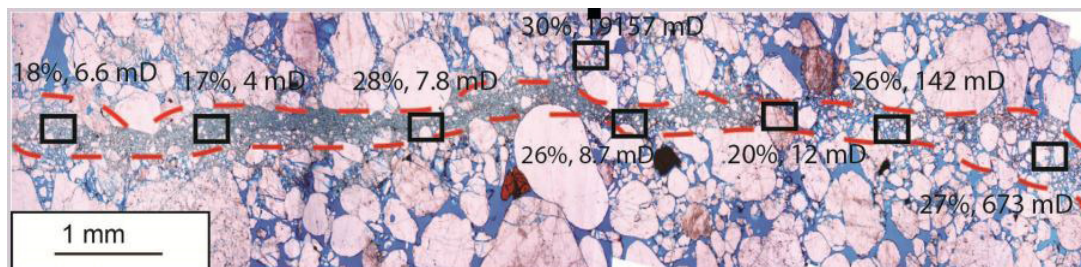


**Figure 7.1** Example of deformation bands and associated variations in flow properties presented in Torabi and Fossen (2009).

Figure 7.2 shows the two cores prepared for the experiment and a schematic representation of the different layers with their associated  $\text{CO}_2$  residual bubbles is shown in Figure 7.3.

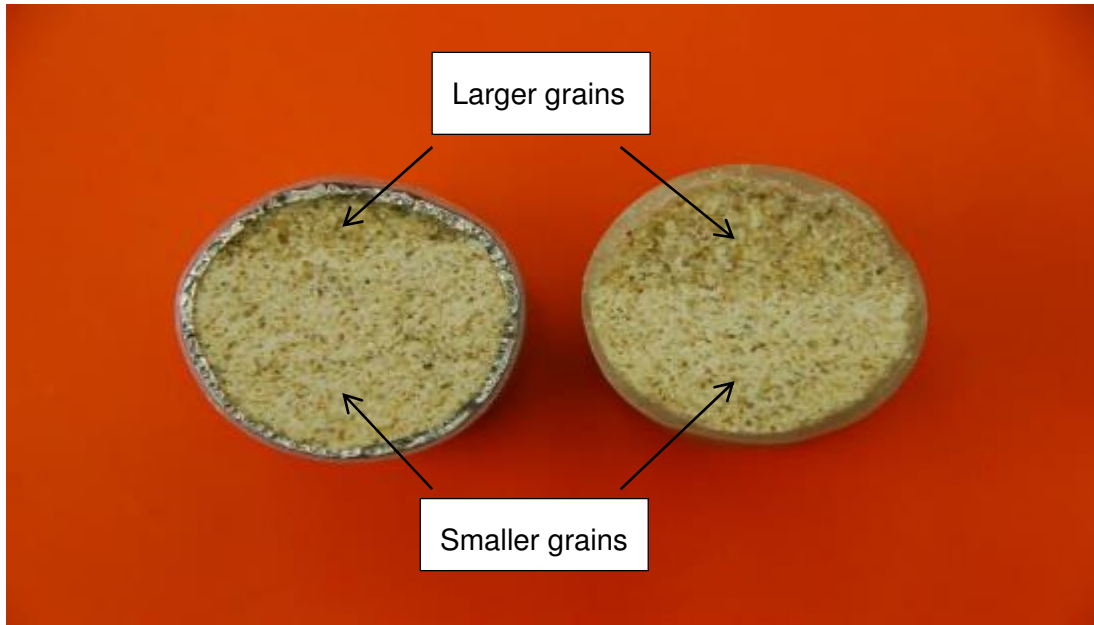


**Figure 7.2** Picture of two Orange Sandstone cores prepared for the experiments showing variations in grain size and cementation. The top darker part is composed of larger and un-cemented grains. The lower brighter part is composed of the same material but have been crushed and cemented due to tectonic stresses. An epoxy resin layer is applied to prevent the friable part of the core to fall apart (see right core). A fine lead foil is used to limit CO<sub>2</sub> diffusion into the core holder (see left core).

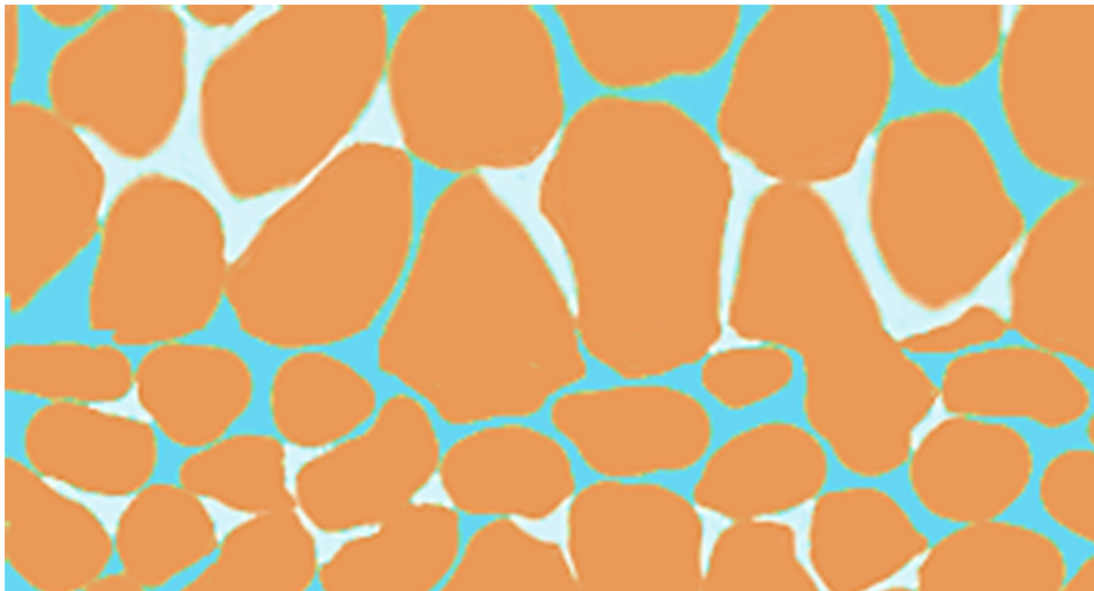


**Figure 7.3** Schematic representation of the region close to the large grains/small grains transition with hypothetical CO<sub>2</sub> ganglia (in white) of different size trapped in the pore space (with grains in brown and brine in blue).

The preparation for the experiment consisted of an Orange core that was successively saturated with water and then CO<sub>2</sub> to establish the end-member saturation profiles, using a Picker medical CT scanner. The

conditions for CO<sub>2</sub> capillary trapping were then created by generating a slow capillary flow of CO<sub>2</sub>-saturated water into a rock core containing only supercritical CO<sub>2</sub>. Capillary trapping was considered established after a day (the first breakthrough of water at the outlet of the core was observed after about one hour); the core holder was then closed on the outlet end to stop fluid flow and was left in a large oven (Figure 7.4) to maintain a constant temperature during the course of the experiment that lasted about 3 months. The experimental pressures and temperatures were close to the critical point of CO<sub>2</sub> with 7.35 MPa and 35°C respectively. The core holder was wrapped in 5 cm thick insulating foam to help maintain a constant temperature. The pore pressure was monitored with a 0-10 MPa Omega pressure transducer. The thermal inertia of the aluminum core holder coupled with the insulation layer allowed the quick transportation of the core holder from the oven to the CT room to conduct CT scans. In total, five of such scans were obtained at days 1, 2, 8, 95 and 97 after completion of the capillary trapping procedure. A fast scanning procedure was used to complete the CT profiles in less than five minutes and avoid significant variations of the fluids and core temperatures. This strategy was successful since during this time span no changes in pore pressure due to possible CO<sub>2</sub> state change were noticeable. The only significant drawback of the fast scanning procedure was the impossibility to precisely image the bubbles and their radius evolution. It was however possible to monitor the time evolution of the CO<sub>2</sub> and water saturations in the different layers.



**Figure 7.4** Experimental set up. In the foreground, CO<sub>2</sub> bottle and ISCO pump. In the background, oven where the core holder and a container filled with CO<sub>2</sub>-saturated water are placed during the experiment.

### 7.3 Experimental results

The experimental results were obtained through image processing of the CT scans using a Matlab code to crop the images and keep the region of interest that is the core center (Figure 7.5). Care was taken to ensure that the core was placed in an identical fashion in the CT scanner for all the scans in order to obtain the most accurate representation of the saturations without using large scale averaging. For instance a small rotation of the core around its long axis would provide accurate saturation results averaged over the cross section but would give unrealistic results at the pixel level (such as saturations lower than 0% or larger than 100%). In practice experimental errors in core placement (rotation plus translation) were too large to avoid unrealistic results at the pixel scale but were low enough to allow the definition of three zones where the saturations could be averaged (Figure 7.6).

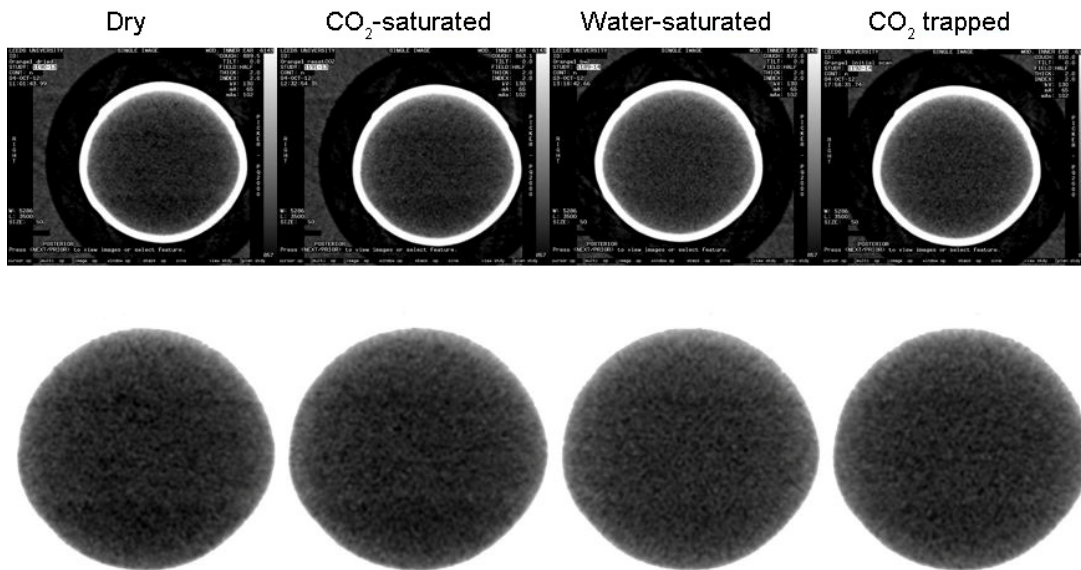


**Figure 7.5** Image segmentation of the CT scans. Cross sections taken at various stages of the experiment are shown. Special attention was put on the core placement (rotation and translation) in order to allow images comparison. Changes in saturation are almost invisible to the naked eye.

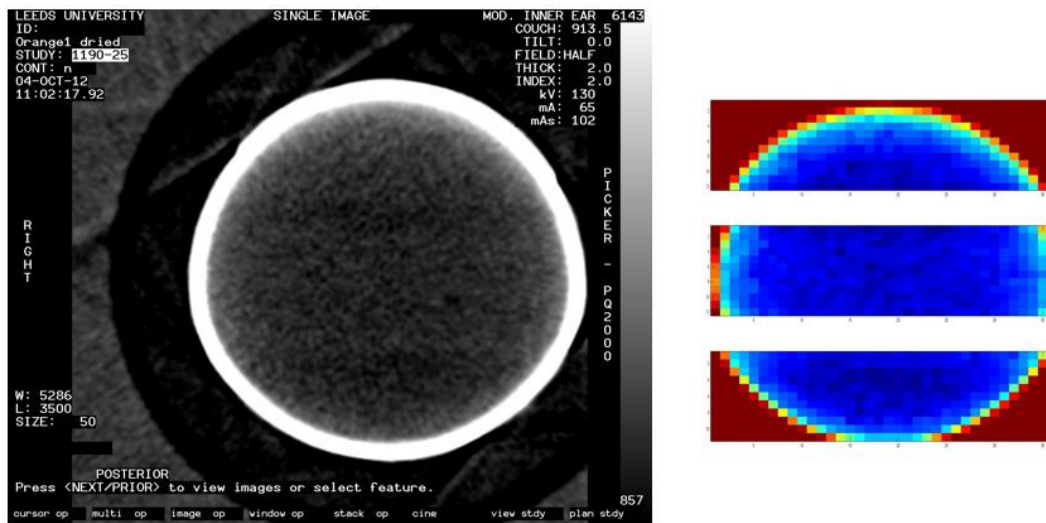


**Figure 7.6** Cross section division in three zones that correspond to the rock core layering. The division is performed manually after image segmentation with Matlab.

The three zone division was done to reflect the layering of the sample. The top third of the sample was composed of crushed and well cemented grains belonging to a cataclastic band, the lower third was representative of the main sample block with poorly cemented (sand) and large grains (650  $\mu\text{m}$  on average, roughly one order of magnitude larger than the crushed grains); the middle part was intermediate with small, cemented grains but a large

porosity. The porosity profiles of the three zones are shown on Figure 7.7. The top part of the core had a porosity of 10% on average while the bottom and middle parts had a porosity of 15-16%.

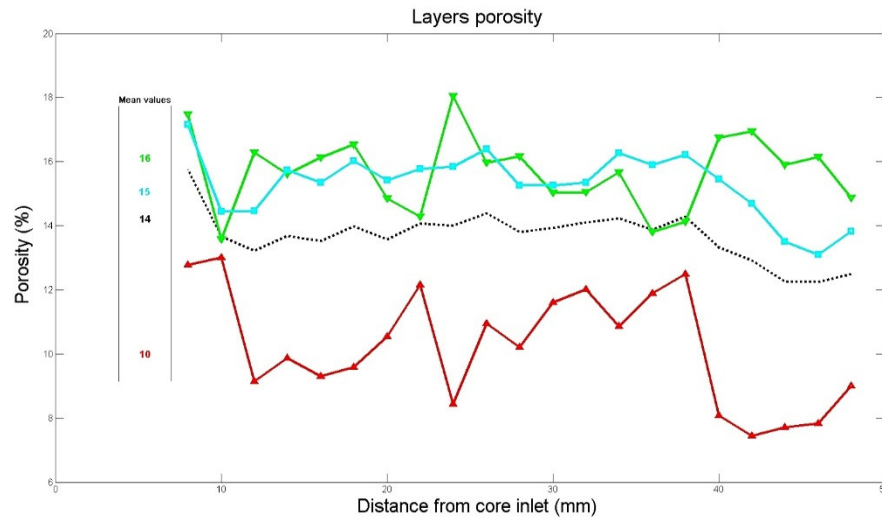


**Figure 7.7** Porosity profiles showing the dichotomy between the top layer (red triangles) and the middle and bottom layers (blue squares and green triangles respectively). The dotted black curve is the mean porosity along the core and is fairly constant.

Figure 7.8 shows the CO<sub>2</sub> saturation profile in the sample, within one day of the completion of the CO<sub>2</sub> capillary trapping procedure. This figure shows that the total amount of initially trapped CO<sub>2</sub> is very high, 44%, making capillary trapping an apparently very efficient CO<sub>2</sub> sequestration mechanism. Also evident from this figure is a CO<sub>2</sub> saturation gradient from the inlet to the outlet with comparatively more CO<sub>2</sub> at the inlet than at the outlet; it is unclear if this was due to the experimental protocol or to the rock's intrinsic properties. Uncertainties on the saturation measurement can typically attain  $\pm 5\%$  in absolute value. The saturation gradient is quite visible on the top and middle sections of the core but less on the bottom section. The bottom section also displays a much lower CO<sub>2</sub> saturation. The higher absolute saturation and steeper saturation gradient in the top and middle zones may have arisen if the injected water partially bypassed these zones and went preferentially through the high permeability bottom region. In summary the rock core initially contain two regions, the top and middle ones, with smaller pore size and larger CO<sub>2</sub> saturation (about 50%) and one bottom region with a larger pore size and a lower CO<sub>2</sub> saturation (about 25%). Assuming a correlation between bubbles and pore sizes it was expected that CO<sub>2</sub> would be transferred from the top and middle section of the core towards the bottom.

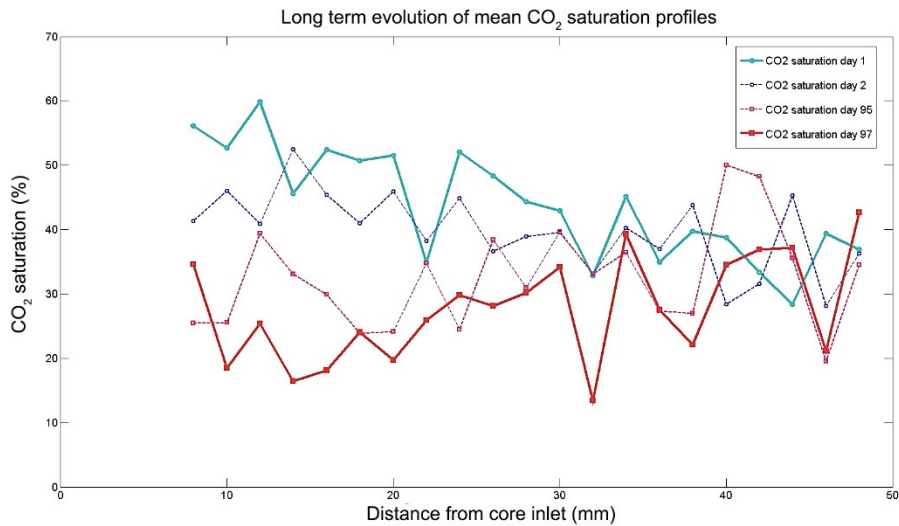


**Figure 7.8** Time evolution of the average saturation profile (averaged over the whole core).

Figure 7.9 displays the evolution of the CO<sub>2</sub> saturation in the whole core between the beginning and the end of the experiment. A rather surprising result is that the total CO<sub>2</sub> saturation significantly decreases with time. One possible explanation is that at early stages all CO<sub>2</sub> bubbles start to dissolve since the capillary pressure puts them out of equilibrium with respect to the surrounding fluid. Another possibility is that the pore pressure was lower during the capillary trapping procedure which leads to CO<sub>2</sub> bubble shrinking later on. As for the longer term trend one explanation is that dissolved CO<sub>2</sub> escaped the core despite the presence of the lead foil but there are no evidences for that. There might be some lateral transfer involved given the visible reduction in the CO<sub>2</sub> saturation gradient from inlet to outlet but it is impossible to give a definite interpretation because of the large and complex variations in saturation along the core axis.

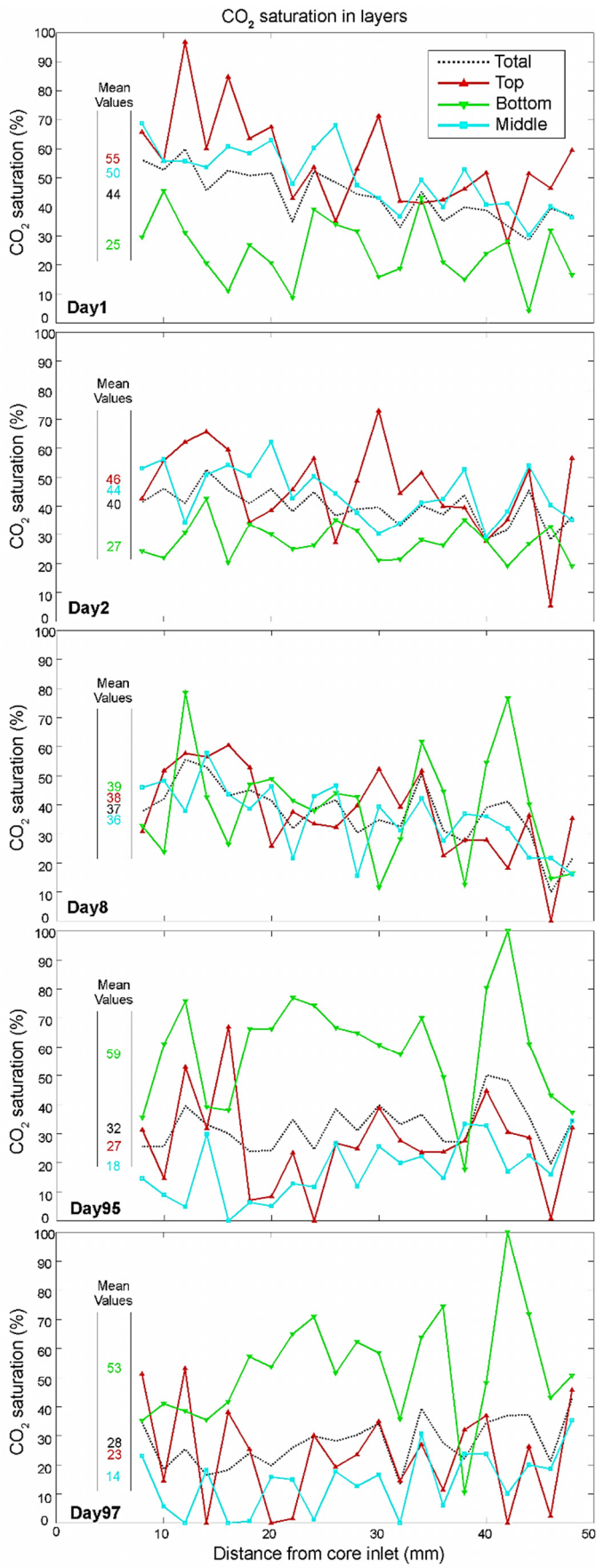


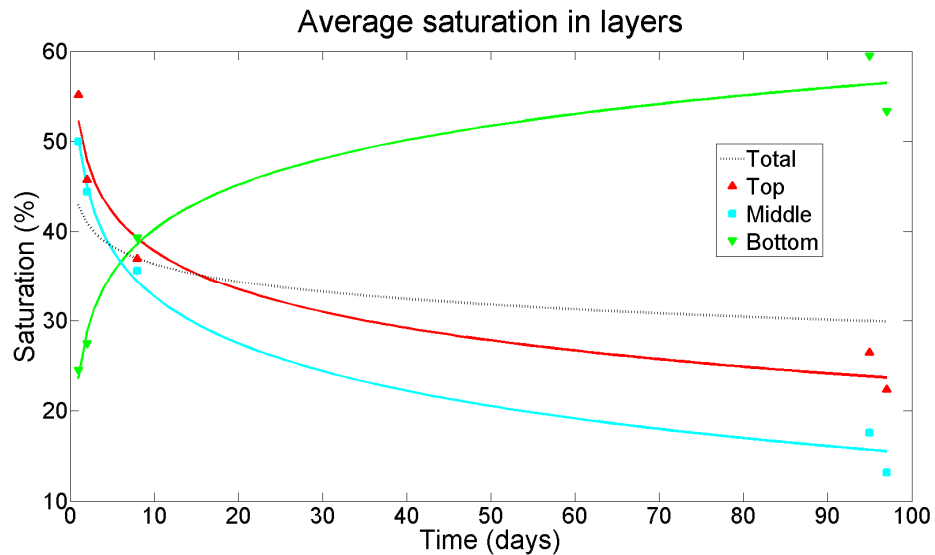
Figure 7.9 Time evolution of the CO<sub>2</sub> saturation in the different layers.

Figure 7.9 shows the evolution of the CO<sub>2</sub> saturation in the three regions of the core with time. It is evident from this figure that the CO<sub>2</sub> saturation in the bottom layer increased at the expense of the top and middle regions as predicted by the thermodynamic model outlined above. The vertical CO<sub>2</sub> transfer seems to be spread over the whole length of the core and is taking place against gravity which very likely indicates a transfer by diffusion. Advection against gravity seems very unlikely since bubbles are normally capillary trapped and have a lower density than water; moreover there should be no water pressure gradient in such static conditions (core holder closed on one end and constant pressure maintained on the other end).

The redistribution of CO<sub>2</sub> was fast at the early stages (days 1-2-8) and had probably reached a stable configuration well before the end of the experiment (days 95-97). The repeatability of the measurements is just correct (see days 95-97) with an uncertainty of about 10% on the saturation value remaining.

It is easier to visualize the CO<sub>2</sub> transfer by plotting the mean saturation of each layer against time and this is done in Figure 7.10. Given the uncertainty in the measurements and the scarcity of data points it is uncertain how quickly the CO<sub>2</sub> transferred, but a logarithmic law seems to give a good fit to the data. The trends are in good agreement with the hypothesis that CO<sub>2</sub> is transferred from the top and middle regions towards the bottom one. For instance it appears that the middle region is depleted in CO<sub>2</sub> before the upper one.

After about 100 days the CO<sub>2</sub> saturation in the fine-grained "small bubbles" regions decreased from 50-55% to 15-25% while it increased in the coarse "large bubbles" top region from 25% to 55%.



**Figure 7.10** Time evolution of the mean CO<sub>2</sub> saturation over the core length in each layer.

## 7.4 Numerical Simulation of CO<sub>2</sub> Redistribution

Attempts were made to simulate this experiment with a purpose-written Matlab code. The primary goal was to evaluate the possibility of such CO<sub>2</sub> transfer to happen due to capillary pressure and CO<sub>2</sub> diffusion driving forces. The second goal was to understand the influence of the different variables on the characteristics of the CO<sub>2</sub> transfer such as its magnitude and speed. The final goal was to extrapolate the results to a reservoir scale problem.

### 7.4.1 Code description

Following the work of Streets and Quake (2010) on the Ostwald ripening of clusters during protein crystallization; and of Chiotellis and Campbell (2003) and Shah et al. (1998) on the proving of bread dough, a Matlab code was developed to simulate the dissolution and growth of CO<sub>2</sub> bubbles in a pore fluid (Appendix D). In this code the physical space is divided into open volumes containing water and CO<sub>2</sub> bubbles of various sizes. In each volume the water pressure  $P_{\infty}$  and temperature  $T$  are considered constant. The CO<sub>2</sub> concentration in the water  $C_{\infty}$  is allowed to vary instantaneously and homogeneously across the whole volume as CO<sub>2</sub> bubbles shrink or expand. A schematic representation and the main parameterization of such volumes is presented in Figure 7.11. The molar transfer of CO<sub>2</sub> between the bubbles and the water  $Q$  is a function of the interfacial concentration  $C^*$  (which depends on the bubble pressure) and on the CO<sub>2</sub> diffusion coefficient  $D_{CO_2}$  according to Equation 7.1 (Adapted from Shah et al., 1998).

$$Q = \frac{dn}{dt} = \frac{Z\pi D^2}{6RT} \left( 3P_\infty + \frac{8\gamma}{D} \right) \frac{dD}{dt} \approx 2\mathcal{D}_{CO_2}(\pi D)(C_\infty - C^*) \quad (7.1)$$

Where  $n$  is the number of CO<sub>2</sub> moles in the bubble,  $Z$  the compressibility factor of CO<sub>2</sub>,  $D$  the CO<sub>2</sub> bubble diameter and  $\gamma$  the CO<sub>2</sub>-water interfacial tension.

The bubble pressure is calculated using the Young-Laplace equation and is initially higher than the fluid pressure for all bubble sizes due to surface tension. The bubble interfacial CO<sub>2</sub> concentration  $C^*$  is calculated at every time step for the new bubble pressure using the equations of Duan and Sun (2003) for CO<sub>2</sub> solubility. According to Equation 7.1 small bubbles dissolve faster than larger ones. As small bubbles dissolve, the CO<sub>2</sub> concentration in the water  $C_\infty$  can rise sufficiently to exceed the interfacial concentration  $C^*$  of larger bubbles and drive further growth. Rearranging Equation 7.1, the variation in bubble size is calculated with Equation 7.2 at every time step.

$$\frac{dD}{dt} = \frac{12RT\mathcal{D}_{CO_2}(C_\infty - C^*)}{3P_\infty + 8\gamma} \quad (7.2)$$

It is possible to define separate volumes containing different bubble size distributions analogous to the separate layers in the layered core used in the experiment. The movement of aqueous CO<sub>2</sub> between separate volumes is controlled by diffusion and is calculated using an explicit finite difference scheme.

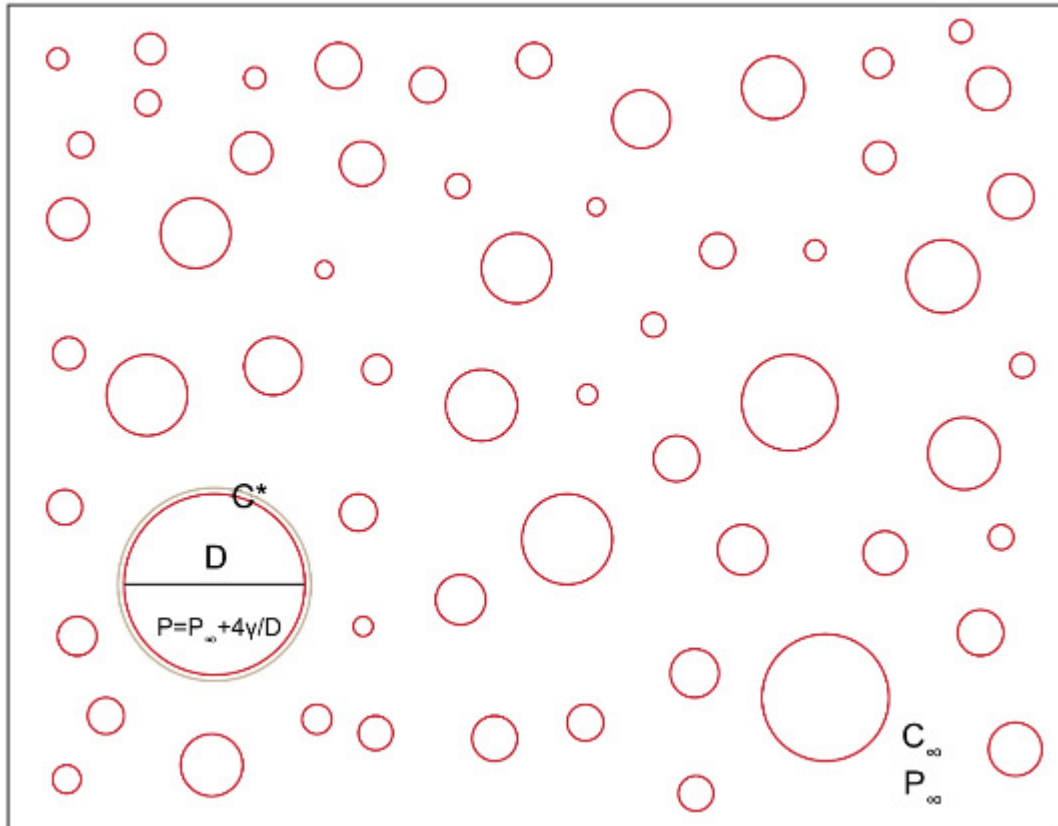


**Figure 7.11** Schematic representation of a simulation volume with basic parameters involved in the calculations. The volumes are open (e.g. if CO<sub>2</sub> bubbles dissolve the volume is refilled with external water). The spherical bubbles behave as if growing or dissolving in an infinite volume (e.g. there is no competition between bubbles for the assimilation of nearby aqueous CO<sub>2</sub>). Possible bubble coalescence is also neglected.

#### **7.4.2 Simulation results**

The parameters used for the simulations are detailed in table 7.1. For simplicity only two volumes (layers) were used in all simulations. In each simulation all parameters were identical in the two layers apart from the bubble size distribution and the initial CO<sub>2</sub> saturation. Layer 1, containing the smallest bubbles had an initial CO<sub>2</sub> saturation of 50% while Layer 2, containing the larger bubbles, had an initial CO<sub>2</sub> saturation of 25%. These values were based on the initial conditions of the experiment. A temperature of 35 °C and a background pressure of 7.35 MPa (not for all simulations) were also chosen to mimic experimental conditions.

It is expected that the interlayer CO<sub>2</sub> transfer will primarily depend on the absolute bubble sizes in layers 1 and 2, the bubble size difference between layers 1 and 2 as well as on other background parameters such as CO<sub>2</sub> diffusion coefficient and fluid pressure. Several simulations series were designed to investigate those effects separately.

An important preliminary remark is that all simulations were initiated with the same CO<sub>2</sub> saturations and that at constant CO<sub>2</sub> saturation in a Layer, a multiplication of bubble radius by 10 correspond to a division of the initial bubble number by 1000 and an augmentation of the total bubble surface by 100, this translate into a division of the interfacial area per unit volume by 10. The effect of this is a reduction in the overall CO<sub>2</sub> diffusion across bubbles.



A first simulation series (1a, 1b and 1c) was made to evaluate the effect of absolute bubble sizes and bubble sizes ratio between the two layers for the timing of the interlayer CO<sub>2</sub> transfer. The bubble sizes ranged between 5 and 500µm and thus could be representative of a large number of bubbles expected in real rocks. Figure 7.12 shows the CO<sub>2</sub> saturation in the two volumes and the evolution of bubble sizes in the three cases 1a, 1b and 1c. The fastest case in term of CO<sub>2</sub> transfer is 1a, which corresponds to the smallest bubbles and to a bubble radius ratio of 10. In case 1b the radius ratio has been increased to 100 which should accentuate the interfacial concentration gradient between small and large bubbles and thus the CO<sub>2</sub> exchange rate. This is however counterbalanced by the lower interfacial area per unit volume in Layer 2 which is filled with 500 µm diameter bubbles (instead of 50 µm in case 1a). In case 1c the bubble sizes in all volumes have been multiplied by 10 compared to case 1a, this produced a much slower CO<sub>2</sub> transfer.

The intermediate conclusions that can be drawn from these first simulations are the following: the key conclusion is that accounting only for the diffusion of CO<sub>2</sub> through bubbles of carefully selected radiuses it is possible to reproduce the experimental saturation reversal after three months. The saturation changes are linear in the simulations whereas the experimental results suggested that the CO<sub>2</sub> saturation change followed a logarithmic law. However the experimental data could be equally well fit by the simulated trend, because of the paucity of data points. Another discrepancy is that the overall CO<sub>2</sub> saturation does not decrease in the simulation but is constant, as required by the boundary conditions.

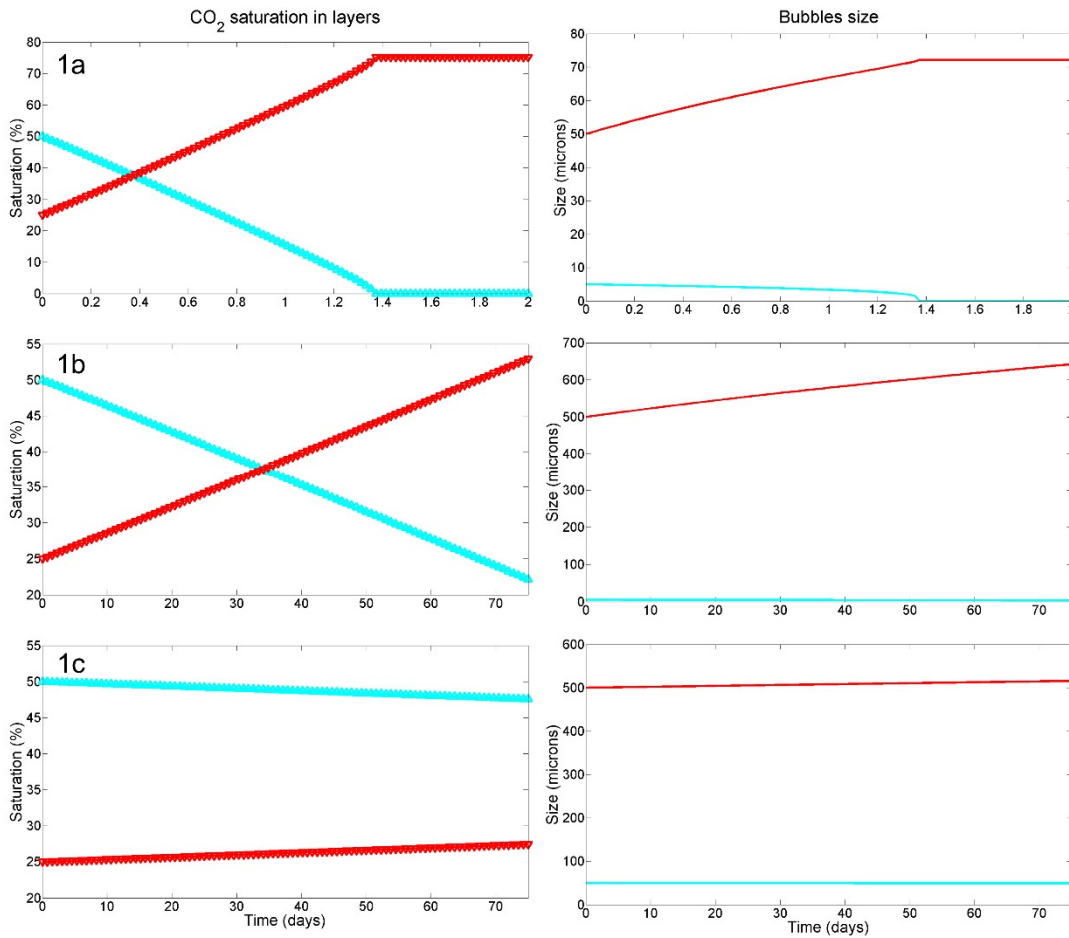


**Figure 7.12** Results from the simulation series 1a, 1b and 1c. The variations in CO<sub>2</sub> saturation in layers 1 and 2 are shown on the left in blue and red respectively. The corresponding variations in bubbles population size in layers 1 and 2 are shown on the right (in this simulation series all bubbles from each layer are the same size).

The water pressure also exerts a strong influence on CO<sub>2</sub> transfer, especially around the critical point of CO<sub>2</sub>. This effect is studied in cases 2a and 2b. In these two cases the bubbles size distribution is now composed of 30 different sizes linearly spaced between 10 and 100 μm in the layer 1 and between 100 and 1000 μm in layer 2. There are an identical number of bubbles for each size and the initial saturations are still 25% and 50%. The only difference between cases 2a and 2b is the background water pressure (Table 7.1) that is set to 7.35 and 5 MPa respectively. At subcritical conditions (case 2b) CO<sub>2</sub> solubility is much more sensitive to pressure, which leads to faster bubble dissolution and growth, see Figure 7.13.

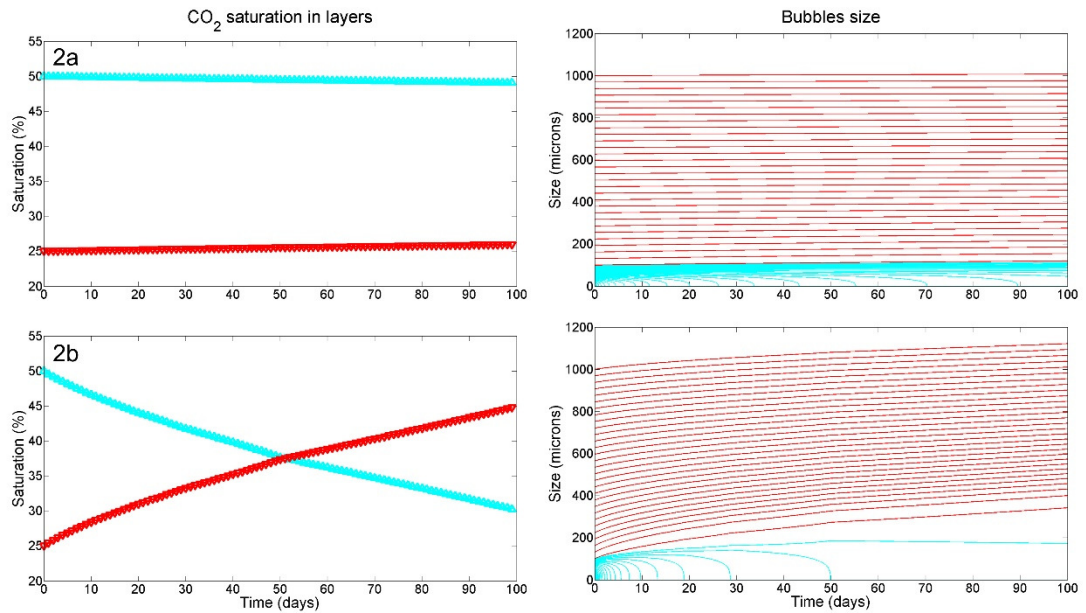


**Figure 7.13** Results from simulations 2a (top) and 2b (bottom). Now on the left side are represented the evolution of 30 different bubble sizes in both layers (blue for layer 1 and red for layer 2). The CO<sub>2</sub> transfer is much faster in case 2b where the background pressure is sub-critical.

The third simulation series (3a, 3b and 3c) examined the effect of restricting the bubble size to progressively smaller sizes in the small bubble layer (Layer 1). Cases 3a, 3b and 3c shown in Figure 7.14 illustrate how the saturation change speeds up as the initial size of the bubbles is reduced in the small bubble layer. Since pore size data for the different layers of the Orange sand is lacking it is not possible to directly compare the simulation results to the experimental data, however it appears that the case 3b best reproduces the experimental time needed for the saturation in the two layers to cross over.

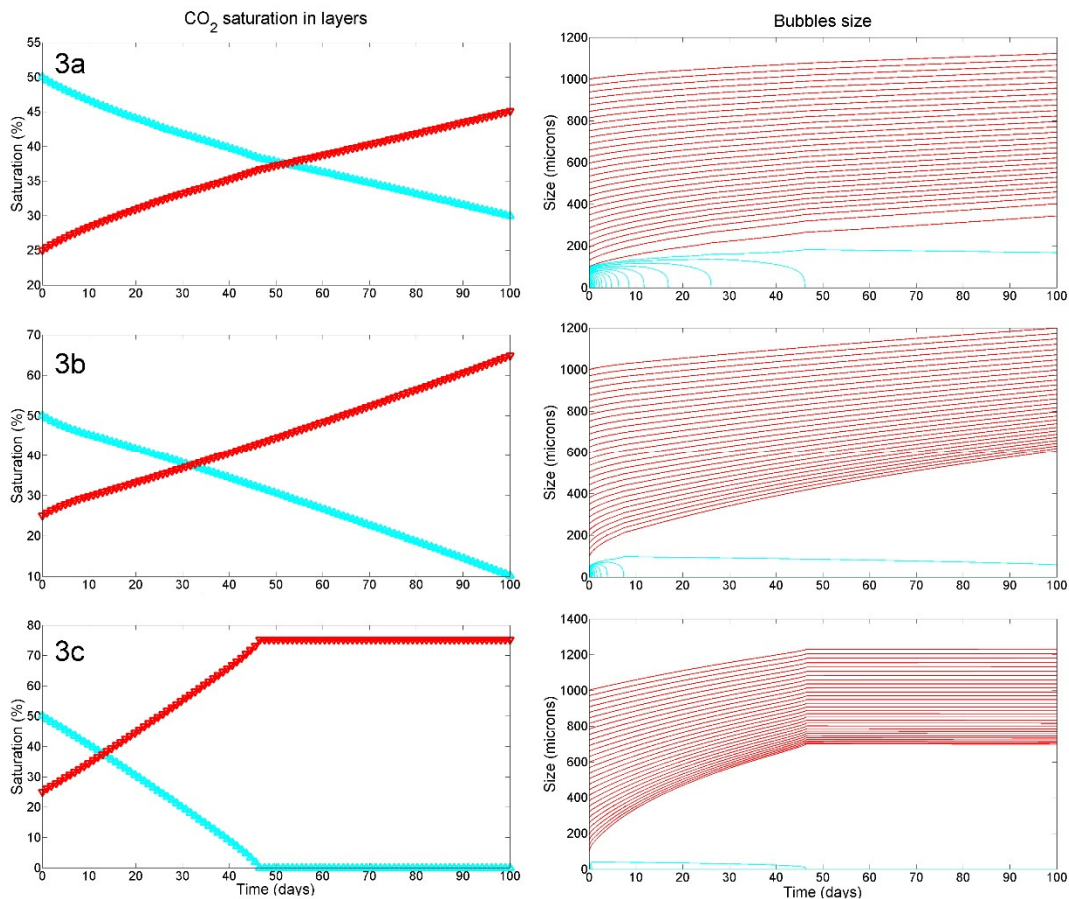


**Figure 7.14** Results from simulations 3a, 3b and 3c. The bubble sizes range and magnitude of the small bubble layer (Layer 1, in blue) are gradually reduced from simulations 3a to 3b to 3c. The bubbles size range is reduced from 2-100 $\mu\text{m}$  to 2-50 $\mu\text{m}$  and then to 2-20 $\mu\text{m}$ , see Table 7.1. This produces a faster  $\text{CO}_2$  transfer with faster dissolution of smaller bubbles.

A side observation is that the upper and lower bounds of the bubbles size distribution are of primary importance (over the presence of intermediate bubble sizes). Simulations 2b, 2b' and 2b'' (Figure 7.15) demonstrate that the main effect of adding more intermediate size is to smooth the  $\text{CO}_2$  background concentration ( $C_\infty$ ) curve while the saturation curves remain almost unchanged. This means that faster simulations using less complex size distributions can correctly capture the system evolution; although this might not be the case anymore when using non-linear size distributions.

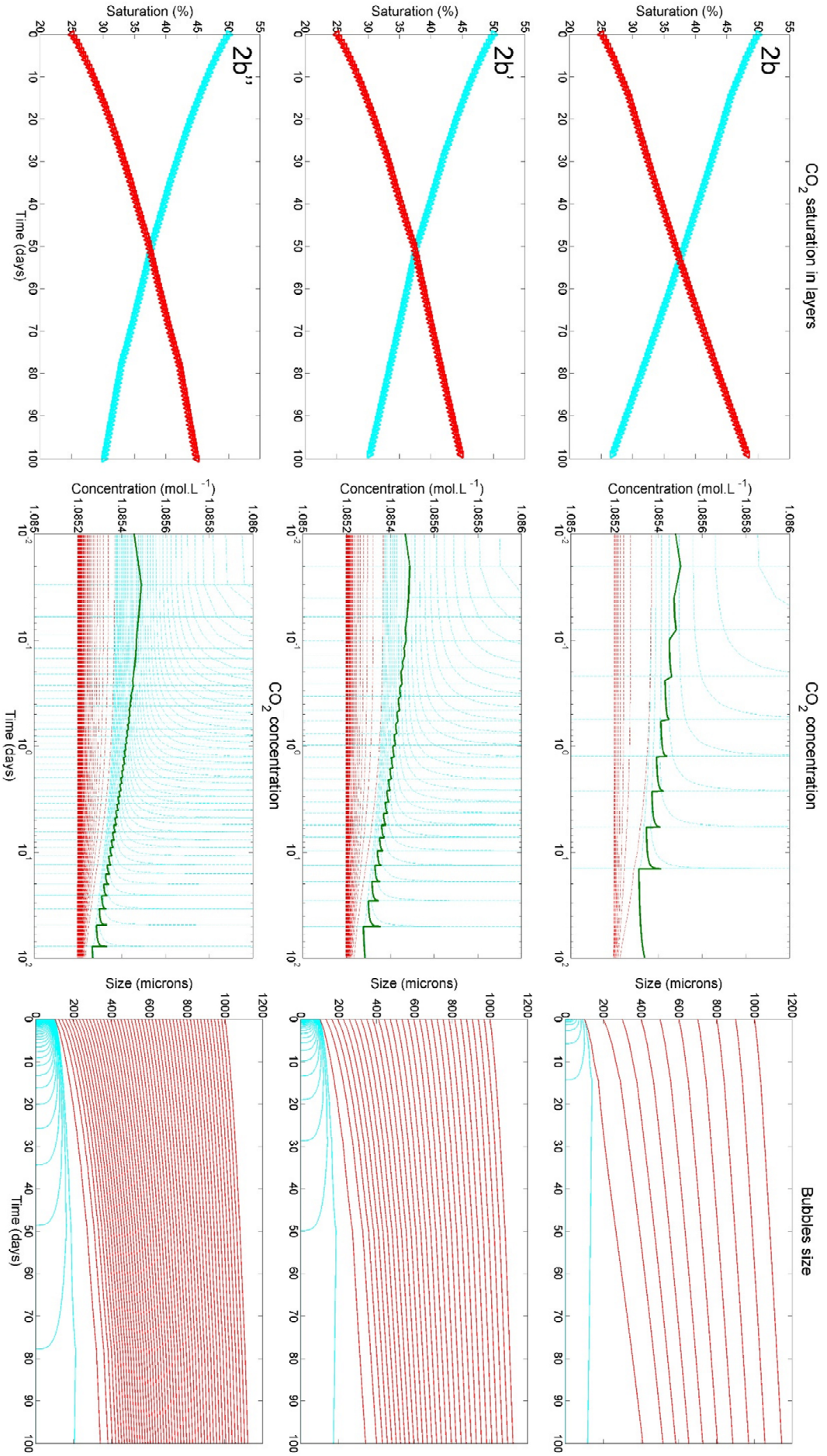


**Figure 7.15** Results from simulations 2b, 2b' and 2b'' where only the number of intermediate sizes have been modified (see Table 7.1). The CO<sub>2</sub> concentration plots represent the time evolution of  $C_{\infty}$  (in green), and  $C^*$  for each bubble size and in each layers (in blue and red). Values of  $C^*$  are typically lower for larger bubbles (in red). The fast acceleration of bubble dissolution is illustrated by the  $C^*$  curves from the small bubble layer (in blue); the curves become vertical when the bubbles radius approach zero.

So far the simulations support the hypothesis that CO<sub>2</sub> from smaller bubbles will migrate into larger ones on the timescale of the experiment. It seems also possible to find a set of bubble size distributions for which the simulations would replicate some or even all experimental observations, unfortunately the actual bubble size distributions in the experiment are not known.

However, up until now, the simulations have only considered the diffusion of CO<sub>2</sub> at the bubble interfaces and not between the different layers. The homogenization of  $C_{\infty}$  between the layers was considered instantaneous, said differently, all the aqueous CO<sub>2</sub> produced and consumed by bubbles dissolution and growth was distributed across all layers as if they were infinitely close. This is a significant idealization since diffusion across layers should in fact be the limiting factor of CO<sub>2</sub> transfer at the reservoir scale. Previous simulation series neglecting this diffusion could be completed on a shorter time due to their greater numerical stability. Previous simulation series were useful at identifying potential cases of interest to be re-used in an extended code including inter-layer diffusion.

Simulations 4a, 4b (Figure 7.16) use the same parameters as case 3c (very fast CO<sub>2</sub> transfer case) and include inter-layer diffusion. Cases 4a and 4b differ in the value of the diffusion coefficient. The representative distance between the two layers was set to 1cm. Both simulations show the layers behaving more independently than in case 3c with redistribution of bubble sizes within layers as well as between them; in both layers the smaller bubbles start to dissolve for the benefit of larger ones. After a very short time only the larger bubbles remain in the "small bubbles" layer. This process is also happening more slowly in the "large bubbles" layer, where more diffusion is needed to change bubble size. Since this ripening effect occurs internally, the CO<sub>2</sub> saturation is not affected but is limited instead by the diffusion of CO<sub>2</sub> between the two layers. Using a fast diffusion coefficient of  $10^{-8}$  m<sup>2</sup>/s it is possible to simulate a significant modification of the saturation over the timescale and length scale of the experiment with a saturation

reversal after three months between layers separated by 1 cm of aqueous fluid.

Despite the large number of variables, it is very difficult to reproduce the experimental results in full, and especially the very fast variation of the first week. The simulations indicate that the saturation change depends mainly on the background (water) pressure, the size of the bubbles and the inter layer CO<sub>2</sub> diffusion. Although in detail the agreement between the simulations and the experiment is not perfect the simulations allow the possibility of significant CO<sub>2</sub> exchange at the experiment time and length scales. This is however achieved by using a very high CO<sub>2</sub> diffusion coefficient. It would be useful to conduct simulations with a smaller spatial discretization (more layers) as considerable saturation change could then occur locally close to the interface between the large bubble and small bubble layers.

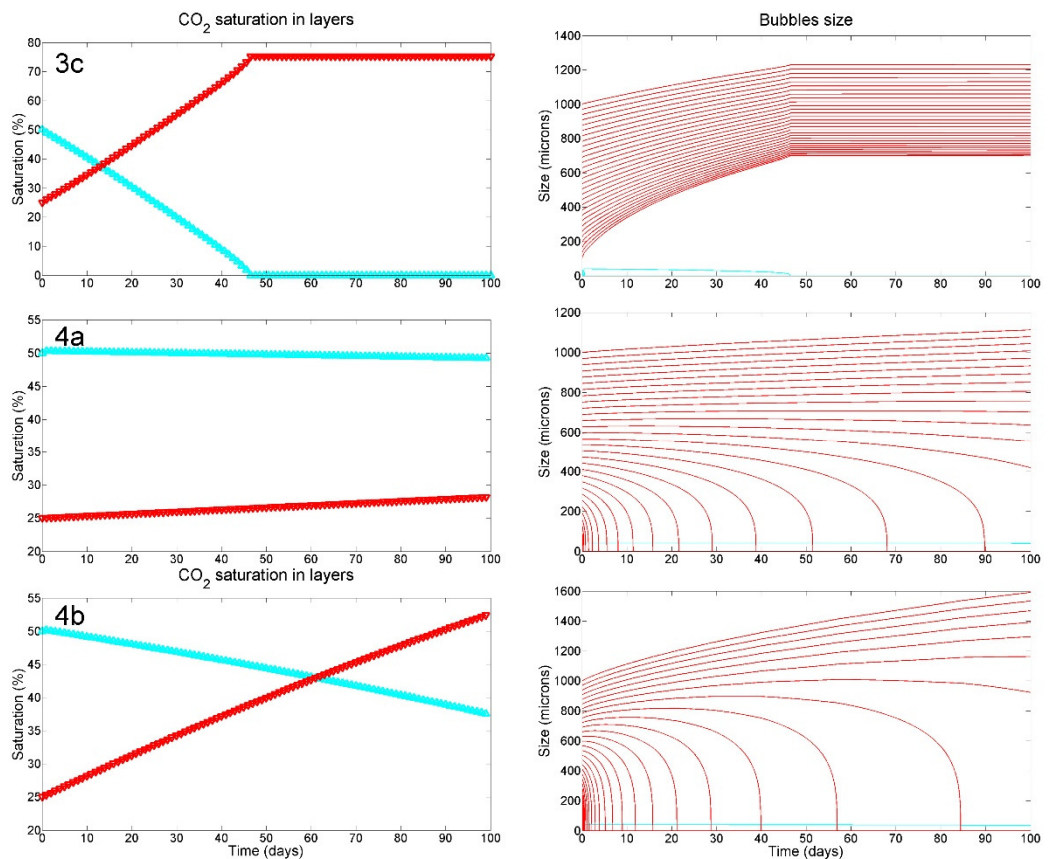


**Figure 7.16** Results from simulations 3c, 4a and 4b where inter layer diffusion have been introduced in cases 4a and 4b with a diffusion coefficient of  $10^{-9}$  and  $10^{-8}$  respectively.

## 7.5 Conclusions

The experiment performed on CO<sub>2</sub> behaviour in layered sandstone did result in CO<sub>2</sub> transfer downwards into a layer with coarser pores. To definitely clear remaining doubts on the exact processes at stake it would be necessary to image the bubbles, although duplication of the experiment would also be helpful, including more data points. Finally it would be very beneficial to conduct an experiment with a core drilled perpendicular instead of parallel to the layers. This way CT scans profiles could show the gradual variation of the saturation away from the interfaces between layers.

The study presented here suggests strongly that significant CO<sub>2</sub> transfer can occur between nearby rock layers on short time scales. Preferential CO<sub>2</sub> transfer into layers with coarser pores would increase CO<sub>2</sub> mobility and reduce brine mobility in these regions. In contrast, the dissolution of CO<sub>2</sub> in layers with fine pores could increase the mobility of the brine phase and reduce the mobility of CO<sub>2</sub>. What could be the implications of such local process (centimeter and month length and time scales) once up-scaled at the reservoir level? Considering an ideal reservoir with successive coarser and finer horizontal layers this would decrease the vertical fluid mobility and increase the horizontal one. If vertical mobility of CO<sub>2</sub> is an issue then capillary trapping instability would in fact participate to improve sequestration security. Similarly the presence of deformation bands next to faults (potential leakage paths) could reduce leakage risks. Another possibility is that this process would only become significant on longer length and time scales. Finally, this study used realistic although arbitrary pore size variations and would benefit from an exhaustive petrological study including mercury porosimetry to identify more relevant real rock scenarios.

## **Chapter 8**

### **Conclusions and future work.**

#### **8.1 Summary and conclusions.**

##### **8.1.1 CO<sub>2</sub>-Fluid-Rock reactions.**

It is expected that the injected CO<sub>2</sub> will interact with host rocks, modify their injectivity and give rise to potentially unwanted variability in other fundamental rock properties such as sonic velocity and strength. These outcomes need to be understood and anticipated. On longer time scales, continued interactions along leakage paths could also affect GCS operations. Since geochemical reactions are necessary to trap the CO<sub>2</sub> efficiently in aqueous or mineral forms, engineering solutions must be found to take advantage of chemical reactions while avoiding adverse effects.

The principal objectives of the work presented here was to evaluate potential impacts of geochemical interactions on GCS operation parameters by focusing on fast reactions such as CO<sub>2</sub> dissolution and carbonates dissolution/precipitation. From these investigations emerged new ideas and insights into the potential impacts of chemical reactions for GCS security and efficiency; new questions aroused about the capacity of current tools to predict and monitor these impacts and exposed the need to acquire more data concerning those processes.

Putting aside potential long term containment issues, late GCS failures were due to the lack of well injectivity (Hosa, 2011). Possible injectivity evolution near the well on the short term is therefore a subject of concerns as it is dependent on complex thermal, mechanical, chemical and hydrological coupled processes. This complexity can explain the ambiguity in published data concerning changes in injectivity during EOR operations (Cailly et al., 2005) although it is clear that some of them can be attributed to fast CO<sub>2</sub>-brine-rock interactions triggered by CO<sub>2</sub> dissolution.

##### **8.1.1.1 Experimental investigations on the nature and implications of geochemical reactions.**

The first experimental series presented in Chapter 3 demonstrated that small amounts of calcite present in rock cores dissolved at a rate determined by the rate of acid supply. The results shown significant increase in permeability of cores in which calcite had dissolved; this increase was larger than

predicted by classical porosity-permeability relationships. At the reservoir scale the interaction between CO<sub>2</sub> and calcite should be the same provided that the reservoir rock is similar to the one used in the experiments. If calcite dissolution does not bring other deleterious effects it could be enhanced to achieve larger injection rates by maximising CO<sub>2</sub> solubility either by co-injecting water or by using WAG injection schemes.

Chapter 5 brought other perspectives concerning the usefulness of fluid rock reactions by questioning the complications brought by concomitant mechanical properties modifications. Both sonic velocity and rock strength parameters were largely modified by calcite dissolution. At the reservoir scale the implications are twofold. Firstly, modifications in sonic velocity can complicate seismic monitoring operations. Secondly, reduction in rock strength can threaten reservoir and well integrity under high stress conditions.

In Chapter 6 the interest shifted from calcite dissolution to calcite precipitation as this would eventually happen in the reservoir as CO<sub>2</sub>-saturated fluid migrates towards lower pressure regions. In these experimental conditions calcite precipitation effectively followed CO<sub>2</sub> degassing although the exact mechanisms remained obscured by the lack of experimental data. A likely interpretation of the observations is that fluid depressurization and CO<sub>2</sub> degassing lead to strong calcite supersaturation and subsequent ACC homogeneous precipitation. In summary this study suggest that leakage paths from the reservoir to the surface could self-heal through homogeneous precipitation of calcite.

In an effort to investigate longer term processes able to modify the sequestration efficiency an experiment was designed to monitor residual CO<sub>2</sub> stability (Chapter 7). The experiment illustrated the occurrence of CO<sub>2</sub> movement from small pore size rock layers to larger pore size ones on the time scale of weeks and length scale of centimeters. At the reservoir scale this could be a first order effect modifying sequestration efficacy.

Considering horizontal layering of the reservoir with centimeter scale heterogeneity throughout, the experimental results suggest a corresponding layering of the capillary trapped CO<sub>2</sub>. A possible outcome of this would be the reduction of the vertical CO<sub>2</sub> mobility and an increase in the horizontal mobility. This process could also become significant in proximity of faults where deformation bands can occur and present strong heterogeneities at fine scales. If vertical upward migration of CO<sub>2</sub> is the main security issue

then these observations suggest an increase of CO<sub>2</sub> sequestration security with time.

### **8.1.1.2 Simulating and predicting the outcome of geochemical reactions.**

A logical extension of the experimental work presented above was to develop and test methods able to simulate and predict the observations. As a general rule predictive modelling needs to be constrained by field data and experiments. This is even truer in the case of geochemical reactions in the context of GCS due to the issues of scale and heterogeneity. Geochemical reactions produced by CO<sub>2</sub> injection need to be up-scaled from the pore scale to the reservoir scale.

Experiments alone can remain ambiguous and provide only qualitative information on the petrological relationships studied, Chapter 3 also revealed that classical macroscale porosity-permeability relationships were inadequate to describe pore scale modifications of the porous medium. To address this issue significant efforts have been produced to develop pore scale modelling solutions.

Advances in rock imaging techniques now allow the acquisition of mineralogical data on top of geometry data. Using such information Chapter 4 demonstrated that the consequences of geochemical reactions on fluid transport could be anticipated with pore scale fluid flow modelling using the transport code FLUENT. This has been facilitated by the relative homogeneity of the samples studied and by the fact that geometrical features created by geochemical reactions were largely above the resolution of the images. The main finding is that FLUENT simulations were more reliable than macroscopic relationships to calculate the variation in permeability caused by rock dissolution.

The evolution of capillary trapped CO<sub>2</sub> was also simulated with a home-made Matlab code and the results were presented in Chapter 7. A simple bubble model was able to qualitatively reproduce experimental results. More experimental data would have been necessary to improve the model parametrization and fitting (e.g. exact pore sizes, CO<sub>2</sub> diffusion coefficient, rate of CO<sub>2</sub> transfer between layers...). The computing resources (personal computer) was well suited to simulate the bubbles evolution in small volumes for a three months period but would be inappropriate to simulate the same processes over an entire reservoir and for longer periods. The simulation of this process on short length scales seems appropriate since it

is limited by the CO<sub>2</sub> diffusion in brine. In conclusion these results raise interesting questions about the long term fate of CO<sub>2</sub> but more efforts are needed to simulate the impact at the reservoir scale.

### **8.1.1.3 Integration of this thesis work for improved injection monitoring.**

Monitoring the CO<sub>2</sub> injection is primordial in the GCS chain as it can condition public acceptance and will likely be necessary to comply with international and national regulations. Up to now there has been limited post-injection data published but proven methods exist to monitor fluids in reservoirs (e.g. seismic surveys) and to some extent it is also possible to monitor chemical reactions with direct sampling at observation wells. Using the information provided in this thesis it would be in theory possible to evaluate the extent and localization of chemical reactions: this could be done by acquiring sonic velocity variation data and converting it into variations in porosity (Chapter 5). With the porosity information available it would be possible to simulate or calculate the variations in other important rock properties such as permeability and yield strength (Chapters 3, 4 and 5).

## **8.2 Remaining questions and future work.**

The experiments generally concerned a limited amount of samples and cores relative to the extent of potential reservoirs and their heterogeneity. Still those measurements proved to be essential to obtain relevant input parameters in reservoir models and to improve the interpretation of CO<sub>2</sub> injection parameters.

The experiments and simulation presented in chapters 3 to 6 relied mainly of calcite reactivity in response to CO<sub>2</sub> injection. The process of calcite (or other reactive minerals) dissolution and precipitation is not site specific so that generic conclusions can be drawn: the studies presented laid foundations to show the significance of a small amount of chemical reactions for GCS operations. Although the observed significance of calcite dissolution is specific to our experimental conditions, the results imply that fluid rock interactions should not be neglected when designing GCS operations even though it seems limited in extent. The results also show that current tools to evaluate the impact of reactions might be inappropriate given the pore scale nature of the interactions. It appears that careful examinations of the reservoir petrology coupled with experiments and simulations similar to the

one presented could be very beneficial to develop strategies to avoid adverse effects and to take advantage of the system reactivity.

Future work might include other rock samples in order to study the impact of mineral dissolution rocks for which parameters such as initial permeability, porosity, mineralogy and sonic velocity are different. These experiments should be combined with pore scale modelling investigations in order to continue testing this promising technique.

To build-up on Chapter 3 work it could be beneficial to use different injection schemes such as WAG or co-injection of CO<sub>2</sub> and brine. This should reduce the reactivity of the system as CO<sub>2</sub> and brine would not be mixed prior to being injected but would be closer to real case scenarios. A decrease in reactivity might on the other hand increase the distance over which reactions occur and give rise to more homogeneous dissolution. Similarly it would be beneficial to measure the change in relative permeability produced during mineral reactions although this is much more difficult and time consuming than absolute permeability experiments.

The use of pore scale fluid flow modelling to simulate reactions and changes in permeability as presented in Chapter 4 is very promising. To overcome some of the issues raised it could be beneficial to try to obtain larger models and very high resolution images of potential low permeability rock regions if they seem to contribute significantly to the flow. Larger models would enforce model representativeness and high resolution images could allow multi-scale analysis and simulations aiming to obtain accurate absolute permeability predictions. Another development of the methods described would be to extend the simulations to two-phase flow problems although this might be extremely problematic in terms of computing resources.

In this work the evaluation of changes in mechanical properties caused by chemical reactions as only been achieved by means of experiments (Chapter 5) and it could be interesting to develop numerical methods similar to the one presented in Chapter 4 but applied to mechanical properties. Both experiments and simulations could aim at understanding longer term (slower) deformations (e.g. creep deformation) occurring in the rock after mineral reaction occurred. An extended study including various rock samples could also be very meaningful given the great variability in reservoir rocks mineralogy and mechanical properties.

As already mentioned in Chapter 6 additional experiments will be necessary to evaluate the hypotheses formulated and provide a definitive interpretation

of the calcite precipitation results. For instance it would be beneficial to conduct an analysis to detect possible particles of calcite in suspension flushed at the outlet of the core. It would also be beneficial to vary the experimental parameters such as pressure drop, sample dimension, sample nature or experimental time to determine the main parameters upon which the observed CO<sub>2</sub> degassing and calcite precipitation depends.

As mentioned in Chapter 7 it would be necessary to obtain fine images of the bubbles, this could be achieved by using a micro-CT scanner similar to the one used to obtain rock models used in Chapter 4; duplication of the experiment would also be helpful, including more data points. Finally it would be very beneficial to conduct an experiment with a core drilled perpendicular instead of parallel to the layers. This way CT scans could show the gradual variation of the saturation away from the interfaces between layers.

A general observation concerning the present work is that some geochemical aspects were simplified and some neglected that could have impacted the results significantly. Maybe the most significant aspect neglected is the presence of impurities in the gas stream (O<sub>2</sub>, N<sub>2</sub>, SO<sub>2</sub>, H<sub>2</sub>S) that could produce different reactions or enhance the system reactivity. It is also possible that specific reservoir microbial ecosystems could affect chemical reactions significantly.

A concluding remark is that the best use of knowledge and data gained during this work would be their integration into reservoir scale simulations integrating hydrological, mechanical, thermal and chemical effects when they are relevant.

## Bibliography

- Adler, P. M. (1992). *Porous media: geometry and transports*: Butterworth-Heinemann.
- Al-Raoush, R., & Papadopoulos, A. (2010). Representative elementary volume analysis of porous media using X-ray computed tomography. *Powder Technology*, *200*(1-2), 69-77. doi: 10.1016/j.powtec.2010.02.011
- Allan, M. M., Turner, A., & Yardley, B. W. D. (2011). Relation between the dissolution rates of single minerals and reservoir rocks in acidified pore waters. *Applied Geochemistry*, *26*(8), 1289-1301. doi: 10.1016/j.apgeochem.2011.05.002
- Allen, D. E., Strazisar, B. R., Soong, Y., & Hedges, S. W. (2005). Modelling carbon dioxide sequestration in saline aquifers: Significance of elevated pressures and salinities. *Fuel Processing Technology*, *86*(14-15), 1569-1580. doi: 10.1016/j.fuproc.2005.01.004
- Anderson, E. (1905). The dynamics of faulting. *Transactions of the Edinburgh Geological Society*, *8*(3), 387-402.
- Andreani, M., Gouze, P., Luquot, L., & Jouanna, P. (2008). Changes in seal capacity of fractured claystone caprocks induced by dissolved and gaseous CO<sub>2</sub> seepage. *Geophysical Research Letters*, *35*(14). doi: 10.1029/2008gl034467
- Andreani, M., Luquot, L., Gouze, P., Godard, M., Hoise, E., & Gibert, B. (2009). Experimental Study of Carbon Sequestration Reactions Controlled by the Percolation of CO<sub>2</sub>-Rich Brine through Peridotites. *Environmental Science & Technology*, *43*(4), 1226-1231. doi: 10.1021/es8018429
- Angeli, M., Soldal, M., Skurtveit, E., & Aker, E. (2009). Experimental percolation of supercritical CO<sub>2</sub> through a caprock. *Greenhouse Gas Control Technologies* *9*, *1*(1), 3351-3358. doi: 10.1016/j.egypro.2009.02.123
- Anselmetti, F. S., & Eberli, G. P. (1993). Controls on sonic velocity in carbonates. *Pure and Applied Geophysics*, *141*(2-4), 287-323. doi: 10.1007/bf00998333
- Apps, J. A., Zheng, L., Zhang, Y., Xu, T., & Birkholzer, J. T. (2010). Evaluation of Potential Changes in Groundwater Quality in Response to CO<sub>2</sub> Leakage from Deep Geologic Storage. *Transport in Porous Media*, *82*(1), 215-246. doi: 10.1007/s11242-009-9509-8
- Arts, R., Eiken, O., Chadwick, A., Zweigel, P., van der Meer, L., & Zinszner, B. (2004). Monitoring of CO<sub>2</sub> injected at Sleipner using time-lapse

- seismic data. *Energy*, 29(9-10), 1383-1392. doi: 10.1016/j.energy.2004.03.072
- Audigane, P., Gaus, I., Czernichowski-Lauriol, I., Pruess, K., & Xu, T. F. (2007). Two-dimensional reactive transport modelling of CO<sub>2</sub> injection in a saline Aquifer at the Sleipner site, North Sea. *American Journal of Science*, 307(7), 974-1008. doi: 10.2475/07.2007.02
- Bacci, G., Korre, A., & Durucan, S. (2011). An experimental and numerical investigation into the impact of dissolution/precipitation mechanisms on CO<sub>2</sub> injectivity in the wellbore and far field regions. *International Journal of Greenhouse Gas Control*, 5, 579-588. doi: 10.1016/j.ijggc.2010.05.007
- Bachaud, P., Berne, P., Renard, F., Sardin, M., & Leclerc, J. R. (2011). Use of tracers to characterize the effects of a CO<sub>2</sub>-saturated brine on the petrophysical properties of a low permeability carbonate caprock. *Chemical Engineering Research & Design*, 89(9), 1817-1826. doi: 10.1016/j.cherd.2010.11.004
- Bachu, S., & Adams, J. J. (2003). Sequestration of CO<sub>2</sub> in geological media in response to climate change: capacity of deep saline aquifers to sequester CO<sub>2</sub> in solution. *Energy Conversion and Management*, 44(20), 3151-3175. doi: 10.1016/s0196-8904(03)00101-8
- Bachu, S., & Bennion, D. B. (2009). Interfacial Tension between CO<sub>2</sub>, Freshwater, and Brine in the Range of Pressure from (2 to 27) MPa, Temperature from (20 to 125) degrees C, and Water Salinity from (0 to 334 000) mg(.)L(-1). *Journal of Chemical and Engineering Data*, 54(3), 765-775. doi: 10.1021/je800529x
- Bachu, S., Gunter, W. D., & Perkins, E. H. (1994). Aquifer disposal of CO<sub>2</sub> – Hydrodynamic and mineral trapping. *Energy Conversion and Management*, 35(4), 269-279. doi: 10.1016/0196-8904(94)90060-4
- Backhaus, S., Turitsyn, K., & Ecke, R. (2011). Convective instability and mass transport of diffusion layers in a Hele-Shaw geometry. *Physical Review Letters*, 106(10), 104501.
- Bando, S., Takemura, F., Nishio, M., Hihara, E., & Akai, M. (2004). Viscosity of aqueous NaCl solutions with dissolved CO<sub>2</sub> at (30 to 60) degrees C and (10 to 20) MPa. *Journal of Chemical and Engineering Data*, 49(5), 1328-1332. doi: 10.1021/je049940f
- Bateman, K., Rochelle, C., Lacinska, A., & Wagner, D. (2011). CO<sub>2</sub>-porewater-rock reactions - Large-scale column experiment (Big Rig II). *10th International Conference on Greenhouse Gas Control Technologies*, 4, 4937-4944. doi: 10.1016/j.egypro.2011.02.463
- Batzle, M., & Wang, Z. J. (1992). Seismic properties of pore fluids. *Geophysics*, 57(11), 1396-1408. doi: 10.1190/1.1443207

- Bear, J. (2013). *Dynamics of fluids in porous media*: Courier Dover Publications.
- Bear, J., & Bachmat, Y. (1990). *Introduction to Modelling of Transport Phenomena in Porous Media*: Springer.
- Benezeth, P., Menez, B., & Noiriél, C. (2009). CO<sub>2</sub> geological storage: Integrating geochemical, hydrodynamical, mechanical and biological processes from the pore to the reservoir scale Preface. *Chemical Geology*, 265(1-2), 1-2. doi: 10.1016/j.chemgeo.2009.05.006
- Bennion, D. B., & Bachu, S. (2008). Drainage and imbibition relative permeability relationships for supercritical CO<sub>2</sub>/brine and H<sub>2</sub>S/brine systems in intergranular sandstone, carbonate, shale, and anhydrite rocks. *Spe Reservoir Evaluation & Engineering*, 11(3), 487-496.
- Benson, S. M., & Cole, D. R. (2008). CO<sub>2</sub> Sequestration in Deep Sedimentary Formations. *Elements*, 4(5), 325-331. doi: 10.2113/gselements.4.5.325
- Benson, S., R. Pini, C. Reynolds, and S. Krevor. (2013). Relative Permeability Analysis to Describe Multi-phase Flow in CO<sub>2</sub> Storage Reservoirs (No. 2). *Global CCS Institute*
- Bergmo, P. E. S., Grimstad, A. A., & Lindeberg, E. (2011). Simultaneous CO<sub>2</sub> injection and water production to optimise aquifer storage capacity. *International Journal of Greenhouse Gas Control*, 5(3), 555-564. doi: 10.1016/j.ijggc.2010.09.002
- Bertier, P., Swennen, R., Laenen, B., Lagrou, D., & Dreesen, R. (2006). Experimental identification of CO<sub>2</sub>–water–rock interactions caused by sequestration of CO<sub>2</sub> in Westphalian and Buntsandstein sandstones of the Campine Basin (NE-Belgium). *Journal of Geochemical Exploration*, 89(1), 10-14.
- Bickle, M., Kampman, N., & Wigley, M. (2013). Natural Analogues. *Reviews in Mineralogy and Geochemistry*, 77(1), 15-71. doi: 10.2138/rmg.2013.77.2
- Biot, M. A. (1956a). Theory of propagation of elastic waves in a fluid-saturated porous fluid. 1. Low frequency range. *Journal of the Acoustical Society of America*, 28(2), 168-178. doi: 10.1121/1.1908239
- Biot, M. A. (1956b). Theory of propagation of elastic waves in a fluid-saturated porous fluid. 2. Higher frequency range. *Journal of the Acoustical Society of America*, 28(2), 179-191. doi: 10.1121/1.1908241
- Birkholzer, J. T., Nicot, J. P., Oldenburg, C. M., Zhou, Q., Kraemer, S., & Bandilla, K. (2011). Brine flow up a well caused by pressure perturbation from geologic carbon sequestration: Static and dynamic

- evaluations. *International Journal of Greenhouse Gas Control*, 5(4), 850-861. doi: <http://dx.doi.org/10.1016/j.ijggc.2011.01.003>
- Bjørlykke, K., & Gran, K. (1994). Salinity variations in North Sea formation waters: implications for large-scale fluid movements. *Marine and Petroleum Geology*, 11(1), 5-9. doi: [http://dx.doi.org/10.1016/0264-8172\(94\)90003-5](http://dx.doi.org/10.1016/0264-8172(94)90003-5)
- Blunt, M., & King, P. (1991). Relative permeabilities from 2-dimensional and 3-dimensional pore scale network modelling. *Transport in Porous Media*, 6(4), 407-433.
- Blunt, M. J., Bijeljic, B., Dong, H., Gharbi, O., Iglauer, S., Mostaghimi, P., Paluszny, A., Pentland, C. (2013). Pore-scale imaging and modelling. *Advances in Water Resources*, 51, 197-216. doi: [10.1016/j.advwatres.2012.03.003](http://dx.doi.org/10.1016/j.advwatres.2012.03.003)
- Blunt, M. J., Jackson, M. D., Piri, M., & Valvatne, P. H. (2002). Detailed physics, predictive capabilities and macroscopic consequences for pore-network models of multiphase flow. *Advances in Water Resources*, 25(8-12), 1069-1089. doi: [10.1016/s0309-1708\(02\)00049-0](http://dx.doi.org/10.1016/s0309-1708(02)00049-0)
- Boait, F., White, N., Chadwick, A., Noy, D., & Bickle, M. (2011). Layer spreading and dimming within the CO<sub>2</sub> plume at the Sleipner Field in the North Sea. *10th International Conference on Greenhouse Gas Control Technologies*, 4, 3254-3261. doi: [10.1016/j.egypro.2011.02.244](http://dx.doi.org/10.1016/j.egypro.2011.02.244)
- Bodnar, R. J., Steele-MacInnis, M., Capobianco, R. M., Rimstidt, J. D., Dillmore, R., Goodman, A., & Guthrie, G. (2013). PVTX Properties of H<sub>2</sub>O-CO<sub>2</sub>-"salt" at PTX Conditions Applicable to Carbon Sequestration in Saline Formations. In D. J. DePaolo, D. R. Cole, A. Navrotsky & I. C. Bourg (Eds.), *Geochemistry of Geologic CO<sub>2</sub> Sequestration* (Vol. 77, pp. 123-152). Chantilly: Mineralogical Soc Amer.
- Bondino, I., Hamon, G., Kallel, W., & Kachuma, D. (2013). Relative Permeabilities From Simulation in 3D Rock Models and Equivalent Pore Networks: Critical Review and Way Forward. *Petrophysics*, 54(6), 538-546.
- Bowker, K. A., & Shuler, P. J. (1991). Carbon-dioxide injection and resultant alteration of the Weber Sandstone, Rangely field, Colorado. *Aapg Bulletin-American Association of Petroleum Geologists*, 75(9), 1489-1499.
- Bradshaw, J., Bachu, S., Bonijoly, D., Burruss, R., Holloway, S., Christensen, N. P., & Mathiassen, O. M. (2007). CO<sub>2</sub> storage capacity estimation: Issues and development of standards. *International Journal of Greenhouse Gas Control*, 1(1), 62-68.

- Bredehoeft, J. D., Wolff, R. G., Keys, W. S., & Shuter, E. (1976). Hydraulic fracturing to determine regional in situ stress field, Piceance basin, Colorado. *Geological Society of America Bulletin*, 87(2), 250-258. doi: 10.1130/0016-7606(1976)87<250:hftdr>2.0.co;2
- Brown, L. T. (2002). *Integration of rock physics and reservoir simulation for the interpretation of time-lapse seismic data at Weyburn Field, Saskatchewan*. Colorado School of Mines.
- Burton, M., & Bryant, S. L. (2007). *Eliminating buoyant migration of sequestered CO<sub>2</sub> through surface dissolution: implementation costs and technical challenges*. Paper presented at the SPE Annual Technical Conference and Exhibition.
- Buscheck, T. A., Sun, Y., Hao, Y., Wolery, T. J., Bourcier, W., Tompson, A. F., Jones, E.D., Julio Friedmann, S., Aines, R. D. (2011). Combining brine extraction, desalination, and residual-brine reinjection with CO<sub>2</sub> storage in saline formations: Implications for pressure management, capacity, and risk mitigation. *Energy Procedia*, 4, 4283-4290.
- Butler, J.H. and S.A. Montzka. (2013). The NOAA annual greenhouse gas index (AGGI), NOAA/ESRL Global Monitoring Division, <http://www.esrl.noaa.gov/gmd/aggi/aggi.html>.
- Cailly, B., Le Thiez, P., Egermann, P., Audibert, A., Vidal-Gilbert, S., & Longaygue, X. (2005). Geological storage of CO<sub>2</sub>: A state-of-the-art of injection processes and technologies. *Oil & gas science and technology*, 60(3), 517-525.
- Calvert, R. (2005). 4D technology: where are we, and where are we going? *Geophysical Prospecting*, 53(2), 161-171. doi: 10.1111/j.1365-2478.2004.00469.x
- Canal, J., Delgado, J., Falcón, I., Yang, Q., Juncosa, R., & Barrientos, V. (2012). Injection of CO<sub>2</sub>-Saturated Water through a Siliceous Sandstone Plug from the Hontomin Test Site (Spain): Experiment and Modelling. *Environmental Science & Technology*, 47(1), 159-167.
- Carey, J. W. (2013). Geochemistry of wellbore integrity in CO<sub>2</sub> sequestration: Portland cement-steel-brine-CO<sub>2</sub> interactions. *Reviews in Mineralogy and Geochemistry*, 77(1), 505-539.
- Carey, J. W. (2014). Failure (Escape of Fluids) of Wellbore Systems: Los Alamos National Laboratory (LANL).
- Carey, J. W., Wigand, M., Chipera, S. J., WoldeGabriel, G., Pawar, R., Lichtner, P. C., Wehner, S.C., Raines, M.A., Guthrie Jr, G. D. (2007). Analysis and performance of oil well cement with 30 years of CO<sub>2</sub> exposure from the SACROC Unit, West Texas, USA. *International Journal of Greenhouse Gas Control*, 1(1), 75-85.

- Carman, P. C. (1997). Fluid flow through granular beds. *Chemical Engineering Research & Design*, 75, S32-S48. doi: 10.1016/s0263-8762(97)80003-2
- Carroll, S. A., & Knauss, K. G. (2005). Dependence of labradorite dissolution kinetics on CO<sub>2</sub>, Al (aq), and temperature. *Chemical Geology*, 217(3), 213-225.
- Castagna, J. P., & Backus, M. (1993). Offset-dependent reflectivity-theory and practice of AVO analysis. *Investigations in Geophysics series*, 8.
- Castagna, J. P., Batzle, M. L., & Eastwood, R. L. (1985). Relationships between compressional-wave and shear-wave velocities in clastic silicate rocks. *Geophysics*, 50(4), 571-581. doi: 10.1190/1.1441933
- Celia, M. A., Nordbotten, J. M., Court, B., Dobossy, M., & Bachu, S. (2011). Field-scale application of a semi-analytical model for estimation of CO<sub>2</sub> and brine leakage along old wells. *International Journal of Greenhouse Gas Control*, 5(2), 257-269. doi: <http://dx.doi.org/10.1016/j.ijggc.2010.10.005>
- Cenedese, A., & Viotti, P. (1996). Lagrangian analysis of nonreactive pollutant dispersion in porous media by means of the particle image velocimetry technique. *Water Resources Research*, 32(8), 2329-2343. doi: 10.1029/96wr00605
- Chadwick, R. A., Arts R., & Eiken, O. (2005). 4D seismic quantification of a growing CO<sub>2</sub> plume at Sleipner, North Sea. *Geological Society, London, Petroleum Geology Conference series*, 6, 1385-1399. doi: 10.1144/0061385
- Chadwick, R.A., Arts, R., Eiken, O., Williamson, P., & Williams, G. (2006a). Geophysical monitoring of the CO<sub>2</sub> plume at Sleipner, North Sea: an outline review. In: Lombardi, S., Altunia, L.K., and Beaubien, S.E. (Eds.) *Advances in the Geological Storage of Carbon Dioxide*. Springer, Dordrecht, NATO Science, IV Earth and Environmental Sciences Vol. 65, 303-314.
- Chadwick, R. A., Williams, G. A., Williams, J. D. O., & Noy, D. J. (2012). Measuring pressure performance of a large saline aquifer during industrial-scale CO<sub>2</sub> injection: The Utsira Sand, Norwegian North Sea. *International Journal of Greenhouse Gas Control*, 10, 374-388. doi: 10.1016/j.ijggc.2012.06.022
- Chadwick, R. A., Noy, D. J., & Holloway, S. (2009). Flow processes and pressure evolution in aquifers during the injection of supercritical CO<sub>2</sub> as a greenhouse gas mitigation measure. *Petroleum Geoscience*, 15(1), 59-73. doi: 10.1144/1354-079309-793
- Chapman, M., Zatsepin, S., & Crampin, S. (2000). Time-lapse seismic changes in a CO<sub>2</sub> injection process in a fractured reservoir [Exp. Abs.]. *Society of Exploration Geophysicists*, 1536-1539.

- Chapuis, R. P., & Aubertin, M. (2003). On the use of the Kozeny-Carman equation to predict the hydraulic conductivity of soils. *Canadian Geotechnical Journal*, 40(3), 616-628. doi: 10.1139/t03-013
- Chen, S., & Doolen, G. D. (1998). Lattice Boltzmann method for fluid flows. *Annual Review of Fluid Mechanics*, 30, 329-364. doi: 10.1146/annurev.fluid.30.1.329
- Chiotellis, E., & Campbell, G. (2003). Proving of bread dough I: modelling the evolution of the bubble size distribution. *Food and bioproducts processing*, 81(3), 194-206.
- Chiquet, P., Daridon, J. L., Broseta, D., & Thibeau, S. (2007). CO<sub>2</sub>/water interfacial tensions under pressure and temperature conditions of CO<sub>2</sub> geological storage. *Energy Conversion and Management*, 48(3), 736-744. doi: 10.1016/j.enconman.2006.09.011
- Church, J. A., & White, N. J. (2006). A 20th century acceleration in global sea-level rise. *Geophysical Research Letters*, 33(1). doi: 10.1029/2005gl024826
- Coates, G. R., Xiao, L., Prammer, M. G. (2009). NMR logging – Principles and applications. Halliburton
- Cole, I. S., Corrigan, P., Sim, S., & Birbilis, N. (2011). Corrosion of pipelines used for CO<sub>2</sub> transport in CCS: Is it a real problem? *International Journal of Greenhouse Gas Control*, 5(4), 749-756. doi: 10.1016/j.ijggc.2011.05.010
- Coles, M. E., Hazlett, R. D., Spanne, P., Soll, W. E., Muegge, E. L., & Jones, K. W. (1998). Pore level imaging of fluid transport using synchrotron X-ray microtomography. *Journal of Petroleum Science and Engineering*, 19(1-2), 55-63. doi: 10.1016/s0920-4105(97)00035-1
- Cooper, J., & Dooley, R. (2008). Release of the IAPWS formulation 2008 for the viscosity of ordinary water substance: The International Association of the Properties of Water and Steam, Berlin, Germany.
- Daccord, G., Lenormand, R., & Lietard, O. (1993). Chemical dissolution of a porous medium by a reactive fluid. 1. Model for the wormholing phenomenon. *Chemical Engineering Science*, 48(1), 169-178. doi: 10.1016/0009-2509(93)80293-y
- Daccord, G., Nittmann, J., & Stanley, H. E. (1986). Radial viscous fingers and diffusion-limited aggregation: Fractal dimension and growth sites. *Physical Review Letters*, 56(4), 336.
- Daley, T. M., Myer, L. R., Peterson, J. E., Majer, E. L., & Hoversten, G. M. (2008). Time-lapse crosswell seismic and VSP monitoring of injected CO<sub>2</sub> in a brine aquifer. *Environmental Geology*, 54(8), 1657-1665. doi: 10.1007/s00254-007-0943-z

- Daval, D., Sissmann, O., Corvisier, J., Garcia, B., Martinez, I., Guyot, F., & Hellmann, R. (2010). *The effect of silica coatings on the weathering rates of wollastonite (CaSiO<sub>3</sub>) and forsterite (Mg<sub>2</sub>SiO<sub>4</sub>): an apparent paradox?* Paper presented at the Water Rock Interaction-WRI-13 Proceedings of the 13Th international conference on Water Rock Interaction WRI-13-Guanajuato, Mexico, 16-20 August 2010.
- De Yoreo, J. J., Waychunas, G. A., Jun, Y.-S., & Fernandez-Martinez, A. (2013). In situ investigations of carbonate nucleation on mineral and organic surfaces. *Reviews in Mineralogy and Geochemistry*, 77(1), 229-257.
- DECC, C. (2012). Roadmap: Supporting the deployment of Carbon Capture and Storage in the UK. *UK Department of Energy and Climate Change*.
- Deng, H., Ellis, B. R., Peters, C. A., Fitts, J. P., Crandall, D., & Bromhal, G. S. (2013). Modifications of carbonate fracture hydrodynamic properties by CO<sub>2</sub>-acidified brine flow. *Energy & Fuels*, 27(8), 4221-4231.
- Diamond, L. W., & Akinfiev, N. N. (2003). Solubility of CO<sub>2</sub> in water from–1.5 to 100° C and from 0.1 to 100 MPa: evaluation of literature data and thermodynamic modelling. *Fluid phase equilibria*, 208(1), 265-290.
- Domenico, S. N. (1984). Rock lithology and porosity determination from shear and compressional wave velocity. *Geophysics*, 49(8), 1188-1195. doi: 10.1190/1.1441748
- Duan, Z. H., Hu, J. W., Li, D. D., & Mao, S. D. (2008). Densities of the CO<sub>2</sub>-H<sub>2</sub>O and CO<sub>2</sub>-H<sub>2</sub>O-NaCl systems up to 647 K and 100 MPa. *Energy & Fuels*, 22(3), 1666-1674. doi: 10.1021/ef700666b
- Duan, Z. H., & Sun, R. (2003). An improved model calculating CO<sub>2</sub> solubility in pure water and aqueous NaCl solutions from 273 to 533 K and from 0 to 2000 bar. *Chemical Geology*, 193(3-4), 257-271. doi: 10.1016/s0009-2541(02)00263-2
- Duan, Z. H., Sun, R., Zhu, C., & Chou, I. M. (2006). An improved model for the calculation of CO<sub>2</sub> solubility in aqueous solutions containing Na<sup>+</sup>, K<sup>+</sup>, Ca<sup>2+</sup>, Mg<sup>2+</sup>, Cl<sup>-</sup>, and SO<sub>4</sub><sup>2-</sup>. *Marine Chemistry*, 98(2-4), 131-139. doi: 10.1016/j.marchem.2005.09.001
- Duchateau, C., & Broseta, D. (2012). A simple method for determining brine–gas interfacial tensions. *Advances in Water Resources*, 42(0), 30-36. doi: <http://dx.doi.org/10.1016/j.advwatres.2012.03.008>
- EIA. (2014). International Energy Outlook 2014: World Petroleum and Other Liquid Fuels. Report number: DOE/EIA-0484(2014). Washington. DC: Office of Integrated and International Energy Analysis.

- Ellis, B. R., Crandell, L. E., & Peters, C. A. (2010). Limitations for brine acidification due to SO<sub>2</sub> co-injection in geologic carbon sequestration. *International Journal of Greenhouse Gas Control*, 4(3), 575-582. doi: 10.1016/j.ijggc.2009.11.006
- Ellis, B. R., Fitts, J. P., Bromhal, G. S., McIntyre, D. L., Tappero, R., & Peters, C. A. (2013). Dissolution-driven permeability reduction of a fractured carbonate caprock. *Environmental engineering science*, 30(4), 187-193.
- Ellis, J. S., & Bazylak, A. (2012). Dynamic pore network model of surface heterogeneity in brine-filled porous media for carbon sequestration. *Physical Chemistry Chemical Physics*, 14(23), 8382-8390. doi: 10.1039/C2CP40812K
- Ellis, J. S., & Bazylak, A. (2013). Investigation of contact angle heterogeneity on CO<sub>2</sub> saturation in brine-filled porous media using 3D pore network models. *Energy Conversion and Management*, 68(0), 253-259. doi: <http://dx.doi.org/10.1016/j.enconman.2013.01.019>
- Ennis-King, J., Preston, I., & Paterson, L. (2005). Onset of convection in anisotropic porous media subject to a rapid change in boundary conditions. *Physics of Fluids (1994-present)*, 17(8), 084107.
- Espinoza, D. N., & Santamarina, J. C. (2010). Water-CO<sub>2</sub>-mineral systems: Interfacial tension, contact angle, and diffusion-Implications to CO<sub>2</sub> geological storage. *Water Resources Research*, 46, 10. doi: 10.1029/2009wr008634
- Everett, D. (1961). The thermodynamics of frost damage to porous solids. *Trans. Faraday Soc.*, 57, 1541-1551.
- Fenghour, A., Wakeham, W. A., & Vesovic, V. (1998). The viscosity of carbon dioxide. *Journal of Physical and Chemical Reference Data*, 27(1), 31-44.
- Fernandez-Martinez, A., Hu, Y., Lee, B., Jun, Y. S., & Waychunas, G. A. (2013). In situ determination of interfacial energies between heterogeneously nucleated CaCO<sub>3</sub> and quartz substrates: thermodynamics of CO<sub>2</sub> mineral trapping. *Environ Sci Technol*, 47(1), 102-109. doi: 10.1021/es3014826
- Ferreol, B., & Rothman, D. H. (1995). Lattice-Boltzmann simulations of flow through Fontainebleau Sandstone. *Transport in Porous Media*, 20(1-2), 3-20. doi: 10.1007/bf00616923
- Figueroa, J. D., Fout, T., Plasynski, S., McIlvried, H., & Srivastava, R. D. (2008). Advances in CO<sub>2</sub> capture technology—The U.S. Department of Energy's Carbon Sequestration Program. *International Journal of Greenhouse Gas Control*, 2(1), 9-20. doi: [http://dx.doi.org/10.1016/S1750-5836\(07\)00094-1](http://dx.doi.org/10.1016/S1750-5836(07)00094-1)

- Flnkenrath, M. (2011). Cost and performance of carbon dioxide capture from power generation: OECD Publishing.
- Fleury, M., & Deschamps, H. (2009). Viscosity and Electrical Conductivity of Aqueous NaCl Solutions with Dissolved CO<sub>2</sub>. In J. Gale, H. Herzog & J. Braitsch (Eds.), *Greenhouse Gas Control Technologies 9* (Vol. 1, pp. 3129-3133). Amsterdam: Elsevier Science Bv.
- Gardner, G. H. F., Gardner, L. W., & Gregory, A. R. (1974). Formation velocity and density – Diagnostic basics for stratigraphic traps. *Geophysics*, 39(6), 770-780. doi: 10.1190/1.1440465
- Gasda, S. E., Bachu, S., & Celia, M. A. (2004). Spatial characterization of the location of potentially leaky wells penetrating a deep saline aquifer in a mature sedimentary basin. *Environmental Geology*, 46(6-7), 707-720. doi: 10.1007/s00254-004-1073-5
- Gassmann, F. (1951). The elasticity of porous media. *Mitteilungen aus dem Institut für Geophysik, ETH Zurich*(17), 23 pp.-23 pp.
- Gaus, I. (2010). Role and impact of CO<sub>2</sub>-rock interactions during CO<sub>2</sub> storage in sedimentary rocks. *International Journal of Greenhouse Gas Control*, 4(1), 73-89. doi: 10.1016/j.ijggc.2009.09.015
- Gherardi, F., Audigane, P., & Gaucher, E. C. (2012). Predicting long-term geochemical alteration of wellbore cement in a generic geological CO<sub>2</sub> confinement site: Tackling a difficult reactive transport modelling challenge. *Journal of Hydrology*, 420, 340-359.
- Gherardi, F., Xu, T. F., & Pruess, K. (2007). Numerical modelling of self-limiting and self-enhancing caprock alteration induced by CO<sub>2</sub> storage in a depleted gas reservoir. *Chemical Geology*, 244(1-2), 103-129. doi: 10.1016/j.chemgeo.2007.06.009
- Giammar, D. E., Bruant, R. G., & Peters, C. A. (2005). Forsterite dissolution and magnesite precipitation at conditions relevant for deep saline aquifer storage and sequestration of carbon dioxide. *Chemical Geology*, 217(3-4), 257-276. doi: 10.1016/j.chemgeo.2004.12.013
- Gilfillan, S. M. V., Lollar, B. S., Holland, G., Blagburn, D., Stevens, S., Schoell, M., Cassidy, M., Ding, Z. J., Zhou, Z., Lacrampe-Couloume, G., Ballentine, C. J. (2009). Solubility trapping in formation water as dominant CO<sub>2</sub> sink in natural gas fields. *Nature*, 458(7238), 614-618. doi: 10.1038/nature07852
- Giorgis, T., Carpita, M., & Battistelli, A. (2007). 2D modelling of salt precipitation during the injection of dry CO<sub>2</sub> in a depleted gas reservoir. *Energy Conversion and Management*, 48(6), 1816-1826. doi: 10.1016/j.enconman.2007.01.012
- Goodman, A., Bromhal, G., Strazisar, B., Rodosta, T., & Guthrie, G. (2013). Comparison of publicly available methods for development of

geologic storage estimates for carbon dioxide in saline formations. *National Energy Technology Laboratory Technical Report Series*.

- Gouze, P., Luquot, L., Andreani, M., Pepe, G., Dweik, P., & Jouanna, P. (2010). Clay particles decohesion during dissolved and gaseous CO<sub>2</sub> injection through fractured claystone. *Water-Rock Interaction XIII*, 863-866.
- Gouze, P., & Luquot, L. (2011). X-ray microtomography characterization of porosity, permeability and reactive surface changes during dissolution. *Journal of Contaminant Hydrology*, 120-21, 45-55. doi: 10.1016/j.jconhyd.2010.07.004
- Gunter, W., Wiwehar, B., & Perkins, E. (1997). Aquifer disposal of CO<sub>2</sub>-rich greenhouse gases: extension of the time scale of experiment for CO<sub>2</sub>-sequestering reactions by geochemical modelling. *Mineralogy and Petrology*, 59(1-2), 121-140.
- Hamm, L. M., Bourg, I. C., Wallace, A. F., & Rotenberg, B. (2013). Molecular Simulation of CO<sub>2</sub>- and CO<sub>3</sub>-Brine-Mineral Systems. *Reviews in Mineralogy and Geochemistry*, 77(1), 189-228. doi: 10.2138/rmg.2013.77.6
- Han, D., Nur, A., & Morgan, D. (1986). Effects of porosity and clay content on wave velocities in sandstones. *Geophysics*, 51(11), 2093-2107. doi: 10.1190/1.1442062
- Han, D. H., & Batzle, M. L. (2004). Gassmann's equation and fluid-saturation effects on seismic velocities. *Geophysics*, 69(2), 398-405. doi: 10.1190/1.1707059
- Han, W. S., Lee, S. Y., Lu, C., McPherson, B. J., & Esser, R. (2009). Role of correlation structures of permeability field on residual trapping mechanisms and buoyancy-driven CO<sub>2</sub> migration. *Greenhouse Gas Control Technologies 9*, 1(1), 3493-3498. doi: 10.1016/j.egypro.2009.02.141
- Hangx, S., Spiers, C., & Peach, C. (2010). Creep of simulated reservoir sands and coupled chemical - mechanical effects of CO<sub>2</sub> injection. *Journal of Geophysical Research: Solid Earth (1978–2012)*, 115(B9).
- Hangx, S. J. T., & Spiers, C. J. (2009). Reaction of plagioclase feldspars with CO<sub>2</sub> under hydrothermal conditions. *Chemical Geology*, 265(1-2), 88-98. doi: 10.1016/j.chemgeo.2008.12.005
- Hansen, J., Sato, M., Ruedy, R., Lo, K., Lea, D. W., & Medina-Elizade, M. (2006). Global temperature change. *Proceedings of the National Academy of Sciences of the United States of America*, 103(39), 14288-14293. doi: 10.1073/pnas.0606291103

- Hao, Y., Sun, Y., & Nitao, J. (2011). Overview of NUFT: a versatile numerical model for simulating flow and reactive transport in porous media. *Groundwater Reactive Transport Models*, 213-240.
- Hassanzadeh, H., Pooladi-Darvish, M., & Keith, D. W. (2009). Accelerating CO<sub>2</sub> dissolution in saline aquifers for geological storage □ Mechanistic and sensitivity studies. *Energy & Fuels*, 23(6), 3328-3336.
- Hawkes, C. D., McLellan, P. J., & Bachu, S. (2005). Geomechanical Factors Affecting Geological Storage of CO<sub>2</sub> in Depleted Oil and Gas Reservoirs. doi: 10.2118/05-10-05
- Hazi, G., Imre, A. R., Mayer, G., & Farkas, I. (2002). Lattice Boltzmann methods for two-phase flow modelling. *Annals of Nuclear Energy*, 29(12), 1421-1453. doi: 10.1016/s0306-4549(01)00115-3
- Hedges, L. O., & Whitlam, S. (2012). Patterning a surface so as to speed nucleation from solution. *Soft Matter*, 8(33), 8624-8635. doi: 10.1039/C2SM26038G
- Heinemann, N., Wilkinson, M., Haszeldine, R. S., Fallick, A. E., & Pickup, G. E. (2013). CO<sub>2</sub> sequestration in a UK North Sea analogue for geological carbon storage. *Geology*, 41(4), 411-414.
- Hendriks, C., Graus, W., & Van Bergen, F. (2004). Global carbon dioxide storage potential and costs.
- Hendriks, C. A., & Blok, K. (1993). Underground storage of carbon-dioxide. *Energy Conversion and Management*, 34(9-11), 949-957. doi: 10.1016/0196-8904(93)90041-8
- Hepple, R. P., & Benson, S. M. (2005). Geologic storage of carbon dioxide as a climate change mitigation strategy: performance requirements and the implications of surface seepage. *Environmental Geology*, 47(4), 576-585. doi: 10.1007/s00254-004-1181-2
- Highley, D. E., & Committee, M. R. C. (1977). *Silica*: HM Stationery Office.
- Hill, R. (1952). The Elastic Behaviour of a Crystalline Aggregate. *Proceedings of the Physical Society. Section A*, 65(5), 349.
- Hillis, R. R. (2001). Coupled changes in pore pressure and stress in oil fields and sedimentary basins. *Petroleum Geoscience*, 7(4), 419-425. doi: 10.1144/petgeo.7.4.419
- Holloway, S., & Savage, D. (1993). The potential for aquifer disposal of carbon-dioxide in the UK. *Energy Conversion and Management*, 34(9-11), 925-932. doi: 10.1016/0196-8904(93)90038-c
- Hosa, A., Esentia, M., Stewart, J., & Haszeldine, S. (2011). Injection of CO<sub>2</sub> into saline formations: Benchmarking worldwide projects. *Chemical Engineering Research and Design*, 89(9), 1855-1864.

- Houndfield, G. N. (1973). Computerized transverse axial scanning (Tomography). 1. Description of system. *British Journal of Radiology*, 46(552), 1016-1022.
- Hovorka, S. D., Benson, S. M., Doughty, C., Freifeld, B. M., Sakurai, S., Daley, T. M., Kharaka, Y. K., Holtz, M.H., Trautz, R.C., Nance, H. S. (2006). Measuring permanence of CO<sub>2</sub> storage in saline formations: the Frio experiment. *Environmental Geosciences*, 13(2), 105-121.
- Hu, J. W., Duan, Z. H., Zhu, C., & Chou, I. M. (2007). PVTx properties of the CO<sub>2</sub>-H<sub>2</sub>O and CO<sub>2</sub>-H<sub>2</sub>O-NaCl systems below 647 K: Assessment of experimental data and thermodynamic models. *Chemical Geology*, 238(3-4), 249-267. doi: 10.1016/j.chemgeo.2006.11.011
- IAPWS. (2014). Revised Release on the IAPWS Formulation 1995 for the Thermodynamic Properties of Ordinary Water Substance for General and Scientific Use.
- Ide, S. T., Jessen, K., & Orr, F. M. (2007). Storage of CO<sub>2</sub> in saline aquifers: Effects of gravity, viscous, and capillary forces on amount and timing of trapping. *International Journal of Greenhouse Gas Control*, 1(4), 481-491. doi: 10.1016/s1750-5836(07)00091-6
- IEA. (2008). Energy Technology Perspectives: Scenarios and Strategies to 2050, OECD/IEA, Paris.
- IEA. (2009). Technology Roadmap 2009, Carbon capture and storage, S.16. OECD/IEA
- IEA. (2010a). Energy technology perspectives. OECD/IEA, Paris, France.
- Iglauer, S., Paluszny, A., Pentland, C. H., & Blunt, M. J. (2011). Residual CO<sub>2</sub> imaged with X-ray micro-tomography. *Geophysical Research Letters*, 38, 6. doi: 10.1029/2011gl049680
- IPCC. (2007). Climate Change 2007: The Scientific Basis. Contribution of Working Group I to the Fourth Assessment Report of the Intergovernmental Panel on Climate Change, edited by S. Solomon et al., Cambridge Univ. Press, New York.
- IPCC. (2013). *Climate Change 2013: The Physical Science Basis. Contribution of Working Group I to the Fifth Assessment Report of the Intergovernmental Panel on Climate Change* (T. F. Stocker, D. Qin, G.-K. Plattner, M. Tignor, S. K. Allen, J. Boschung, A. Nauels, Y. Xia, V. Bex & P. M. Midgley Eds.). Cambridge, United Kingdom and New York, NY, USA: Cambridge University Press.
- Izgec, O., Demiral, B., Bertin, H., & Akin, S. (2008). CO<sub>2</sub> injection into saline carbonate aquifer formations I: laboratory investigation. *Transport in Porous Media*, 72(1), 1-24. doi: 10.1007/s11242-007-9132-5
- Jaeger, J., & Cook, N. (1979). Fundamentals of rock mechanics. *Mathuen, London*.

- Johnson, J. W., & Nitao, J. J. (2003). Reactive transport modelling of geologic CO<sub>2</sub> sequestration at Sleipner. *Greenhouse Gas Control Technologies*, 1, 327-332.
- Johnson, J. W., Nitao, J. J., & Knauss, K. G. (2004). Reactive transport modelling of CO<sub>2</sub> storage in saline aquifers to elucidate fundamental processes, trapping mechanisms and sequestration partitioning. *Geological storage of carbon dioxide*, 233, 107-128.
- Jordan, P., & Doughty, C. (2009). Sensitivity of CO<sub>2</sub> migration estimation on reservoir temperature and pressure uncertainty. In J. Gale, H. Herzog & J. Braitsch (Eds.), *Greenhouse Gas Control Technologies 9* (Vol. 1, pp. 2825-2832). Amsterdam: Elsevier Science Bv.
- Juanes, R., Spiteri, E. J., Orr, F. M., & Blunt, M. J. (2006). Impact of relative permeability hysteresis on geological CO<sub>2</sub> storage. *Water Resources Research*, 42(12), 13. doi: 10.1029/2005wr004806
- Jung, J.-W., & Wan, J. (2012). Supercritical CO<sub>2</sub> and Ionic Strength Effects on Wettability of Silica Surfaces: Equilibrium Contact Angle Measurements. *Energy & Fuels*, 26(9), 6053-6059. doi: 10.1021/ef300913t
- Kampman, N., Bickle, M., Wigley, M., & Dubacq, B. (2014a). Fluid flow and CO<sub>2</sub>-fluid-mineral interactions during CO<sub>2</sub>-storage in sedimentary basins. *Chemical Geology*, 369(0), 22-50. doi: <http://dx.doi.org/10.1016/j.chemgeo.2013.11.012>
- Kampman, N., Bickle, M., Wigley, M., & Dubacq, B. (2014b). Fluid flow and CO<sub>2</sub>-fluid-mineral interactions during CO<sub>2</sub> storage in sedimentary basins. *Chemical Geology*, 369, 22-50.
- Kaszuba, J., Yardley, B., & Andreani, M. (2013). Experimental perspectives of mineral dissolution and precipitation due to carbon dioxide-water-rock interactions. *Reviews in Mineralogy and Geochemistry*, 77(1), 153-188.
- Kaszuba, J. P., Janecky, D. R., & Snow, M. G. (2005). Experimental evaluation of mixed fluid reactions between supercritical carbon dioxide and NaCl brine: Relevance to the integrity of a geologic carbon repository. *Chemical Geology*, 217(3-4), 277-293. doi: 10.1016/j.chemgeo.2004.12.014
- Ketzer, J. M., Iglesias, R., Einloft, S., Dullius, J., Ligabue, R., & de Lima, V. (2009). Water-rock-CO<sub>2</sub> interactions in saline aquifers aimed for carbon dioxide storage: Experimental and numerical modelling studies of the Rio Bonito Formation (Permian), southern Brazil. *Applied Geochemistry*, 24(5), 760-767. doi: 10.1016/j.apgeochem.2009.01.001
- Kharaka, Y. K., Cole, D. R., Hovorka, S. D., Gunter, W. D., Knauss, K. G., & Freifeld, B. M. (2006). Gas-water-rock interactions in Frio Formation

following CO<sub>2</sub> injection: Implications for the storage of greenhouse gases in sedimentary basins. *Geology*, 34(7), 577-580. doi: 10.1130/g22357.1

- Kiehl, J. T., & Trenberth, K. E. (1997). Earth's annual global mean energy budget. *Bulletin of the American Meteorological Society*, 78(2), 197-208. doi: 10.1175/1520-0477(1997)078<0197:eagmeb>2.0.co;2
- Kim, T. W., Tokunaga, T. K., Shuman, D. B., Sutton, S. R., Newville, M., & Lanzirotti, A. (2012). Thickness measurements of nanoscale brine films on silica surfaces under geologic CO<sub>2</sub> sequestration conditions using synchrotron X-ray fluorescence. *Water Resources Research*, 48. doi: 10.1029/2012wr012200
- Kim, Y., Wan, J. M., Kneafsey, T. J., & Tokunaga, T. K. (2012). Dewetting of Silica Surfaces upon Reactions with Supercritical CO<sub>2</sub> and Brine: Pore-Scale Studies in Micromodels. *Environmental Science & Technology*, 46(7), 4228-4235. doi: 10.1021/es204096w
- King, M., Mubarak, A., Kim, J., & Bott, T. (1992). The mutual solubilities of water with supercritical and liquid carbon dioxides. *The Journal of Supercritical Fluids*, 5(4), 296-302.
- Kjøller, C., Weibel, R., Bateman, K., Laier, T., Nielsen, L. H., Frykman, P., & Springer, N. (2011). Geochemical impacts of CO<sub>2</sub> storage in saline aquifers with various mineralogy—Results from laboratory experiments and reactive geochemical modelling. *Energy Procedia*, 4(0), 4724-4731. doi: <http://dx.doi.org/10.1016/j.egypro.2011.02.435>
- Knauss, K. G., Johnson, J. W., & Steefel, C. I. (2005). Evaluation of the impact of CO<sub>2</sub>, co-contaminant gas, aqueous fluid and reservoir rock interactions on the geologic sequestration of CO<sub>2</sub>. *Chemical Geology*, 217(3-4), 339-350. doi: 10.1016/j.chemgeo.2004.12.017
- Knorr, W. (2009). Is the airborne fraction of anthropogenic CO<sub>2</sub> emissions increasing? *Geophysical Research Letters*, 36. doi: 10.1029/2009gl040613
- Krevor, S. C. M., Pini, R., Li, B. X., & Benson, S. M. (2011). Capillary heterogeneity trapping of CO<sub>2</sub> in a sandstone rock at reservoir conditions. *Geophysical Research Letters*, 38, 5. doi: 10.1029/2011gl048239
- Kummerow, J., & Spangenberg, E. (2011). Experimental evaluation of the impact of the interactions of CO<sub>2</sub>-SO<sub>2</sub>, brine, and reservoir rock on petrophysical properties: A case study from the Ketzin test site, Germany. *Geochemistry Geophysics Geosystems*, 12, 10. doi: 10.1029/2010gc003469
- Kvamme, B., & Liu, S. (2009). Reactive transport of CO<sub>2</sub> in saline aquifers with implicit geomechanical analysis. *Energy Procedia*, 1(1), 3267-3274.

- Kwok, R., & Rothrock, D. A. (2009). Decline in Arctic sea ice thickness from submarine and ICESat records: 1958-2008. *Geophysical Research Letters*, *36*. doi: 10.1029/2009gl039035
- Lamy-Chappuis, B., Angus, D., Fisher, Q., Grattoni, C., Yardley, B. W. D. (2014). Rapid porosity and permeability changes of calcareous sandstone due to CO<sub>2</sub>-enriched brine injection. *Geophysical Research Letters*, *41*, 399-406, doi: 10.1002/2013GL058534
- Langan, R. T., Lazaratos, S. K., Harris, J. M., Vassiliou, A. A., Jensen, T. L., & Fairborn, J. W. (1997). Imaging of a Stratigraphically Complex Carbonate Reservoir with Crosswell Seismic Data *Carbonate Seismology* (pp. 417-424).
- Lashof, D. A. (1989). The dynamic greenhouse – Feedback processes that may influence future concentrations of atmospheric trace gases and climate-change. *Climatic Change*, *14*(3), 213-242. doi: 10.1007/bf00134964
- Lemmon, E., McLinden, M., & Friend, D. (2005). Thermophysical properties of fluid systems. *NIST chemistry webbook, NIST standard reference database*, 69.
- Lenormand, R., Touboul, E., & Zarcone, C. (1988). Numerical models and experiments on immiscible displacements in porous media. *Journal of Fluid Mechanics*, *189*, 165-187. doi: 10.1017/s0022112088000953
- Leonenko, Y., & Keith, D. W. (2008). Reservoir engineering to accelerate the dissolution of CO<sub>2</sub> stored in aquifers. *Environmental Science & Technology*, *42*(8), 2742-2747.
- Li, G. (2003). 4D seismic monitoring of CO<sub>2</sub> flood in a thin fractured carbonate reservoir. *The Leading Edge*, *22*(7), 690-695. doi: 10.1190/1.1599698
- Li, L., Peters, C. A., & Celia, M. A. (2006). Upscaling geochemical reaction rates using pore-scale network modelling. *Advances in water resources*, *29*(9), 1351-1370.
- Li, X., Ross, D. A., Trusler, J. P., Maitland, G. C., & Boek, E. S. (2013). Molecular dynamics simulations of CO<sub>2</sub> and brine interfacial tension at high temperatures and pressures. *J Phys Chem B*, *117*(18), 5647-5652. doi: 10.1021/jp309730m
- Lichtner, P. (1999). FLOTRAN user's guide, report, Los Alamos Natl. Lab., Los Alamos, NM.
- Lindeberg, E., & Wesselberg, D. (1997). Vertical convection in an aquifer column under a gas cap of CO<sub>2</sub>. *Energy Conversion and Management*, *38*, S229-S234. doi: 10.1016/s0196-8904(96)00274-9

- Lowden, B., Braley, S., Hurst, A., & Lewis, J. (1992). Sedimentological studies of the Cretaceous Lochaline Sandstone, NW Scotland. *Geological Society, London, Special Publications*, 62(1), 159-162.
- Lu, J. M., Kharaka, Y. K., Thordsen, J. J., Horita, J., Karamalidis, A., Griffith, C., Hakala, J. A., Ambats, G., Cole, D. R., Phelps, T. J., Manning, M. A., Cook, P. J., Hovorka, S. D. (2012). CO<sub>2</sub>-rock-brine interactions in Lower Tuscaloosa Formation at Cranfield CO<sub>2</sub> sequestration site, Mississippi, USA. *Chemical Geology*, 291, 269-277. doi: 10.1016/j.chemgeo.2011.10.020
- Lu, P., Fu, Q., Seyfried, W. E., Hereford, A., & Zhu, C. (2011). Navajo Sandstone-brine-CO<sub>2</sub> interaction: implications for geological carbon sequestration. *Environmental Earth Sciences*, 62(1), 101-118. doi: 10.1007/s12665-010-0501-y
- Lucier, A., Zoback, M., Gupta, N., & Ramakrishnan, T. S. (2006). Geomechanical aspects of CO<sub>2</sub> sequestration in a deep saline reservoir in the Ohio River Valley region. *Environmental Geosciences*, 13(2), 85-103. doi: 10.1306/eg.11230505010
- Lumley, D. E. (2001). Time-lapse seismic reservoir monitoring. *Geophysics*, 66(1), 50-53. doi: 10.1190/1.1444921
- Luquot, L., & Gouze, P. (2009). Experimental determination of porosity and permeability changes induced by injection of CO<sub>2</sub> into carbonate rocks. *Chemical Geology*, 265(1-2), 148-159. doi: 10.1016/j.chemgeo.2009.03.028
- MacMinn, C. W., Szulczewski, M. L., & Juanes, R. (2011). CO<sub>2</sub> migration in saline aquifers: regimes in migration with dissolution. *10th International Conference on Greenhouse Gas Control Technologies*, 4, 3904-3910. doi: 10.1016/j.egypro.2011.02.328
- Mao, S., & Duan, Z. H. (2008). The P,V,T,x properties of binary aqueous chloride solutions up to T=573 K and 100 MPa. *Journal of Chemical Thermodynamics*, 40(7), 1046-1063. doi: 10.1016/j.jct.2008.03.005
- Mao, S. D., & Duan, Z. H. (2009). The Viscosity of Aqueous Alkali-Chloride Solutions up to 623 K, 1,000 bar, and High Ionic Strength. *International Journal of Thermophysics*, 30(5), 1510-1523. doi: 10.1007/s10765-009-0646-7
- Mao, S. D., Duan, Z. H., Hu, J. W., & Zhang, D. H. (2010). A model for single-phase PVTx properties of CO<sub>2</sub>-CH<sub>4</sub>-C<sub>2</sub>H<sub>6</sub>-N<sub>2</sub>-H<sub>2</sub>O-NaCl fluid mixtures from 273 to 1273 K and from 1 to 5000 bar. *Chemical Geology*, 275(3-4), 148-160. doi: 10.1016/j.chemgeo.2010.05.004
- Marsden, R. (2007). Geomechanics for reservoir management. *Algeria Well Evaluation Conference: 398*.
- Mathias, S. A., Hardisty, P. E., Trudell, M. R., & Zimmerman, R. W. (2009). Approximate Solutions for Pressure Buildup During CO<sub>2</sub> Injection in

- Brine Aquifers. *Transport in Porous Media*, 79(2), 265-284. doi: 10.1007/s11242-008-9316-7
- Matteo, E. N., & Scherer, G. W. (2012). Experimental study of the diffusion-controlled acid degradation of Class H Portland cement. *International Journal of Greenhouse Gas Control*, 7(0), 181-191. doi: <http://dx.doi.org/10.1016/j.ijggc.2011.07.012>
- Mavko, G., & Jizba, D. (1991). Estimating grain-scale fluid effects on velocity dispersion in rocks. *Geophysics*, 56(12), 1940-1949. doi: 10.1190/1.1443005
- Mavko, G., Mukerji, T., & Dvorkin, J. (2009). *The rock physics handbook: Tools for seismic analysis of porous media*: Cambridge university press.
- Mavko, G., Tapan Mukerji,, & Dvorkin., J. (2009). *The Rock Physics Handbook*: Cambridge University Press.
- McCoy, S. T., & Rubin, E. S. (2008). An engineering-economic model of pipeline transport of CO<sub>2</sub> with application to carbon capture and storage. *International Journal of Greenhouse Gas Control*, 2(2), 219-229. doi: [http://dx.doi.org/10.1016/S1750-5836\(07\)00119-3](http://dx.doi.org/10.1016/S1750-5836(07)00119-3)
- McCune, C. C., Fogler, H. S., & Kline, W. E. (1979). Experimental-technique for obtaining permeability-porosity relationship in acidized porous-media. *Industrial & Engineering Chemistry Fundamentals*, 18(2), 188-191. doi: 10.1021/i160070a016
- Metz, B., Davidson, O., De Coninck, H., Loos, M., & Meyer, L. (2005). IPCC, 2005: IPCC special report on carbon dioxide capture and storage. Prepared by Working Group III of the Intergovernmental Panel on Climate Change. *Cambridge, United Kingdom and New York, NY, USA*, 442 pp.
- Meyer, R. (2001). 4D seismic and time-lapse reservoir geology: CREWES research report, 13. 895-906.
- Michael, K., Golab, A., Shulakova, V., Ennis-King, J., Allinson, G., Sharma, S., & Aiken, T. (2010). Geological storage of CO<sub>2</sub> in saline aquifers - A review of the experience from existing storage operations. *International Journal of Greenhouse Gas Control*, 4(4), 659-667. doi: 10.1016/j.ijggc.2009.12.011
- Miller, R. D., Raef, A., Byrnes, A., Lambrecht, J., & Harrison, W. (2004). 4-D high-resolution seismic reflection monitoring of miscible CO<sub>2</sub> injected into a carbonate reservoir in the Hall-Gurney Field. *Russell County, Kansas [Exp. Abs.]: Society of Exploration Geophysicists*.
- Mondal, M. K., Balsora, H. K., & Varshney, P. (2012). Progress and trends in CO<sub>2</sub> capture/separation technologies: A review. *Energy*, 46(1), 431-441. doi: 10.1016/j.energy.2012.08.006

- Moroni, M., & Cushman, J. H. (2001). Three-dimensional particle tracking velocimetry studies of the transition from pore dispersion to Fickian dispersion for homogeneous porous media. *Water Resources Research*, 37(4), 873-884. doi: 10.1029/2000wr900364
- Morse, J. W., & Arvidson, R. S. (2002). The dissolution kinetics of major sedimentary carbonate minerals. *Earth-Science Reviews*, 58(1-2), 51-84. doi: 10.1016/s0012-8252(01)00083-6
- Murphy, W., Reischer, A., & Hsu, K. (1993). Modulus decomposition of compressional and shear velocities in sand bodies. *Geophysics*, 58(2), 227-239.
- Mutoru, J. W., Leahy - Dios, A., & Firoozabadi, A. (2011). Modelling infinite dilution and Fickian diffusion coefficients of carbon dioxide in water. *Aiche Journal*, 57(6), 1617-1627.
- Nakashima, Y., & Yamaguchi, T. (2004). DMAP. m: A Mathematica® program for three-dimensional mapping of tortuosity and porosity of porous media. *Bulletin – Geological Survey Japan*, 55, 93-103.
- Nelson, P. H. (1994). Permeability-porosity relationships in sedimentary rocks. *The log analyst*, 35(03).
- Neufeld, J. A., Hesse, M. A., Riaz, A., Hallworth, M. A., Tchelepi, H. A., & Huppert, H. E. (2010). Convective dissolution of carbon dioxide in saline aquifers. *Geophysical Research Letters*, 37, 5. doi: 10.1029/2010gl044728
- Nielsen, L. C., Bourg, I. C., & Sposito, G. (2012). Predicting CO<sub>2</sub>-water interfacial tension under pressure and temperature conditions of geologic CO<sub>2</sub> storage. *Geochimica et Cosmochimica Acta*, 81, 28-38.
- Nogues, J. P., Fitts, J. P., Celia, M. A., & Peters, C. A. (2013). Permeability evolution due to dissolution and precipitation of carbonates using reactive transport modelling in pore networks. *Water Resources Research*, 49(9), 6006-6021.
- Noiriel, C., Madé, B., & Gouze, P. (2007). Impact of coating development on the hydraulic and transport properties in argillaceous limestone fracture. *Water Resources Research*, 43(9).
- Nordbotten, J. M., & Celia, M. A. (2006). Similarity solutions for fluid injection into confined aquifers. *Journal of Fluid Mechanics*, 561, 307-327. doi: 10.1017/s0022112006000802
- Nordbotten, J. M., Kavetski, D., Celia, M. A., & Bachu, S. (2008). Model for CO<sub>2</sub> Leakage Including Multiple Geological Layers and Multiple Leaky Wells. *Environmental Science & Technology*, 43(3), 743-749. doi: 10.1021/es801135v
- Nourgaliev, R. R., Dinh, T. N., Theofanous, T. G., & Joseph, D. (2003). The lattice Boltzmann equation method: theoretical interpretation,

- numerics and implications. *International Journal of Multiphase Flow*, 29(1), 117-169. doi: 10.1016/s0301-9322(02)00108-8
- Ogilvie, S. R., & Glover, P. W. (2001). The petrophysical properties of deformation bands in relation to their microstructure. *Earth and Planetary Science Letters*, 193(1), 129-142.
- Ostrander, W. J. (1984). Plane-wave reflection coefficients for gas sands at non-normal angles of incidence. *Geophysics*, 49(10), 1637-1648. doi: 10.1190/1.1441571
- Ott, H., de Kloe, K., Marcelis, F., & Makurat, A. (2011). Injection of supercritical CO<sub>2</sub> in brine saturated sandstone: Pattern formation during salt precipitation. *Energy Procedia*, 4, 4425-4432.
- Palandri, J. L., & Kharaka, Y. K. (2004). A compilation of rate parameters of water-mineral interaction kinetics for application to geochemical modelling: DTIC Document.
- Pape, H., Clauser, C., & Iffland, J. (1999). Permeability prediction based on fractal pore-space geometry. *Geophysics*, 64(5), 1447-1460. doi: 10.1190/1.1444649
- Pape, H., Clauser, C., & Iffland, J. (2000). Variation of permeability with porosity in sandstone diagenesis interpreted with a fractal pore space model. *Pure and Applied Geophysics*, 157(4), 603-619. doi: 10.1007/pl00001110
- Parkhurst, D. L., & Appelo, C. (2013). *Description of Input and Examples for PHREEQC Version 3--a Computer Program for Speciation, Batch-reaction, One-dimensional Transport, and Inverse Geochemical Calculations*.
- Parkhurst, D. L., Kipp, K. L., & Charlton, S. R. (2010). PHAST Version 2—A program for simulating groundwater flow, solute transport, and multicomponent geochemical reactions. *US Geological Survey techniques and methods*, 6, A35.
- Pentland, C. H., El-Maghraby, R., Iglauer, S., & Blunt, M. J. (2011). Measurements of the capillary trapping of super-critical carbon dioxide in Berea sandstone. *Geophysical Research Letters*, 38, 4. doi: 10.1029/2011gl046683
- Perrin, J. C., Krause, M., Kuo, C. W., Miljkovic, L., Charoba, E., & Benson, S. M. (2009). Core-scale experimental study of relative permeability properties of CO<sub>2</sub> and brine in reservoir rocks. *Greenhouse Gas Control Technologies* 9, 1(1), 3515-3522. doi: 10.1016/j.egypro.2009.02.144
- Peters, C. A. (2009). Accessibilities of reactive minerals in consolidated sedimentary rock: An imaging study of three sandstones. *Chemical Geology*, 265(1-2), 198-208. doi: 10.1016/j.chemgeo.2008.11.014

- Plug, W. J., & Bruining, J. (2007). Capillary pressure for the sand-CO<sub>2</sub>-water system under various pressure conditions. Application to CO<sub>2</sub> sequestration. *Advances in Water Resources*, 30(11), 2339-2353. doi: 10.1016/j.advwatres.2007.05.010
- Plummer, L., Wigley, T., & Parkhurst, D. (1978). The kinetics of calcite dissolution in CO<sub>2</sub>-water systems at 5 degrees to 60 degrees C and 0.0 to 1.0 atm CO<sub>2</sub>. *American Journal of Science*, 278(2), 179-216.
- Pokrovsky, O. S., Golubev, S. V., & Schott, J. (2005). Dissolution kinetics of calcite, dolomite and magnesite at 25 degrees C and 0 to 50 atm pCO<sub>2</sub>. *Chemical Geology*, 217(3-4), 239-255. doi: 10.1016/j.chemgeo.2004.12.012
- Pokrovsky, O. S., Golubev, S. V., Schott, J., & Castillo, A. (2009). Calcite, dolomite and magnesite dissolution kinetics in aqueous solutions at acid to circumneutral pH, 25 to 150° C and 1 to 55 atm PCO<sub>2</sub>: New constraints on CO<sub>2</sub> sequestration in sedimentary basins. *Chemical Geology*, 265(1), 20-32.
- Prigiobbe, V., Costa, G., Baciocchi, R., Hänchen, M., & Mazzotti, M. (2009). The effect of and salinity on olivine dissolution kinetics at 120C. *Chemical Engineering Science*, 64(15), 3510-3515. doi: <http://dx.doi.org/10.1016/j.ces.2009.04.035>
- Pruess, K. (2009). Formation dry-out from CO<sub>2</sub> injection into saline aquifers: 2. Analytical model for salt precipitation. *Water Resources Research*, 45, 6. doi: 10.1029/2008wr007102
- Pruess, K., & Müller, N. (2009). Formation dry - out from CO<sub>2</sub> injection into saline aquifers: 1. Effects of solids precipitation and their mitigation. *Water Resources Research*, 45(3).
- Qi, R., LaForce, T. C., & Blunt, M. J. (2009). Design of carbon dioxide storage in aquifers. *International Journal of Greenhouse Gas Control*, 3(2), 195-205. doi: 10.1016/j.ijggc.2008.08.004
- Raabe, D. (2004). Overview of the lattice Boltzmann method for nano- and microscale fluid dynamics in materials science and engineering. *Modelling and Simulation in Materials Science and Engineering*, 12(6), R13-R46. doi: 10.1088/0965-0393/12/6/r01
- Radilla, G., Kacem, M., Lombard, J. M., & Fourar, M. (2010). Transport Properties of Lavoux Limestone at Various Stages of CO<sub>2</sub>-Like Acid-Rock Alteration. *Oil & Gas Science and Technology-Revue D Ifp Energies Nouvelles*, 65(4), 557-563. doi: 10.2516/ogst/2009081
- Ramaswamy, V., Schwarzkopf, M. D., Randel, W. J., Santer, B. D., Soden, B. J., & Stenchikov, G. L. (2006). Anthropogenic and natural influences in the evolution of lower stratospheric cooling. *Science*, 311(5764), 1138-1141. doi: 10.1126/science.1122587

- Rasool, S. I., & Debergh, C. (1970). Runaway greenhouse and accumulation of CO<sub>2</sub> in Venus atmosphere. *Nature*, 226(5250), 1037-&. doi: 10.1038/2261037a0
- Raymer, L. L., Hunt, E. R., & Gardner, J. S. (1980). *An Improved Sonic Transit Time-To-Porosity Transform*.
- Regnault, O., Lagneau, V., Catalette, H., & Schneider, H. (2005). Experimental study of pure mineral phases/supercritical CO<sub>2</sub> reactivity. Implications for geological CO<sub>2</sub> sequestration. *Comptes Rendus Geoscience*, 337(15), 1331-1339. doi: 10.1016/j.crte.2005.07.012
- Rimmele, G., Barlet-Gouedard, V., & Renard, F. (2010). Evolution of the Petrophysical and Mineralogical Properties of Two Reservoir Rocks Under Thermodynamic Conditions Relevant for CO<sub>2</sub> Geological Storage at 3 km Depth. *Oil & Gas Science and Technology-Revue D Ifp Energies Nouvelles*, 65(4), 565-580. doi: 10.2516/ogst/2009071
- Rodriguez-Blanco, J. D., Shaw, S., & Benning, L. G. (2011). The kinetics and mechanisms of amorphous calcium carbonate (ACC) crystallization to calcite, via vaterite. *Nanoscale*, 3(1), 265-271.
- Rosenbauer, R. J., Koksalan, T., & Palandri, J. L. (2005). Experimental investigation of CO<sub>2</sub>-brine-rock interactions at elevated temperature and pressure: Implications for CO<sub>2</sub> sequestration in deep-saline aquifers. *Fuel Processing Technology*, 86(14-15), 1581-1597. doi: 10.1016/j.fuproc.2005.01.011
- Rosenqvist, J., Kilpatrick, A. D., & Yardley, B. W. D. (2012). Solubility of carbon dioxide in aqueous fluids and mineral suspensions at 294 K and subcritical pressures. *Applied Geochemistry*, 27(8), 1610-1614. doi: 10.1016/j.apgeochem.2012.03.008
- Ross, G. D., Todd, A. C., Tweedie, J. A., & Will, A. G. (1982). *The dissolution effects of CO<sub>2</sub>-brine systems on the permeability of UK and North Sea calcareous sandstones*. Paper presented at the SPE Enhanced Oil Recovery Symposium.
- Rutqvist, J., Birkholzer, J., Cappa, F., & Tsang, C. F. (2007). Estimating maximum sustainable injection pressure during geological sequestration of CO<sub>2</sub> using coupled fluid flow and geomechanical fault-slip analysis. *Energy Conversion and Management*, 48(6), 1798-1807. doi: 10.1016/j.enconman.2007.01.021
- Rutqvist, J., Birkholzer, J. T., & Tsang, C. F. (2008a). Coupled reservoir-geomechanical analysis of the potential for tensile and shear failure associated with CO<sub>2</sub> injection in multilayered reservoir-caprock systems. *International Journal of Rock Mechanics and Mining Sciences*, 45(2), 132-143. doi: 10.1016/j.ijrmms.2007.04.006

- Rutqvist, J., Birkholzer, J. T., & Tsang, C. F. (2008b). Coupled reservoir-geomechanical analysis of the potential for tensile and shear failure associated with CO<sub>2</sub> injection in multilayered reservoir-caprock systems.
- Sabine, C. L., Feely, R. A., Gruber, N., Key, R. M., Lee, K., Bullister, J. L., Wanninkhof, R., Wong, C. S., Wallace, D. W. R., Tilbrook, B., Millero, F. J., Peng, T. H., Kozyr, A., Ono, T., Rios, A. F. (2004). The oceanic sink for anthropogenic CO<sub>2</sub>. *Science*, *305*(5682), 367-371. doi: 10.1126/science.1097403
- Sahimi, M. (1993). Flow phenomena in rocks - From continuum models to fractals, percolation, cellular-automata, and simulated annealing. *Reviews of Modern Physics*, *65*(4), 1393-1534. doi: 10.1103/RevModPhys.65.1393
- Santer, B. D., Taylor, K. E., Wigley, T. M. L., Johns, T. C., Jones, P. D., Karoly, D. J., Mitchell, J. F. B., Oort, A. H., Penner, J. E., Ramaswamy, V., Schwarzkopf, M. D., Stouffer, R. J., Tett, S. (1996). A search for human influences on the thermal structure of the atmosphere. *Nature*, *382*(6586), 39-46. doi: 10.1038/382039a0
- Santer, B. D., Wehner, M. F., Wigley, T. M. L., Sausen, R., Meehl, G. A., Taylor, K. E., Ammann, C., Arblaster, J., Washington, W. M., Boyle, J. S., Bruggemann, W. (2003). Contributions of anthropogenic and natural forcing to recent tropopause height changes. *Science*, *301*(5632), 479-483. doi: 10.1126/science.1084123
- Sasaki, K., Fujii, T., Nilbori, Y., Ito, T., & Hashida, T. (2008). Numerical simulation of supercritical CO<sub>2</sub> injection into subsurface rock masses. *Energy Conversion and Management*, *49*(1), 54-61. doi: 10.1016/j.enconman.2007.05.015
- Sato, K., Mito, S., Horie, T., Ohkuma, H., Saito, H., Watanabe, J., & Yoshimura, T. (2011). Monitoring and simulation studies for assessing macro- and meso-scale migration of CO<sub>2</sub> sequestered in an onshore aquifer: Experiences from the Nagaoka pilot site, Japan. *International Journal of Greenhouse Gas Control*, *5*(1), 125-137. doi: 10.1016/j.ijggc.2010.03.003
- Sayegh, S., Krause, F., Girard, M., & DeBree, C. (1990). Rock/Fluid Interactions of Carbonated Brines in a Sandstone Reservoir: Pembina Cardium Alberta Canada. *SPE Formation Evaluation*, *5*(04), 399-405.
- Schaef, H. T., Miller, Q. R. S., Thompson, C. J., Loring, J. S., Bowden, M. S., Arey, B. W., . . . Rosso, K. M. (2013). Silicate Carbonation in Supercritical CO<sub>2</sub> Containing Dissolved H<sub>2</sub>O: An in situ High Pressure X-Ray Diffraction and Infrared Spectroscopy Study. *Energy Procedia*, *37*(0), 5892-5896. doi: <http://dx.doi.org/10.1016/j.egypro.2013.06.514>
- Schaef, H. T., Windisch, C. F., McGrail, B. P., Martin, P. F., & Rosso, K. M. (2011). Brucite Mg(OH<sub>2</sub>) carbonation in wet supercritical CO<sub>2</sub>: An in

- situ high pressure X-ray diffraction study. *Geochimica et Cosmochimica Acta*, 75(23), 7458-7471. doi: 10.1016/j.gca.2011.09.029
- Shah, P., Campbell, G., McKee, S., & Rielly, C. (1998). Proving of bread dough: modelling the growth of individual bubbles. *Food and bioproducts processing*, 76(2), 73-79.
- Shao, H., Ray, J. R., & Jun, Y.-S. (2010). Dissolution and precipitation of clay minerals under geologic CO<sub>2</sub> sequestration conditions: CO<sub>2</sub>-brine- phlogopite interactions. *Environmental Science & Technology*, 44(15), 5999-6005.
- Sheriff, R. E., and L. P. Geldart. (1995). Exploration Seismology. *Cambridge Univ. Press, New York*, 592 pp.
- Shi, J. Q., Sinayuc, C., Durucan, S., & Korre, A. (2012). Assessment of carbon dioxide plume behaviour within the storage reservoir and the lower caprock around the KB-502 injection well at In Salah. *International Journal of Greenhouse Gas Control*, 7, 115-126. doi: 10.1016/j.ijggc.2012.01.002
- Shiraki, R., & Dunn, T. L. (2000). Experimental study on water-rock interactions during CO<sub>2</sub> flooding in the Tensleep Formation, Wyoming, USA. *Applied Geochemistry*, 15(3), 265-279. doi: 10.1016/s0883-2927(99)00048-7
- Sholokhova, Y., Kim, D., & Lindquist, W. B. (2009). Network flow modelling via lattice-Boltzmann based channel conductance. *Advances in Water Resources*, 32(2), 205-212. doi: 10.1016/j.advwatres.2008.10.016
- Soliva, R., Schultz, R. A., Ballas, G., Taboada, A., Wibberley, C., Sallet, E., & Benedicto, A. (2013). A model of strain localization in porous sandstone as a function of tectonic setting, burial and material properties; new insight from Provence (southern France). *Journal of Structural Geology*, 49, 50-63.
- Solomon, S., Plattner, G. K., Knutti, R., & Friedlingstein, P. (2009). Irreversible climate change due to carbon dioxide emissions. *Proceedings of the National Academy of Sciences of the United States of America*, 106(6), 1704-1709. doi: 10.1073/pnas.0812721106
- Sonnenthal, E., Ito, A., Spycher, N., Yui, M., Apps, J., Sugita, Y., Conrad, M., Kawakami, S. (2005). Approaches to modelling coupled thermal, hydrological, and chemical processes in the Drift Scale Heater Test at Yucca Mountain. *International Journal of Rock Mechanics and Mining Sciences*, 42(5-6), 698-719. doi: 10.1016/j.ijrmms.2005.03.009
- Soong, Y., Goodman, A. L., McCarthy-Jones, J. R., & Baltrus, J. P. (2004). Experimental and simulation studies on mineral trapping of CO<sub>2</sub> with

- brine. *Energy Conversion and Management*, 45(11-12), 1845-1859.  
doi: 10.1016/j.enconman.2003.09.029
- Span, R., & Wagner, W. (1996). A new equation of state for carbon dioxide covering the fluid region from the triple-point temperature to 1100 K at pressures up to 800 MPa. *Journal of Physical and Chemical Reference Data*, 25(6), 1509-1596.
- Spycher, N., & Pruess, K. (2005). CO<sub>2</sub>-H<sub>2</sub>O mixtures in the geological sequestration of CO<sub>2</sub>. II. Partitioning in chloride brines at 12–100° C and up to 600 bar. *Geochimica Et Cosmochimica Acta*, 69(13), 3309-3320.
- Spycher, N., Pruess, K., & Ennis-King, J. (2003). CO<sub>2</sub>-H<sub>2</sub>O mixtures in the geological sequestration of CO<sub>2</sub>. I. Assessment and calculation of mutual solubilities from 12 to 100° C and up to 600 bar. *Geochimica et Cosmochimica Acta*, 67(16), 3015-3031.
- Steefel, C. (2006). Crunch-users guide. USA. Lawrence Berkeley Laboratory.
- Steefel, C. I. (2009). CrunchFlow. *Software for Modelling Multicomponent Reactive Flow and Transport. User's Manual*. Lawrence Berkeley National Laboratory, Berkeley, USA.
- Steefel, C. I., DePaolo, D. J., & Lichtner, P. C. (2005). Reactive transport modelling: An essential tool and a new research approach for the Earth sciences. *Earth and Planetary Science Letters*, 240(3), 539-558.
- Steefel, C. I., & Maher, K. (2009). Fluid-Rock Interaction: A Reactive Transport Approach. In E. H. Oelkers & J. Schott (Eds.), *Thermodynamics and Kinetics of Water-Rock Interaction* (Vol. 70, pp. 485-532). Chantilly: Mineralogical Soc Amer.
- Steefel, C. I., & Van Cappellen, P. (1990). A new kinetic approach to modelling water-rock interaction - the role of nucleation, precursors, and ostwald ripening. *Geochimica et Cosmochimica Acta*, 54(10), 2657-2677. doi: 10.1016/0016-7037(90)90003-4
- Streets, A. M., & Quake, S. R. (2010). Ostwald ripening of clusters during protein crystallization. *Physical review letters*, 104(17), 178102.
- Tanino, Y., & Blunt, M. J. (2012). Capillary trapping in sandstones and carbonates: Dependence on pore structure. *Water Resources Research*, 48(8), W08525. doi: 10.1029/2011WR011712
- Tartakovsky, A. M., Redden, G., Lichtner, P. C., Scheibe, T. D., & Meakin, P. (2008). Mixing - induced precipitation: Experimental study and multiscale numerical analysis. *Water Resources Research*, 44(6).

- Teufel, L. W., Rhett, D. W., & Farrell, H. E. (1991). *Effect of Reservoir Depletion And Pore Pressure Drawdown On In Situ Stress And Deformation In the Ekofisk Field, North Sea*.
- Tokunaga, T. K., & Wan, J. (2013). Capillary Pressure and Mineral Wettability Influences on Reservoir CO<sub>2</sub> Capacity. *Reviews in Mineralogy and Geochemistry*, 77(1), 481-503. doi: 10.2138/rmg.2013.77.14
- Torabi, A., & Fossen, H. (2009). Spatial variation of microstructure and petrophysical properties along deformation bands in reservoir sandstones. *AAPG bulletin*, 93(7), 919-938.
- Tosaya, C., & Nur, A. (1982). Effects of diagenesis and clays on compressional velocities in rocks. *Geophysical Research Letters*, 9(1), 5-8. doi: 10.1029/GL009i001p00005
- Townend, J., & Zoback, M. D. (2000). How faulting keeps the crust strong. *Geology*, 28(5), 399-402. doi: 10.1130/0091-7613(2000)28<399:hfkts>2.0.co;2
- van der Meer, L. G. H. (1992). Investigations regarding the storage of carbon dioxide in aquifers in the Netherlands. *Energy Conversion and Management*, 33(5-8), 611-618. doi: [http://dx.doi.org/10.1016/0196-8904\(92\)90063-3](http://dx.doi.org/10.1016/0196-8904(92)90063-3)
- Vanorio, T., & Mavko, G. (2011). Laboratory measurements of the acoustic and transport properties of carbonate rocks and their link with the amount of microcrystalline matrix. *Geophysics*, 76(4), E105-E115. doi: 10.1190/1.3580632
- Vanorio, T., Nur, A., & Ebert, Y. (2011). Rock physics analysis and time-lapse rock imaging of geochemical effects due to the injection of CO<sub>2</sub> into reservoir rocks. *Geophysics*, 76(5), O23-O33. doi: 10.1190/geo2010-0390.1
- Vargaftik, N. B. (1975). Tables on the thermophysical properties of liquids and gases in normal and dissociated states.
- Vogel, H. J., Tolke, J., Schulz, V. P., Krafczyk, M., & Roth, K. (2005). Comparison of a Lattice-Boltzmann model, a full-morphology model, and a pore network model for determining capillary pressure-saturation relationships. *Vadose Zone Journal*, 4(2), 380-388. doi: 10.2136/vzj2004.0114
- Wang, J., Ryan, D., Anthony, E. J., Wildgust, N., & Aiken, T. (2011). Effects of impurities on CO<sub>2</sub> transport, injection and storage. *Energy Procedia*, 4(0), 3071-3078. doi: <http://dx.doi.org/10.1016/j.egypro.2011.02.219>
- Wang, Y., Zhang, C., Wei, N., Oostrom, M., Wietsma, T. W., Li, X., & Bonneville, A. (2013). Experimental study of crossover from capillary to viscous fingering for supercritical CO<sub>2</sub>-water displacement in a

homogeneous pore network. *Environ Sci Technol*, 47(1), 212-218.  
doi: 10.1021/es3014503

- Wang, Z., Hirsche, W. K., & Sedgwick, G. (1991). *Seismic velocities in carbonate rocks: Can Pet Technol V30, N2, March–April 1991, P112–122*. Paper presented at the International Journal of Rock Mechanics and Mining Sciences & Geomechanics Abstracts.
- Watson, M. N., Zwingmann, N., & Lemon, N. M. (2004). The Ladbroke Grove–Katnook carbon dioxide natural laboratory: A recent CO<sub>2</sub> accumulation in a lithic sandstone reservoir. *Energy*, 29(9), 1457-1466.
- White, C. M., Strazisar, B. R., Granite, E. J., Hoffman, J. S., & Pennline, H. W. (2003). Separation and capture of CO<sub>2</sub> from large stationary sources and sequestration in geological formations—coalbeds and deep saline aquifers. *Journal of the Air & Waste Management Association*, 53(6), 645-715.
- White, C. M., Strazisar, B. R., Granite, E. J., Hoffman, J. S., & Pennline, H. W. (2003). Separation and capture of CO<sub>2</sub> from large stationary sources and sequestration in geological formations - Coalbeds and deep saline aquifers. *Journal of the Air & Waste Management Association*, 53(6), 645-715.
- Wibberley, C. A., Petit, J.-P., & Rives, T. (2000). Mechanics of cataclastic 'deformation band' faulting in high-porosity sandstone, Provence. *Comptes Rendus de l'Académie des Sciences-Series IIA-Earth and Planetary Science*, 331(6), 419-425.
- Wigand, M., Kaszuba, J. P., Carey, J. W., & Hollis, W. K. (2009). Geochemical effects of CO<sub>2</sub> sequestration on fractured wellbore cement at the cement/caprock interface. *Chemical Geology*, 265(1-2), 122-133. doi: 10.1016/j.chemgeo.2009.04.008
- Wigley, M., Kampman, N., Chapman, H., Dubacq, B., & Bickle, M. (2013). In situ redeposition of trace metals mobilized by CO<sub>2</sub> - charged brines. *Geochemistry, Geophysics, Geosystems*, 14(5), 1321-1332.
- Wildenschild, D., & Sheppard, A. P. (2013). X-ray imaging and analysis techniques for quantifying pore-scale structure and processes in subsurface porous medium systems. *Advances in Water Resources*, 51, 217-246. doi: 10.1016/j.advwatres.2012.07.018
- Withjack, E. M. Computed Tomography for Rock-Property Determination and Fluid-Flow Visualization. doi: 10.2118/16951-PA
- Wollenweber, J., Alles, S., Busch, A., Krooss, B. M., Stanjek, H., & Littke, R. (2010). Experimental investigation of the CO<sub>2</sub> sealing efficiency of caprocks. *International Journal of Greenhouse Gas Control*, 4(2), 231-241. doi: 10.1016/j.ijggc.2010.01.003

- Wollenweber, J., Alles, S. A., Kronimus, A., Busch, A., Stanjek, H., & Krooss, B. M. (2009). Caprock and overburden processes in geological CO<sub>2</sub> storage: An experimental study on sealing efficiency and mineral alterations. *Greenhouse Gas Control Technologies* 9, 1(1), 3469-3476. doi: 10.1016/j.egypro.2009.02.138
- Wood, A. B. (1941). *A textbook of sound: being an account of the physics of vibrations with special reference to recent theoretical and technical developments*: The Macmillan company.
- Wyllie, M., Gardner, G., & Gregory, A. (1962). Studies of elastic wave attenuation in porous media. *Geophysics*, 27(5), 569-589. doi: 10.1190/1.1439063
- Xiao, Y. T., Xu, T. F., & Pruess, K. (2009). The effects of gas-fluid-rock interactions on CO<sub>2</sub> injection and storage: insights from reactive transport modelling. *Greenhouse Gas Control Technologies* 9, 1(1), 1783-1790. doi: 10.1016/j.egypro.2009.01.233
- Xu, T., Apps, J. A., Pruess, K., & Yamamoto, H. (2007). Numerical modelling of injection and mineral trapping of CO<sub>2</sub> with H<sub>2</sub>S and SO<sub>2</sub> in a sandstone formation. *Chemical Geology*, 242(3), 319-346.
- Xu, T. F., Kharaka, Y. K., Doughty, C., Freifeld, B. M., & Daley, T. M. (2010). Reactive transport modelling to study changes in water chemistry induced by CO<sub>2</sub> injection at the Frio-I Brine Pilot. *Chemical Geology*, 271(3-4), 153-164. doi: 10.1016/j.chemgeo.2010.01.006
- Xu, T. F., & Pruess, K. (2001). Modelling multiphase non-isothermal fluid flow and reactive geochemical transport in variably saturated fractured rocks: 1. Methodology. *American Journal of Science*, 301(1), 16-33. doi: 10.2475/ajs.301.1.16
- Xu, T. F., Spycher, N., Sonnenthal, E., Zhang, G. X., Zheng, L. E., & Pruess, K. (2011). TOUGHREACT Version 2.0: A simulator for subsurface reactive transport under non-isothermal multiphase flow conditions. *Computers & Geosciences*, 37(6), 763-774. doi: 10.1016/j.cageo.2010.10.007
- Zhang, W., Li, Y. L., Xu, T. F., Cheng, H. L., Zheng, Y., & Xiong, P. (2009). Long-term variations of CO<sub>2</sub> trapped in different mechanisms in deep saline formations: A case study of the Songliao Basin, China. *International Journal of Greenhouse Gas Control*, 3(2), 161-180. doi: 10.1016/j.ijggc.2008.07.007
- Zhang, X. X., Deeks, L. K., Bengough, A. G., Crawford, J. W., & Young, L. M. (2005). Determination of soil hydraulic conductivity with the lattice Boltzmann method and soil thin-section technique. *Journal of Hydrology*, 306(1-4), 59-70. doi: 10.1016/j.jhydrol.2004.08.039
- Zhu, C. (2005). In situ feldspar dissolution rates in an aquifer. *Geochimica et Cosmochimica Acta*, 69(6), 1435-1453.

- Zimmer, M., Pilz, P., & Erzinger, J. (2011). Long-term surface carbon dioxide flux monitoring at the Ketzin carbon dioxide storage test site. *Environmental Geosciences*, 18(2), 119-130.
- Zoback, M. D., & Gorelick, S. M. (2012). Earthquake triggering and large-scale geologic storage of carbon dioxide. *Proceedings of the National Academy of Sciences*, 109(26), 10164-10168. doi: 10.1073/pnas.1202473109
- Zoback, M. D., & Zinke, J. C. (2002). Production-induced normal faulting in the Valhall and Ekofisk oil fields. *Pure and Applied Geophysics*, 159(1-3), 403-420. doi: 10.1007/pl00001258
- Zu, Y. Q., & He, S. (2013). Phase-field-based lattice Boltzmann model for incompressible binary fluid systems with density and viscosity contrasts. *Physical Review E*, 87(4), 23. doi: 10.1103/PhysRevE.87.043301

## List of Parameters

- a Pore radius
  - $C^*$  Bubble interfacial CO<sub>2</sub> concentration
  - $C_\infty$  CO<sub>2</sub> concentration in the water
  - D CO<sub>2</sub> bubble diameter
  - $f$  Body force
  - $K$  Bulk modulus
  - $n$  Number of moles
  - P Pressure ( $P_f$  is the pore fluid pressure)
  - $P$  Mean effective compressive stress
  - $Q$  Differential stress
  - $q$  Fluid flux
  - $R_h$  Mean hydraulic radius
  - $S$  Wetted area
  - $u$  Velocity
  - $V$  Pore volume
  - $V_p$  P wave velocity
  - $V_s$  S wave velocity
  - Z Compressibility factor
- 
- $\gamma$  Surface tension
  - $\theta$  Fluids contact angle
  - $\kappa$  Permeability
  - $\eta$  Dynamic viscosity
  - $\mu$  Frictional strength
  - $M$  Shear modulus
  - $\rho$  Density
  - $\sigma$  Stress
  - $\tau$  Tortuosity
  - $\tau_0$  Cohesion
  - $\varphi$  Angle of internal friction
  - $\phi$  Porosity

## Appendix A Construction of mineral maps.

Elements maps are binarized using a built-in threshold function in MATLAB (Figure A1). Reference: Otsu, N., "A Threshold Selection Method from Gray-Level Histograms," *IEEE Transactions on Systems, Man, and Cybernetics*, Vol. 9, No. 1, 1979, pp. 62-66.

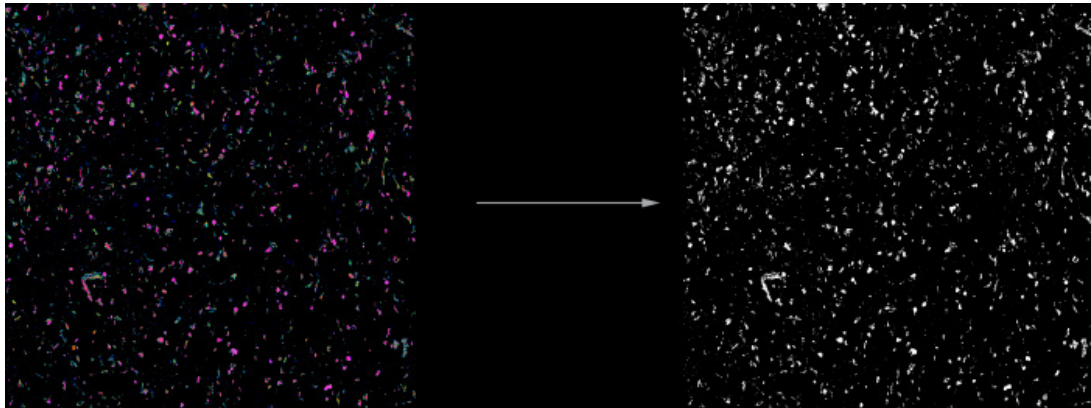


**Figure A1** Binarization of element maps.

By applying simple arithmetic calculations to element maps it is possible to construct mineralogical maps. For example Albite will be at the intersection of the Na and Al maps, it can be noted  $Albite = Na \cap Al$ . Other minerals were obtained with the following rules:

$$Dolomite = Ca \cap Mg,$$

$$Calcite = Ca - Dolomite,$$

$$Microcline \cup Muscovite(White\ Mica) \cup Illite = K \cap Al,$$

$$Kaolinite = Al - (K \cap Na),$$

$$Quartz = Si - All\ elements,$$

$$Pyrite = Fe - All\ elements.$$

Finally, at each mineral map is assigned a colour and the different maps are superposed on a backscattered image. Some ambiguity remains concerning Microcline, Muscovite and Illite. This ambiguity can be removed by considering for example that Microcline is brighter than Muscovite and Illite (on a grey scale image) or by looking at the K and Al levels in details. The accuracy of the mineral maps was then checked manually by manually checking a hundred points with SEM-EDS.

## Appendix B

### Details of the calculation of dimensionless parameters for Table 3.3

The Reynolds number was calculated in the following manner:

$Re = \frac{\rho v L}{\mu}$  (B.1), where  $\rho$  ( $\text{Kg.m}^{-3}$ ) is the fluid density,  $v$  ( $\text{m.s}^{-1}$ ) the fluid interstitial velocity,  $L$  (m) a characteristic dimension (here: the mean pore diameter divided by 4, i.e. the cross sectional area of the pore divided by the wetted perimeter) and  $\mu$  (Pa.s) is the fluid dynamic viscosity.

The fluid velocity was calculated with Equation B.2:

$v = \frac{Q\varphi}{A}$  (2), where  $Q$  ( $\text{m}^3.\text{s}^{-1}$ ) is the flow rate,  $A$  ( $\text{m}^2$ ) is the cross sectional area of the core and  $\varphi$  is the porosity.

The Péclet number is defined for fluid flows as the ratio of advective transport rate over diffusive transport rate:

$Pe = \frac{Lv}{D}$  (3), here I took  $L = 100\mu\text{m}$  (i.e. the mean pore diameter),  $v$  is the fluid interstitial velocity as calculated with Eq. 2, and  $D = 7.5 \cdot 10^{-9} \text{m}^2.\text{s}^{-1}$  is the diffusion coefficient of  $\text{Ca}^{2+}$  cations.

If  $Pe > 1$ , the relevant Da number to characterize the reactive transport is the ratio of acid renewal rate due to advection over the acid consumption rate. Considering that the representative chemical reaction is  $\text{CaCO}_3 + \text{H}^+ \rightarrow \text{Ca}^{2+} + \text{HCO}_3^-$ , it follows:

$Da = \frac{Q[\text{H}^+]_{inlet}}{Q\Delta Ca}$  (4), where  $Q$  is the flow rate and  $\Delta Ca = [\text{Ca}]_{outlet} - [\text{Ca}]_{inlet}$ . Note that this Da number is averaged over the whole core volume.

## Appendix C Random walk Matlab code

```
Connect=dlmread('E:\THESE\Rock models (Benoit)\Rock models
(Benoit)\CB 1mm3\1mm3CB_TLporesconnect350.txt');
% Read the model txt file

n=round(length(Connect)^(1/3));
N=n^3;

%-----
% Exit faces
Exit=zeros(n^3,1);
for r=1:n:n^3-n+1,Exit(r)=1;
end
for r=n:n:n^3,Exit(r)=1;
end
vv=[1:n,n^2-n+1:n^2];
for p=0:n-1,v=p*n^2;V=v+vv;Exit(V)=1;
end
Exit(1:n^2)=1;
Exit(n^3-n^2+1:n^3)=1;

%-----
%%%%%%%%%%%%%%%%%%%%%%%%%%%%%%%%%%%%%%%%%%%%%%%%%%%%%%%%%%%%%%%%%%%%%%%%
%_Simulation Parameters_____
%%%%%%%%%%%%%%%%%%%%%%%%%%%%%%%%%%%%%%%%%%%%%%%%%%%%%%%%%%%%%%%%%%%%%%%%

Num_Walkers=100;
TimeSteps=6*n^2

%%%%%%%%%%%%%%%%%%%%%%%%%%%%%%%%%%%%%%%%%%%%%%%%%%%%%%%%%%%%%%%%%%%%%%%%

Time=0:1:TimeSteps;

%%%%%%%%%%%%%%%%%%%%%%%%%%%%%%%%%%%%%%%%%%%%%%%%%%%%%%%%%%%%%%%%%%%%%%%%
%Initial Position

RandomPosition=randi(length(Connect),Num_Walkers,1);
PositionPW=[];
PW=0;
for k=1:Num_Walkers
    if Connect(RandomPosition(k,1))==0
        PositionPW=[PositionPW;RandomPosition(k,1)];
        PW=PW+1;
    end
end

clear RandomPosition

%%%%%%%%%%%%%%%%%%%%%%%%%%%%%%%%%%%%%%%%%%%%%%%%%%%%%%%%%%%%%%%%%%%%%%%%
% 6 possible jumps

Transport=[-n^2,-n,-1,1,n,n^2];
```

```
%%%%%%%%%%%%%%%%%%%%%%%%%%%%%%%%%%%%%%%%%%%%%%%%%%%%%%%%%%%%%%%%%%%%%%%%
%-----
% Diffusion in poresconnect

CountConnect=zeros (length (Time), 1);
Porosityconnect=(length (Connect)-sum (Connect))/length (Connect)
Position=PositionPW;

for t=2:length (Time)
    for k=1:PW

        % If particle reached exit at the previous step the
particle don't move....
        if imag (Position (k, 1))==0
            % else the particle perform a random discrete step
            r=randi ([1, 6]);
            New=Position (k, 1)+Transport (r);
            if New>0 && New<=N
                if Connect (New)==0
                    Position (k, 1)=New;
                % Check if particles reached the exit
                if Exit (Position (k, 1))==1
                    Position (k, 1)=N*li;
                % Count the particles exiting the domain at one time step
                C=C+1;
            end
        end
    end
end

    end

    CountConnect (t)=CountConnect (t-1)+C;
end
disp ('Poresconnect done')
clear Connect
```

```
%%%%%%%%%%%%%%%%%%%%%%%%%%%%%%%%%%%%%%%%%%%%%%%%%%%%%%%%%%%%%%%%%%%%%%%%
%%%%%%%%%%%%%%%%%%%%%%%%%%%%%%%%%%%%%%%%%%%%%%%%%%%%%%%%%%%%%%%%%%%%%%%%
%%%%%%%%%%%%%%%%%%%%%%%%%%%%%%%%%%%%%%%%%%%%%%%%%%%%%%%%%%%%%%%%%%%%%%%%
%-----
% Diffusion in poresdilate

Countdilate=zeros (length (Time), 1);
Dilate=dlmread ('E:\THESE\Rock models (Benoit)\Rock models
(Benoit)\CB 1mm3\1mm3CB_TLporesdilate350.txt');
Porositydilate=(length (Dilate)-sum (Dilate))/length (Dilate)
Position=PositionPW;

for t=2:length (Time)
    C=0;
    for k=1:PW
        if imag (Position (k, 1))==0
            r=randi ([1, 6]);
            New=Position (k, 1)+Transport (r);
            if New>0 && New<=N
                if Dilate (New)==0
                    Position (k, 1)=New;
                if Exit (Position (k, 1))==1
                    Position (k, 1)=N*li;
                end
            end
        end
    end
end
```

```
        C=C+1;
    end
    end
    end
    end
    end
    Countdilate(t)=Countdilate(t-1)+C;
end

toc
disp('Poresdilate done')
clear Dilate
%%%%%%%%%%%%%%%%%%%%%%%%%%%%%%%%%%%%%%%%%%%%%%%%%%%%%%%%%%%%%%%%%%%%%%%%
%-----

% Diffusion in porescalcite
Countcalcite=zeros(length(Time),1);
Calcite=dlmread('E:\THESE\Rock models (Benoit)\Rock models
(Benoit)\CB 1mm3\1mm3CB_TLcalcite350.txt');
Porositycalcite=(length(Calcite)-sum(Calcite))/length(Calcite)
Position=PositionPW;
tic

for t=2:length(Time)
    C=0;
    for k=1:PW
        if imag(Position(k,1))==0, r=randi([1,6]);
            New=Position(k,1)+Transport(r);
            if New>0 && New<=N
                if Calcite(New)==0, Position(k,1)=New;
                if Exit(Position(k,1))==1, Position(k,1)=N*1i; C=C+1;
            end
            end
            end
            end
        end
        Countcalcite(t)=Countcalcite(t-1)+C;
    end
    toc
    disp('Porescalcite done')
    clear Calcite
    %%%%%%%%%%%%%%%%%%%%%%%%%%%%%%%%%%%%%%%%%%%%%%%%%%%%%%%%%%%%%%%%%%%%%%%%%
    %-----

% Diffusion in Bulk

CountBulk=zeros(length(Time),1);
Position=PositionPW;
tic
for t=2:length(Time)
    C=0;
    for k=1:PW
        if imag(Position(k,1))==0, r=randi([1,6]);
            New=Position(k,1)+Transport(r);
            if New>0 && New<=N, Position(k,1)=New;
            if Exit(Position(k,1))==1, Position(k,1)=N*1i; C=C+1;
            end
            end
            end
            end
        end
    end
end
```

```
CountBulk(t)=CountBulk(t-1)+C;
end
clear PositionPW Exit
toc
disp('bulk done')

%%%%%%%%%%%%%%%%%%%%%%%%%%%%%%%%%%%%%%%%%%%%%%%%%%%%%%%%%%%%%%%%%%%%%%%%
%%%%%%%%%%%%%%%%%%%%%%%%%%%%%%%%%%%%%%%%%%%%%%%%%%%%%%%%%%%%%%%%%%%%%%%%
%%%%%%%%%%%%%%%%%%%%%%%%%%%%%%%%%%%%%%%%%%%%%%%%%%%%%%%%%%%%%%%%%%%%%%%%
%-----
%% Fitting
disp('new fitting')
exponent=linspace(-12.6,-11.6,10);
square_errorconnect=zeros(length(exponent),1);
square_errordilate=zeros(length(exponent),1);
square_errorcalcite=zeros(length(exponent),1);
square_error_bulk=zeros(length(exponent),1);
a=10^-3

%%%%%%%%%%%%%%%%%%%%%%%%%%%%%%%%%%%%%%%%%%%%%%%%%%%%%%%%%%%%%%%%%%%%%%%%
Trunc=TimeSteps/5
%%%%%%%%%%%%%%%%%%%%%%%%%%%%%%%%%%%%%%%%%%%%%%%%%%%%%%%%%%%%%%%%%%%%%%%%
c0=PW/(a^3)

CoCo=CountConnect(Trunc:end);
Codi=Countdilate(Trunc:end);
Coca=Countcalcite(Trunc:end);
Cobu=CountBulk(Trunc:end);

for e=1:length(exponent)

    Diff=10^exponent(e);

N=Nakashima(a,c0,Diff,Time);

square_errorconnect(e)=mean((N(Trunc:end)')-CoCo).^2);
square_errordilate(e)=mean((N(Trunc:end)')-Codi).^2);
square_errorcalcite(e)=mean((N(Trunc:end)')-Coca).^2);
square_error_bulk(e)=mean((N(Trunc:end)')-Cobu).^2);
end
disp('Fit done')

eeconnect=find(square_errorconnect==min(square_errorconnect));
eedilate=find(square_errordilate==min(square_errordilate));
eecalcite=find(square_errorcalcite==min(square_errorcalcite));
eeBulk=find(square_error_bulk==min(square_error_bulk));

Nconnect=Nakashima(a,c0,10^exponent(eeconnect),Time);
Ndilate=Nakashima(a,c0,10^exponent(eedilate),Time);
Ncalcite=Nakashima(a,c0,10^exponent(eecalcite),Time);
Nbulk=Nakashima(a,c0,10^exponent(eeBulk),Time);

Dconnect=10^exponent(eeconnect);
Ddilate=10^exponent(eedilate);
Dcalcite=10^exponent(eecalcite);
Dbulk=10^exponent(eeBulk);

Tau_connect=(10^exponent(eeBulk)/10^exponent(eeconnect))^0.5
Tau_dilate=(10^exponent(eeBulk)/10^exponent(eedilate))^0.5
Tau_calcite=(10^exponent(eeBulk)/10^exponent(eecalcite))^0.5
```





```
P1=real(exp(T/304.1282*sum(ai(1:4)).*(1-
T/304.1282).^ti(1:4)))*7.3773*10);%CO2 vap pressure
elseif T>305 && T<=405
    P1=75+(T-305)*1.25;
elseif T>405
    P1=200;
end

%Fitting coeffs
c=[28.9447706,-0.411370585,3.36389723*10^-4;...
-0.0354581768,6.07632013*10^-4,-1.98298980*10^-5;...
-4770.67077,97.5347708,0;...
1.02782768*10^-5,0,0;...
33.8126098,0,0;...
9.04037140*10^-3,0,0;...
-1.14934031*10^-3,0,0;...
-0.307405726,-0.0237622469,2.12220830*10^-3;...
-0.0907301486,0.0170656236,-5.24873303*10^-3;...
9.32713393*10^-4,0,0;...
0,1.41335834*10^-5,0];

a=[1,-7.1734882*0.1,-6.5129019*0.01,5.0383896,-16.063152,-
1.5693490*0.1;...
4.7586835*10^-3,1.5985379*10^-4,-2.1429977*10^-4,-
4.4257744*10^-3,-2.7057990*10^-3,4.4621407*10^-4;...
-3.3569963*10^-6,-4.9286471*10^-7,-1.1444930*10^-6,0,0,-
9.1080591*10^-7;...
0,0,0,1.9572733,1.4119239*0.1,0;...
-1.3179396,0,0,0,0,0;...
-3.8389101*10^-6,-2.7855285*10^-7,-1.1558081*10^-
7,2.4223436*10^-6,8.1132965*10^-7,1.0647399*10^-7;...
0,1.1877015*10^-9,1.1952370*10^-9,0,0,2.4273357*10^-10;...
2.2815104*10^-3,0,0,-9.3796135*10^-4,-1.1453082*10^-4,0;...
0,0,0,-1.5026030,2.3895671,3.5874255*0.1;...
0,0,0,3.0272240*10^-3,5.0527457*10^-4,6.3319710*10^-5;...
0,0,0,-31.377342,-17.763460,-249.89661;...
0,-96.539512,-221.34306,-12.847063,985.92232,0;...
0,4.4774938*0.1,0,0,0,0;0,101.81078,71.820393,0,0,888.76800;...
0,5.3783879*10^-6,6.6089246*10^-6,-1.5056648*10^-5,-
5.4965256*10^-7,-6.6348003*10^-7];

% Calculation
frac_CO2=(PP*10^-5-PH20)/(PP*10^-5); %mole fraction in vapor phase
% Interaction parameters
muCO2_RT=c(1,1)+c(2,1)*T+c(3,1)/T+c(4,1)*T^2+c(5,1)/(630-
T)+c(6,1)*PP*10^-5+c(7,1)*PP*10^-5*log(T)+c(8,1)*PP*10^-
5/T+c(9,1)*PP*10^-5/(630-T)+...
c(10,1)*(PP*10^-5)^2/(630-T)^2+c(11,1)*T*log(PP*10^-5);

lambda_CO2_Na=c(1,2)+c(2,2)*T+c(3,2)/T+c(4,2)*T^2+c(5,2)/(630-
T)+c(6,2)*PP*10^-5+c(7,2)*PP*10^-5*log(T)+c(8,2)*PP*10^-
5/T+c(9,2)*PP*10^-5/(630-T)+...
c(10,2)*(PP*10^-5)^2/(630-T)^2+c(11,2)*T*log(PP*10^-5);

zeta_CO2_Na_Cl=c(1,3)+c(2,3)*T+c(3,3)/T+c(4,3)*T^2+c(5,3)/(630-
T)+c(6,3)*PP*10^-5+c(7,3)*PP*10^-5*log(T)+c(8,3)*PP*10^-
5/T+c(9,3)*PP*10^-5/(630-T)+...
c(10,3)*(PP*10^-5)^2/(630-T)^2+c(11,3)*T*log(PP*10^-5);

if T>=273 && T<=573 && PP*10^-5<=P1
    aa=a(:,1);
```

```
elseif T>=273 && T<=340 && PP*10^-5>P1 && PP*10^-5<=1000
    aa=a(:,2);
elseif T>340 && T<=435 && PP*10^-5>P1 && PP*10^-5<=1000
    aa=a(:,4);
end

%-----

R=8.3144321*1000;          %Specific gas constant (m3 Pa)/(K kmol)
MolarMassCO2=44;         %g/mol
[density_CO2, cv, cp, SoS]=span_wagner(PP, T);
Compressfactor=PP*MolarMassCO2/(density_CO2*R*T);

%-----

Lwatersat=(100-LCO2SAT)./100;

LDiff=zeros(NLayers,binum);
for g=1:binum
    LDiff(:,g)=DiffCO2.*Lporo./tortuosity;
end

LDIFF=[LDiff(1,1);LDiff(:,1);LDiff(1,end)];

%%%%%%%%%%%%%%%%%%%%%%%%%%%%%%%%%%%%%%%%%%%%%%%%%%%%%%%%%%%%%%%%%%%%%%%%
%=====
%=====

%%%%%%%%%%%%%%%%%%%%%%%%%%%%%%%%%%%%%%%%%%%%%%%%%%%%%%%%%%%%%%%%%%%%%%%%
% Initialisation%
%%%%%%%%%%%%%%%%%%%%%%%%%%%%%%%%%%%%%%%%%%%%%%%%%%%%%%%%%%%%%%%%%%%%%%%%

fugacity_CO2=aa(1)+(aa(2)+aa(3)*T+aa(4)/T+aa(5)/(T-150))*PP*10^-
5+(aa(6)+aa(7)*T+aa(8)/T)*(PP*10^-5)^2+...
(aa(9)+aa(10)*T+aa(11)/T)*log(PP*10^-
5)+(aa(12)+aa(13)*T)/(PP*10^-5)+aa(14)/T+aa(15)*T^2;
Cbulk_init=exp(log(frac_CO2*fugacity_CO2*PP*10^-5)-muCO2_RT-
2*lambda_CO2_Na*(mNa+mK+2*mCa+2*mMg)-...
zeta_CO2_Na_Cl*mCl*(mNa+mK+mMg+mCa)+0.07*mSO4);% (mol/Kg)

TOTAL=zeros(1,1);          %Total amount of CO2 moles

LBubble_size=LSize./10^6;          %Diameter of Bubbles (m)
LBubble_size_NEW=LBubble_size;

LVolumeCO2init=sum(LBubble_num.*4/3*pi.*(LBubble_size./2).^3,2); %I
nitial volume of CO2 per Layer

%-----
% Set number of bubbles to match input CO2 saturation
LCO2satinit=LVolumeCO2init.*100./(Lvolumefraction.*Lporo);
LCorrectsat=LCO2satinit./LCO2SAT;
for i=1:NLayers
    LBubble_num(i,:)=LBubble_num(i,:)./LCorrectsat(i);
end
LBubble_num;
%-----
% Corrected volumes and saturations

LVolumeCO2init=sum(LBubble_num.*4/3*pi.*(LBubble_size./2).^3,2); %m
3
```

```
VolumeCO2init=sum(LVolumeCO2init);

%CO2sat=zeros(1,TimeSteps);
CO2satinit=VolumeCO2init.*100./sum(Lvolumefraction.*Lporo);CO2sat(1)
)=CO2satinit;
LCO2satinit=LVolumeCO2init.*100./(Lvolumefraction.*Lporo);
%-----

LPbubble=PP+4.*gamma./LBubble_size; %Capillary pressure
LPbubble_NEW=LPbubble;

LCinterface=zeros(NLayers,binum); %Interface concentration
LCinterface_NEW=LCinterface;

%%%%%%%%%%%%%%%%%%%%%%%%%%%%%%%%%%%%%%%%%%%%%%%%%%%%%%%%%%%%%%%%%%%%%%%%
frac_CO2=(LPbubble.*10^-5-PH20)./(LPbubble.*10^-5);
muCO2_RT=c(1,1)+c(2,1)*T+c(3,1)/T+c(4,1)*T^2+c(5,1)/(630-
T)+c(6,1).*LPbubble*10^-5+c(7,1).*LPbubble*10^-
5*log(T)+c(8,1).*LPbubble*10^-5./T+c(9,1).*LPbubble*10^-5./(630-
T)+...
c(10,1).*(LPbubble*10^-5).^2./(630-
T)^2+c(11,1)*T*log(LPbubble*10^-5);
lambda_CO2_Na=c(1,2)+c(2,2)*T+c(3,2)/T+c(4,2)*T^2+c(5,2)/(630-
T)+c(6,2).*LPbubble*10^-5+c(7,2).*LPbubble*10^-
5*log(T)+c(8,2).*LPbubble*10^-5./T+c(9,2).*LPbubble*10^-5./(630-
T)+...
c(10,2).*(LPbubble*10^-5).^2./(630-
T)^2+c(11,2)*T*log(LPbubble*10^-5);
zeta_CO2_Na_Cl=c(1,3)+c(2,3)*T+c(3,3)/T+c(4,3)*T^2+c(5,3)/(630-
T)+c(6,3).*LPbubble*10^-5+c(7,3).*LPbubble*10^-
5*log(T)+c(8,3).*LPbubble*10^-5./T+c(9,3).*LPbubble*10^-5./(630-
T)+...
c(10,3).*(LPbubble*10^-5).^2./(630-
T)^2+c(11,3)*T*log(LPbubble*10^-5);
fugacity_CO2=aa(1)+(aa(2)+aa(3)*T+aa(4)/T+aa(5)/(T-
150)).*LPbubble*10^-5+(aa(6)+aa(7)*T+aa(8)/T)*(PP*10^-5).^2+...
(aa(9)+aa(10)*T+aa(11)/T).*log(LPbubble*10^-
5)+(aa(12)+aa(13)*T)./(LPbubble*10^-5)+aa(14)/T+aa(15)*T^2;
%%%%%%%%%%%%%%%%%%%%%%%%%%%%%%%%%%%%%%%%%%%%%%%%%%%%%%%%%%%%%%%%%%%%%%%%
LCinterface=exp(log(frac_CO2.*fugacity_CO2.*LPbubble*10^-5)-
muCO2_RT-2*lambda_CO2_Na*(mNa+mK+2*mCa+2*mMg)-...
zeta_CO2_Na_Cl*mCl*(mNa+mK+mMg+mCa)+0.07*mSO4);% (mol/Kg)

LCbulk=zeros(NLayers,binum);
LCbulk(:,:)=Cbulk_init; %Bulk concentration pL(kmol/m3)

LTransfer=zeros(NLayers,1); LTransfer(:,1)=0; %Transfer
bubbles<=>bulk pL(kmol)

LCO2sat=zeros(NLayers,1); LCO2sat(:,1)=LCO2satinit; %CO2 sat pL(%)

LCO2solinit=Cbulk_init.*Lvolumefraction.*Lporo.*(1-
LCO2satinit./100); %Initial dissolved CO2 pL(kmol)

LCO2sol=zeros(NLayers,1); LCO2sol(:,1)=LCO2solinit;
```

```
TOTALinit=sum(LVolumeCO2init.*PP./ (Compressfactor*R*T)+LCO2solinit);

TOTAL(1)=TOTALinit;

%=====
% Data sampling settings

DATA_Points=round(linspace(2,TimeSteps, iters));
%DATA_time=dtstart*DATA_Points;%./ (3600*24);
DATA_time=zeros(1,length(DATA_Points));
LDATA_size=zeros(NLayers,binum,length(DATA_Points));
LDATA_pressure=zeros(NLayers,binum,length(DATA_Points));
LDATA_Cinterface=zeros(NLayers,binum,length(DATA_Points));
LDATA_num=zeros(NLayers,binum,length(DATA_Points));
LDATA_Cbulk=zeros(NLayers,length(DATA_Points));
LDATA_Transfer=zeros(NLayers,length(DATA_Points));
LDATA_Lsat=zeros(NLayers,length(DATA_Points));
LDATA_sat=zeros(1,length(DATA_Points));
LDATA_flux=zeros(NLayers-1,length(DATA_Points));
LDATA_total=zeros(1,length(DATA_Points));
LDATA_GAS=zeros(NLayers,length(DATA_Points));
LDATA_SOL=zeros(NLayers,length(DATA_Points));
%=====
%=====
%%%%%%%%%%%%%%%%%%%%%%%%%%%%%%%%%%%%%%%%%%%%%%%%%%%%%%%%%%%%%%%%%%%%%%%%%%

%%%%%%%%%%%%%%%%%%%%%%%%%%%%%%%%%%%%%%%%%%%%%%%%%%%%%%%%%%%%%%%%%%%%%%%%%%
% Main Code%
%%%%%%%%%%%%%%%%%%%%%%%%%%%%%%%%%%%%%%%%%%%%%%%%%%%%%%%%%%%%%%%%%%%%%%%%%%

k=1;
time=0;
for n=2:1:TimeSteps

ControlP=LPbubble>0;
%-----
-----
%New pressure using last step diameter
%New interface Concentration use new bubble Pressure

    LPbubble_NEW=PP+4*gamma./ (LBubble_size).*ControlP;
    LPbubble_NEW(isnan(LPbubble_NEW))=0;

%%%%%%%%%%%%%%%%%%%%%%%%%%%%%%%%%%%%%%%%%%%%%%%%%%%%%%%%%%%%%%%%%%%%%%%%%%
%%%%%%%%%%%%%%%%%%%%%%%%%%%%%%%%%%%%%%%%%%%%%%%%%%%%%%%%%%%%%%%%%%%%%%%%%%
frac_CO2=(LPbubble_NEW.*10^-5-PH20)./ (LPbubble_NEW.*10^-5);
muCO2_RT=c(1,1)+c(2,1)*T+c(3,1)/T+c(4,1)*T^2+c(5,1)/(630-
T)+c(6,1).*LPbubble_NEW*10^-5+c(7,1).*LPbubble_NEW*10^-
5*log(T)+c(8,1).*LPbubble_NEW*10^-5./T+c(9,1).*LPbubble_NEW*10^-
5./ (630-T)+...
    c(10,1).*(LPbubble_NEW*10^-5).^2./ (630-
T)^2+c(11,1)*T*log(LPbubble_NEW*10^-5);
%lambda_CO2_Na=c(1,2)+c(2,2)*T+c(3,2)/T+c(4,2)*T^2+c(5,2)/(630-
T)+c(6,2).*LPbubble_NEW*10^-5+c(7,2).*LPbubble_NEW*10^-
5*log(T)+c(8,2).*LPbubble_NEW*10^-5./T+c(9,2).*LPbubble_NEW*10^-
5./ (630-T)+...
%    c(10,2).*(LPbubble_NEW*10^-5).^2./ (630-
T)^2+c(11,2)*T*log(LPbubble_NEW*10^-5);
%zeta_CO2_Na_Cl=c(1,3)+c(2,3)*T+c(3,3)/T+c(4,3)*T^2+c(5,3)/(630-
T)+c(6,3).*LPbubble_NEW*10^-5+c(7,3).*LPbubble_NEW*10^-
```

```
5*log(T)+c(8,3).*LPbubble_NEW*10^-5./T+c(9,3).*LPbubble_NEW*10^-
5./(630-T)+...
%      c(10,3)*(LPbubble_NEW*10^-5).^2./(630-
T)^2+c(11,3)*T*log(LPbubble_NEW*10^-5);
fugacity_CO2=aa(1)+(aa(2)+aa(3)*T+aa(4)/T+aa(5)/(T-
150)).*LPbubble_NEW*10^-5+(aa(6)+aa(7)*T+aa(8)/T)*(PP*10^-5).^2+...
(aa(9)+aa(10)*T+aa(11)/T).*log(LPbubble_NEW*10^-
5)+(aa(12)+aa(13)*T)./(LPbubble_NEW*10^-5)+aa(14)/T+aa(15)*T^2;
%%%%%%%%%%%%%%%%%%%%%%%%%%%%%%%%%%%%%%%%%%%%%%%%%%%%%%%%%%%%%%%%%%%%%%%%
%%%%%%%%%%%%%%%%%%%%%%%%%%%%%%%%%%%%%%%%%%%%%%%%%%%%%%%%%%%%%%%%%%%%%%%%

%
LCinterface=(exp(log(frac_CO2.*fugacity_CO2.*LPbubble_NEW*10^-5)-
muCO2_RT-2*lambda_CO2_Na*(mNa+mK+2*mCa+2*mMg)-...
%      zeta_CO2_Na_Cl*mCl*(mNa+mK+mMg+mCa)+0.07*mSO4)).*ControlP;%
(mol/Kg)
LCinterface=(exp(log(frac_CO2.*fugacity_CO2.*LPbubble_NEW*10^-5)-
muCO2_RT));% (mol/Kg)
LCinterface(isnan(LCinterface))=0;

%-----
%New diameter after dt, evolving from last step conditions

LBubble_size_NEW=LBubble_size+(Compressfactor*12*R*T.*DiffCO2.*(LCb
ulk-LCinterface)./(3*PP.*LBubble_size+8*gamma)).*dtstart.*ControlP;
%-----
% REST

LREST=(LPbubble.*4/3.*pi.*(LBubble_size./2).^3)./(Compressfactor*R*
T).*LBubble_num.*(LBubble_size_NEW<0);

      LBubble_num=LBubble_num.*(LBubble_size_NEW>0);
%-----
% Transfer (kmol)
      LTransfer=sum(-2*pi.*DiffCO2.*LBubble_size.*(LCbulk-
LCinterface).*LBubble_num.*dtstart+LREST,2);
      LPbubble=LPbubble_NEW.*(LBubble_size_NEW>0);
      LBubble_size=LBubble_size_NEW.*(LBubble_size_NEW>0);

%-----
% New values for Cbulk, CO2 sat , dissolved CO2. Before diffusion
between
% layers
      gasCO2=sum(LBubble_num.*4/3*pi.*(LBubble_size./2).^3,2);
      LCO2sat=gasCO2.*100./(Lvolumefraction.*Lporo);
%-----

%-----
LCO2sol=LCO2sol+LTransfer;

LCbulk=(LCO2sol./(Lvolumefraction.*Lporo.*(1-
LCO2sat./100)))*ones(1,binum);

%-----
%-----
% Flux between layers

LCbulk_NEW=[LCbulk(1,1);LCbulk(:,1);LCbulk(1,end)];
```

```
LCbulk=(LCbulk_NEW(2:end-
1)+dtstart.*DiffCO2/(DX^2).*(LCbulk_NEW(3:end)+LCbulk_NEW(1:end-2)-
2.*LCbulk_NEW(2:end-1)))*ones(1,binum);

LCO2sol=LCbulk(:,1).*(Lvolumefraction.*Lporo.*(1-LCO2sat./100));

%-----
%=====
%Data Sampling
if n==round(DATA_Points(k))

% Total amount of CO2 in system "FOR CONTROL"
TOTAL=sum(gasCO2).*PP./(Compressfactor*R*T)+sum(LCO2sol);
CO2sat=sum(gasCO2).*100./sum(Lvolumefraction.*Lporo);
%-----
-----

    LBubble_size;
    LDATA_size(:, :, k)=LBubble_size;
    LDATA_pressure(:, :, k)=LPbubble;
    LDATA_Cinterface(:, :, k)=LCinterface;
    LDATA_num(:, :, k)=LBubble_num;

    DATA_time(1, k)=time/(3600*24);
    LDATA_GAS(:, k)=gasCO2.*PP./(Compressfactor*R*T);
    LDATA_SOL(:, k)=LCO2sol;

    LDATA_Cbulk(:, k)=LCbulk(:, 1);
    LDATA_Transfer(:, k)=LTransfer;
    LDATA_Lsat(:, k)=LCO2sat;
    LDATA_sat(k)=CO2sat;
    LDATA_flux(:, k)=JLiLj;
    LDATA_total(1, k)=TOTAL;
    k=k+1;
end

end
```